UNIVERSITY OF BIRMINGHAM

Effective Nanomaterials for Active Drug Delivery

by

Ismail Adwibi

A thesis submitted to the University of Birmingham for the degree of DOCTOR OF PHILOSOPHY

School of Geography, Earth and Environmental Sciences

College of Life and Environmental Sciences

University of Birmingham

February 2024

Abstract:

In the field of nanomedicine, materials in the nanoscale range play a crucial role as diagnostic instruments and targeted carriers of therapeutic compounds. This relatively new but rapidly advancing discipline offers promising applications. For example, by utilising engineered nanoparticles, cellular processes can be specifically targeted for immediate healing or early detection of illnesses. Nanomedicine has shown great potential in treating various medical conditions, by using chemotherapeutic drugs and immunotherapeutic agents.

This research focuses on the synthesis of monodisperse batches of gold nanoparticles with various coating agents, with the objective of controlling their size within the range 8 and 60 nm in diameter, with the purpose to test and identify an optimal size for drug delivery. Subsequently, modified citrate gold nanoparticles were conjugated with two different types of medicines called amantadine and remdesivir, expanding the possibilities for their use in nanomedicine.

This doctoral project involves the encapsulation of amantadine into polymeric nanoparticles made of poly lactide-co-glycolic acid, leveraging their unique bioavailability and low toxicity properties. The polymeric nanoparticles are engineered to minimise toxicity and immunogenicity, ensuring compatibility with biological systems. Furthermore, these engineered nanoparticles exhibit target-specific properties through functionalisation with ligands that recognise specific receptors or markers present on the surface of diseased cells or tissues. Consequently, they enable targeted delivery of amantadine and remdesivir drugs to the desired location within the J774 cell line macrophages. Additionally, the

formation of biodegradable polymers enables the controlled release of the encapsulated amantadine drug.

Thus, herein, the conjugation of the two drugs to gold nanoparticles and the encapsulation of amantadine drug in polymeric nanoparticles aimed to achieve several outcomes, including improving drug delivery, enabling controlled drug release, enhancing drug solubility and bioavailability, and ensuring the protection and stability of drugs. All of these goals contribute to the development of more efficient, precise, and safe drug delivery systems in the field of nanomedicine.

بسم الله الرحمن الرحيم

Acknowledgement

At the outset, I would like to start by saying ''Alhamdulillah'' to finish my PhD. Firstly, I would like to thank my lead supervisor, Eugenia (Éva) Valsami-Jones, for all her guidance and support through my PhD's journey, and she indeed deserves the most of my gratitude. She has played a major role in this success by giving me the valuable advice and guidance necessary to develop my research capabilities. Also, my special thanks to my co-supervisor, Dr. Hanene Ali-Boucetta, for her excellent ideas and support.

The contributions of Nicholas Davidson for significant laboratory support, Christopher Stark for ICP-OES analysis, and Dr. Peng Zhang for research support in the School of Geography, Earth and Environmental Science at the University of Birmingham, in addition to Theresa Morris for TEM analysis in the School of Metallurgy and Materials at the University of Birmingham, will be much appreciated. I would like to express my sincere thanks to my colleagues in the Nano Research group in the School of Geography, Earth and Environmental Science at the University of Birmingham especially for Ana Isabel Carrazco Quevedo, Taiwo Hassan Akere and Bashiru Ibrahim for training support.

I am also very grateful to the Libyan Ministry of Education for their confidence in me and for giving me this opportunity to develop my research skills. I will never forget the support of my father, mother, brothers and sisters throughout my educational career and since my childhood. These moments will remain in my memory for the rest of my life. And all thanks, respect, and appreciation to my

beloved wife and children, who were patient with me until I finished my honorary doctorate.

List of Publications

This thesis has four research chapters that are in preparation for publication in peer-reviewed journals.

- **Adwibi, I.A.**, Zhang, P., Ali-Boucetta, H., & Valsami-Jones, E. (2024) An innovative technique for synthesis and size tuning of gold nanoparticles

- **Adwibi, I.A.**, Ali-Boucetta, H., & Valsami-Jones, E. (2024) Enhanced Conjugation of Amantadine to gold nanoparticles via carbetamide cross-linking chemistry

- **Adwibi, I.A.**, Ali-Boucetta, H., & Valsami-Jones, E. (2024) Amantadine Encapsulation in PLGA Polymeric Nanoparticles: Leveraging Pluronic F68 and Oleic Acid as Enhancing Agents

- **Adwibi, I.A.**, Ali-Boucetta, H., & Valsami-Jones, E. (2024) Conjugation of Remdesivir with Gold Nanoparticles for Enhanced Therapeutic Efficacy

Table of Contents

List of Figures

List of Tables

List of Abbreviations

$OH^{\bullet}$	hydroxyl radical
%	percentage
µs	micro second
^{13}C	carbon thirteen
^{1}H	proton
AA	ascorbic acid
Ag NO_3	silver nitrate
Ag NPs	silver nanoparticles
AMTD	amantadine
AMTD/Au NPs	Amantadine-conjugated gold nanoparticles
ANOVA	Analysis of Variance
Au NPs	gold nanoparticles
Au-S	gold-sulfur bond
BBB	blood brain barrier
BMP-2	bone morphogenetic protein
BSA	bovine serum albumin
C	carbon atom
C=O	carbonyl group
CDC_{l3}	deuterated chloroform
CDI	carbonyl diimidazole
C-H	a methyl group
cm	centimetre
CMC	critical micelle concentration

CNTs	carbon nanotubes
CO_2	carbon dioxide
COOH	carboxylic acid
COX-2	cyclooxygenase-2
CS	chitosan
CTAB	hexadecyl trimethyl ammonium bromide
Cu	copper
Cu NPs	copper nanoparticles
$CuCl_2$	Copper (II) chloride
d.nm	diameter value in nanometer
DDC	N,N′-dicyclohexylcarbodiimide
DDs	Drug Delivery system
Dh	hydrodynamic diameter
DHLA	Dihydrolipoic acid
DMEM	Dulbecco's Modified Eagles Medium
DNA	Deoxyribonucleic acid
EAS	electrophilic aromatic substitution
ECACC	European Collection of Authenticated Cell Cultures
EDC	N-(3-Dimethylaminopropyl)-*N*′-ethylcarbodiimide hydrochloride
Eng NPs	Engineered nanoparticles
FBS	fetal bovine serum
FTIR	fourier transform infrared
FWHM	full width at half maximum

H_2O_2	hydrogen peroxide
$HAuCl_4$	chloroauric acid
He	Helium
HEPES	4-(2-hydroxyethyl)-1-piperazineethanesulfonic acid
HIV	human immunodeficiency virus
IgG	Immunoglobulin G
IR	infrared (IR)
J774	cell line macrophages
K^+	potassium ion
K-562	lymphoblast cells
L NPs	lipid nanoparticles
LDH	lactate dehydrogenase
LSPR	Localised surface plasmon resonance
Mb	myoglobin
mg	milligram
mm	millimetre
MRI	Magnetic resonance imaging
MTT	1-(4,5-Dimethylthiazol-2-yl)-3,5-diphenylformazan
MUDA	11-mercaptoundecanoic acid
mV	millivolt
MWCNTs	Multi-walled carbon nanotubes
N	nitrogen atom
Na^+	sodium ion
NaCl	sodium chloride

NAS	nucleophilic aromatic substitution reaction
NDDN	Nanomedicine, Drug Delivery & Nanotoxicology
$-NH_2$	Primary amine
NHS	N-Hydroxy succinimide
NLCs	Nanostructured lipid carriers
nm	nanometre
NMs	nanomaterials
NMDA	N-methyl-D-aspartate, glutamate receptors
OCT 3	Organic Cation Transporter 3
OD	optical density
O-H	hydroxyl group
P NPs	polymeric nanoparticles
P value	probability value
Pb	lead (chemical element)
PBS	phosphate buffer solution
PD	Parkinson's disease
PDI	poly dispersity index
PEG	Poly (ethylene glycol)
PEG-Au NPs	Poly (ethylene glycol)-gold nanoparticles
PEO	polyethylene oxide
PGA	Poly glycolic acid
pH	potential of hydrogen
pKa	The acid dissociation constant
PLA	poly lactic acid

PLGA	poly (D, L-Lactide-co-glycolide)
PLGA NPs	poly lactide-co-glycolide nanoparticles
ppm	parts per million
PPO	polypropylene oxide
PVA	polyvinyl alcohol
QDs	quantum dots
r	correlation coefficient
R^2	regression square
R_2-NH	secondary amine group
R-COO^-	carboxylate group
REM	Remdesivir
REM/Au NPs	Remdesivir-conjugated gold nanoparticles
RF	radio-frequency
RNA	Ribonucleic acid
R-NH_2	primary amine group
R-NHCO-	amide
ROS	reactive oxygen species
R-SH	free thiol group
SL NPs	Solid-lipid nanoparticles
SPIO NPs	Superparamagnetic iron oxide nanoparticles
SPR	surface plasmon resonance
SRB	Sulforhodamine-B
S-S	disulfide bond
std.	standard

Sulfo-NHS	Sulfo-N-Hydroxy succinimide
SWCNTs	single-walled carbon nanotubes
TEM	transmission electron microscopy
TGA	thermogravimetric analysis
THF	tetrahydrofuran
TiO_2 NPs	silicon dioxide nanoparticles
TS	trolamine salicylate
US FDA	The United States Food and Drug Administration
V	Volume
XTT	2,3-Bis-(2-Methoxy-4-Nitro-5-Sulfophenyl)-2H-Tetrazolium-5-Carboxanilide
ζ	zeta potential
α	Cronbach's alpha or coefficient alpha
N	number of items
$\bar{c}$	average covariance between item-pairs
$\bar{v}$	average variance

Chapter (1): Introduction

1.1 Background

The development of drug delivery using nanocarriers represents a significant advancement in the field of pharmaceutical sciences. It aims to improve therapeutic outcomes by enhancing the delivery of drugs to specific targets in the body while minimizing side effects (Afzal et al., 2022).

Nanoparticles within the size rang 1-100 nm can be utilised for encapsulation or transportation of therapeutic agents such as drugs, genes or proteins (Din et al., 2017; S. Hong et al., 2020; R. Singh & Lillard Jr, 2009). Traditional drug delivery systems often face limitations such as poor bioavailability, rapid clearance from the body or lack of specificity for diseased tissues. Therefore, nowadays nanoparticles offer unique advantages that address these challenges (Afzal et al., 2022; Patra et al., 2018).

Nanoparticles can be designed with precise control over their size, shape, surface properties and drug-loading capacity. These properties enable them to overcome biological barriers, enhance drug stability and improve drug solubility. Additionally, their small size allows for increased cellular uptake, prolonged circulation time and the potential for passive or active targeting to specific tissues or cells (Mitchell et al., 2021; Su & M. Kang, 2020; Waheed et al., 2022).

Various types of nanoparticles have been developed, including liposomes, polymeric nanoparticles, dendrimers, micelles, solid lipid nanoparticles and inorganic nanoparticles such as gold or iron oxide nanoparticles. Each type offers distinct characteristics and can be tailored to accommodate different types of

drugs and target specific diseases or organs (Majumder et al., 2019; Patra et al., 2018).

The development of drug delivery using nanoparticles has significantly impacted several areas of medicine. It has provided new treatment options for diseases such as cancer, cardiovascular disorders, neurological disorders, and infectious diseases (Mohamed et al., 2022; Saeedi et al., 2019; A. P. Singh et al., 2019; Yao et al., 2020). By encapsulating drugs within nanocarriers, it is possible to improve drug stability, extend drug release, reduce systemic toxicity, and achieve localised and sustained drug delivery (De et al., 2022).

Furthermore, nanocarriers have opened avenues for combination therapy, where multiple drugs or therapeutic agents can be co-encapsulated within a single nanocarrier to enhance treatment efficacy (Konhäuser et al., 2022). Despite the tremendous potential of nanocarriers, challenges remain in terms of manufacturing scalability, regulatory considerations, and long-term safety assessments. Nonetheless, ongoing research and technological advancements continue to drive the development of innovative drug delivery systems using nanocarriers, with the ultimate goal of revolutionising drug delivery for improved patient outcomes.

1.2 Research Gap

Gold nanoparticles (Au NPs) currently have significant applications in various fields due to their unique properties. The term ‘’tuned’’ gold nanoparticles refers to nanoparticles whose size, shape or surface properties have been precisely controlled or engineered to achieve specific characteristics, enabling

functionalisation of biomolecules for biomedical applications (S. Liu & Lämmerhofer, 2019; Piella et al., 2016; Sivaraman et al., 2010; Suchomel et al., 2018).

Carbodiimide cross-linking chemistry is a versatile and widely used method in the field of drug delivery, offering a means to modify and enhance the properties of biomolecules and materials for improved therapeutic outcomes. This chemical reaction involves the activation of carboxylic acid groups to facilitate the formation of covalent bonds between molecules, resulting in cross-linked structures. The carbodiimide reagent acts as a coupling agent, mediating the reaction between carboxylic acid groups and amine groups, leading to the formation of stable amide bonds. Carbodiimide cross-linking chemistry comes with certain limitations and challenges. One of the most common challenges is cytotoxicity, particularly for water-soluble substances, such as 1-ethyl-3-(3-dimethylaminopropyl) carbodiimide called EDC, which can exhibit cytotoxic effects at higher concentrations. Researchers addressed these limitations by combining carbodiimide cross-linking with other techniques or modifying the reaction conditions (Joshi et al., 2011).

Furthermore, determining the optimal drug loading capacity within poly (lactic-co-glycolic acid) nanoparticles (PLGA NPs) while maintaining controlled and sustained release profiles is a challenge. There is a need to establish a balance between achieving high drug encapsulation efficiency and minimising burst release, especially for hydrophilic or high-dose drugs (Hines & Kaplan, 2013; Makadia & Siegel, 2011).

1.3 Nanotechnology

Nanomaterials (NMs) fall within the range size 1-100 nm, they have a wide spectrum of uses, especially in the biomedical field. The potential to control their physicochemical properties such as biocompatibility, surface area and surface chemistry offers the possibility to influence cellular processes (Kong et al., 2017; Patra et al., 2018). At present, there are several NMs utilised as drug carriers for treatment purposes. For example, there is a considerable number of studies in the literature that investigate the significant importance and outcomes of engineered nanoparticles (Eng NPs) such as gold nanoparticles (Au NPs), silver nanoparticles (Ag NPs), polymeric (P NPs) and liposome-based nanoparticles (L NPs), superparamagnetic iron oxide nanoparticles (SPIO NPs), and quantum dots (QDs) (Murthy, 2007; Sztandera et al., 2018; Z. Wang et al., 2020; Yin et al., 2020).

These novel nanomaterials were developed for biomedical (Mabrouk et al., 2021), environmental (Dong et al., 2014), and energy applications (X. Wang & Chen, 2018) and nano-biostructured systems for the innovation of bio-catalytic processes in the food industry (Neethirajan & Jayas, 2011). For example, hybrid nanomaterials composed of inorganic and organic compounds were discovered for cancer imaging (He & Lin, 2015). Advancements in nanomaterials were reported by El-Sayed & Kamel, (2020) concerning the drug and gene release.

Nanomaterials offer numerous benefits and potential applications, but they also come with certain limitations and challenges that need to be carefully addressed. One of the most common limitations of nanomaterials include, the toxicity effect of very small nanoparticles. Therefore, researchers addressed these challenges

by modifying the surface of nanomaterials with biocompatible coatings or molecules to enhance their biocompatibility and reduce potential toxicity (Gao et al., 2012; Maulik et al., 2009; Sangwan & Seth, 2021).

1.4 Classifications of Nanomaterials

Nanomaterials can be classified based on various attributes, including their composition, size, shape and other physicochemical properties.

1.4.1 Polymeric Nanoparticles

Polymeric nanoparticles are a type of nanomaterial composed of synthetic or natural polymers with high molecular weight. Therefore, they are characterised with relatively large particles size range from 1 to 1000 nm (Zielińska et al., 2020). They can be used for loading active drug molecules to give the advantage of controlling drug release at a specific duration (Muhamad12 et al., 2014; Senapati et al., 2018; Sur et al., 2019). They can be chemically modified or engineered to exhibit specific characteristics, such as biodegradability, biocompatibility, and controlled degradation rates. For example, the process of encapsulating drug molecules within polymeric NPs is known as drug loading, and it involves several strategies to achieve efficient encapsulation and controlled release. These techniques involving, the emulsion techniques (Halnor et al., 2018), nanoprecipitation (Yadav & Sawant, 2010), self-assembly (Dahiya & Dahiya, 2021) or by active loading for the hydrophobic drugs (J.-M. Lim et al., 2019).

In addition, these polymeric nanoparticles have the ability to protect drug molecules from any undesirable enzymatic degradation and improve their bioavailability and therapeutic index (Chenthamara et al., 2019). Furthermore, it

was reported that the toxicity of drug molecules can be reduced, and their bioavailability improved when loaded into polymeric nanoparticles such as poly (lactide-co-glycolide) (PLGA) nanoparticles (Escalona-Rayo et al., 2019).

Various types of polymeric nanoparticles have been employed to load active drug molecules, taking into account their chemical properties and the intended route of administration. Although, different medicines have varying chemical properties, in consequence, the selection of a polymer for drug loading must align with these properties to ensure proficient encapsulation and controlled release of the drug. For instance, Escalona-Rayo et al. (2019) discovered the acetylated dextran-based nanoparticles for loading Hyperforin. In addition, study conducted by Moncalvo et al. (2020), for application of Poly (ethylene glycol) (PEG) as a delivery system for proteins, demonstrating its potential to enhance protein stability, solubility, and bioavailability, while also reducing their toxicity and extending the half-life of therapeutic proteins. Thus, the choice of polymer affects the biodegradability and biocompatibility of the resulting NPs. Biodegradable polymers like PLGA are commonly used to ensure safe breakdown and elimination of NPs in the body (Makadia & Siegel, 2011).

1.4.2 Lipid-Based Nanoparticles

Lipid-based nanoparticles can be classified into three different types: liposomes, solid-lipid nanoparticles (SLNPs), and nanostructured lipid carriers (NLCs). These nanoparticles can exhibit promising delivery of hydrophobic and hydrophilic molecules with low toxic effects (Ghasemiyeh & Mohammadi-Samani, 2018). In addition, lipid-based nanoparticles play a crucial role in controlled drug release and have the ability to prolong the half-life of these active drug molecules

based on the therapeutic target site (Davis & Brewster, 2004). They can be modified with other chemicals to improve their solubility and overcome any fast-rate clearance conditions induced by the immune system (Davis & Brewster, 2004).

It has been reported that liposomes are one of the most lipid-based nanoparticles applied in drug delivery systems (DDs) owing to their biocompatibility and biodegradability (García-Pinel et al., 2019). They are comprised of phospholipids, which spontaneously form a double layer termed a lipid bilayer (Chaffey, 2003). The hydrophobic tail is usually sandwiched between the hydrophilic head layers, as shown in **Figure 1.1**.

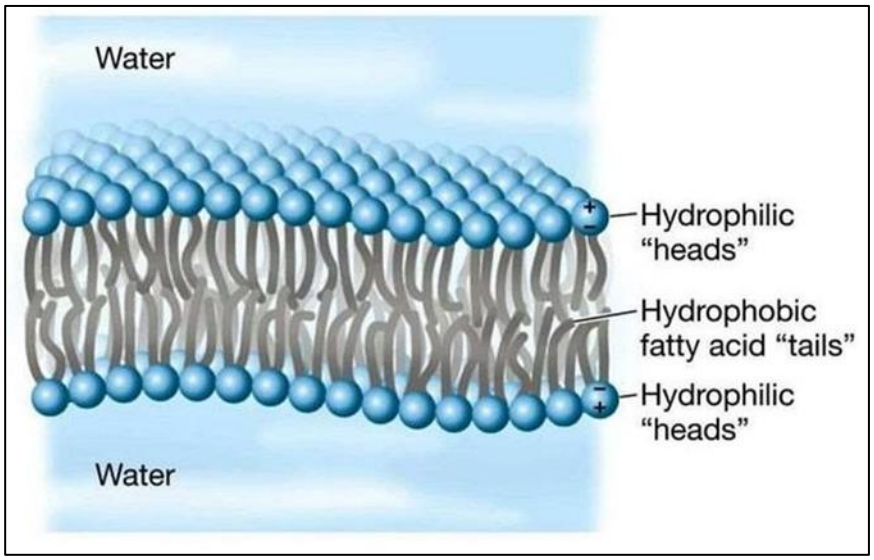

Figure 1. 1. Schematic of the phospholipid bilayer consists of amphiphilic phospholipid molecules arranged with hydrophilic heads and hydrophobic fatty acid tails (Chaffey, 2003).

1.4.3 Magnetic Nanoparticles

Magnetic nanoparticles can be categorised as a type of nanoparticles that can be manipulated using a magnetic field (Dasari et al., 2022). Typically, they consist of a magnetic core made of materials such as iron, nickel, or cobalt, which is coated with chemical agents on the surface of the nanoparticles, as depicted in **Figure 1.2**. Magnetic nanoparticles can be functionalised with ligands that target specific cells, tissues, or organs. When an external magnetic field is applied, these nanoparticles can be guided precisely to the desired target site, allowing for localised drug (Prijic & Sersa, 2011).They may have certain disadvantages, such as potential harm to healthy tissue surrounding cancer cells, limited ability to generate heat within cancerous tissue, and insufficient heat for treating certain types of cancer (Flores-Rojas et al., 2022). Moreover, they exhibit limitations in terms of low therapeutic effectiveness, particularly when employed in ocular drug delivery systems (Schneider-Futschik & Reyes-Ortega, 2021).

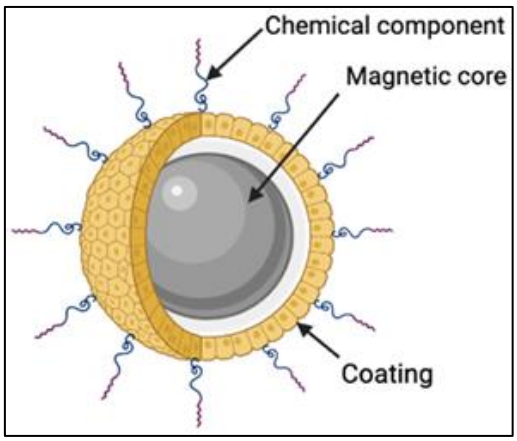

Figure 1. 2. Magnetic nanoparticles composition. The magnetic core is composed of magnetic material, often iron oxide or other magnetic alloys. The surface is typically coated with stabilising agents (Dasari et al., 2022).

1.4.4 Silica Nanoparticles

Silica is abundant in the natural environment (in rocks and soils) and is commonly synthesised for a range of applications, such as, for example, as a food additive (Bitar et al., 2012). In the biomedical field, silica serves various purposes, including acting as an ingredient in pharmaceuticals and vitamins to prevent sedimentation in liquid suspensions (Bitar et al., 2012). Consequently, the utilisation of silica nanoparticles, which, compositionally, consist of silicon dioxide (SiO_2), has gained momentum in different domains, including drug delivery systems. For instance, mesoporous silica-based nanoparticles have recently emerged as a promising nanocarrier for treating various diseases (Karaman & Kettiger, 2018). However, Bharti et al. (2015) have reported a significant drawback of mesoporous silica-based nanoparticles concerning the interaction between the nanoparticles' surface silanol group and the phospholipids on the red blood cell membrane, which may result in hemolysis, the abnormal destruction of red blood cells (Bharti et al., 2015).

1.4.5 Carbon-Based Nanoparticles

Carbon-based nanomaterials possess exceptional physical and chemical properties, making them highly appropriate for biomedical applications, particularly in the field of drug delivery (Zare et al., 2021). Notably, carbon nanotubes (CNTs) have gained significant attention as potential drug carriers within living cells, as they can easily penetrate a biological cell membrane (Cha, 2013; Chen et al., 2008). CNTs can be classified into two primary categories based on the number of carbon layers they consist of: single-walled carbon nanotubes (SWCNTs) and multi-walled carbon nanotubes (MWCNTs). These

nanotubes possess a simple chemical structure and exhibit remarkably high thermal conductivity at temperatures above 300 K, owing to the strength of their atomic bonds (Q. Zhang et al., 2002). However, the utilisation of CNTs involves limitations, including impurities, irregular morphology, large surface area that facilitates protein opsonisation, insolubility, and hydrophobicity (Chatterjee & Deopura, 2002; P.-X. Hou et al., 2008; Porwal et al., 2017; Simon et al., 2019).

1.4.6 Metallic Nanoparticles

Metallic nanoparticles are composed solely of metals such as copper, silver, or gold (Khan et al., 2019). These nanoparticles have been the subject of investigation for over a century and have recently found significant applications in biomedical sciences (Klębowski et al., 2018). Various techniques can be employed for the preparation of noble metal-based nanoparticles. For instance, the reduction of metal precursors such as copper (II) chloride ($CuCl_2$), silver nitrate ($AgNO_3$), or chloroauric acid ($HAuCl_4$) using appropriate reducing agents is considered one of the most popular methods to obtain respectively copper, silver or gold nanoparticles (Betancourt-Galindo et al., 2014; García-Barrasa et al., 2011; Kimling et al., 2006). Furthermore, the manipulation of different parameters including pH, temperature, concentration ratio, capping agents and reaction duration time can influence the formation of nanoparticles with distinct sizes and shapes (An & Somorjai, 2012).

1.4.6.1 Copper Nanoparticles

Copper nanoparticles are particularly attractive for various applications due to the low cost and abundance of copper (Cu) in nature (Evano et al., 2008). Cu possesses unique physical and chemical properties that make it a catalytically

active material (Gawande et al., 2016). Copper-based nanocatalysts find numerous applications in nanotechnology, including electrocatalysis and photocatalysis (Gawande et al., 2016). Additionally, Copper nanoparticles have the advantage of forming highly stable nanoparticles when they undergo oxidation (Gawande et al., 2016). However, despite the extensive use of bulk copper in various industries such as optics and electronics, the application of copper nanoparticles (Cu NPs) has been limited due to their intrinsic instability under atmospheric conditions, which makes them prone to oxidation (Gawande et al., 2016).

1.4.6.2 Silver Nanoparticles

Silver nanoparticles (Ag NPs) possess notable characteristics such as high conductivity, strong signal capacity, and biocompatibility, making them valuable components in electrochemical sensor platforms due to their unique properties. In the past two decades, researchers have dedicated significant efforts to develop new techniques utilising silver nanoparticles and their composites for biotechnological applications (X.-F. Zhang et al., 2016). Notably, Ag NPs exhibit antibacterial and anticancer properties. Several mechanisms reported in the literature regarding the eradication of undesirable cells by silver nanoparticles. For instance, when Ag NPs accumulate in endosomes, they are transported by organelles to the lysosomal function. Within the lysosomal acidic environment, silver ions are released, which disrupt cellular homeostasis, leading to apoptotic cell death (Kovács et al., 2022; Walker et al., 2018). However, it is important to consider the limitations of silver nanoparticles before their commercialisation or clinical application. Studies have discovered that only a very small fraction of

nanoparticles can reach the intended target site for delivery. Therefore, it has been suggested that high-affinity strategies employing specific ligands for active cellular nano-delivery should be developed to enhance the likelihood of cellular uptake (H. I. O. Gomes et al., 2021; Henrich-Noack et al., 2019; Kovács et al., 2022; Rosenblum et al., 2018).

1.4.6.3 Gold Nanoparticles

Gold nanoparticles (Au NPs) are widely recognised as the most stable nanoparticles among other metallic counterparts (Hu et al., 2020). They possess reliable biocompatibility and can be easily functionalised, which has garnered significant attention by researchers who are exploring synthesis and size control techniques (Amina & Guo, 2020; L. A. Dykman & Bogatyrev, 2007). In the literature, various techniques have been employed for the synthesis of Au NPs, including microwave-assisted methods (Gutiérrez-Wing et al., 2012; Huang et al., 2022). Ngo et al. (2016) described a low-cost and effective technique for microwave heating synthesis of Au NPs specifically for *E. coli* bacteria detection. Furthermore, a green synthesis approach utilising plant extracts as reducing agents has been reported by Elia *et al.*, in 2014.

Chemical and electrochemical methods are also employed for Au NPs synthesis (Herizchi et al., 2016). The Turkevich method, a commonly used technique, involves the use of sodium citrate as a reducing agent to prepare stabilised Au-NPs (Turkevitch et al., 1951). This method has been updated, wherein chloroauric acid ($HAuCl_4$) is reduced through interaction with trisodium citrate under vigorous stirring at approximately 600 rpm and heating between 100 °C and 150 °C for a specific duration (Herizchi et al., 2016). Various other chemical

techniques have been reported, employing reducing agents such as tannic acid, ascorbic acid, and hexadecyl trimethyl ammonium bromide (CTAB) to synthesise Au NPs with different shapes and size control (Wei et al., 2021). Biologically generated or bacteria- and fungi-mediated gold nanoparticles are believed to exhibit higher stability compared to other methods (Hammami & Alabdallah, 2021). Overall, in recent studies, there has been significant progress in preparing stabilised Au NPs with controllable properties and a range of structures. Gold nanostructures can be categorised into clusters, spheres, nanotubes, nanorods, and nanoshells based on their size and shape, as illustrated in **Figure 1.3** (Venditti, 2019).

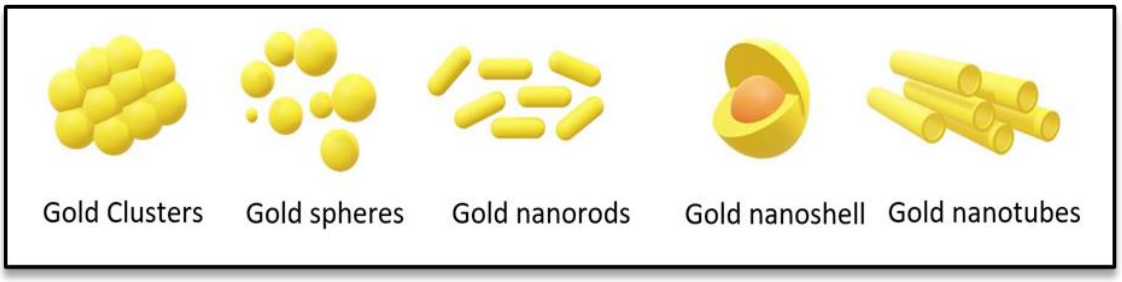

Figure 1. 3. Schematic representation of common nanostructures of gold nanoparticles, including clusters, spheres, nanorods, nanoshells, and nanotubes. This schematic drawn based on information from Venditti (2019).

Different shapes and sizes of gold nanoparticles can be synthesised by manipulating parameters such as chemical reducing agents, temperature, and pH. For instance, the citrate reduction method has been employed to synthesise Au NPs with a spherical shape (Polte et al., 2010). Gold nanorods, on the other hand, can be prepared using a seed-mediated growth mechanism (Nikoobakht & El-Sayed, 2003). In 1997, Averitt et al. reported the synthesis of gold nanoshells with an inner Au_2S core (Averitt et al., 1997). Furthermore, by controlling the pH

and temperature effects and utilising a strong reducing agent like tannic acid in combination with an excess amount of trisodium citrate reagent, small gold nanoparticles can be controlled to sub-10 nm sizes (Piella et al., 2016). In conclusion, the manipulation of parameters such as temperature, pH, and chemical reducing agents plays a crucial role in tailoring the formation of gold nanoparticles with diverse shapes and sizes.

1.5 Physicochemical Properties of Au NPs

Gold nanoparticles exhibit several unique properties, including low toxicity, uniform morphology, and a large surface-to-volume ratio (Yeh et al., 2012). One of the significant physical properties of Au NPs is the localised surface plasmon resonance (LSPR), which is closely related to their optical properties (De Marchi et al., 2019). The LSPR causes nanoparticles strongly to absorb or scatter light. The LSPR absorption peak can be shifted to maximum wavelengths by varying the nanoparticle size and shape, leading to distinct optical behaviours. Au NPs can also exhibit colours (ranging from red to blue), depending on their size, shape, and surface chemistry (X. Huang & El-Sayed, 2010). Extensive research has focused on Au NPs in the literature, particularly in recent years, in the context of biomedical applications such as biosensors, drug nanocarriers, and environmental security (Ghosh et al., 2008; Hassanisaadi et al., 2021; Saha et al., 2012). The key reason for their success, specifically in biomedical applications, lies in their diverse optical properties associated with surface plasmons (Amendola et al., 2017; Austin et al., 2015). The conduction electrons surrounding the surface of Au NPs are easily polarised, which is a crucial factor enabling their preferred interaction with electromagnetic fields and the generation

of nonlinear optical phenomena. As a result, Au NPs are capable of amplifying electromagnetic fields at nanometric distances (Amendola et al., 2017).

Au NPs have an absorption peak in the region of 500–550 nm. This absorption band is known as a surface plasmon band, which results from the conduction electrons' collective oscillation caused by the incident photons' resonant excitation (Yeh et al., 2012). It was revealed that spherical Au NPs have the ability to exhibit the characteristic of a bright red colour as a function of their size (Amendola et al., 2017; Colomban, 2009). Consequently, several factors can be used to determine nanoparticle growth by cluster aggregation, including a significant red shift for the LSPR, broadening the LSPR band, and changing of a gold suspension colour from red to blue due to interaction between particles as discussed earlier (A. Gomes et al., 2021; X. Huang & El-Sayed, 2010; Sharma et al., 2020).

The LSPR absorption band originates from the collective oscillation collected by excited electrons. As demonstrated by Choi et al. (2011), the mechanism involves the absorption of photons by the free electrons surrounding the gold surface, a process attributed to thermal effects. These free electrons can flow between atoms but are unable to leave the surface of gold nanoparticles. This establishes gold as a plasmon composed of positively charged protons fixed in position and negatively charged electrons exhibiting high mobility. At plasma frequency, these free electrons can only oscillate rapidly once exposed to electromagnetic waves. This is because the electromagnetic waves impinge on the surface of Au NPs at a specific depth. Thus, the free electrons are collectively shifted by the electric field within the gold nanoparticles, and as a result, electrons with negative

charges are accumulated on the surface at one side of the gold nanoparticles, producing coherent oscillation in response to the electric field of incident light as demonstrated in **Figure 1.4** (Choi et al., 2011).

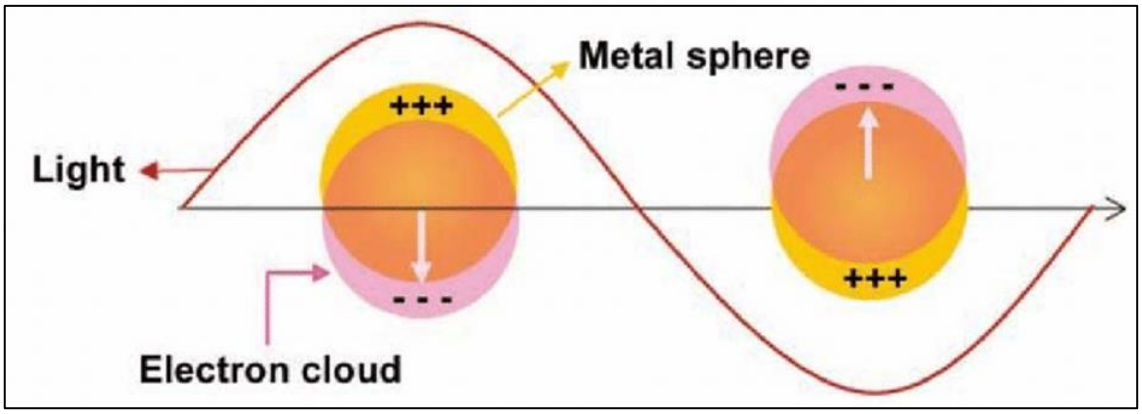

Figure 1. 4. Collective oscillation phenomenon of free conduction electrons, known as surface plasmon resonance, in gold nanoparticles (Choi et al., 2011).

A notable enhancement in the thermal conductivity induced by the colloidal suspensions of gold nanoparticles has been reported in the literature (Patel et al., 2003; Putnam et al., 2006; Shalkevich et al., 2010). The application of small-sized nanoparticles characterised by a large surface area has the ability not only to enhance heat transfer but also to improve the stability of nanoparticles in the colloidal solution by protecting them against particle sedimentation (Shalkevich et al., 2010).

Recently, various types of metallic and non-metallic nanoparticles with different shapes were suspended in solution to be used as heat transfer nanofluids (Assael et al., 2006; T.-K. Hong et al., 2005; N. Jha & Ramaprabhu, 2008; C. H. Li & Peterson, 2007; Zhu et al., 2007). Shalkevich et al. (2010) conducted a study

involving the synthesis of gold nanoparticles covering various size ranges, from 2 to 45 nm. Subsequently, they evaluated their thermal conductivity in nanofluids based on particle size and concentration ratio. Notably, findings indicated that Au NPs of 40 nm exhibited the highest thermal conductivity enhancement, reaching 1.4%. In contrast, other experimental investigations focused on carbon nanotubes (CNTs) demonstrated even more substantial enhancements, exceeding 100% (Shalkevich et al., 2010).

On the other hand, a significant enhancement in the electrical field has been observed for Au NPs due to their unique physicochemical properties. For instance, Tommalieh et al. (2020) investigated the effect of using various concentrations of gold nanoparticles to enhance the electrical conductivity performance of a mixture containing polyvinyl alcohol (PVA) and chitosan (CS). Au NPs can also be utilised in the solid state to improve the electrical conductivity of carbon fibre electrodes (Del Castillo-Castro et al., 2007; Demir et al., 2019). They exhibit high electrical conductivity and are resistant to oxidation and corrosion (Chan et al., 2019; Haruta & Daté, 2001; Tang et al., 2019). These chemical properties and compatibilities have increased the importance of Au NPs applications, particularly in the medical field (L. Dykman & Khlebtsov, 2012; Giljohann et al., 2010).

1.6 Functionalisation of Au NPs with Thiol Containing Compound

Gold nanoparticles have become a favoured choice for drug delivery vehicles due to their ease of functionalisation (Joshi et al., 2011; S. Liu & Lämmerhofer, 2019; Schulz et al., 2016; Thambiraj et al., 2018; Zhou et al., 2009). These nanoparticles are innovative materials in the realm of drug delivery systems (P.

M. Tiwari et al., 2011). The primary reason is that Au NPs, especially when modified with thiol-containing compounds, possess excellent stability properties as carriers (L. A. Dykman & Bogatyrev, 2007). The scientific literature contains numerous techniques for modifying Au NPs, considering factors such as their size and shape (Amina & Guo, 2020). The distinctive surface chemistry and strong affinity of Au NPs towards thiol groups play a vital role in their customisation with biomedical agents (Shukla et al., 2005). Additionally, Au NPs have the capability to directly bind to drug molecules, proteins, DNA and RNA, enzymes, and even antibodies, as a result of their surface chemistry. For instance, Podsiadlo et al. (2008) discovered the synthesis of Au NPs and their functionalisation with the 6-mercaptopurine molecule for therapeutic purposes as an anti-leukemia drug. This type of functionalisation was based on the formation of a gold-sulphur bond (Au-S). This is a strong bond, and recently it has been exploited as molecular contact (Kokkin et al., 2015). Nanomaterials that show high stability, in particular with thiolate functionalities, are considered to be highly promising components in nanotechnology devices (Negishi et al., 2013). However, Brust et al. (1994a) stated that thiolate-coated Au NPs exhibit a high degree of stability even at high temperatures after the functionalisation process, making them suitable for various applications in catalysis, sensing, and electronics. Furthermore, Whetten et al. (1996) demonstrated specific stable clusters, so-called nanocrystals, which can be made based on the reduction of metal ions at the oil-water interface by using alkyl thiolate as a surfactant with a reducing agent (Whetten et al., 1996). They also revealed that surface saturation and stabilisation can be modified by increasing the mole ratio of the thiol compound and by greater exposure to a reducing reagent. At their characterisation with high-resolution electron

microscopy, it was found that each particle has a compact crystalline gold cores up to 3.5 nm in diameter (Whetten et al., 1996). On the other hand, it has been noticed that the Au-S bond has an effective anti-proliferative effect against lymphoblast cells (K-562) in comparison to the effect of the fungal exopolysaccharides (EPS) alone (Hu et al., 2020). Furthermore, Awotunde et al. (2020) stated that the conjugation of free thiol groups present in human serum albumin with Au NPs enhances the stability and biocompatibility of the nanoparticles, making them promising candidates for drug delivery and targeted therapeutic applications. The protein has been modified by the addition of the 2-iminothiolane called Traut's reagent in order to increase the thiol-free groups at the surface of the protein and provide high-stability conjugation. Additionally, for medical applications and biological activities, it was described that Au NPs are also functionalised by polymers terminated with thiol groups. For example, Asadishad et al. (2010) employed folate-poly (ethylene glycol) functionalised gold nanoparticles for targeted drug delivery to cancer cells. Likewise, doxorubicin is a well-known anti-cancer drug that is proposed to be conjugated to hydrophilic polymers in order to reduce its toxicity, in comparison to doxorubicin used alone. This conjugation was also suggested to improve solubility and the short-life of the doxorubicin drug in the body (Veronese et al., 2005). It has also been reported that cationic albumin has been conjugated to pegylated gold nanoparticles for gene target delivery via the blood-brain barrier (BBB) (W. Lu et al., 2006). The work revealed that the developed cationic albumin conjugated to pegylated gold nanoparticles are chemically stable and show higher accumulation in the brain than other albumin pegylated conjugations. Therefore, pegylated gold

nanoparticle conjugates are more desirable conjugates than liposomes because of their physicochemical stability and long-life storage (Perez et al., 2001; Lu et al., 2005). Among other materials, recently a significant interest has arisen in using 11-mercaptoundecanoic acid (MUDA) for functionalisation of Au NPs to be applied in the biomedical field due to the stability that can be provided through the formation of a gold-sulfur bond. In addition to the carboxylic acid group, it can be considered for further conjugation, especially with primary amine-containing drugs, by the formation of a strong amide bond (Ansar et al., 2018). The chemical interaction between the thiol group in the MUDA molecule and gold atom onto the surface of nanoparticles can enhance the solubility of nanoparticles.

As illustrated in **Figure 1.5** below, the interaction of Au-S formation bond involves the displacement of citrate residues from the surface of Au NPs by an organo-thiol compounds such as 11-mercaptoundecanoic acid (DeVetter et al., 2015; Lin et al., 2004; López-Lorente et al., 2014; Perera et al., 2018; Weisbecker et al., 1996). Also, the adsorption characteristics of three types of proteins onto gold surfaces modified with 11-mercaptoundecanoic acid. They found that all types of proteins, including bovine serum albumin (BSA), myoglobin (Mb), and cytochrome-C, were effectively adsorbed onto the MUDA functionalised Au NPs. However, among all proteins, it was noticeable that BSA has the highest affinity to the surface of gold nanoparticles due to the formation of a reversibly bonded protein (Kaufman et al., 2007). Shape, size and surface coating of nanoparticles also play a vital role in the functionalisation process with MUDA. Recently, the effect of MUDA functionalisation onto gold nanorods was studied by Vedhanayagam et al. (2022) in terms of shape influence. However, during

characterisation, they confirmed a clear bioconjugation between the negatively charged MUDA-gold nanorods and cytochrome-C for safe biomedical use. According to the TEM microscopic images, they found that the shape is completely changed to a monodispersed rod-shape due to the interaction with the MUDA cross-linker at high temperature. Moreover, pH values and HEPES buffer solutions also display a significant effect on effective functionalisation with thiol compounds (Vedhanayagam et al., 2022).

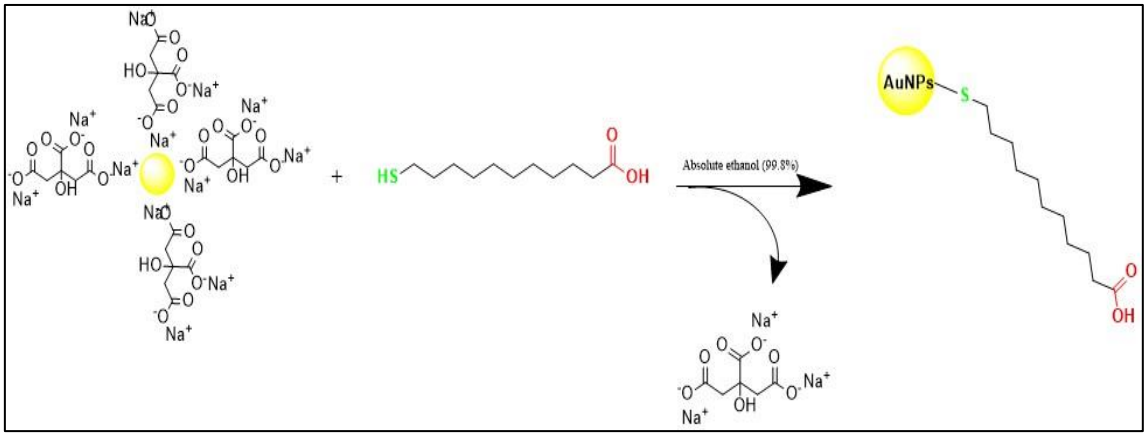

Figure 1. 5. Displacement of citrate residues from the surface of gold nanoparticles occurs due to the introduction of the thiol-containing compound, 11-mercaptoundecanoic acid, during the functionalisation process.

1.7 Drug Delivery Systems

A drug delivery system (DDs) can be described as a novel technology that supports drug transport throughout the human body (Mali, 2015; Shareef et al., 2003; G. Tiwari et al., 2012). The traditional routes, such as pills or injections of drug delivery typically refer to established methods, which have been applied in the pharmaceutical industries. While these routes widely used for drug delivery,

they also come with certain limitations such as enzymatic degradation for orally administered medications (Homayun et al., 2019).

The major disadvantage of the intravenous route is its short half-life, which limits the time that drugs remain in the bloodstream before being eliminated from the body (Bancsi et al., 2019; J. Kim & De Jesus, 2022; Mathaes et al., 2016). Additionally, this route carries the risk of overdose, necessitating precise dosing for patients (Rzasa Lynn & Galinkin, 2018). To address these challenges, researchers have developed advanced drug delivery systems that utilise nanomaterials as carriers (Langer & Peppas, 2003; Patra et al., 2018). Nanomaterials can enhance the pharmacokinetics of drugs by improving their stability, prolonging circulation time, and enabling targeted delivery. For example, nanoparticles can be engineered to evade the immune system, reducing clearance rates and extending their presence in the bloodstream. Furthermore, their ability to encapsulate drugs protects them from degradation, allowing for sustained release over time.

Au NPs and polymeric nanoparticles are particularly promising, as they can easily penetrate the lipid bilayer of cell membranes, making them effective carriers for delivering various medicines to cells (Arvizo et al., 2010; Mazumdar et al., 2021). By leveraging these properties, nanomaterials have the potential to significantly improve the efficacy and safety of intravenous drug delivery systems.

1.7.1 Enhancing Drug Delivery by Conjugation of Medicines to Au NPs

Au NPs are novel nanocarrier extensively studied to be applied in drug delivery systems. For example, Au NPs as a nanocarrier can be considered a colloidal

drug delivery system that is typically smaller than 100 nm in diameter (Afzal et al., 2022). This typical size for Au NPs provides a promising system for the delivery of medicines and improves their bioavailability due to their high surface area-to-volume ratio (Afzal et al., 2022; Yafout et al., 2021). In addition to low toxicity, they have been shown to show improved drug release, and biodistribution (Farooq et al., 2018; Liang et al., 2014). In general, researchers found that drug pharmacokinetics have been significantly changed and improved, in particular after application of Au NPs. Therefore, in recent years, drug conjugation systems using nanoparticles specifically gold nanoparticles draw attraction in the field of nanomedicine (Anik et al., 2022). Conjugation of medicines (chloroquine) containing a primary amine group to modified gold nanoparticles was applied by Joshi et al. (2011) in the presence of *N*-(3-Dimethylaminopropyl)-*N′*-ethyl carbodiimide hydrochloride (EDC) and N-Hydroxy succinimide (NHS) coupling reagents.

In the literature, other types of conjugation using several chemicals were mentioned. For example, divinyl pyrimidine reagents were reported for antibody drug conjugation *in vivo*. Walsh et al. reported the first *in vivo* work for the formation of safe antibody drug conjugates, which have been utilised against several cancer cell lines (Walsh et al., 2022). Additionally, Hanby et al. (2022) investigated the immunoglobulin G (IgG) anti-body dual functionalisation, which was accomplished using a disulfide bridge technique. They demonstrated that this kind of conjugation strategy does not require metal catalysis, which may activate cytotoxicity effects due to the unintended oxidation of amino acid residues (Stadtman, 1990; Hanby et al., 2022).

On the other hand, carbonyldiimidazole (CDI) is one of the carbodiimide cross-linkers used in non-aqueous conditions to activate carboxylic acids for direct conjugation to primary amines ($–NH_2$) via formation of amide bonds. For instance, Hage et al. introduced the first cross-linker called 1,1'-carbonyldiimidazole (CDI) to be utilised for conjugation between the primary amine and carboxyl groups in a protein under physiological conditions at pH between 7.2 and 8 (Hage et al., 2017). However, CDI is one of the electrophilic reactive amides consisting of five-membered heterocyclic rings attached by a carbonyl group in the centre (**Figure 1.6**); therefore, due to the amide nitrogen in the five-membered rings, which can be considered a lone electron pair that exhibits CDI as an effective cross-linker for proteins, especially in aqueous solution at pH 7.2 (Hage et al., 2017). The CDI conjugation involves either the interaction of the primary amine in the lysine chain with the carboxyl group, resulting in urea compounds, or the interaction between the primary amines in lysine and the carboxyl group in the tyrosine side chain, leading to the formation of carbamates (Götze et al., 2014; Hage et al., 2017). Other carbodiimide cross-linkers, *N*-Ethyl-*N*′-(3-dimethylaminopropyl) carbodiimide hydrochloride (EDC) and N,N′-dicyclohexylcarbodiimide (DDC) (**Figure 1.6**), have been studied for primary amine and carboxyl group conjugation through the formation of an amide bond.

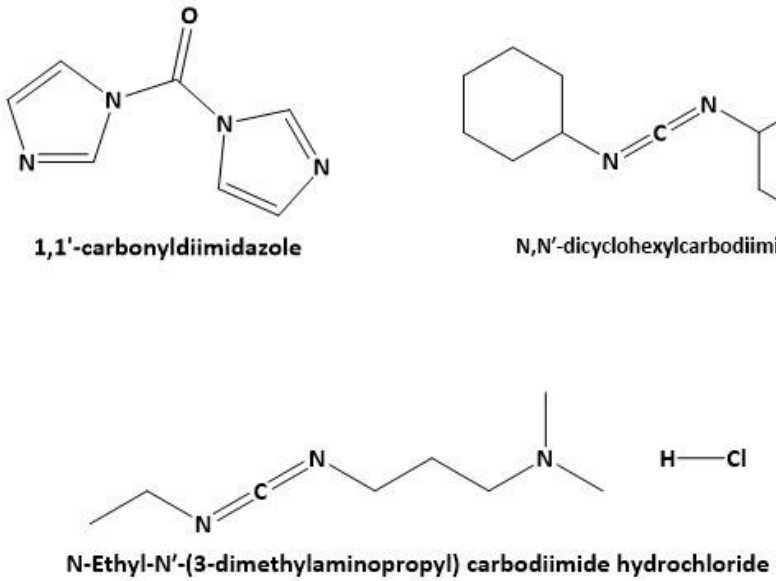

Figure 1. 6. Chemical structures of the carbodiimide cross-linkers used for drug conjugation: carbonyldiimidazole (CDI), N, N′-dicyclohexyl carbodiimide (DDC), and N-Ethyl-N′-(3-dimethylaminopropyl) carbodiimide hydrochloride (EDC).

These are the most common carbodiimide compounds utilised for aqueous and non-aqueous cross-linking, respectively (Busch et al., 2019; Milan-Rois et al., 2022). Although these provide suitable conjugation to carboxyl groups, in recent years, significant clinical success, drug conjugation to NMs, has been witnessed, in particular with the water-soluble EDC cross-linker, in order to provide a promising drug delivery system (Dhas et al., 2018; Sapsford et al., 2013; Tsolekile et al., 2017).

The coupling protocol of EDC always involves the application of *N*-hydroxy succinimide (NHS) or its water-soluble analogue sulfo-NHS, as each of them can provide good stability for the active intermediate and prevent any hydrolysis that

may occur during the formation of the reactive amine by coupling NHS to the carboxyl group, resulting in NHS-ester formation (Spicer et al., 2018).

In the literature, many studies have been published for drug conjugation to NMs based on the application of the EDC/NHS coupling strategy. For example, Bartczak & Kanaras, (2011) represented an optimisation study for the coupling of peptides to gold nanoparticles. They studied the physicochemical properties of this conjugation in order to achieve stable peptide-gold nanoparticle conjugation. Also, Susumu et al. (2010) described the preparation and coupling modification of polyethylene-capped quantum dots with nickel-nitrilotriacetic acid via EDC reagent to form the QDs complex, which has been targeted to 5-His-tagged maltose binding proteins.

On the other hand, TiO_2 nanoparticles and streptavidin conjugation were reported by using both coupling reagents, EDC and sulfo-NHS, in order to be used as soft X-ray probes in combination with nanogold probes (Ashcroft et al., 2008; Susumu et al., (2007)). Moreover, Susumu, et al. (2007) devised a novel ligand attached to quantum dots in order to enhance the biocompatibility of these modified QDs. This modification involves the application of single-chain polyethylene glycol terminated with dihydrolipoic acid (DHLA) attached directly to the QDs by a thiol group, and on the other end of the PEG chain there is a potential biological functional group (amine or carboxyl groups) to promote the further conjugation with an amine-terminated dye via EDC coupling (Susumu et al., 2007).

As discussed in the literature, the mechanism of conjugation between a primary amine group and a carboxylic acid group involves the activation of the carboxylic

acid group terminated-gold nanoparticles by EDC cross-linker in order to form the active intermediate (O-acylisourea), which is unstable and will be replaced by NHS or sulfo-NHS via a nucleophilic attack to produce a stable ester (Asiaei et al., 2015; Crous & Abrahamse, 2020; L. Lu et al., 2021). The latter will considerably improve stable conjugation with medicines containing primary amine groups through the formation of an amide bond at physiological pH values. Despite the ability of EDC to activate the carboxylic acid group in modified gold nanoparticles, EDC cross-linkers can also provide conjugation systems for proteins and peptides due to the presence of both carboxylic acid and primary amine groups (L. Lu et al., 2021). Thus, EDC cross-linking or conjugation will be easier, especially with other molecules that comprise either an amino or carboxyl group in their chemical structure. For example, EDC/NHS cross-linking has been used for peptide coupling to carrier proteins. Therefore, the EDC will react with either the protein carrier or peptide molecule by activating the carboxyl group, leading to the formation of an active intermediate called o-acylisourea. Sulfo-NHS can then be added to prevent any hydrolysis that may occur during the interaction, which later leads to the conjugation by formation of an amide bond at low temperature with very low-cost techniques (L. Lu et al., 2021).

1.7.2 Enhancing Drug Delivery via PLGA Nanoparticles

The biodegradable polymer polylactic-coglycolic acid (PLGA) shows potential application in the biomedical field, especially as a drug delivery carrier (Makadia & Siegel, 2011). PLGA is known as a co-polymer of poly lactic acid (PLA) and poly glycolic acid (PGA) and typically can be defined as the most suitable biomaterial available to control drug release (Makadia & Siegel, 2011). Therefore,

PLGA can be considered one of the United States Food and Drug Administration (U.S. FDA) approved biodegradable polymer that is highly biocompatible and reasonably studied as safe drug vehicle (Makadia & Siegel, 2011). None the less, PLGA is also applied as a carrier for proteins and peptides (Allahyari & Mohit, 2016; Derman et al., 2015; Pudlarz & Szemraj, 2018).

Recently, it was revealed that PLGA can be employed for controlled drug release at desirable doses (Makadia & Siegel, 2011). For instance, the topical anti-inflammatory analgesic effect of the trolamine salicylate (TS) was improved by the application of PLGA-based in situ bio-adhesive film (Y. Kim et al., 2019). Another study conducted by del Castillo-Santaella et al. (2019), which revealed the synthesis of PLGA nanoparticles as a carrier for the bone morphogenetic protein (BMP-2). In addition, the PLGA nanoparticles were also modified by chitosan at different concentration ratios in order to increase the drug encapsulation efficiency. It was found that the drug encapsulation efficiency has been increased to 87.1% and the drug release was faster at acidic conditions approximately at pH 5.5 (B. Lu et al., 2019). Simply, the controlled drug release using PLGA NPs, involves the diffusion, solvent penetration into the PLGA nanoparticles followed by degradation and erosion of the polymer matrix (Hines & Kaplan, 2013).

1.7.2.1 Physicochemical Properties of PLGA Nanoparticles

PLGA is a flexible material that can be modified as nanoparticles with different shapes and sizes. These nanoparticles are able to encapsulate molecules of almost any size (Makadia & Siegel, 2011; Rocha et al., 2022). PLGA is soluble in a variety of typical solvents, such as acetone, tetrahydrofuran (THF), and ethyl

acetate (Makadia & Siegel, 2011; Uhrich et al., 1999; X. S. Wu & Wang, 2001). However, PLGA degrades in water by hydrolysing its ester bonds in water (Yue Wang et al., 2022). The methyl group in the poly lactic acid (PLA) represents the hydrophobic part, which led PLGA NPs to absorb less water and thus degrade more slowly (Yue Wang et al., 2022) (**Figure 1.7**). The effect of the PLGA physical properties on the drug-controlled release is based on different variations such as molecular weight, temperature, the concentration ratio of lactic acid to glycolic acid, and its exposure to water (hydrolysis). The molecular weight and concentration ratio are directly related to the crystallinity of the PLGA polymer. For example, when the PGA is co-polymerised with PLA at a higher concentration ratio, this will increase the hydration effect of PLGA and reduce its crystallinity (Dodda et al., 2022; Makadia & Siegel, 2011; Yue Wang et al., 2022).

In addition, the type of medicine is a key tool that may affect the PLGA's properties as a drug vehicle. Siegel et al., (2006) compared the drug release rate for six different drugs using polylactic-co-glycolic acid (PLGA) polymer pellets. They found that the drug controlled release rate between medicines are significantly different (Siegel et al., 2006). However, the PLGA NPs as a drug carrier can be considered as one of the most effective drug delivery systems because of their bioavailability and biocompatibility (Makadia & Siegel, 2011).

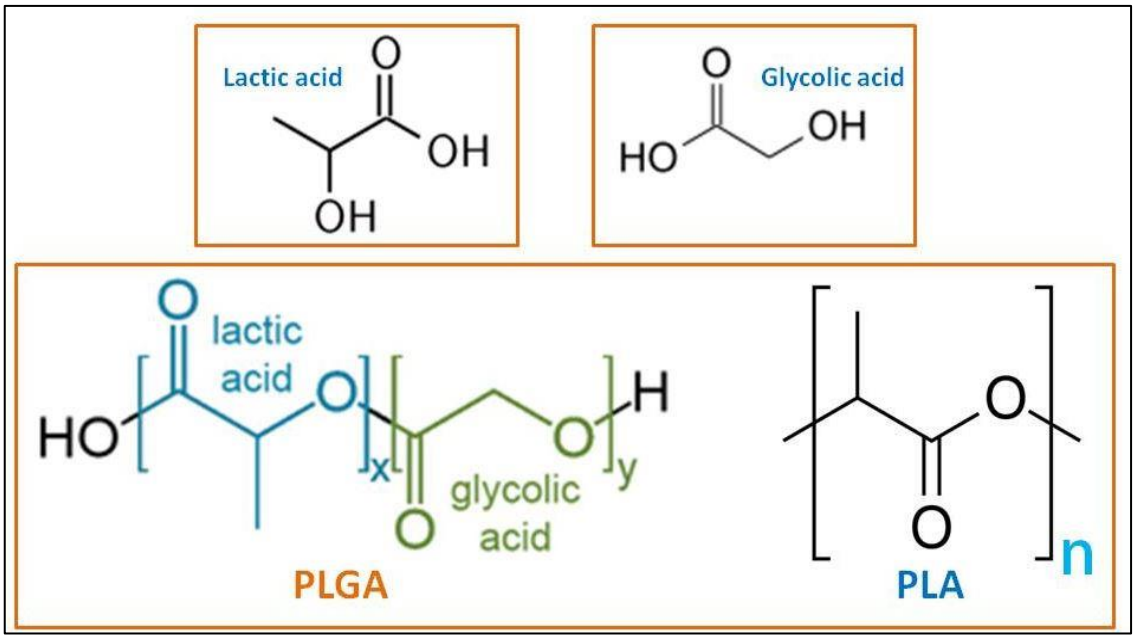

Figure 1. 7. Chemical structure of the biodegradable polymer polylactic-co-glycolic acid (PLGA), illustrating the hydrophobic part, poly lactic acid (PLA) and the hydrophilic component poly glycolic acid (PGA). In the diagram, x and y in PLGA and n in PLA represent the quantity of repeated units (Yue Wang et al., 2022).

1.8 Cellular Uptake and Cell Interactions with Gold Nanoparticles

Several processes for the cellular uptake of Au NPs have been reported in the literature, depending on size, shape, and surface coating. The mechanism of cellular uptake involves the penetration of Au NPs into cells, specifically the barrier of the plasma membrane (Behzadi et al., 2017; Yue et al., 2017). This plasma membrane is selectively permeable to allow molecules to enter and exit the cells. The cellular uptake process depends on molecular size. Smaller molecules, such as sugars, ions, and amino acids, easily penetrate the

membrane by diffusion mechanisms. However, large molecules are generally carried across the membrane by endocytosis, as illustrated in **Figure 1.8** (Alkilany & Murphy, 2010; Lafuente et al., 2020).Endocytosis is a type of active transport in which cells take up molecules intended for internalisation. Phagocytosis ("eating" of cells) and pinocytosis ("drinking" of cells) are two broad categories of endocytosis. In phagocytosis, cells (e.g., macrophages) engulf large particles, larger than 0.5 µm, such as bacteria and cell debris (Lafuente et al., 2020). Pinocytosis mostly describes the uptake of small molecules in the extracellular fluids by cells (e.g., eukaryotes), as illustrated in **Figure 1.8** (Lafuente et al., 2020; Pathak et al., 2023).

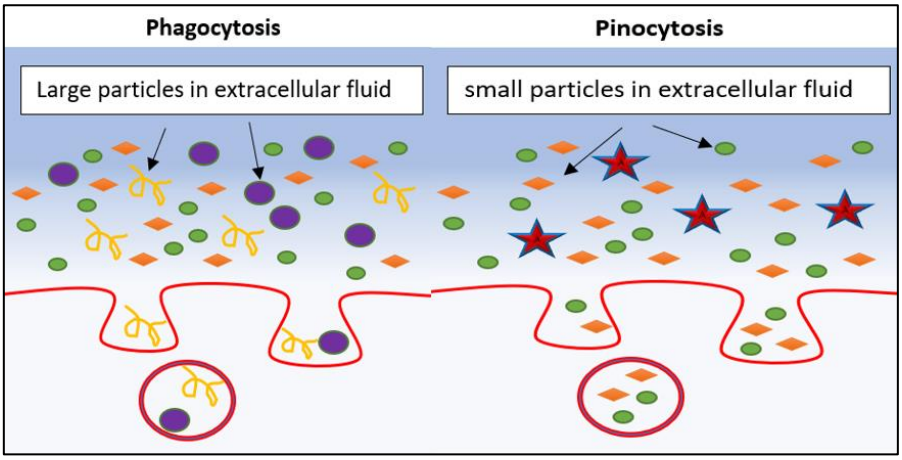

Figure 1. 8. Different endocytosis mechanisms. Pinocytosis and phagocytosis are two categories for endocytosis. While phagocytosis includes the internalisation of big particles or large molecules, whereas pinocytosis involves the internalisation of small molecules from the extracellular fluids (Alkilany & Murphy, 2010; (Lafuente et al., 2020).

However, the interaction between Au NPs and cells involves the formation of nanoparticle-protein complexes. In other words, Au NPs are interacting with proteins in biological fluids and forming a protein corona surrounding the surface of nanoparticles. This protein corona can be recognised by the receptors on the cell membrane, resulting in the uptake of nanoparticles by cells (Oh et al., 2011; P. Wang et al., 2015).

1.9 Cytotoxicity Testing for Au NPs

Although gold nanoparticles have emerged as a promising nanoparticle for drug delivery, it is very important to evaluate the impact of these nanoparticles on living cells (Kus-Liśkiewicz et al., 2021). Thus, several toxicity assays have been reported in the literature to expand our knowledge of the toxicity effects of gold nanoparticles. For example, the lactate dehydrogenase (LHD) assay indicates the toxicity of nanomaterials based on the level of the LDH enzyme in the blood stream, which can be secreted when living tissue or organisms are damaged as a result of a specific disease (Han et al., 2011). The influence of nanoparticles' shape, size, and functionalisation on toxicity and cellular uptake was elucidated. Gold nanoparticles permeate cells via endocytosis, traversing the cell membrane, and exit through exocytosis (Carnovale et al., 2019; Ng et al., 2015). Smaller nanoparticles are easily internalised by cells as they require less energy and a low number of receptors. In contrast, internalisation of larger particles will be limited due to the insufficient number of receptors at the surface of the cell (Carnovale et al., 2019). Therefore, various studies consider a smaller

nanoparticles are more toxic than large nanoparticles (Ai et al., 2011; Steckiewicz et al., 2019).

1.9.1 Influence of Au NPs Characteristics on Toxicity and Cellular Uptake

Key factors such as the shape, size, and surface functionalisation of Au NPs greatly impact their toxicity:

1.9.1.1 Shape of Au NPs

The shape of Au NPs, such as spherical, rod, or star shaped structures, affects their cellular uptake and toxicity. Studies show that rod shaped and other elongated particles might have higher toxic potential compared to spherical nanoparticles due to their greater surface area and unique interaction with the cell membrane, which could disrupt cellular processes (Hu et al., 2020).

1.9.1.2 Size of Au NPs

The size of Au NPs is a critical factor in their cellular uptake and potential toxicity. Smaller nanoparticles can enter cells more easily because they require less energy and fewer receptors to cross the cell membrane than large particles (Carnovale et al., 2019).

1.9.1.3 Functionalisation of Au NPs

The surface chemistry of functionalised Au NPs plays a significant role in cellular interaction and toxicity. AuNPs can be functionalised with various molecules to improve their stability, biocompatibility, and target specificity. For instance, coating Au NPs with biocompatible polymers, like PEG, can reduce toxicity by preventing undesirable protein adsorption and improving circulation time in the bloodstream. However, certain functional groups might increase toxicity by

enhancing the nanoparticle's interaction with cellular membranes, potentially leading to oxidative stress or inflammation, and cell death as described by Boldeiu et al. (2019), Freese et al. (2012) and Vishwakarma et al. (2010).

To summarise, Au NPs offered a great promise as drug delivery systems, therefore, their interactions with cells require evaluation using a range of toxicity assays as described in Chapter 2, section 2.5.3 to understand the behaviour of Au NPs in biological systems.

1.10 J774 Cell Line Macrophages for Cellular Uptake and Toxicity Assays

Macrophages are highly mobile cells with chemotaxis and pathogen engulfment abilities; they offer a significant role in delivering antigens to lymphocytes through immunological responses (Arango Duque & Descoteaux, 2014; Hirayama et al., 2017).

In cell biology and immunology, macrophage cell lines such as J774 and Raw 264.7 can be considered an ideal model system for establishing cellular uptake and toxicity testing (Kant et al., 2002; Lam et al., 2009; Ralph & Nakoinz, 1975, 1977; Unkeless et al., 1979; Dey et al., 2021). These cell line macrophages composed of Toll-like receptors (TLRs), which can be considered as a class of proteins, and they are essential components of the immune response system (El-Zayat et al., 2019). J774 cell line macrophages can be easily maintained and genetically modified; interestingly, they are also being recognised as an ideal model system for quantitative biophysical studies (Santos et al., 2023). Cellular uptake of Au NPs using J774 cell line macrophages was reported in the literature by Dey et al. who found that there was no significant impact on the macrophage

cell line's functions (Dey et al., 2021). Indeed, it was revealed that Au NPs are found to be accumulated in macrophages due to their phagocytic ability to engulf nanomaterials. Thus, these cells have been considered an ideal cell macrophage to study the toxicity effects and cellular uptake, especially for Au NPs (Hussain et al., 2012).

1.11 Aims and Objectives of Research

Drug delivery is a multidisciplinary field focused on designing, developing, and optimising systems and techniques to deliver therapeutic agents, such as drugs and biomolecules, to specific target sites within the body. The goal of drug delivery is to enhance the efficacy and safety of treatments by controlling the release, distribution, and bioavailability of drugs, while minimising side effects and improving patient compliance (De Jong & Borm, 2008; Liang et al., 2014; Mahler & Roy, 2015; X. S. Wu & Wang, 2001). Drug delivery systems (DDs) encompass a wide range of technologies, including nanoparticles (Shilo et al., 2015), liposomes (Düzgüneş et al., 2005), micelles (Kataoka et al., 2012), hydrogels (Yahia, 2017), implants (Chang et al., 2009), patches (Nazary Abrbekoh et al., 2022), and more. DDs includes various several challenges such as complex balance in release kinetics (Shilo et al., 2015).

The fundamental objective of this doctoral research is to develop a thorough understanding of the effectiveness of nanomaterials for the active conjugation of two drug categories, which are amantadine (AMTD) as anti-Parkinson’s disease (PD) medication and remdesivir (REM) for treatment of viral infections.

Initially, this study centers on producing uniform batches of gold nanoparticles using different coating agents. The goal is to regulate their size within the range of 8 to 60 nm, aiming to examine and determine the most suitable size for drug delivery purposes. Then, the synthesised Au NPs were modified with thiol containing compound, 11-mercaptoundecanoic acid (MUDA), followed by their conjugation with amantadine and remdesivir drugs in the presence of a water soluble EDC carbodiimide cross-linker. Furthermore, the toxicity effects and cellular uptake of all forms of synthesised Au NPs and drug conjugated-Au NPs were evaluated using J774 cell line macrophages.

1.12 Thesis Structure

This thesis is divided into seven chapters. The first chapter provides an overview of the significance of Au NPs and their diverse applications in various fields, from nanotechnology to medicine. In chapter two, detailed experimental procedures are outlined and the materials, equipment and techniques used in synthesising and characterising gold nanoparticles are well described.

Chapters 3, 4, 5 and 6 are presenting the outcomes of my research, these chapters showing the results obtained for the synthesis of gold nanoparticles, functionalisation and conjugation of both REM and AMTD medicines to Au NPs, evaluation of physicochemical properties of Au NPs and cellular uptake and cytotoxicity effects of Au NPs, respectively.

In the concluding section (chapter 7), the key findings of my research on Au NPs size control and its implications on the conjugation process were summarised.

Also, the contributions made to this research and the potential avenues for future research are proposed in this chapter.

Chapter (2): Materials and Methods

2.1 Introduction

The initial stage of this work was to synthesise monodisperse batches of Au NPs with several coating agents, aiming to control size to sub-10nm in diameter, the methodology for which will be described here. The synthesis work was followed by the characterisation of the synthesised Au NPs through analytical and microscopic techniques. In addition, this chapter will also introduce the cytotoxicity and cellular uptake assays that have been utilised to investigate, respectively, the toxicity effect of gold nanoparticles and their internalisation into the J744 cell line macrophages.

Characterisation of gold nanoparticles in this project involved measuring the particle size and size distribution using dynamic light scattering (DLS), studying the localised surface plasmon resonance (LSPR) shift by UV-Vis spectrophotometry, the surface particle charge by zeta potential, fourier transform infrared (FTIR) was used to investigate the surface coating of the synthesised gold nanoparticles, and microscopic imaging by transmission electron microscopy (TEM) was used to describe nanoparticle morphological features. Another spectroscopic technique, nuclear magnetic resonance (NMR), was used to investigate the conjugation process of drug molecules to gold nanoparticles by determining the proton and carbon atoms in the chemical structure. The gold nanoparticle concentration in the colloidal solution was also determined by inductively coupled plasma-optical emission spectrometry (ICP-OES). Additionally, a thermogravimetric analyser (TGA) was employed to determine the quantity of coatings loaded onto the surface of gold nanoparticles

by measuring the decomposition caused by varying temperatures over a specified duration.

2.2 Chemicals

All chemicals have been purchased from sigma-Aldrich at high level of purity and utilised without any modification. Trisodium citrate (≥99.0%, CAS 6132-04-3), tannic acid ($C_{76}H_{52}O_{46}$, CAS 1401-55-4), Sodium dodecyl sulfate ($CH_3(CH_2)_{11}OSO_3Na$, CAS No. 151-21-3), polyvinyl pyrrolidone ($(C_6H_9NO)_n$, CAS no. 9003-39-8), poly ethylene glycol 6000 ($H(OCH_2CH_2)_nOH$, CAS no. 25322-68-3), Gold(III) chloride hydrate or chloroauric acid ($HAuCl_4 \cdot aq$, CAS no. 27988-77-8), potassium carbonate (K_2CO_3, CAS no. 584-08-7) sodium carbonate (Na_2CO_3, CAS no. 497-19-8), 11-mercaptoundecanoic acid ($HS(CH_2)_{10}CO_2H$, CAS no. 71310-21-9), 4-mercaptobenzoic acid (99%, $HSC_6H_4CO_2H$, CAS no. 1074-36-8), meso-2,3-Dimercaptosuccinic acid ($HO_2CCH(SH)CH(SH)CO_2H$, CAS no. 304-55-2), ethanol absolute (99.5%, CH_3CH_2OH, CAS no. 64-17-5), sodium hydroxide (NaOH, reagent grade, ≥98%, pellets (anhydrous), CAS no. 1310-73-2), 4-(2-Hydroxyethyl)piperazine-1-ethanesulfonic acid (HEPES, $C_8H_{18}N_2O_4S$, CAS no. 7365-45-9), hydrochloric acid (HCl, CAS no. 7647-01-0). Amantadine hydrochloride or 1-Adamantanamine hydrochloride ($C_{10}H_{17}N \cdot HCl$, CAS no. 665-66-7), EDC (1-ethyl-3-(3-dimethylaminopropyl)carbodiimide hydrochloride)($C_8H_{17}N_3 \cdot HCl$, 25952-53-8), N-Hydroxysuccinimide ($C_4H_5NO_3$, CAS no. 6066-82-6), 2-ethylbutyl (2S)-2 [(2R,3S,4R,5R)-5-(4-aminopyrrolo[2,1-f][1,2,4]triazin-7-yl)-5-cyano3,4 dihydroxyoxolan-2-yl] methoxy phenoxy phosphoryl amino propanoate or can be called remdesivir (GS-5734)(C27H35N6O8P, CAS no. 1809249-37-3, purity > 90%), poly (D, L-Lactide-co-glycolide) PLGA

(lactide:glycolide (50:50), mol wt 30,000-60,000, $[C_3H_4O_2]_x[C_2H_2O_2]_y$, CAS no. 26780-50-7), acetone (ACS reagent, ≥99.5%, CAS no. 67-64-1), Pluronic® F-68 non-ionic surfactant ((C3H6O.C2H4O)x, CAS no. 9003-11-6). Other tools were employed in the experimental work, such as 1.0 µm cellulose nitrate membrane filter and ultrapure water (Milli-Q 18.8 MΩ-cm).

The cell culture media Dulbecco's Modified Eagle Medium with Ultra-glutamine (DMEM, Catalog no. 10569010) was provided by ThermoFisher scientific, Gibco-Fetal Bovine Serum (FBS), penicillin/ streptomycin (10,000 U/ml, Catalog no. 15140122), 3-(4,5-dimethylthiazol-2-yl)-2,5-diphenyltetrazolium bromide or called MTT (C18H16BrN5S, CAS no. 298-93-1), Lactate Dehydrogenase (LDH) Activity Assay Kit (product number: MAK066-1KT), 2,3-Bis-(2-Methoxy-4-Nitro-5-Sulfophenyl)-2H-Tetrazolium-5-Carboxanilide (Cell Proliferation Kit II (XTT), product no. 11465015001), Sulforhodamine-B Assay (5g, product number, S1307), dimethyl sulfoxide ($(CH_3)_2SO$, CAS no. 67-68-5), sterile and filtered phosphate buffer saline (PBS, pH 7.4, product no. P4474-500ML), % 2.5 glutaraldehyde prepared in 0.1 M PBS, aqua regia solution (in the ratio of 68% HNO_3/1% HCl, freshly prepared in the Lab. all toxicity assays and cellular uptake studied were conducted on J774 cell line macrophages.

Other solvents have been applied for characterisation purposes such as deuterated chloroform ($CDCl_3$, the deuteration degree minimum 99.8% for NMR spectroscopy MagniSolv™), and deuterated dimethyl sulfoxide-d_6 ($(CD_3)_2SO$, CAS no. 2206-27-1).

2.3 Methods

2.3.1 Synthesis of Cit-Au NPs Ranging from 20 to 60 nm in Size

A method was published by Nikoobakht and El-Sayed for the synthesis of gold nanorods at low concentrations using a seed-mediated technique (Nikoobakht & El-Sayed, 2003). Herein, this method has been updated in terms of the concentration and type of reducing agent. Briefly, chloroauric acid (1 mL, 25 mM) was injected into a boiled trisodium citrate solution of 38.8 mM prepared in 150 mL of deionised water. Once the colour of the mixture started to change to pink, which meant the formation of gold nanoparticles, 20 mL of this solution was extracted and replaced with the same amount of trisodium citrate solution (2.2 mM). The mixture was left to boil for 15 minutes, and then a similar amount of chloroauric acid was added again to the solution mixture in order to form the second growth solution of gold nanoparticles with a larger size. This procedure was repeated four times, with the aim of producing various sizes of gold nanoparticles up to 60 nm.

2.3.2 Synthesis of TA-Au NPs 15 nm

Tannic acid (TA) is a polyphenolic compound with weak acidity due to the presence of phenol groups in its chemical structure (Jafari et al., 2022). Tannic acid can be considered a strong reducing and stabilising agent that provides very small and stable nanoparticles (Wrigglesworth & Johnston, 2017).

In brief, 1 mL of 0.5 mM tannic acid solution was poured into 25 mL of deionised water containing 2.2 mM trisodium citrate. The solution mixture was left to boil at 70°C under vigorous stirring for 30 minutes. Later, 1 mL of $HAuCl_4$ (20 mM) was injected into the solution and left to boil for another 10 minutes. A change in colour

was observed from colourless to pink within a few minutes, resulting in the formation of tannic acid-gold nanoparticles (TA-Au NPs) with a size of 15 nm in diameter.

2.3.3 Size Tuning of Au NPs

In the literature, very small sizes of gold nanoparticles have been made. For example, Jiang et al. (2020) showed that the critical size of Au NPs to effectively overcome P-glycoprotein multidrug resistance is approximately 10 to 20 nm. This size range allows the nanoparticles to evade recognition and transport by P-glycoprotein, enhancing their therapeutic efficacy in drug-resistant conditions. Thus, herein, two types of chemicals, potassium carbonate (K_2CO_3) and sodium carbonate (Na_2CO_3), were used to tune the size of gold nanoparticles, respectively, to approximately 8 nm and 10 nm diameter.

2.3.3.1 Tuning size of Au NPs to 10 nm

Using sodium carbonate involves dissolving 1.95 g of sodium carbonate, 0.087 g of trisodium citrate, and 0.66 g of tannic acid in 155 mL of deionised water. This mixture was boiled at 70°C for 30 minutes, followed by the addition of 1 mL of chloroauric acid (20 mM), and left to boil for another 20 minutes. The colour changed from colourless to dark blue and then settled on pink. The pH of this mixture was measured, and it was noted at pH 8.5. the size characterised by DLS at approximately 10 nm and TEM shows a little aggregation of nanoparticles.

2.3.3.2 Size Control of Au NPs to 8 nm

For ultra-small gold nanoparticles, potassium carbonate was used as an alternative agent to sodium carbonate to make a very strong alkali solution

mixture in order to tune the size of nanoparticles to 8 nm. In brief, trisodium citrate 2.2 mM, tannic acid 2.5 mM, and potassium carbonate 150 mM were mixed in 155 mL of deionised water and boiled at 70°C under vigorous stirring at 600 rpm for roughly 30 minutes. Then, 1 mL of $HAuCl_4$ (20 mM) was added to this mixture and left to boil for another 20 minutes. Gold nanoparticles with a size of 8 nm were indicated by dynamic light scattering (DLS). In addition to the electron microscopic characterisation by TEM, which demonstrated very small, clear, and well-distributed nanoparticles that for the first time have been made in the literature through monitoring pH via potassium carbonate, the pH has been measured, and it was found at 10.0.

2.3.4 Functionalisation and Drug Conjugation to Au NPs

Functionalising Au NPs, especially with thiol-containing compounds, enhances their stability and biocompatibility. Furthermore, appropriate functionalisation facilitates dependable conjugation with drug molecules, enhancing their bioavailability (Vedhanayagam et al., 2022). In this study, thiol-containing compounds such as 11-mercaptoundecanoic acid (MUDA) have been investigated.

2.3.4.1 MUDA Functionalisation to Cit-Au NPs

MUDA is an organic compound that binds to the surface of gold nanoparticles through thiol ligands, forming Au-S bond. Numerous studies have reported the functionalisation of gold nanoparticles with mercaptoundecanoic acid using various techniques (Joshi et al., 2011; S. Liu & Lämmerhofer, 2019; Mazloomi-Rezvani et al., 2018; Thambiraj et al., 2018; P. M. Tiwari et al., 2011; W. Wang et al., 2013; Woehrle et al., 2005).

In this research, a 10 mM solution of MUDA was prepared in 10 mL of absolute ethanol (98.9%). Subsequently, 2 mL of the MUDA solution was mixed with 1 mL of cit-Au NPs (0.375 mg L^{-1}) in a 15 mL centrifuge tube. This mixture was placed on a mini shaker and agitated at 150 rpm for 45 minutes. A slight colour change was observed, transitioning from deep red to pink. Following this, the functionalised nanoparticles underwent centrifugation at 7000 rpm and 20°C for 55 minutes using a centrifugal system (Centrifuge 5430/5430 R - High-Speed Centrifuge). Subsequently, the particles were washed three times with 400 µL of deionised water and stored in the fridge at 4-6°C.

2.3.4.2 Drug Conjugation to Cit-Au NPs

The conjugation process was based on very simple, novel and inexpensive technique in the presence of 1-ethyl-3-(3-dimethylaminopropyl) carbodiimide hydrochloride (EDC) and N-hydroxysuccinimide (NHS) coupling reagents. Some modifications to parameters such as pH, temperature, buffer solution, and etc., were very important to be applied particularly in the drug conjugation to gold nanoparticle. For example, herein, 4-(2-hydroxyethyl)-1-piperazineethanesulfonic acid also called HEPES buffer solution was utilised in all experimental work of drug conjugation to gold nanoparticles. HEPES is a zwitterionic or di-polar ion buffering agent that widely used in lab researches because it maintains the physiological pH despite the changes that may occurred in other bicarbonate buffers (Inam et al., 2022).

2.3.4.2.1 Amantadine Conjugation to Cit-Au NPs

The process of the conjugated **amantadine** to gold nanoparticles was investigated by the update for a method of chloroquine binding to gold

nanoparticles conducted in the literature by (Joshi et al., 2011). Thus, 200 µL of amantadine drug was mixed with 500 µL of 10 mM MUDA gold nanoparticles (MUDA-AuNPs) and left for approximately 2 minutes. Later, 50 µL of EDC (10 mM) cross-linker was added followed by quick addition of 50 µL of NHS (45 mM) coupling reagent in order to avoid any hydrolysis reactions by formation NHS-ester. This mixture was left for 2 hours to be well-mixed at room temperature and then centrifuged at 11500 rpm and 20˚C for 10 minutes. The pellets of drug-Au NPs conjugates were collected, and the conjugation was investigated by various techniques as shown in Chapter 4 Section 4.3.1.1.

2.3.4.2.2 Remdesivir Conjugation to Cit-Au NPs

For the conjugation of **remdesivir**, the initial step of this study involved preparing a 100 mM HEPES buffer with a pH adjusted to 7.4. Subsequently, 2.5 mg of remdesivir was dissolved in dimethyl sulfoxide (DMSO). Following this, 500 µL of 10 mM MUDA-AuNPs were combined with 100 µL of **remdesivir** in a 2 mL centrifuge tube. Subsequent to that, 50 µL of EDC (10 mM) and 50 µL of NHS (45 mM) were added. The mixture of remdesivir and gold nanoparticles (forming the REM-Au NPs conjugate) was then subjected to agitation on a mini-shaker at 120 rpm for 2 hours. Ultimately, the conjugated nanoparticles were centrifuged, washed twice with 100 µL of deionised water, and subsequently collected for characterisation, the obtained results were illustrated in Chapter 4 Section 4.3.1.2.

2.3.5 Encapsulation of Amantadine into PLGA Polymeric Nanoparticles

The United States Food and Drug Administration (US FDA) has approved the significant application of poly lactic-co-glycolic acid (PLGA) for drug delivery and

other medical purposes due to its distinct properties (Lü et al., 2009). Poly lactic-co-glycolic acid nanoparticles (PLGA NPs) possess the capability to regulate drug release over extended periods (Hines & Kaplan, 2013). Thus, our objective was to investigate this characteristic by encapsulating amantadine for comparison with the AMTD-gold nanoparticle conjugation system. Prior studies have synthesised amantadine-based ion pair-amphiphiles utilising PLGA–PEG–PLGA gel along with oleic acid as a surfactant (Hines & Kaplan, 2013).

The encapsulation process of AMTD into PLGA-NPs was accomplished using a precipitation solvent evaporation technique. Initially, a mixture of 75 mg of PLGA and 2.5 mg of amantadine was dissolved in 5 mL of acetone to form the organic phase. Subsequently, this organic phase was added to 15 mL of Oleic acid and Pluronic F-68 oily phase mixture. Then, this mixture was gently stirred with a magnetic stirrer at room temperature overnight to facilitate acetone evaporation. After a 24-hour duration, the PLGA-NPs became visible. They were subsequently filtered from the suspension through a 1.0 µm cellulose nitrate membrane filter and collected. The remaining acetone was then removed via lyophilisation, and the resulting nanoparticles were stored at room temperature for further characterisation.

2.4 Instrumentation and Characterisation Techniques

Several characterisation techniques were applied in this lab work to investigate synthesised gold nanoparticles or their conjugates and study their physicochemical properties, such as shape, size, stability, surface chemistry, surface charge, solubility, and more. These techniques include UV-Vis spectrophotometric analysis, dynamic light scattering (DLS), zeta potential (ζ),

Fourier transform infrared (FTIR), transmission electron microscopy (TEM), nuclear magnetic resonance (NMR), inductively coupled plasma optical emission spectroscopy (ICP-OES), and thermogravimetric analysis (TGA). In addition, other equipment was used, such as a freeze dryer, used to remove any impurities suspended in the sample, and a sonication water bath employed to re-suspend the sample after centrifugation, ensuring the even distribution of all particles in the sample. All of these tools can be considered integral parts of the sample preparation prior to final characterisation.

2.4.1 UV-Vis Spectrophotometer

In general, UV-Vis spectroscopy refers to the measurement of absorption or reflection of light in the ultraviolet and visible range. A UV-Vis spectrophotometer is a quantitative technique used to measure the amount of light absorbed by substances within the UV-Vis region, typically ranging from approximately 400 to 800 nm (**Figure 2.1**). The mechanism of absorption measurement for the prepared gold nanoparticles involves the evaluation of localised surface plasmon resonance (LSPR). The LSPR spectrum of gold nanoparticles is dependent on their size and shape. Consequently, an increase in size leads to an increase in the absorbance peak of LSPR at the maximum wavelength, as described by (Pedersen & Duncan, 2005). Furthermore, the LSPR spectrum of gold nanoparticles can be easily observed in the visible region, typically ranging from 500 nm to 600 nm, with variations based on their size.

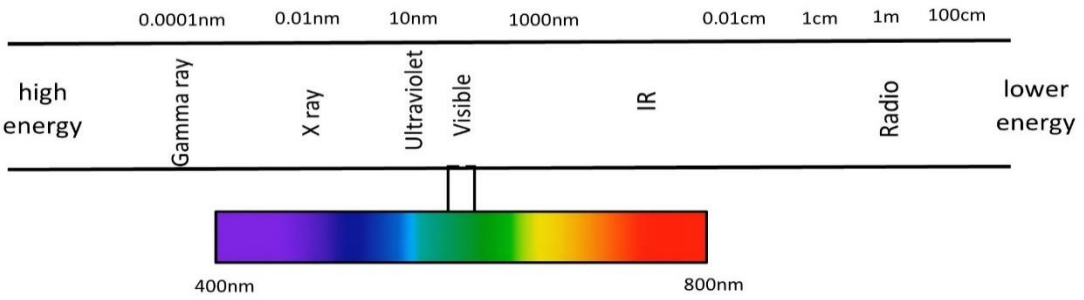

Figure 2. 1. Visible spectrum at wavelength between 400 nm and 800 nm. The LSPR spectrum of gold nanoparticles can be easily observed in the visible region.

A LAMDA® UV-Vis spectrophotometer, supplied by PerkinElmer, has been utilised in this laboratory work for the characterisation of synthesised gold nanoparticles. It is an ultrafast UV-Vis instrument with high performance, capable of measuring the full spectrum in the range of 190 nm to 1100 nm.

2.4.2 Dynamic Light Scattering (DLS)

One of the main principles of dynamic light scattering is to provide precise particle size measurements for nanoparticles based on the Brownian motion of particles (Babick, 2020). According to Berne and Pecora (2000), the Brownian motion describes the variation in movement for both small and large particles in solutions. They explain that smaller particles exhibit faster movement in aqueous solutions compared to larger ones due to the random motion of particles suspended in a fluid. This is known as Brownian motion. Therefore, the light scattered by particles contains detailed information about the diffusion speed and the size distribution of particles in the sample suspension or solution (Berne and

Pecora, 2000). Technically, the size measurement mechanism in DLS can be demonstrated by measuring the motion of particles and optically recording the scattered light signal at a fixed angle, when the laser rays illuminate the nanoparticles, the light is scattered at a fixed angle and recorded. The fluctuations recorded by DLS are related to the scattered light caused by particles moving towards each other (Babick, 2020; Berne & Pecora, 2000; Naiim et al., 2015)(**Figure 2.2**).

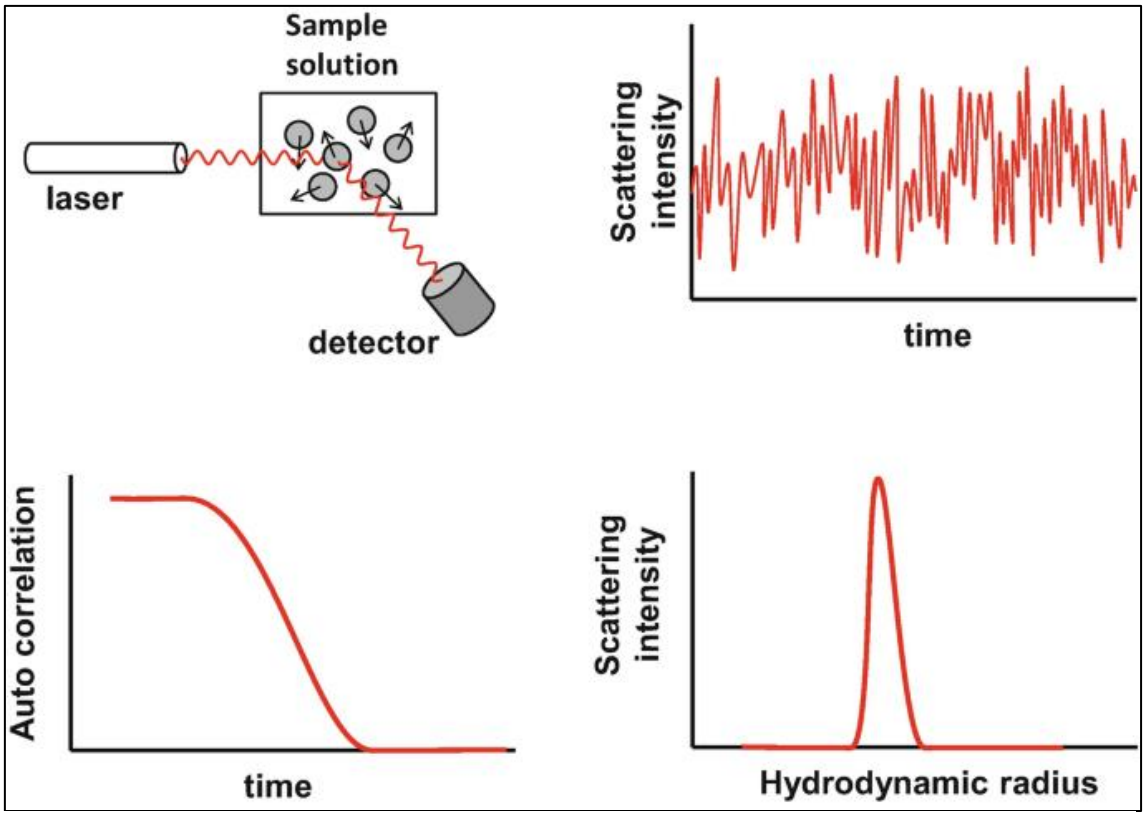

Figure 2. 2. Schematic illustrates the main components for dynamic light scattering (DLS) instrument. When the laser beam hits the particles, the light is scattered based on the particles' movement (Brownian motion) towards each other as a result of collisions. The DLS instrument records the temporal fluctuations by the detector, which contain all the information about particle movement in the sample suspension (Anton Paar, 2023).

The temporal fluctuations recorded by the DLS instrument encompass all the information regarding particle movement in the sample suspension. Furthermore, modern DLS devices have the capability to measure additional parameters such as zeta potential, molecular weight and concentration of numerous samples (Naiim et al., 2015).

The DLS apparatus employed in this study is the Malvern Zetasizer Nano ZS (manufactured by Malvern, UK). The sample was prepared in deionised water at concentration of 1 mgL^{-1}. Seven measurements were applied and then the average calculated.

2.4.3 Zeta Potential

Zeta potential (ζ) is a physical property that describes the surface charge of particles in a liquid or suspension (Samimi et al., 2019). Zeta potential characterisation plays a crucial role in providing information about the surface chemistry, morphology, coatings and films utilised to ensure stable nanoparticles (Arjmandi et al., 2012). It serves as a valuable tool for determining the stability of formulated nanoparticles, even during long-term stability studies. The magnitude of electrostatic repulsion or attraction between nanoparticles, particularly for stability assessments, is a fundamental parameter in zeta potential measurement that can aid in improving suspension formulation (Xu, 2008). Hence, in this research study, the focus was on measuring the surface charge of various types of synthesised gold nanoparticles, including tuned-size gold nanoparticles, functionalised gold nanoparticles, and drug-gold nanoparticle conjugates.

In this study, the surface charge measurement was carried out using one of the recent Zetasizer Malvern® instruments. A total of seven measurements were performed, and their average was subsequently calculated.

2.4.4 Fourier Transform Infrared (FTIR)

Fourier transform infrared (FTIR) is a vibrational spectroscopy technique widely used in the pharmaceutical industry and other sectors. Its primary application is the identification of unknown materials by analysing the functional groups present in their chemical structures (Markovich and Pidgeon, 1991). The characterisation using FTIR varies depending on the material, as it involves the absorption of infrared (IR) light at specific frequencies directly related to the vibrational bond energies between atoms in the molecule, as explained by Markovich and Pidgeon (1991).

Different bonds and molecules exhibit vibrations at different energies, leading to the absorption of different wavelengths of IR radiation and the display of varying intensities (Chabal, 1988). In other words, if molecules A and B have different bond characteristics (such as shorter or longer bonds), they will absorb different wavelengths of IR radiation, resulting in distinctive spectra with varying intensities. Therefore, the FTIR instrument is a valuable tool for determining the functional groups within the chemical structure of compounds by analysing the absorbed IR radiation (Markovich and Pidgeon, 1991). It finds applications in pharmaceutical and food analysis, as well as in the quality screening of formulated products. FTIR is recognised as one of the most reliable, accurate, flexible and simple techniques employed for characterisation purposes in recent times (Tiernan et al., 2020; Van de Voort, 1992).

The FTIR instrument consists of an IR radiation source, an interferometer, a crystal sample stage and a detector. The process begins with the emission of an IR beam from the source, which passes through the interferometer. Inside the interferometer, the IR beam is split by a beam splitter into two different beams that recombine at the splitter, each having travelled a different path length. This recombination creates an interferogram. Subsequently, the combined beam passes through the sample, and the sample absorbs the beam at specific frequencies of energy (**Figure 2.3**). Each sample exhibits a unique frequency absorption pattern, which appears as an interferogram and is detected by the detector. To measure a sample accurately, the instrument typically includes a reference or background beam. The obtained spectrum of the sample is then subtracted from the background spectrum using the FTIR software, commonly known as the FTIR-Library (Chabal, 1988; Rao, 1971; Stuart, 2000; Thompson, 2018).

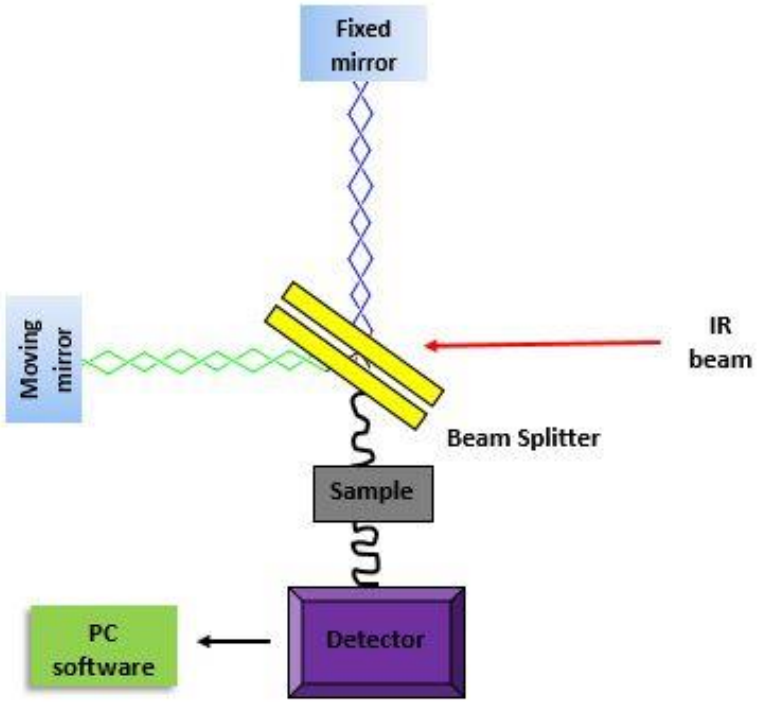

Figure 2. 3. Schematic outlining the basic components of the FTIR interferometer, including the beam splitter, moving and fixed mirrors and the detector which provide detailed information about the sample's molecular composition and structural characteristics.

In this research, samples were characterised using the FTIR instrument provided by PerkinElmer. The characterisation for liquid samples was conducted by applying 100 µL of the sample onto the crystal sample stage, whereas the samples in solid state characterised by placing 1 mg onto the crystal stage.

2.4.5 Transmission Electron Microscopy (TEM)

Transmission electron microscopy (TEM) is an imaging technique that utilises a beam of high-energy electrons to penetrate a solid material (Franken et al., 2020). TEM is considered a cornerstone of modern-day science, made possible by

advancements in materials preparation techniques. The emergence of nanomaterials in the size range of 1-100 nm, which cannot be effectively investigated using conventional microscopes, necessitated the development of transmission electron microscopy as a powerful imaging technique for studying materials at the nanoscale with high magnification (Franken et al., 2020; Piludu et al., 2018).

The concept of TEM imaging involves directing a beam of high-energy electrons through the sample. Basically, **Figure 2.4** provides an overview of the working principle of TEM. The electron beam is generated by a tungsten filament within a vacuum chamber. The emitted electrons are then accelerated and focused using an electromagnetic field. Subsequently, the beam of high-energy electrons passes through the nanomaterial sample, interacts with a phosphor screen, and ultimately generates an image. It is important to note that a brighter image is produced when a greater number of electrons pass through the sample, indicating a lower sample density. Conversely, darker images indicate higher sample density, as the electrons become trapped and cannot pass through the sample (Franken et al., 2020).

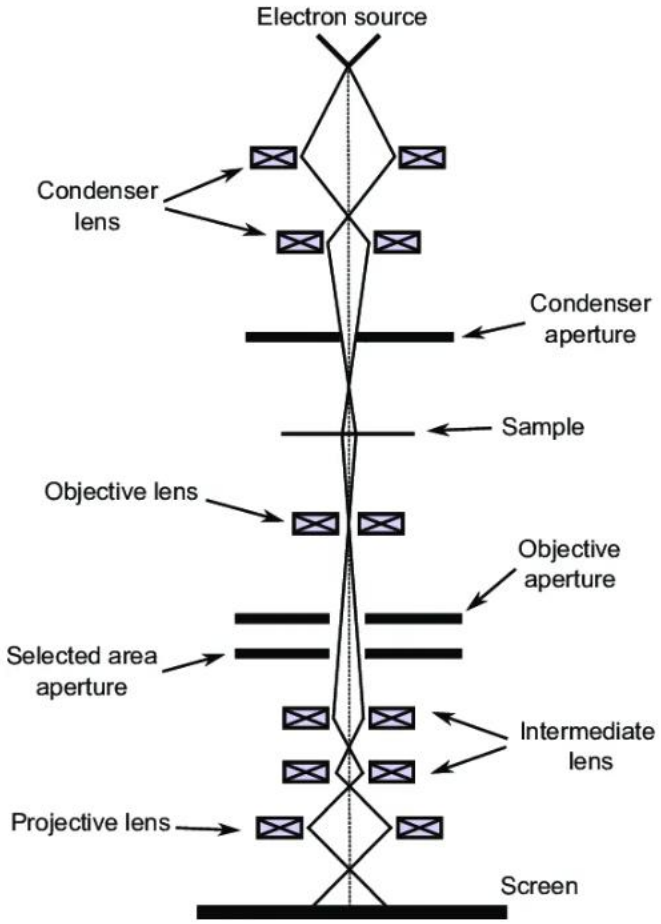

Figure 2. 4. Diagram illustrating the key components of a transmission electron microscope (TEM). The TEM utilises electron beam transmitted through the specimen to generate high-resolution images with detailed structures at the nanoscale (Franken et al., 2020).

A single drop of the well-distributed sample was placed onto a Formvar/carbon grid. Following this, the droplet was allowed to dry and subsequently examined using a Joel 1400 Bio Transmission Electron Microscope (TEM), employing an electron beam current of 80 kV.

2.4.6 Nuclear Magnetic Resonance

Nuclear magnetic resonance (NMR) spectroscopy is a powerful technique for structural characterisation, providing insights into the composition of molecules and their connectivity (Charpentier et al., 2009; Forse et al., 2015). NMR is commonly employed to elucidate the chemical structure of samples, typically in liquid form and dissolved in a specific solvent (Abraham et al., 1998). Zeeman was among the first to investigate the peculiar behaviour of certain nuclei when subjected to a strong magnetic field (Schiff and Snyder, 1939). It is worth noting that isotopes containing an odd number of protons and/or neutrons possess an intrinsic nuclear magnetic moment and angular momentum, known as a nonzero nuclear spin, while nuclides with an even number of both protons and neutrons exhibit a total spin of zero (Abraham et al., 1998). In the laboratory work presented here, the most frequently utilised nuclei for sample characterisation were proton (^{1}H) and carbon (^{13}C). In general, nuclear magnetic resonance spectroscopy operates by examining the interactions between radiofrequency (RF) electromagnetic radiation and the nuclei of molecules when subjected to a strong magnetic field (J. W. Peng et al., 2001). The fundamental principles of nuclear magnetic resonance spectroscopy can be illustrated as described by Nakamura et al. (2015), wherein large superconducting magnets enable the material to exhibit superconductivity, facilitating the transfer of electrons without resistance. To facilitate sample analysis, the NMR instrument used for the work presented here is positioned vertically, opposite the magnetic resonance imaging (MRI), allowing samples to be introduced into the magnetic field from above, as depicted in **Figure 2.5**.

However, once the sample is prepared in specialised NMR tubes, in liquid form, it is referred to as the "solution state" in NMR. On the other hand, for solid-state NMR, where the sample is in the form of a very fine powder, it is placed in an NMR rotor. These rotors are small cylindrical containers with a diameter ranging from approximately 7 to 0.7 mm and a length shorter than 2 cm (Hu et al., 2015).

Although recent NMR magnets no longer rely on liquid nitrogen and instead employ a liquid helium re-liquefaction system to reduce the frequency of liquid helium refills, it is important to note that this information may vary depending on the specific advancements and technologies implemented in NMR instruments.

The characterisation process is explained by Hu et al. (2015), once the sample is inside the magnet, it is positioned within the probe, which is surrounded by a radio-frequency (RF) coil. This coil is constructed from superconducting material, allowing it to transmit radio-frequency pulses to the sample. It is crucial for the material to exhibit superconductivity within the NMR environment to enable the circulation of electrons and the creation of the magnetic field. To maintain the superconducting coil or magnet at a very low temperature, below -240 °C, it is immersed in a bath of liquid helium (He), as depicted in the light grey area in **Figure 2.5**.

Additionally, liquid nitrogen (N) is utilised to create a buffer between the room temperature and the extremely cold temperature of the helium liquid. This arrangement serves to optimise the use of liquid helium, as it prevents excessive boiling and reduces the frequency of refills due to the high cost and limited availability of liquid helium resources, as noted by Hu et al. (2015).

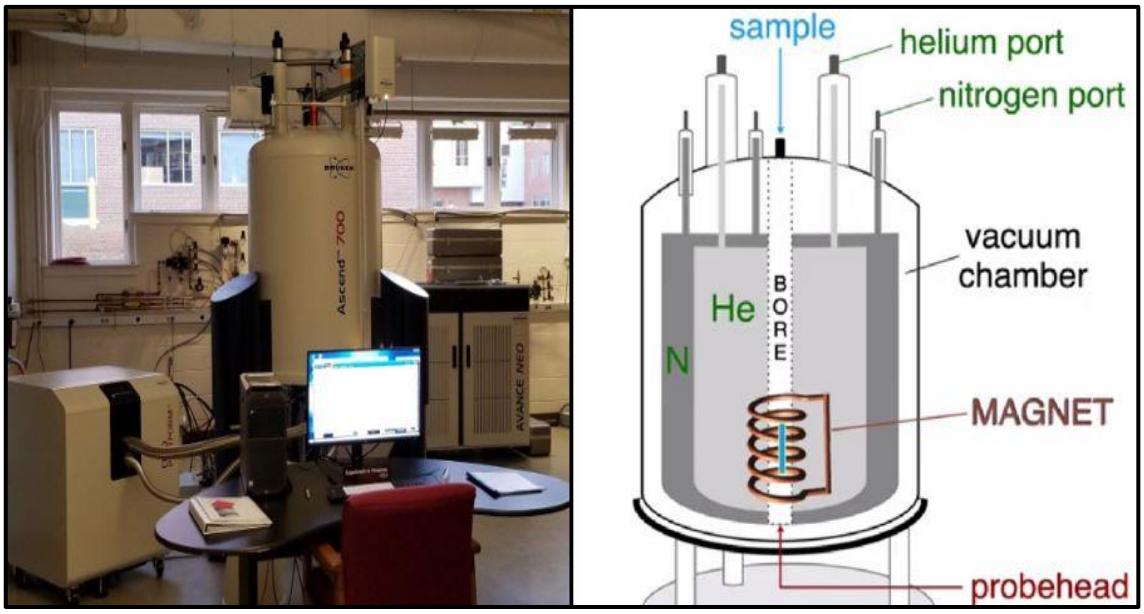

Figure 2. 5. Schematic demonstrates the main components involved in the nuclear magnetic resonance (NMR) spectroscopy. The system includes a powerful magnet, helium and nitrogen ports, sample tube, vacuum chamber, gradient coil, and computer system. These components work collaboratively to generate NMR spectra, providing valuable insights into the molecular structure and composition of the analysed sample (Hu et al., 2015).

In this study, the sample were dissolved in deuterated chloroform at concentration 1 mgL^{-1}, the 600 µL poured into a specific NMR tube (the Kimble Chase NMR Tube High Quality 5 mm 8 Inch Kg-33 500 MHz) and characterisation conducted by the Bruker 400 MHz NMR spectrometer “Puma” provided with Ultra-shield magnet, 5 mm BBFO “smart” probe, and Sample Case autosampler (24 positions).

2.4.7 Inductively Coupled Plasma-Optical Emission Spectrometry

Inductively coupled plasma-Optical emission spectrometry (ICP-OES) utilises a plasma torch. The main principle of the ICP-OES is to quantify certain elements in a sample. This is based on the utilisation of atoms and ions that absorb energy to excite electrons from lower to higher energy levels (Wilschefski & Baxter, 2019). For example, when a lead (Pb) atom acquires energy from the heat from the plasma, electrons will be excited to the higher energy level (E_1); when these electrons return to the lower energy level, called the ground state (E_0), they will emit light of a specific wavelength based on the required energy (Khalid & Kontis, 2008; Wilschefski & Baxter, 2019).

ICP-OES operates by utilising energy from an argon plasma at high temperatures, typically around 10,000 kelvins. During the analysis, both the standards for calibration and the samples are introduced into the plasma through the nebuliser. The sample will be converted to very small droplets in size, called aerosols, once it arrives at the nebuliser and contacts the plasma torch at 10000 kelvins. This will cause atoms in the sample molecules to be atomised and excited electronically. Once electrons return to the ground state, the instrument will measure the light emitted by each element in the sample at a specific wavelength as shown in **Figure 2.6** (X. Hou & Jones, 2000; Yeung et al., 2017).

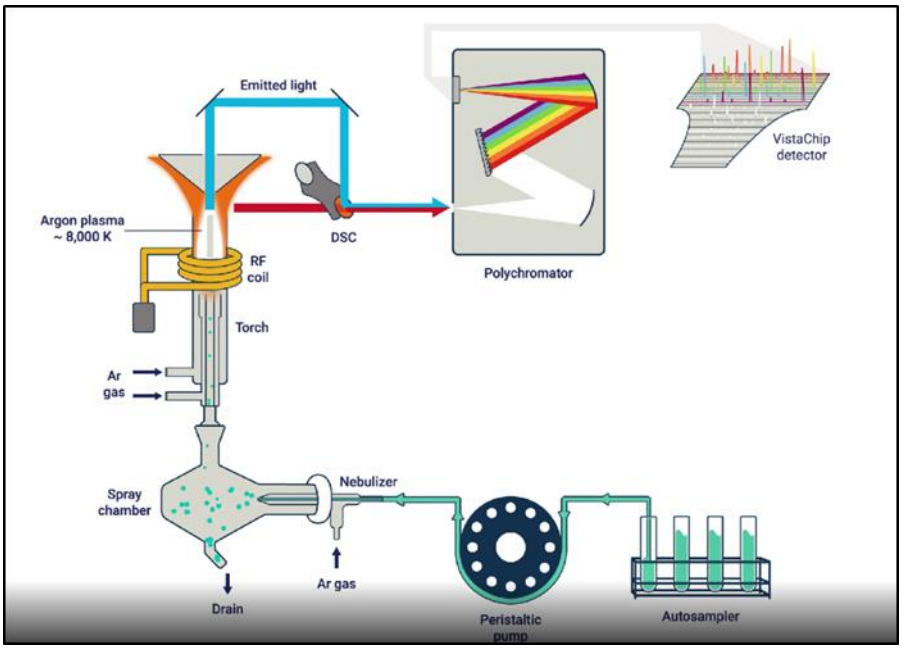

Figure 2. 6. Diagram illustrating the primary components of an inductively coupled plasma-optical emission spectrometer (ICP-OES). The system comprises sample introduction system, an argon gas supply, spray chamber, torch assembly, radiofrequency coil, and data acquisition system. The emitted light from the excited ions providing valuable information about the elemental composition of the sample (Agilent, 2023).

The ICP-MS (Perkin Elmer NexION 300x) was used to quantify the concentration of Au in the synthesised gold nanoparticles. In this study, elemental analysis using ICP-OES involved preparing a series of known concentrations of the analyte as standards, as well as the samples requiring analysis to determine the elements with unknown concentrations.

2.4.8 Thermogravimetric Analysis

Thermogravimetric analysis (TGA) is a technique that measures the mass of a substance as a function of time or temperature. When the substance is subjected to heating in the TGA instrument, its mass may either increase or decrease (Coats and Redfern, 1963; Saadatkhah et al., 2020). In the TGA instrument setup, there is a sample pan equipped with a balance to accurately measure the sample's weight before each analysis process. The instrument also includes a furnace and an inert sample purge gas that regulates the sample environment (**Figure 2.7**). Whether the gas used is inert or reactive, it flows over the sample and exits through the exhaust.

Figure 2. 7. A hyphenated instrument, consisting of a thermogravimetric analyser (far right), a Fourier Transform Infra-Red system (middle) and a Gas Chromatography/Mass Spectrometry System (left) (TGA-IR-GC/MS).

In the work presented here, TGA was employed as a tool for quality assurance and quality control in the analysis of synthesised gold nanoparticles, as well as for assessing the conjugation of remdesivir and amantadine drugs to gold nanoparticles. The utilisation of TGA in these applications is supported by various

studies documented in the literature. For instance, TGA has been suggested for analysing the amount of metallic catalytic residue remaining in carbon nanotubes (Pumera and Iwai, 2009). TGA can be used as a standalone technique or in combination with FTIR for comprehensive characterisation purposes (Ahluwalia, 2023; Loganathan et al., 2017).

TGA analysis in this study was conducted using a PerkinElmer TGA 8000 instrument, employing the subsequent parameters: synthetic air flow rate set at 20 mL/min and a heating rate of 20°C/min with heating effect from 100°C to 900°C.

2.5 Assessment of Cellular Uptake and Cytotoxicity Assay

2.5.1 Cell Culture and Cell Lines

Cell culture can be defined as the process of cell growth under controlled conditions (Mather & Roberts, 1998). Cells are either extracted directly from an organism or from a cell line that has been establish by researchers in the lab. Cell culture enables the study of the physiology and biochemistry of healthy and diseased cells (Mather & Roberts, 1998).

Currently, cell lines are extensively used in cell culture labs due to their low cost, safer for experimentation compared to whole organisms and easy to work as well (Capes-Davis et al., 2019). Herein, J774 cell macrophages were cultured in DMEM cell culture media with ultra-glutamine. DMEM was supplemented with 10% fetal bovine serum (FBS) and 1% penicillin/ streptomycin in a humidified incubator at 37˚C and 5% CO_2.

2.5.2 Cell Growth and Seeding

Firstly, cells were grown through a sequence of passages. Passage number five was used for evaluation of both cellular uptake and cytotoxicity assays in triplicates. For toxicity testing 4.5×10^4 cells /well were seeded in 96 well plate at 37˚C and 5% CO_2 in the incubator for 24 hours. Cellular uptake was conducted by seeding 4×10^3 cells/ well in 6 well plate at 37˚C and 5% CO_2 in the incubator for 48 hours.

2.5.3 Cytotoxicity Assays

In vitro, several types of cytotoxicity assays are utilised as toxicity indicators for drugs and other biological molecules that may work irreversibly on receptors, leading to undesirable cell membrane destruction or the prevention of protein synthesis (Adan, Kiraz and Baran, 2016). These assays are critical in evaluating the potential harmful effects of compounds by measuring cell viability, membrane integrity, and other cellular functions that could be compromised, providing valuable insights into the safety profile of the substances tested. Herein, various assays involved 3-(4,5-dimethylthiazol-2-yl)-2,5-diphenyltetrazolium bromide (MTT), lactate dehydrogenase (LDH), 2,3-bis-(2-methoxy-4-nitro-5-sulfophenyl)-2H-tetrazolium-5-carboxanilide (XTT) cell proliferation assay, and sulforhodamine B (SRB) assay were applied for toxicity studies.

2.5.3.1 MTT Assay

It can be regarded as one of the most widely employed cytotoxicity assays for determining cell viability and proliferation rates. While the exact mechanism of this assay is not yet fully understood, it primarily relies on the reduction reaction carried out by active mitochondria within viable cells (**Figure 2.8**) (B. Jha et al.,

2018; S. Wang et al., 2011). These cells contain NAD (P) H-dependent oxidoreductase enzymes that reduce MTT, resulting in the formation of formazan crystals on the cell surface (S.-W. Lim et al., 2015). An evaluation of cytotoxicity effects for the synthesised gold nanoparticles and drug conjugated Au NPs was conducted using MTT assay in triplicates. The procedure involves seeding 4.5 × 10^4 cells per well in a flat-bottom 96-well plate, followed by incubation at 37°C and 5% CO_2 for 24 hours. Subsequently, the media removed and replaced with fresh media containing a series of various concentrations (1, 2, 3, 5, 15, and 30 µg L^{-1}) of each form of synthesised gold nanoparticles. The plate is then incubated for an additional 24 hours under identical conditions.

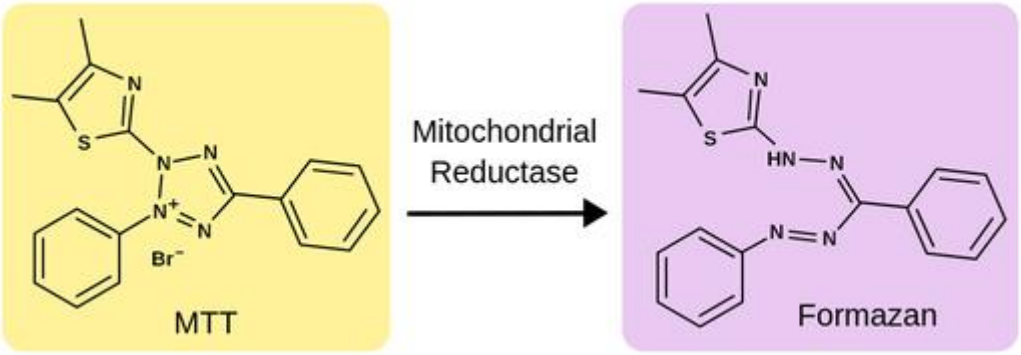

Figure 2. 8. A schematic illustrates the Chemical reduction of MTT to form Formazan by the effect of mitochondrial enzymes (Lim et al., 2015).

After the incubation period, 20 µL of MTT reagent is added to each well, and the plate is further incubated for approximately 4 hours. This led to the formation of formazan crystals on the cell surface. Following this, the solution mixture was removed, and 100 µL of DMSO was added to dissolve the crystals. The well plate

was gently shaken, and the absorbance measured at 595 nm using a TECAN Spark® microplate reader. A control consisting of medium, and cells not treated with nanoparticles has been used for comparison. This experiment has been conducted in triplicates (n=3).

2.5.3.2 LDH Assay

Lactate dehydrogenase can be expressed as intracellular enzyme which responsible for production of body's energy by converting sugars into energy. LDH can be found in most of body tissues and organs (Farhana & Lappin, 2022). LDH cytotoxicity test measures the level of LDH enzyme in the blood or other body fluids (e.g. cell culture media) that secreted from organs such as lungs or living organisms, respectively. When these organs damage, LDH released into the blood stream leading to formation of high levels of the enzyme and indicating that organ is damaged as a result of a specific disease (Farhana & Lappin, 2022). On the other hand, *in vitro* LDH cytotoxicity test has ability to determine LDH levels in cultured cell supernatants using UV colorimetric method. Though, this assay has been utilised to measure the released lactate dehydrogenase enzyme from the cytoplasm of damaged cells. After seeding 4.5×10^4 cells and incubation for 24 hours under similar conditions that has been utilised for MTT. Herein, on the same plate, untreated cells as control, and lysis control cells (termed as maximum LDH activity) were cultured as well overnight. Then, the media replaced with fresh media containing various concentrations 1, 2, 3, 5, 15, and 30 µg L^{-1} of prepared gold nanoparticles and incubated for another 24 hours.

To the lysis control cells, 10 µL of the lysis solution was added and gently mixed. Then, the plate was returned back to the incubator for additional 45 minutes.

Following this, 50 µL of the LDH reaction mixture was added to each well and gently mixed for 30 seconds. The plate was then shielded from direct light by covering it with foil and left to incubate at room temperature for 30 minutes. Then, 50 µL of the stop solution was introduced to each well and mixed thoroughly. Finally, the optical density was measured for both the control and experimental cells at a reference wavelength of 650 nm using a plate reader equipped with a 450 nm filter. It's important to note that in certain scenarios, the absorbance can be measured before adding the LDH stop solution, depending on the reaction rate. For instance, in cases of slow reaction rates indicated by a gradual colour conversion, the addition of the LDH stop solution might not be necessary. This experiment has been conducted in triplicates (n=3).

2.5.3.3 XTT Assay

The XTT assay is generally considered to provide more reliable and consistent results, primarily due to the direct solubility of the formazan product. This makes the XTT assay more amenable to high-throughput screening and prolonged incubation periods. Unlike MTT, XTT does not require a subsequent solvent extraction step as the formazan product is directly soluble in cell culture media, eliminating the need for additional reagents (such as DMSO)(S. Wang et al., 2011). However, the procedure involves measuring the absorbance of produced formazan dye at wavelength 450 nm.

Overall, while both MTT and XTT assays are widely used and provide similar types of information, the XTT assay has gained popularity due to its improved reliability, simplicity, and elimination of the need for a solvent extraction step, making it a preferred choice in many research and high-throughput applications

(Grela et al., 2015; Šatkauskas et al., 2016; Simon-Deckers et al., 2008). This experiment has been conducted in triplicates (n=3).

2.5.3.4 SRB Assay

The sulforhodamine B (SRB) assay is a quantitative method based on the binding of SRB dye to specific proteins within cells. This interaction occurs through sulfonic groups that bind to amino acid residues under mildly acidic conditions, with dissociation occurring under basic conditions (Vichai & Kirtikara, 2006). SRB dye, characterised by its bright-pink colour, which can be extracted from stained cells. Consequently, the quantity of dye extracted directly corresponds to the number of cells (Vichai & Kirtikara, 2006).

During absorbance measurements, the optical density (OD) obtained reflects the protein content within viable cells, serving as a proxy for cell count. In summary, the SRB assay is more sensitive, simple, and reliable assay than XTT and MTT assays due to its stable end point, and suitable signal to noise ratio. The OD of SRB in each well is directly proportional to the cell number so the OD values can be plotted against concentration and the CC_{50} determined (Voigt, 2005). Therefore, data was analysed based on measuring the absorbance at specific wavelength 540 nm for the SRB dye:

$$\text{The \% cell viability} = \frac{\text{OD of the treated cells}}{\text{OD of the controlled cells}} \times 100$$

After seeding cells 4.5×10^4 cells/well and incubation for 24 hours, without removing the media, 100 µL of fixation reagent solution to each well was added and left to be incubated in the fridge at 4°C protected from light for 1 hours. Then,

plate wells were washed several times (2-4 times) with deionised water and left to dry overnight. The main purpose of this wash is to remove any excess fixative reagent or serum protein around the wells. After dry, 100 µL of SRB day is added to every well and allowed to be stained at room temperature for two hours under dark conditions.

Later, the SRB dye solution was removed by 0.1 M acetic acid solution or day wash solution provided by the supplier in the kit assay 2 times (make sure unbound dye is removed). This was followed by drying the well plate at room temperature until any moisture removed. Finally, dried SRB was solubilised by addition of 150 µL of the SRB buffer per well and gently has been shaken for 5 minutes before reading the OD density at 590 nm. The background absorbance was measured with reference filter at 690 nm. This experiment has been conducted in triplicates (n=3).

2.5.4 Quantification of Conjugated and Unconjugated Forms of Au NPs

Gold nanoparticles in cellular uptake were measured by seeding cell macrophages 4×10^3 cells/ well in 6 well plate and incubated at 37°C and 5% CO_2 for 48 hours. In the following day, cells were treated with synthesised gold nanoparticles and left to be incubated under similar conditions for another 24 hours. Then, cells washed with PBS and stored at -20 °C for further use.

For ICP-OES analysis, two concentrations of 68% HNO_3 / 1% HCl, and 2% HNO_3 / 1% HCl stock solution, were freshly prepared. First, the cells injected with 0.5 mL of 68% HNO_3 / 1% HCl solution mixture and left to be digested by cell line

macrophages for about 2 hours. After that, digested cells transferred into 15 mL metal free falcon tubes and diluted with 5 mL of 2% HNO_3, 1% HCl stock solution.

Herein, gold solutions of known standards were utilised to produce a variety of gold concentrations (ranging from 0.01 to 1.0 mg L^{-1}) to calibrate the instrument.

2.6 Data Analyses

Several forms of gold nanoparticles have been synthesised, and their LSPR absorption peak shift, shape, surface chemistry, particle size distribution and zeta potential were determined by using UV-Vis spectrophotometer, TEM, FTIR, and DLS, respectively. Additionally, TGA was also applied to quantify the reagents capping amount based on the effect of temperature over period of time. The recorded experimental data were presented as mean values accompanied by their corresponding standard deviations, for example, as illustrated in Chapter 3 Section 3.2.1 Table 3.1. The variation in size between prepared Au NPs was indicated using one-way ANOVA.

For NMR (Nuclear Magnetic Resonance) spectral data analysis, MestreNova x64, a Chemistry Software Solution, was employed. Moreover, ChemDraw Professional 20.0 was used to draw the chemical structure of the drug molecules. The CC_{50} (half-maximal cytotoxic concentration) for the AMTD/AuNPs and REM/AuNPs was measured using EXCEL Microsoft. For DLS results, Farkas & Kramar, (2021) introduced a method for parameterisation and graphical depiction of dynamic light scattering (DLS) data. This approach aims to enhance the comprehension of DLS data analysis and mitigate potential confusion. In this research, data obtained from DLS were collected at different intensities, therefore

they have been adjusted at similar scale of intensity 1 or 100 as depicted in Chapter 4 Section 4.3.1.1 Figure 4.6.

The Cronbach's alpha, α (or coefficient alpha), developed by Lee Cronbach in 1951, is a measure of internal consistency or reliability of a set of test or survey items, by ensuring that the items are correlated and provide consistent results. It is a powerful method utilised for data analysis to indicate the internal consistency of a set of measurement scales.

All toxicity assays were conducted in triplicates (n=3). Data were represented as mean ±standard deviation (Stdev.). The significant variance using ANOVA was identified at values of $^{**}p < 0.01$, and $^{***}p < 0.001$ as compared to the control (untreated cells). The cell viability was measured based on the following equation:

The % cell viability = Absorbance of treated cells / Absorbance of controlled cells × 100.

Chapter (3): Synthesis and Size Tuning of Gold Nanoparticles

3.1 Introduction

Many challenges remain in the synthesis and size tuning of Au NPs, since size precision can better ensure successful application of the produced particles. The size and properties of synthesised Au NPs also influence their stability and fate. A range of synthesis techniques are available, aiming to produce advanced Au NPs with exceptional characteristics, particularly for applications in the fields of medicine, engineering, physics and even environmental safety.

Au NPs are well studied due to their stability, inert nature and limited toxicity. In this chapter, several techniques for the synthesis and size control of Au NPs down to 8 nm were employed. Particles of approximately 8 nm in size strike a balance between stability, loading capacity and the capability to evade the immune system. The technique of size control was based on monitoring the pH of chloroauric acid solution mixture in the presence of potassium carbonate (K_2CO_3) and in combination with trisodium citrate and tannic acid as the reducing agents. In addition to the 8 nm, a variety of particle sizes (up to 60 nm) were also produced. The larger Au NPs were synthesised using a standard sodium carbonate ($NaNO_3$) capping method. The produced particles underwent comprehensive characterisation using various analytical techniques, including UV-Vis spectrophotometry, Dynamic Light Scattering (DLS), and Transmission Electron Microscopy (TEM). The aim of this characterisation was to perform a detailed comparison between the ultra-small Au NPs produced using the novel synthesis approach developed here, and the Au NPs capped with the standard technique involving sodium carbonate.

3.2 Results and Discussion

3.2.1 Particle Size and Size Distribution of Synthesised Au NPs

The methodology used to produce the particles was described earlier (Chapter 2, Section 2.3). The results in **Table 3.1** shows the nominal size, pH, and the capping agents used in the preparation of Au NPs.

Table 3. 1. Primary synthesis conditions for the gold nanoparticles (Au NPs) produced by various capping agents potassium carbonate (K-Au NPs), sodium carbonate (Na-Au NPs), tannic acid (TA-Au NPs), trisodium citrate (cit-Au NPs), sodium dodecyl sulfate (SDS-Au NPs), and poly (ethylene glycol) (PEG- Au NPs).

Au NPs	Nominal size	pH	Capping agent
K-TA-AuNPs	8 nm	10.0	K_2CO_3 & $C_{76}H_{52}O_{46}$
Na-TA-AuNPs	10 nm	8.5	Na_2CO_3 & $C_{76}H_{52}O_{46}$
TA-AuNPs (1.5 mM)	12 nm	6.6	$C_{76}H_{52}O_{46}$
TA-cit-AuNPs (0.5 mM)	13 nm	6.6	$C_{76}H_{52}O_{46}$ & $Na_3C_6H_5O_7$
TA-AuNPs (0.75)	14 nm	6.0	$C_{76}H_{52}O_{46}$
TA-AuNPs (0.5 mM)	15 nm	5.8	$C_{76}H_{52}O_{46}$
SDS-AuNPs	16 nm	6.2	$NaC_{12}H_{25}SO_4$
Cit-AuNPs (1 mM)	20 nm	6.0	$Na_3C_6H_5O_7$
PEG-AuNPs	28 nm	5.6	$(C_2H_4O)_n$
Cit-AuNPs (0.8 mM)	40 nm	5.4	$Na_3C_6H_5O_7$
Cit-AuNPs (0.6 mM)	60 nm	5.2	$Na_3C_6H_5O_7$

Nanoparticles prepared using potassium carbonate and sodium carbonate were adjusted to sizes of 8.77 ±0.92 nm and 10.68 ±0.68 nm at pH values 10.0 and 8.5, respectively. In contrast, nanoparticles synthesised under acidic conditions exhibited particle sizes of 20.54 ±0.45 nm, 40.59 ±0.83 nm, and 60.67 ±0.71 nm at pH values 6.01, 5.4, and 5.2, respectively (Table 3.2).

This research also involves an examination of how modifying the temperature while producing Au NPs can influence the rate at which their size increases. For instance, in this study, the impact of temperatures 120°C and 70°C during the synthesis of cit-Au NPs (20.54 ±0.45 nm) and TA-Au NPs (10.68 ±0.68 nm), respectively, was explored (Chapter 3, Section 3.2.7).

The particle size distribution of the prepared gold nanoparticles, ranging from 8 nm to 60 nm, were characterised using DLS, a technique that analyses the Brownian motion of nanoparticles in solution (Whitehead et al., 2021). **Figure 3.1** and **Table 3.2** illustrate the characterisation of the Au NPs with different sizes. The results indicated that all peaks corresponding to the prepared nanoparticles exhibit a monodispersed pattern, as evidenced by the low polydispersity index (PDI) recorded by DLS (**Table 3.2**).

In this study, poly (ethylene glycol) (PEG) was utilised as a capping agent for the synthesis of one set of Au NPs (Table 3.1). Previously, Manson et al. demonstrated how capping gold nanoparticles with PEG improves their stability both *in vitro* and *in vivo* (Manson et al., 2011a). Based on the results obtained, it becomes evident that PEG-6000, serving as the capping agent, effectively

contributes to the production of stable gold nanoparticles with a diameter of approximately 28.41 ±0.43 nm (**Figure 3.1**).

Additionally, the anionic surfactant sodium dodecyl sulfate (SDS) was utilised to control the size and ensure long shelf-life stability of the gold nanoparticles. By using SDS as a surfactant to stabilise the nanoparticles' surface, their size was effectively controlled to approximately 16.31 ±0.38 nm, as confirmed by DLS characterisation. This result aligns with the findings of Cabrera et al. (2017) who conducted research on using SDS in a green synthesis method to control the size of gold nanoparticles. They observed that the majority of the particle diameters were found to be between 16 nm and 22 nm (Cabrera et al., 2017). The use of SDS in this study thus corroborates the earlier research regarding size control in Au NPs.

In **Figure 3.1**, the results clearly demonstrate effective control of the size of gold nanoparticles to 16.31 ±0.38 nm with the presence of SDS surfactant. Such surfactants are known for their ability to disperse gold nanoparticles and prevent their aggregation, thereby enhancing the nanoparticles' shelf life (Morsy, 2014).

Tannic acid was also employed to control the size of the nanoparticles, and its significant role in tuning the size of gold nanoparticles to less than 20 nm is depicted in **Figure 3.1**. At various concentrations 0.5, 0.75 and 1.5 mM, tannic acid yielded different sizes of gold nanoparticles at 15.11 ±0.64 nm, 14.35 ±0.75 nm, and 12.57 ±0.88 nm, respectively. This technique demonstrated that tannic acid has the capability to control smaller sizes of gold nanoparticles compared to the use of citrate as the reducing agent. This effect is attributed to the presence

of hydroxyl groups in tannic acid's chemical structure, as described by Ide & Davis (2014). According to the results presented in **Figure 3.1**, it was observed that increasing the concentration of tannic acid as a reducing agent resulted in a reduction of nanoparticle size. This phenomenon can be attributed to the presence of multiple hydroxyl groups in tannic acid, which react with a constant ratio of gold ions in chloroauric acid, thereby accelerating the nucleation process and leading to the formation of smaller nanoparticles.

A study by H. Kim et al. (2016) stated the concentration effect of the reducing reagent on synthesis of gold nanoparticles, where an increase in the reducing agent concentration resulted in smaller nanoparticle sizes. Additionally, tannic acid's antioxidant activity has been suggested as a reason for its ability to tune gold nanoparticles to very small sizes (Aromal and Philip, 2012; Gülçin et al., 2010). The antioxidant properties of tannic acid enable the release of freely reactive hydrogen atoms, although the exact mechanism is still not fully understood (Ahmad et al., 2010; Ahmad, 2014). The polyphenolic structure of tannic acid, comprising hydrophilic and hydrophobic components, contributes to its antioxidant action and plays a significant role as a reducing agent in the formation of very small gold nanoparticles.

The size of gold nanoparticles was further tuned to sub-10 nm using a novel technique that involved adjusting the pH of a gold solution mixture with potassium carbonate (K_2CO_3) in the presence of tannic acid and trisodium citrate agents. The effectiveness of this technique was compared with the use of sodium carbonate (Na_2CO_3) in achieving the synthesis of ultra-small nanoparticles through pH control at basic conditions (**Figure 3.1).**

Potassium carbonate and sodium carbonate are salts that contain only one carboxylate group, in contrast to trisodium citrate, which contains three carboxylate groups. This structural difference makes it easier for biomolecules to replace the single carboxylate group in nanoparticles synthesised with potassium carbonate, compared to those made with the trisodium citrate agent (Lambros et al., 2022). Additionally, gold nanoparticles synthesised with potassium carbonate exhibit a strong attachment to molecules with thiol or amine groups, displacing carbonate (Woehrle et al., 2005). Moreover, carbonate has been shown to provide high loading amounts of conjugation, especially with proteins (Lambros et al., 2022).

Thus, based on the data shown in **Figure 3.1**, it can be observed that potassium carbonate successfully controlled the size of the nanoparticles to 8.77 ±0.928 nm diameter by controlling the pH at basic conditions (pH 10.0). Potassium carbonate can act as a pH regulator in nanoparticle solutions due to its ability to function as a buffering agent. When added to a solution containing nanoparticles, potassium carbonate can interact with acids or bases present, helping to maintain a stable pH level by resisting significant changes in acidity or alkalinity (Piella et al., 2016). The carbonate ions in potassium carbonate can react with acids, reducing the increase in acidity, or with bases, curbing excessive alkalinity, thereby assisting in stabilising the pH of the nanoparticle solution. Moreover, pH can influence the kinetics of the reduction process used to synthesise Au NPs. By adjusting the pH using potassium carbonate, the reduction rate can be changed, impacting the nucleation and growth of the nanoparticles. This, in turn, can affect the size of the Au NPs (Piella et al., 2016).

Overall, adjusting the pH of the solution with potassium carbonate indirectly affects the reduction kinetics, stability, and surface characteristics of Au NPs. These combined factors play a substantial role in governing the nanoparticle size during their synthesis.

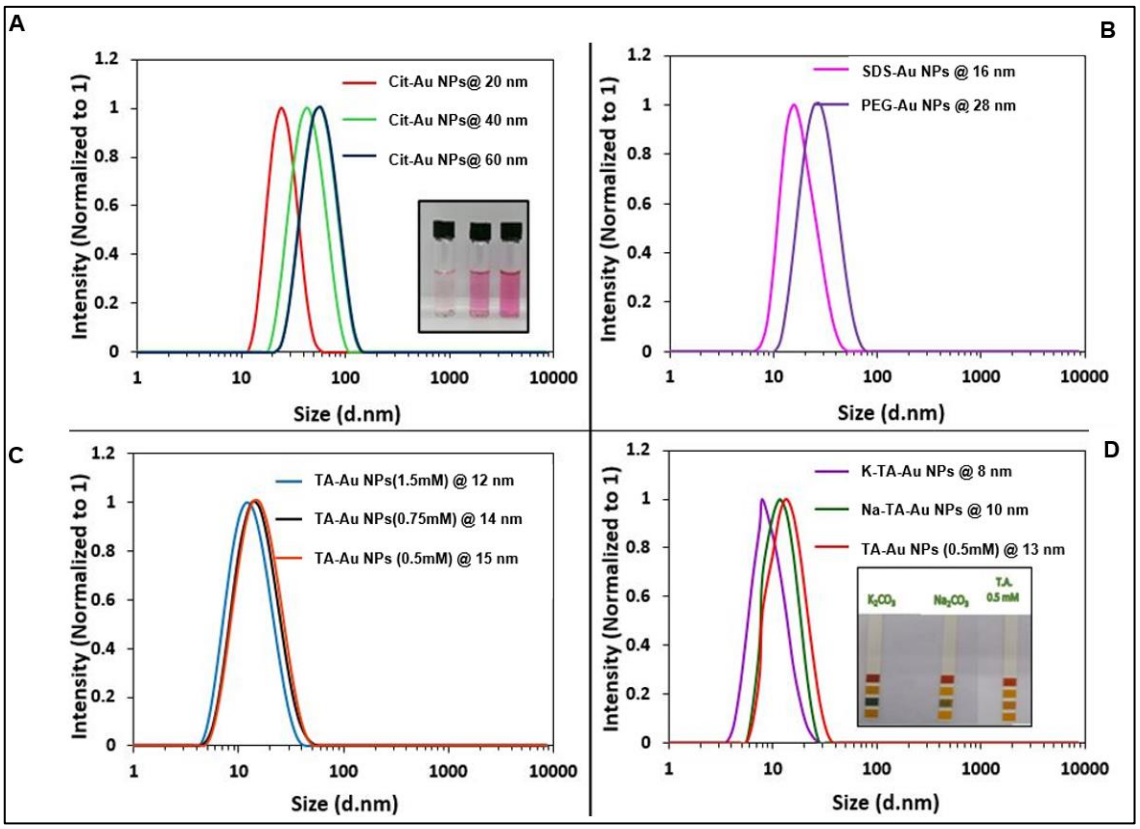

Figure 3. 1. DLS particles size measurements for synthesised Au NPs. A: trisodium citrate gold nanoparticles (Cit-Au NPs) 20 nm, 40 nm, and 60 nm prepared at various concentrations 1mM, 0.8mM, and 0.6mM, respectively. B: Au NPs capped by sodium dodecyl sulfate 0.38mM at 16 nm. In addition to 28 nm size of Au NPs capped with poly (ethylene glycol). C: nanoparticle sizes at 12 nm, 14 nm, and 15 nm prepared by tannic acid 1.5mM, 0.75mM, and 0.5mM, respectively. D; tuned size gold nanoparticles (K-TA-Au NPs) and (Na-TA-AuNPs) prepared in the presence of potassium carbonate and sodium carbonate, respectively, at different concentrations 0.2M and 0.12M.

Table 3. 2. Particle sizes, standard deviation, and zeta potential measured using DLS, and UV-vis.

Synthesised Au NPs	Capping agents	Concentration	DLS (nm)	STD (d. nm)	UV-Vis (λ_{max})	DLS (zeta potential)	DLS (PDI)
K-TA-Au NPs	K_2CO_3, TA	0.2 M	8.77 nm	±0.92	516 nm	-38.1 mV	0.127
Na-TA-Au NPs	Na_2CO_3, TA	0.12 M	10.68 nm	±0.68	520 nm	-21.5 mV	0.214
TA-Au NPs	TA	1.5 mM	12.57 nm	±0.88	520 nm	-10.5 mV	0.381
TA-cit-Au NPs	TA, Na_3citrate	0.5 mM	13.11 nm	±0.44	520 nm	-11.8 mV	0.110
TA-Au NPs	TA	0.75 mM	14.35 nm	±0.75	520 nm	-12.5 mV	0.431
TA-Au NPs	TA	0.5 mM	15.11 nm	±0.64	520 nm	-13.2 mV	0.341
SDS-Au NPs	SDS	0.38mM	16.31 nm	±0.38	522 nm	-37.1 mV	0.173
Cit-Au NPs	Na_3citrate	1 mM	20.54 nm	±0.45	524 nm	-33.1 mV	0.095
PEG-Au NPs	PEG		28.41 nm	±0.43	524 nm	-33.6 mV	0.270
Cit-Au NPs	Na_3citrate	0.8 mM	40.59 nm	±0.83	532 nm	-34.8 mV	0.219
Cit-Au NPs	Na_3citrate	0.6 mM	60.67 nm	±0.71	538 nm	-33.8 mV	0.310

3.2.2 Zeta Potential in Stability Studies of Au NPs

Zeta potential measurements are important in determining the stability of nanoparticles by providing a measure of the charge surrounding the surface of colloidal nanoparticles (Xu, 2008). While various techniques can be used for the synthesis of gold nanoparticles, there is a likelihood that the synthesised nanoparticles may be somewhat unstable or have a short shelf life. Suspended Au NPs with high surface charge are expected to repel one another, leading to stabilised nanoparticles with a long-term shelf life (Vijayakumar, 2014). It has been reported that the optimal zeta potential value for a stable nanoparticle suspension falls outside the range of -10 mV to +10 mV (Xu, 2008).

Herein, the zeta potential for the synthesised Au NPs involving, cit-Au NPs, PEG-Au NPs, SDS-Au NPs, TA-Au NPs, K-TA-A uNPs and Na-TA-Au NPs was determined. Each form of synthesised Au NPs was measured six times, the mean, standard deviation, and variance were statistically indicated and introduced in **Appendix 1**. Notably, in **Figure 3.2**, the gold nanoparticles synthesised with tannic acid gold nanoparticles (TA-Au NPs), showed the highest zeta potential (or low negative surface charge) value at -11.45 ±0.34 mV, followed by sodium carbonate (Na-TA-Au NPs), having a size of 10.68 ±0.68 nm, exhibited zeta potential value of -21.58 ±0.13 mV compared to the other nanoparticles. In contrast, the gold nanoparticles synthesised with potassium carbonate (K-TA-AuNPs), with a size of 8.77 ± 0.92 nm, displayed the lowest zeta potential (or highly negative surface charge) value of -38.33 ±0.28 mV. Additionally, both

PEG-AuNPs and cit-Au NPs displayed zeta potential at close values -33.81 ±0.35 mV and -33.64 ±0.22 mV, respectively.

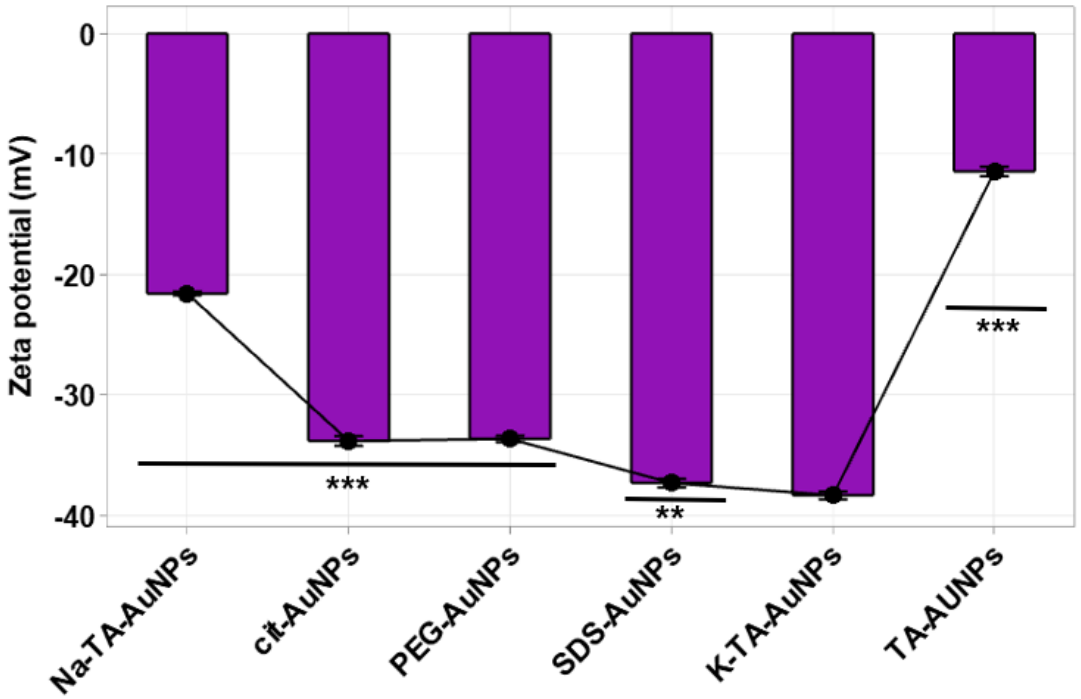

Figure 3. 2. Zeta potential measured by Dynamic Light Scattering (DLS) for the synthesised gold nanoparticles, including Na-TA-Au NPs, cit-Au NPs, PEG-Au NPs, SDS-Au NPs, K-TA-Au NPs, and TA-Au NPs. Results were compared to the tuned size of nanoparticles K-TA-Au NPs with 8 nm size. The observed differences in zeta potential of prepared Au NPs represented as means ± standard deviation (SD) of six independent experiments. Bars with a symbol (*) show statistical differences (** $p < 0.05$, and *** $p < 0.001$) compared with the tuned size nanoparticles K-TA-Au NPs.

3.2.3 Shifts in Surface Plasmon Resonance at Maximum Wavelength

The surface plasmon resonance (SPR) phenomenon involves the interaction between the electric fields of electromagnetic waves, such as visible light, and the collective oscillation of electrons at the surface of gold nanoparticles (X. Huang & El-Sayed, 2010; Jain et al., 2008). The gold nanoparticles synthesised using various techniques, had their SPR absorption peaks determined, using a UV-Vis spectrophotometer. The results showed significant shifts resulting from size differences (**Figure 3.3**). The SPR absorption peaks for Au NPs prepared using potassium carbonate (K-TA-Au NPs), sodium carbonate (Na-TA-Au NPs), tannic acid (TA-Au NPs), trisodium citrate (cit-Au NPs), and polyethylene glycol (PEG-Au NPs) with particle sizes of 8.77 ±0.928 nm, 10.68 ±0.68 nm, 15.11 ±0.64 nm, 20.54 ±0.45 nm, and 28.41 ±0.43 nm were detected at maximum wavelengths of 516 nm, 520 nm, 520 nm, 524 nm, and 524 nm, respectively. Furthermore, the cit-Au NPs with larger sizes of 40.59 ±0.83 nm and 60.67 ±0.71 nm exhibited a significant shift in the SPR absorption peaks towards maximum wavelengths of 532 nm and 538 nm, respectively, as showed in **Figure 3.3.**

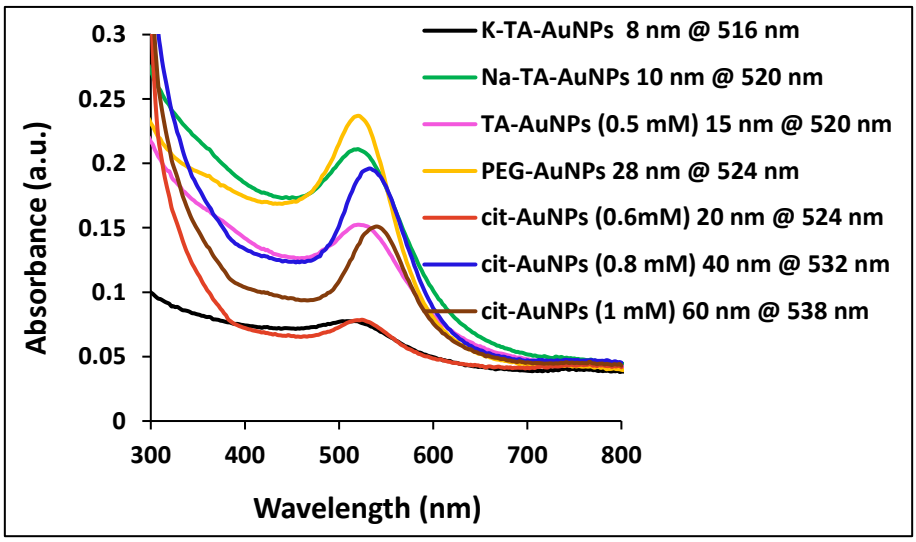

Figure 3. 3. Surface plasmon resonance peaks for the synthesised Au NPs determined through UV-Vis spectrophotometry. Larger nanoparticles exhibit a high maximum wavelength, contrasting with the smaller nanoparticles.

3.2.4 Morphological Transformation of Au NPs

As described earlier, gold nanoparticles were synthesised using different methods, including potassium carbonate (K-TA-AuNPs), sodium carbonate (Na-TA-AuNPs), tannic acid (TA-AuNPs), and trisodium citrate (cit-AuNPs) to control particle nucleation and/or act as capping agent. **Figure 3.4** presents TEM images that offer detailed visualisation of the nanoparticles' morphology. The TEM images illustrate that gold nanoparticles tuned to a size of 8.77 ±0.928 nm possess a well-defined, homogenous, and spherical shape. These nanoparticles are evenly dispersed in the solution without any signs of aggregation, as depicted in **Figure 3.4a**. Conversely, gold nanoparticles tuned to a size of 10.68 ±0.68 nm using sodium carbonate in the presence of a combination of tannic acid and trisodium citrate reagents display significant clusters of nanoparticles (**Figure 3.4b**).

The size control of gold nanoparticles, whether achieved using tannic acid alone or in combination with trisodium citrate, was investigated through microscopic analysis. TA-AuNPs (15.11 ±0.64 nm) exhibited a characteristic linear chain and spherical shape, as shown in **Figure 3.4c**. Similarly, gold nanoparticles prepared using a combination of both tannic acid and sodium citrate reagents at various concentration ratios were also examined through TEM imaging. These nanoparticles displayed a variety of linear chains connected to each other,

influenced by the steric forces acting on the nanoparticle surfaces, as depicted in **Figure 3.4d**. Notably, the TEM images in **Figure 3.4d & 3.4e** demonstrated that these nanoparticles are well-monodispersed in the colloidal solution and can be identified as non-aggregated gold nanoparticles with specific sizes illustrated in Chapter 3 Table 3.1. Lastly, the gold nanoparticles prepared using the citrate reduction technique displayed monodispersity with homogeneous size and spherical shape of 20 nm (**Figure 3.4f**).

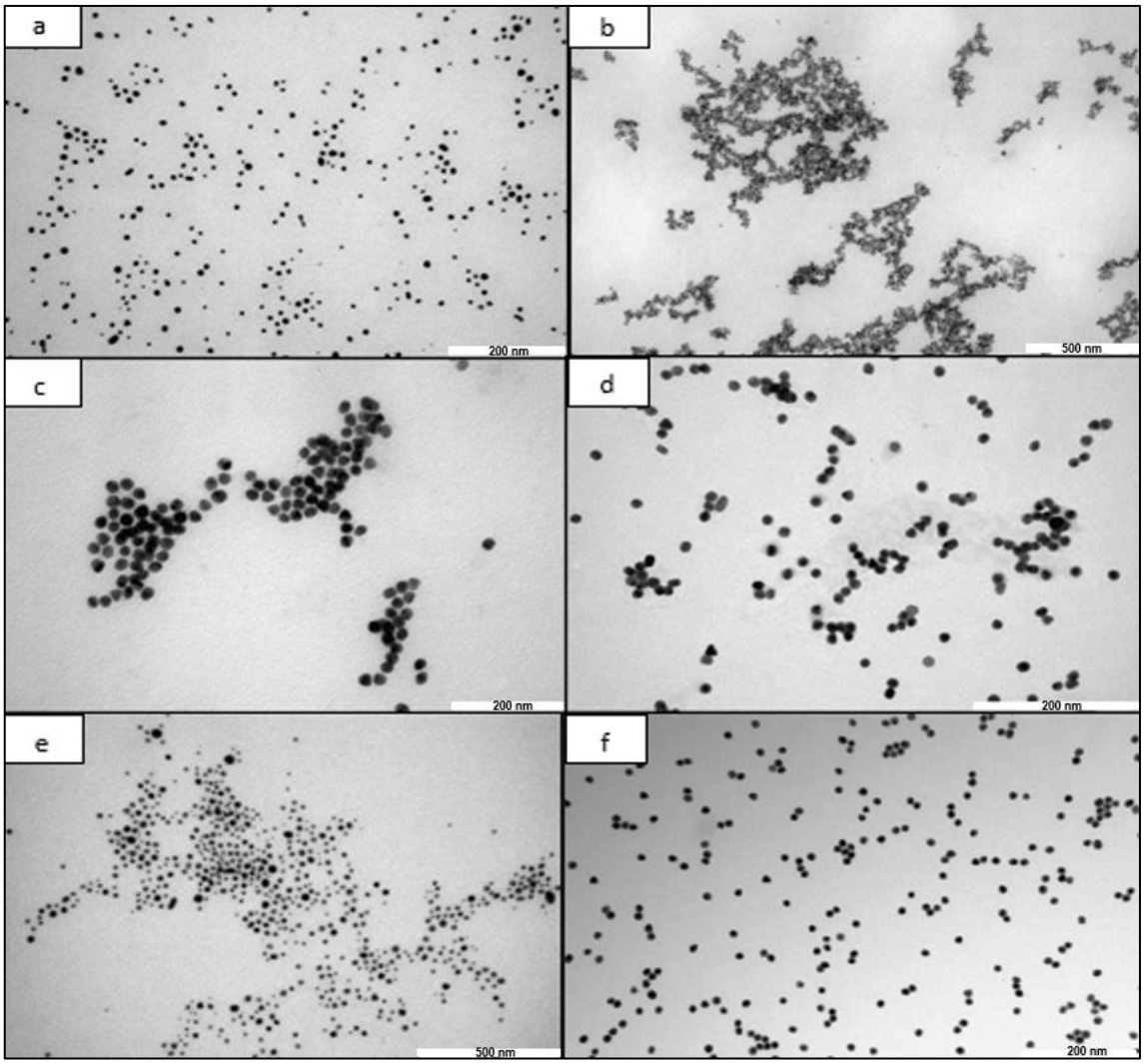

Figure 3. 4. TEM images at different scale bars (200 and 500 nm), showing the morphology and homogeneity of the following prepared gold nanoparticles: a) potassium carbonate, b) sodium carbonate, c) tannic acid (alone), d & e) tannic acid & trisodium citrate (in combination), and f) trisodium citrate (alone).

Additionally, TEM imaging was conducted for the nanoparticles prepared using several surfactants, including polyethylene glycol (PEG), polyvinyl pyrrolidone (PVP), sodium dodecyl sulfate (SDS), and ascorbic acid (AA) (**Figure 3.5**). The electron microscopic images illustrate the effect of using different agents on the morphology of the prepared nanoparticles. For instance, PEG-gold nanoparticles exhibit a narrow size distribution and do not aggregate (**Figure 3.5a**). When PEG

molecules are coated onto the surface of gold nanoparticles, they form a protective layer around the particles. The long, flexible PEG chains create a steric barrier that prevents particles from coming into close contact and aggregating. This steric hindrance inhibits the attractive van der Waals forces that typically lead to aggregation (Suk et al., 2016). In the case of SDS-gold nanoparticles, it is evident that these nanoparticles appear in an aggregated form, forming clusters (**highlighted with a red circle**, **Figure 3.5b**).

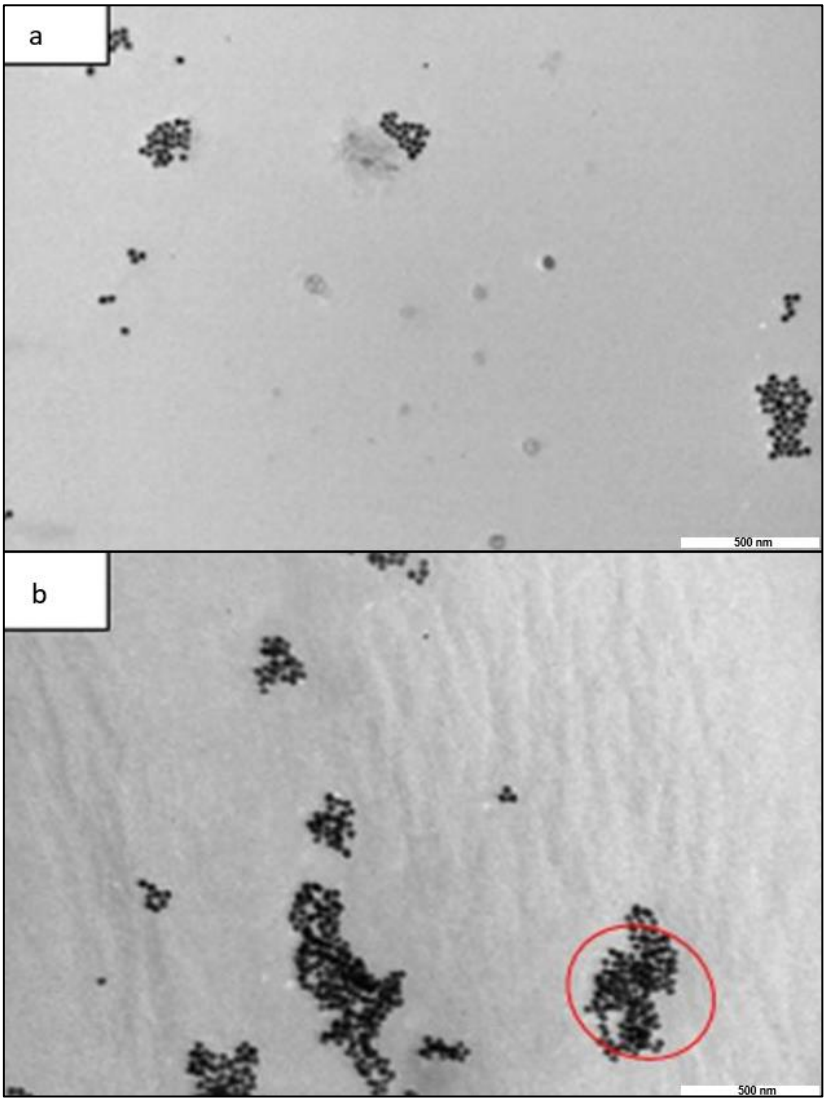

Figure 3. 5. Transmission electron microscopic images at nanoscale bar 500nm, showing gold nanoparticles: a) PEG-gold nanoparticles, and b) sodium dodecyl sulfate (SDS-Au NPs). The red circle shows the aggregation of SDS-AuNPs.

Gold nanoparticles prepared using polyvinyl pyrrolidone were observed in various non-spherical shapes, such as triangles, pentagons, and hexagons as indicated by red arrows in **Figure 3.6a**. Conversely, gold nanoparticles synthesised using ascorbic acid (AA) were found to be well-defined, monodispersed particles with a uniform size distribution, as observed through TEM imaging (**Figure 3.6b**).

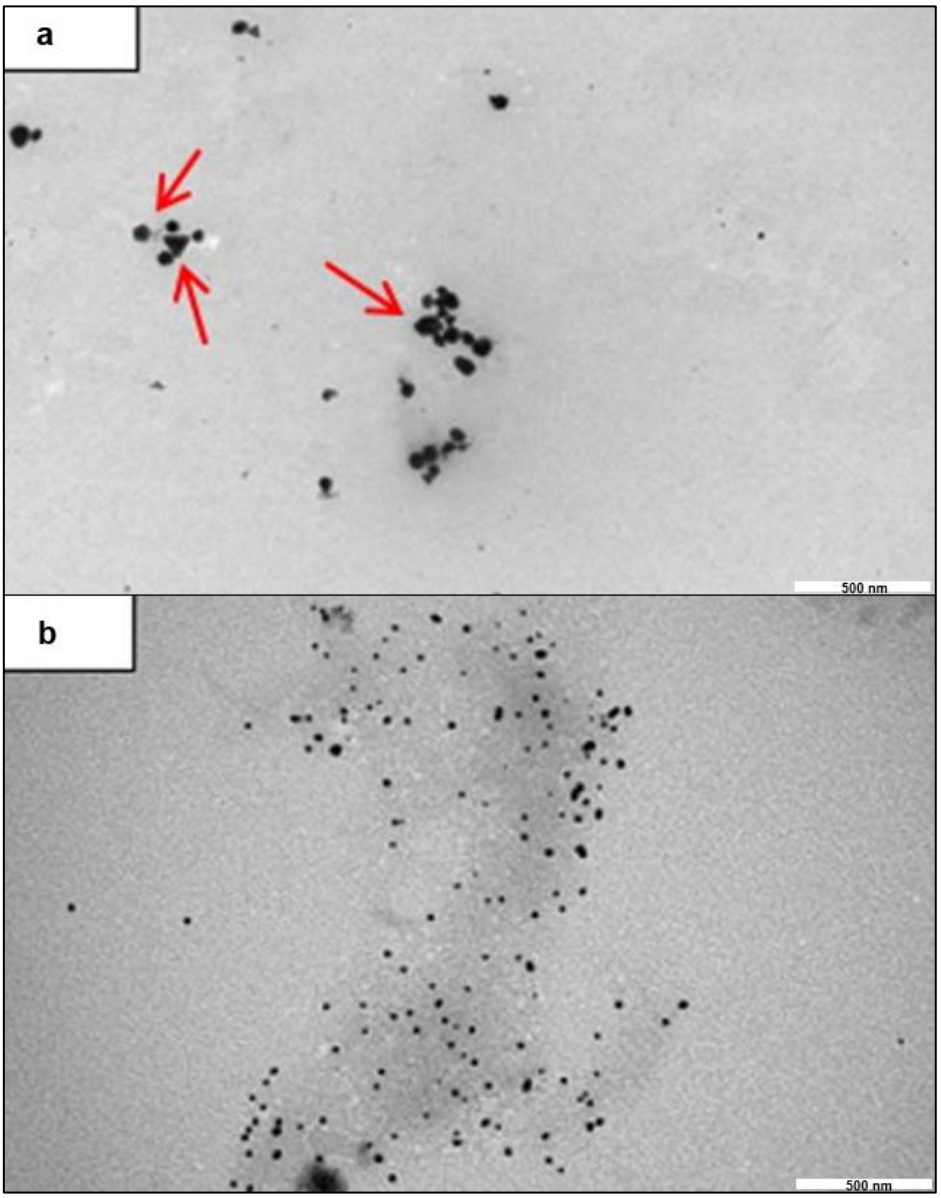

Figure 3. 6. TEM images for a variety of gold nanoparticles: a) polyvinyl pyrrolidone (PVP-Au NPs), and b) ascorbic acid gold nanoparticles (AA-Au NPs) with different sizes at nanoscale bar 500 nm.

3.2.5 Analysis of Functional Groups for Identifying Functionalised Au NPs

Fourier Transform Infrared Spectroscopy (FTIR) is a valuable analytical method was employed to characterise and analyse functionalised gold nanoparticles. In **Figure 3.7**, the FTIR spectra of the trisodium citrate (standard) and the produced cit-Au NPs nanoparticles have been illustrated, highlighting the main peaks. The bands at 1390 cm^{-1} and 1571 cm^{-1} are corresponding to the presence of asymmetric and symmetric carbonyl group (C=O) stretch of carboxylate ion in the structure of trisodium citrate after reduction and formation of gold nanoparticles, respectively (Ingole et al., 2010; Hu et al., 2012).

The small band at 1241 cm^{-1} more likely relates to the presence of C-O group of trisodium citrate (**Figure 3.7**). Whereas the bands at 2924 cm^{-1} and 3300 cm^{-1} correspond to the C-H and O-H stretch, respectively, which indicates effective capping of gold nanoparticles with trisodium citrate (Ingole et al., 2010; Hu et al., 2012). Another effect concerning trisodium citrate-capped nanoparticles is the noticeable shift of the C-O stretch towards lower wavenumbers, specifically at 1241 cm^{-1}, accompanied by a peak of very low intensity, as illustrated in **Figure 3.7**.

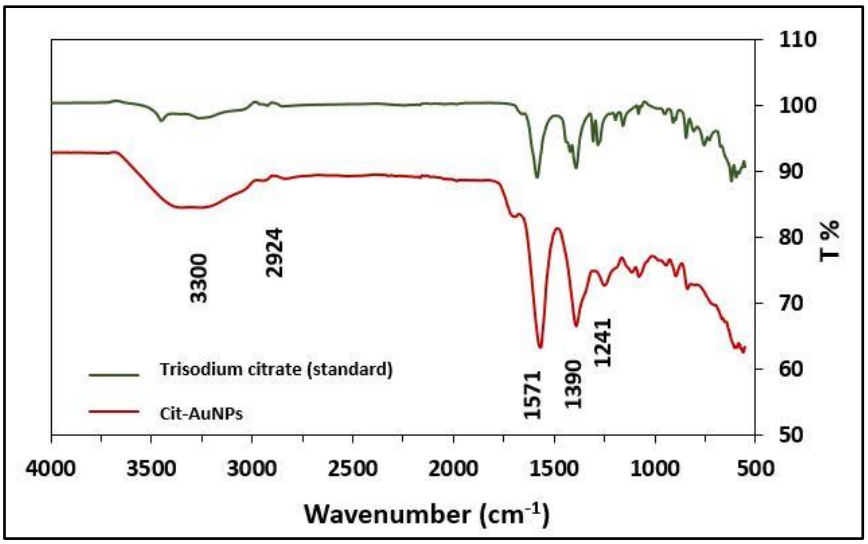

Figure 3. 7. FTIR spectra illustrating the main peaks for both standard trisodium citrate (green) and cit-AuNPs (red).

For gold nanoparticles produced using PEG compound, the peak at 1711 cm^{-1} is a distinctive feature indicating the formation of PEG-gold nanoparticles. This peak arises due to the formation of an ester group through the attachment of the carboxylate group of trisodium citrate to the end chain of polyethylene glycol, resulting in the formation of gold nanoparticles coated with PEG on the surface (Manson et al., 2011). Notably, in the FTIR spectra of standard PEG, this specific band is not present, as shown in **Figure 3.8**. In contrast, the bands observed at 2850 cm^{-1} and 2919 cm^{-1} in the FTIR spectra of PEG-AuNPs correspond to the C-H stretching vibrations in the formulated PEG- AuNPs. Similar bands are also present in the FTIR spectra of the standard PEG (blue line in **Figure 3.8**), indicating the presence of C-H stretching in the PEG compound itself.

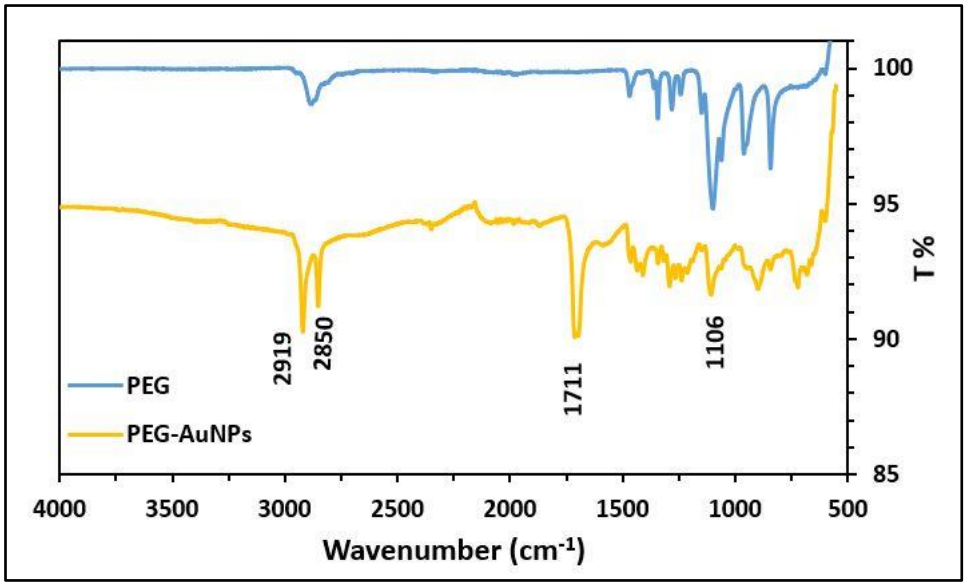

Figure 3. 8. chemical functional groups for both standard polyethylene glycol (blue) and PEG-gold nanoparticles (orange) investigated by FTIR. The ester group exhibited at the wavenumber 1711 cm^{-1} belongs to the PEG-AuNPs.

Finally, gold nanoparticles were synthesised, and their surface was capped with tannic acid (TA). The main peaks observed for TA-gold nanoparticles, as shown in **Figure 3.9** are located at 3205 cm^{-1}, 2914 cm^{-1}, 2851 cm^{-1}, 1562 cm^{-1} and 1386 cm^{-1}. These peaks correspond to characteristic vibrations of functional groups present in the tannic acid coating. Notably, the fingerprint region of the FTIR spectrum for the TA-gold nanoparticles is entirely distinct from that of the standard tannic acid.

The band at 3205 cm^{-1} is clearly attributed to the O-H stretching vibration present in both tannic acid (standard) and TA-gold nanoparticles (TA-AuNPs) due to the presence of multiple hydroxyl groups in their chemical structure. Furthermore, the bands observed at 2914 cm^{-1} and 2851 cm^{-1} are distinctive and indicative of the

presence of C-H stretching vibrations in TA-AuNPs, as shown in **Figure 3.9**. The vibration band associated with the hydroxyl group (OH) is characterised by a broad and intense peak observed in the region of approximately 3200 cm^{-1} to 3600 cm^{-1} in the FTIR spectrum. This specific spectral range is commonly known as the "hydroxyl stretching region" and indicates the stretching vibration of the O-H bond in molecules containing hydroxyl groups (Filopoulou et al., 2021).

The band at 1562 cm^{-1} is typically associated with the presence of carboxylate ($-COO^-$) stretching in that region, indicating the oxidation of polyphenol groups in tannic acid during the gold reduction process. This observation confirms the formation of gold nanoparticles capped with tannic acid. Additionally, the stretching peak appearing at 1386 cm^{-1} can also be attributed to the presence of the ($-CH_2$) group, further supporting the evidence of tannic acid capping on the surface of gold nanoparticles (**Figure 3.9**).

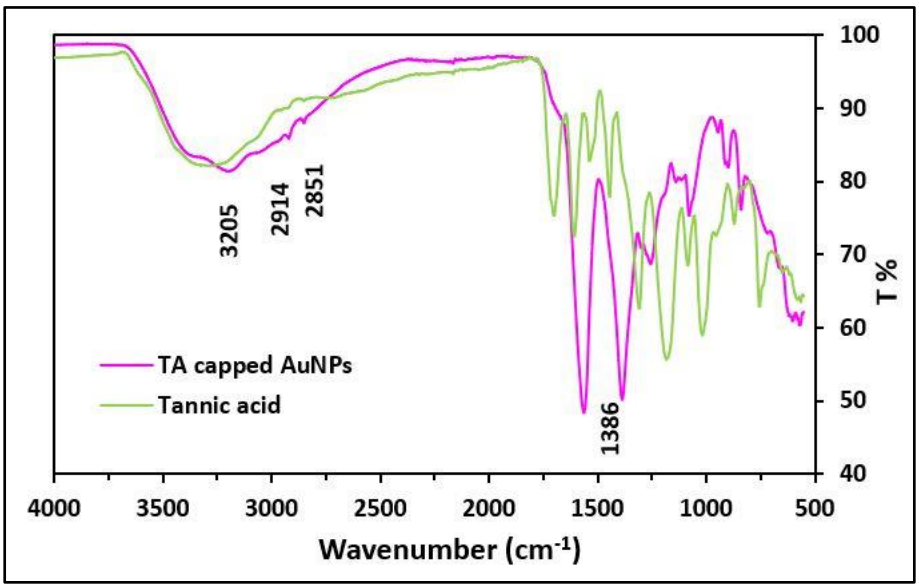

Figure 3. 9. FTIR spectra highlights the functional groups present in both standard tannic acid (green) and the prepared tannic acid-gold nanoparticles (purple).

In conclusion, FTIR is a reliable technique that can be used for identifying the chemical structure of molecules by determining the functional groups present in specific regions of the IR spectra. The technique has some limitations for characterising Au NPs involving, the sample to be in a solid or liquid form. Additionally, gold nanoparticles have a relatively low dipole moment, and their IR absorption bands can be weak or absent in the FTIR spectrum. This makes it challenging to directly identify Au NPs solely based on FTIR (Kamnev, 2013; Proniewicz et al., 2021).

3.2.6 Quantification of adsorbed molecules onto Gold Nanoparticle Surface

Thermogravimetric analysis (TGA) is a thermal analysis method that measures the change in weight of a sample as a function of temperature. When applied to the study of adsorbed ions on gold nanoparticles, it can provide information about the amount and thermal stability of the adsorbate species. Two different types of gold nanoparticles including, cit-AuNPs (20.54 ±0.45 nm) and TA-AuNPs (15.11 ±0.64 nm) were characterised using TGA to quantify the amount of surrounding agent loss from the surface of gold nanoparticles. The weight loss of citrate anions was firstly measured. Previous studies have shown that trisodium citrate can form strong bonds with the gold surface through its central carboxylate group (Bajaj et al., 2020). Therefore, by characterising and quantifying the citrate ions adsorbed onto the gold nanoparticle surface using TGA, it was observed that the citrate decomposed with a mass loss of approximately 0.78 mg (> 90%) when subjected to controlled temperature for 50 minutes, as illustrated in **Figure 3.10.**

Tannic acid gold nanoparticles (TA-AuNPs) were prepared at smaller sizes ranging from 10 nm to 16 nm at various concentrations. The TA-capped gold nanoparticles synthesised using a 0.5 mM tannic acid reducing agent were analysed using the thermogravimetric analyser with a heating rate of 10°C/ min up to 1000°C. Based on the TGA results shown in **Figure 3.10**, it is evident that the weight loss commenced within the first twenty minutes, followed by complete decomposition at approximately 25 minutes of the sample run. Notably, the curve of the TGA results for TA-AuNPs started to fluctuate after about 30 minutes of the sample run. This could indicate that there are multiple thermal events occurring during the analysis. Each event is associated with specific weight changes in the sample, which are likely caused by different processes taking place at different temperature ranges. The fluctuation of the TGA analysis curve may also occur due to weight loss caused by the evaporation of solvent or removal of surfactants or capping agents (Bajaj et al., 2020).

In conclusion, as described by Chairam et al. (2017), the first stage of weight loss after about 10 minutes usually involves the release of absorbed water. This is followed by a significant weight loss between 20 and 100 minutes. Additionally, tannic acid was completely decomposed after 25 minutes.

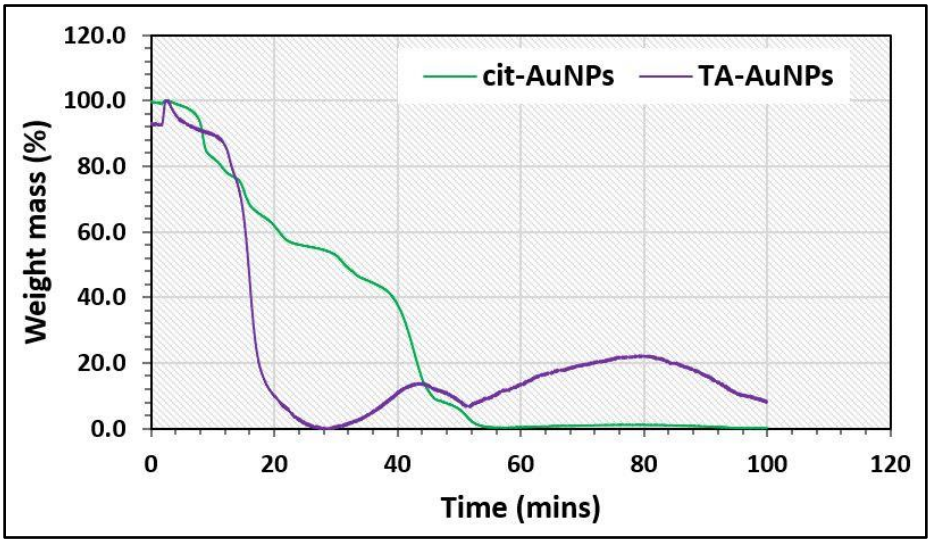

Figure 3. 10. Thermogravimetric analysis (TGA) employed for the quantification of citrate and tannic acid ions on the surfaces of gold nanoparticles (AuNPs), illustrating the distinct profiles for citrate-gold nanoparticles (cit-AuNPs) and tannic acid-gold nanoparticles (TA-AuNPs).

3.2.7 Effect of Temperature on Size Growth of Au NPs During the Reaction

This study refers to investigating how changing the temperature during the synthesis of Au NPs may impact on the size growth rate. For example, herein, the effect of temperature 120°C and 70°C during the synthesis of cit-Au NPs and TA-Au NPs, respectively was studied. From **Figure 3.11**, tannic acid-gold nanoparticles (TA-Au NPs) showed an increase in size for up to 16 nm over time of 140 minutes at 70°C. Whereas the cit-AuNPs observed with fast growth rate approximately 60 nm at 120°C within 100 minutes. This variation in the size growth rate was statistically determined using one-way ANOVA at 37.5% and 71.6% for the TA-Au NPs and cit-Au NPs, respectively (**Figure3.11**).

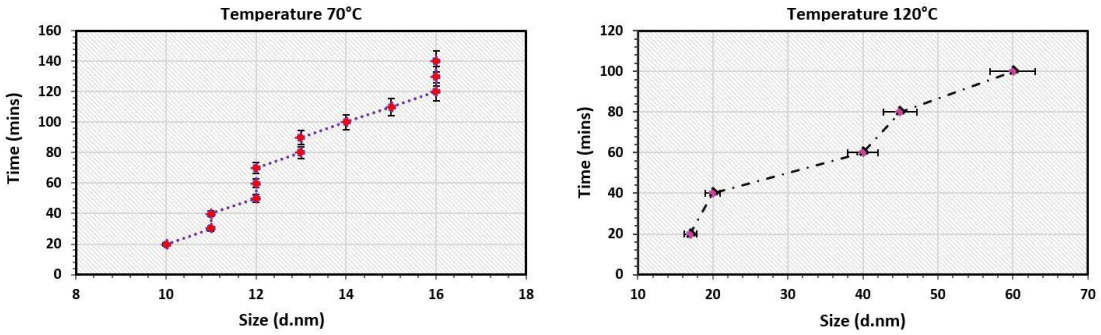

Figure 3. 11. Monitoring the size growth rates of tannic acid-gold nanoparticles (TA-AuNPs) at 70°C (left) and trisodium citrate-gold nanoparticles (cit-AuNPs) at 120°C (right) during the synthesis. A comparative analysis shows that TA-AuNPs exhibit a slower growth rate of 37.5%, while cit-AuNPs demonstrate a higher growth rate of 71.6%. This variation in the size growth rate was statistically determined using one-way ANOVA.

3.2.8 The Influence of pH on the Size of the Synthesised Au NPs

Through the process of gold nanoparticles synthesis, the pH value has been effectively monitored to control size. Herein, during size control to sub-10 nm, it was found that the size decreases by monitoring the pH value at basic conditions. The size decreased to very small nanoparticles 8 nm at pH 10.0 (**Figure 3.12**). The pH of the reaction solution is monitored and carefully controlled during the synthesis in the range of pH 8.0 and 10.0.

At basic conditions, the pH (8.0-10.0) influences the reduction rate of gold ions and the interaction between the gold species and stabilising agents present in the solution (e.g., trisodium citrate). By altering the pH, the rates of nucleation

and growth were controlled, influencing the final size and morphology of the Au NPs (Jayalakshmi et al., 2014; Marciniak et al., 2020). In **Figure 3.12**, results show the size for the nanoparticles prepared by potassium carbonate and sodium carbonate was controlled to 8.77 ±0.92 nm and 10.68 ±0.68 nm at pH values 10.0 and 8.5, respectively. In contrast to those nanoparticles synthesised at acidic conditions with particle sizes of 20.54 ±0.45 nm, 40.59 ±0.83 nm and 60.67 ±0.71 nm at pH values 6.01, 5.4 and 5.2, respectively. This variation was significantly different at determined *P <0.05 and ***P < 0.001.

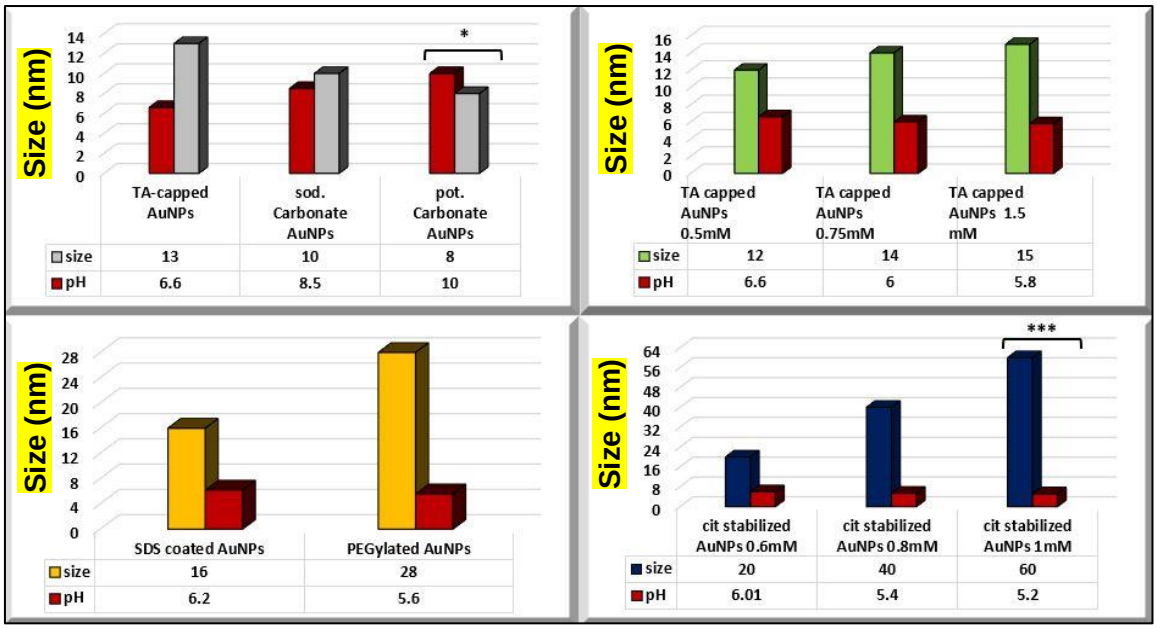

Figure 3. 12. Investigating the pH variation and its impact on size control for various types of gold nanoparticles (AuNPs) including K-TA-Au NPs, Na-TA-Au NPs, TA-AuNPs, SDS-AuNPs, and PEG-AuNPs, and cit-AuNPs. The observed differences were found to be statistically significant at *P <0.05 and ***P <0.001.

3.2.9 How Coatings Affect the Size of Gold Nanoparticles

Excipients are inactive substances added to formulated drugs, providing protection, stability, enhanced bioavailability, and improved patient compliance (Chaudhari & Patil, 2012). Their application by pharmaceutical manufacturers in drug formulation is considered integral to the drug manufacturing process, given their ability to enhance drug efficacy and patient acceptability (Chaudhari & Patil, 2012). Herein, the effect of several types of coatings including sodium dodecyl sulfate (SDS), trisodium citrate, polyethylene glycol (PEG), polyvinyl pyrrolidone (PVP), ascorbic acid (AA) and starch was studied. These substances are aiding to provide stability by prevention of nanoparticle aggregation over the expected shelf-life. Characterisation was employed by dynamic light scattering (DLS) to measure the particles size and size distribution (**Figure 5.4**).

As known that both PEG and PVP are considered as polymers with high molecular weight. Therefore, by their attachments to the surface of gold nanoparticles, the size will increase. Additionally, the application of starch as coating agent on gold nanoparticles results a significant size increase compared to polyethylene glycol and polyvinyl pyrrolidone as demonstrated in **Figure 5.4**. This difference can be attributed to the higher molecular weight of starch, which is classified as a polysaccharide composed of ten to thousands of monosaccharide molecules linked together by glycoside linkages (Castro et al., 2005; Tester et al., 2004).

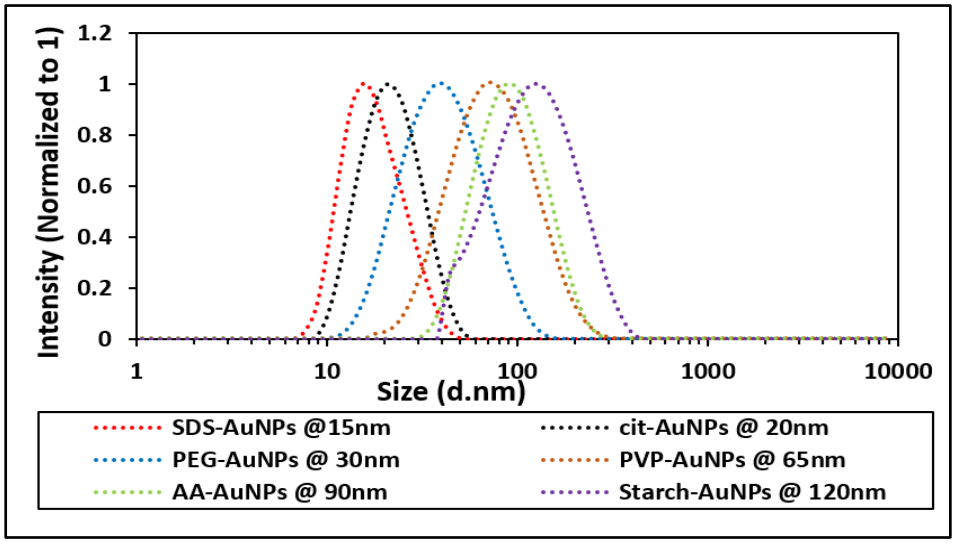

Figure 5. 1. DLS measurements investigating the impact of various coatings, including sodium dodecyl sulfate (SDS), trisodium citrate, polyethylene glycol (PEG), polyvinyl pyrrolidone (PVP), ascorbic acid (AA), and starch, on the sizes of gold nanoparticles.

3.3 Conclusion

This chapter explores various techniques utilised for the synthesis of gold nanoparticles with sizes ranging from 8 nm to 60 nm. The study employed different variations involving pH, temperature, concentration and reducing agents to achieve size control, particularly aiming for sub-10 nm diameters. The obtained results showed that the 20.54 ±0.45 nm trisodium citrate-gold nanoparticles (cit-Au NPs) exhibited the most stability in the colloidal solution. Their morphology was investigated using electron microscopy, showing a monodispersed nanoparticles and homogeneous spherical shape.

Additionally, the results indicated that the surface charge plays a significant role in size control of nanoparticles in the presence of trisodium citrate at a high temperature of 150˚C. For example, the anionic surfactant called sodium dodecyl sulfate (SDS) showed size control for gold nanoparticles at 16.31 ±0.38 nm in diameter.

Finally, uniform gold nanoparticles with a narrow particle size distribution were prepared based on monitoring the pH at basic conditions. Notably, the pH variation was found to have a significant effect on controlling the size of nanoparticles to around 8 nm in diameter.

Chapter (4): Strategies for Functionalisation of Au NPs, Drug Conjugation and Encapsulation

4.1 Introduction

This chapter focuses on the three key steps involved in the development of drug delivery using Au NPs: functionalisation of Au NPs, drug conjugation, and drug encapsulation. Herein, three types of gold nanoparticles PEG-Au NPs, TA-Au NPs, and cit-Au NPs were selected for functionalisation with MUDA. The choice was based on the stability and biocompatibility conditions of the prepared Au NPs measured and showed in Chapter 3, sections 3.2.7 and 3.2.8,

The first step is the functionalisation of Au NPs carried out by binding the thiol group in MUDA to the surface of PEG-Au NPs, TA-Au NPs, and cit-Au NPs. The trisodium citrate molecules on the gold nanoparticle surface can be readily displaced by other molecules with a stronger affinity for the gold surface through a nucleophilic attack by thiol groups (Bürgi, 2015).

The functionalisation process involved the formation of Au-S bond between the gold atoms of the synthesised gold nanoparticles and thiol groups in the MUDA molecule. MUDA has a unique property and plays a significant role in the stability of gold nanoparticles (Laaksonen et al., 2006). Following this, the research presented in this chapter focused around the development of a novel conjugation technique for two types of medicines: amantadine (AMTD), used for the treatment of Parkinson's disease (PD), and remdesivir (REM), utilised for RNA viral infections. This conjugation technique involves the formation of an amide bond by adding a water-soluble carbodiimide cross-linker known as 1-ethyl-3-(3-dimethylaminopropyl) carbodiimide (EDC), in the presence of N-hydroxysuccinimide (NHS). Furthermore, the process of encapsulating the

amantadine drug within PLGA polymeric nanoparticles has been comprehensively examined and presented in this chapter.

4.2 Functionalisation of Au NPs with Thiol-Containing Compounds

Gold nanoparticles are functionalised with thiol-containing compounds to enhance their stability and biocompatibility. This functionalisation enables reliable conjugation with drug molecules, leading to improved bioavailability (Vedhanayagam et al., 2022).

11-mercaptoundecanoic acid (MUDA), a thiol-containing compound was employed for functionalising different forms of gold nanoparticles: cit-Au NPs, PEG-Au NPs and TA-Au NPs. The application of MUDA in the functionalisation of Au NPs provides exceptional stability to the synthesised nanoparticles. The functionalisation process mainly involved mixing the synthesised gold nanoparticles with MUDA dissolved in absolute ethanol. The choice of solvent was based on the high solubility of thiol compounds in organic solvents compared to the aqueous solutions (Howard, 1996).

4.2.1 Results and Discussion

The particle size and size distribution of the three forms of the synthesised gold nanoparticle involving, cit-Au NPs, PEG-Au NPs and TA-Au NPs were measured. As can be seen in **Figure 4.1**, after functionalisation with MUDA, the sizes increased to 78 nm, 60 nm and 165 nm. This increase in size can be attributed to the formation of strong Au-S bonds resulting from the attachment of thiol groups to the surface of Au NPs. The size increase for the MUDA-cit-AuNPs can be attributed to the interaction between the citrate ions surrounding the gold

nanoparticles and the thiol group in the MUDA molecule. The thiol group displaces the citrate ligands through a nucleophilic attack. Thiol groups are known to have a strong affinity for the surface of Au NPs leading to the formation of Au-S strong bonds (Gao et al., 2012).

In case of polyethylene glycol-gold nanoparticles (MUDA-PEG-AuNPs), the size change was observed after MUDA modification, by increasing from 30 nm to approximately 60 nm, with a PDI of 0.270 (**Figure 4.1**). This indicated the formation of PEG-MUDA on the surface of Au NPs. The PEG-MUDA provides excellent chemical stabilisation for the gold nanoparticles. The displacement of PEG ligands from the surface of the gold nanoparticles with a thiol-containing carboxyl monolayer remains challenging, and the mechanism behind this, still not fully understood (Heuer-Jungemann et al., 2019).

TA-Au NPs were also functionalised with MUDA. According to the DLS data presented in **Figure 4.1**, the modified MUDA-TA-Au NPs exhibited the largest particle size approximately 165 nm. This phenomenon was explained by Mazloomi-Rezvani et al. (2018), who proposed that the interaction between the hydroxyl groups in tannic acid and the thiol groups in MUDA leads to the formation of aggregated nanoparticles due to the reduction in repulsive forces between the surfaces of the nanoparticles.

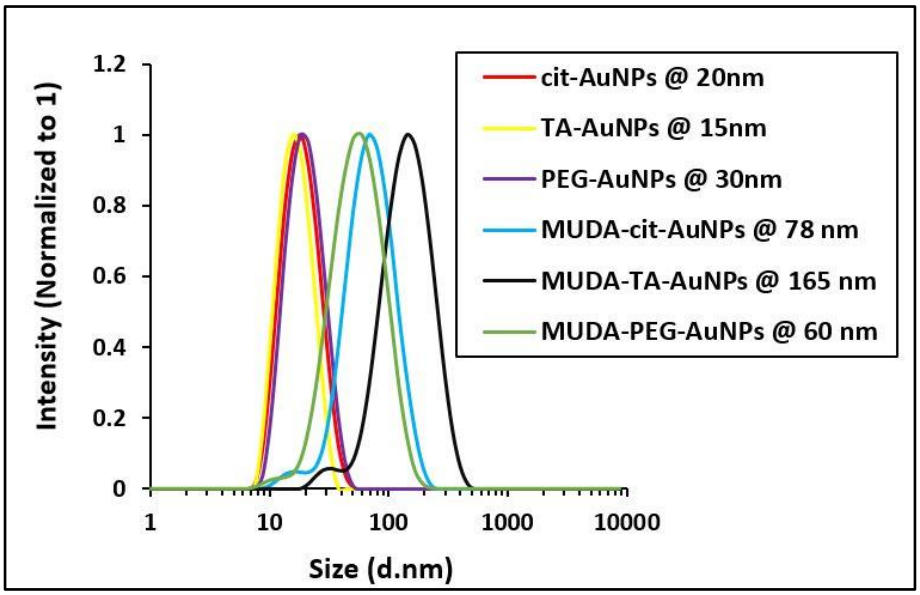

Figure 4. 1. DLS (Dynamic Light Scattering) technique was employed to measure the particle sizes of three types of functionalised gold nanoparticles, each containing 11-mercaptoundecanoic acid (MUDA) thiol-based compounds: - MUDA-cit-Au NPs, MUDA-TA-Au NPs, and MUDA-PEG-Au NPs.

The optical properties of modified gold nanoparticles were characterised using UV-Vis spectroscopy. The position and intensity of the LSPR peaks are influenced by the size, shape and surface chemistry of the gold nanoparticles. After functionalisation with MUDA, the LSPR peak position and intensity changed, indicating alterations in the nanoparticle's optical properties (**Figure 4.2**). This involves the LSPR peak position shifted to a specific wavelength at 578 nm, 572 nm and 566 nm for MUDA-TA-Au NPs, MUDA-cit-Au NPs and MUDA-PEG-Au NPs, respectively. In a study conducted by S. Peng et al. (2010), it was observed that the shift in the LSPR peaks occurred along with noticeable

broadening of the peaks at maximum wavelengths for all prepared gold nanoparticles. This broadening phenomenon was attributed to the increase in nanoparticle size or aggregation effects.

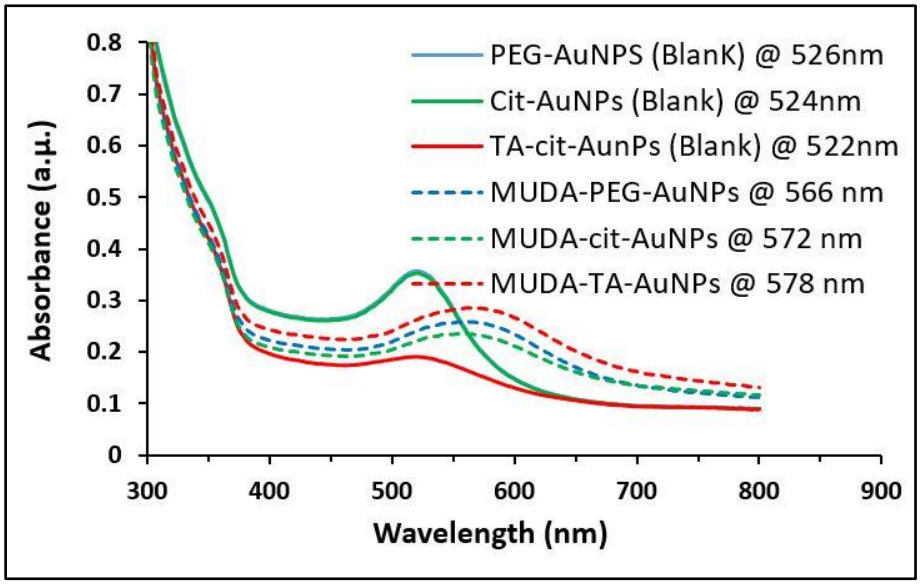

Figure 4. 2. Localised Surface Plasmon Resonance (LSPR) peak shift for the modified Au NPs: citrate-gold nanoparticles, polyethylene glycol-gold nanoparticles and tannic acid-gold nanoparticles exhibited at specific wavelengths 572 nm, 566 nm and 578 nm, respectively.

The morphology of the synthesised gold nanoparticles, PEG-Au NPs, cit-Au NPs, and TA-Au NPs, along with their functionalisation by carboxylic acid group, were investigated using transmission TEM (**Figure 4.3**). The synthesised nanoparticles made by citrate, tannic acid, and polyethylene glycol reduction are all well-distributed and stable in the colloidal solution. This is attributed to the electrostatic repulsion between nanoparticles in the colloidal solution, as discussed in the investigation and assessment of the physicochemical properties of gold nanoparticles in Chapter 5. For cit-Au NPs, significant changes in particle size and size distribution were observed, with moderate aggregation as indicated

by the red circle in **Figure 4.3d**. After functionalisation with MUDA, the MUDA-PEG-AuNPs exhibited aggregation, noticeable in **Figure 4.3e** where certain nanoparticles, marked by red arrows, appeared to aggregate. This behaviour could potentially be attributed to the interaction between the hydroxyl group within PEG's chemical structure and the thiol groups present in MUDA. Despite the similarity in characteristics between thiol and hydroxyl groups (Reusch, 1999), the reduction in electrostatic repulsion between these groups might contribute to the observed aggregation effect, as illustrated in **Figures 4.3e** and **4.3f.**

FTIR was also applied to study the chemical structure of the synthesised and MUDA-modified gold nanoparticles by identifying their chemical functional groups. First, MUDA (standard) and MUDA-citrate-gold nanoparticles (MUDA-cit-AuNPs) were investigated as illustrated in **Figure 4.4**. From the FTIR spectra of

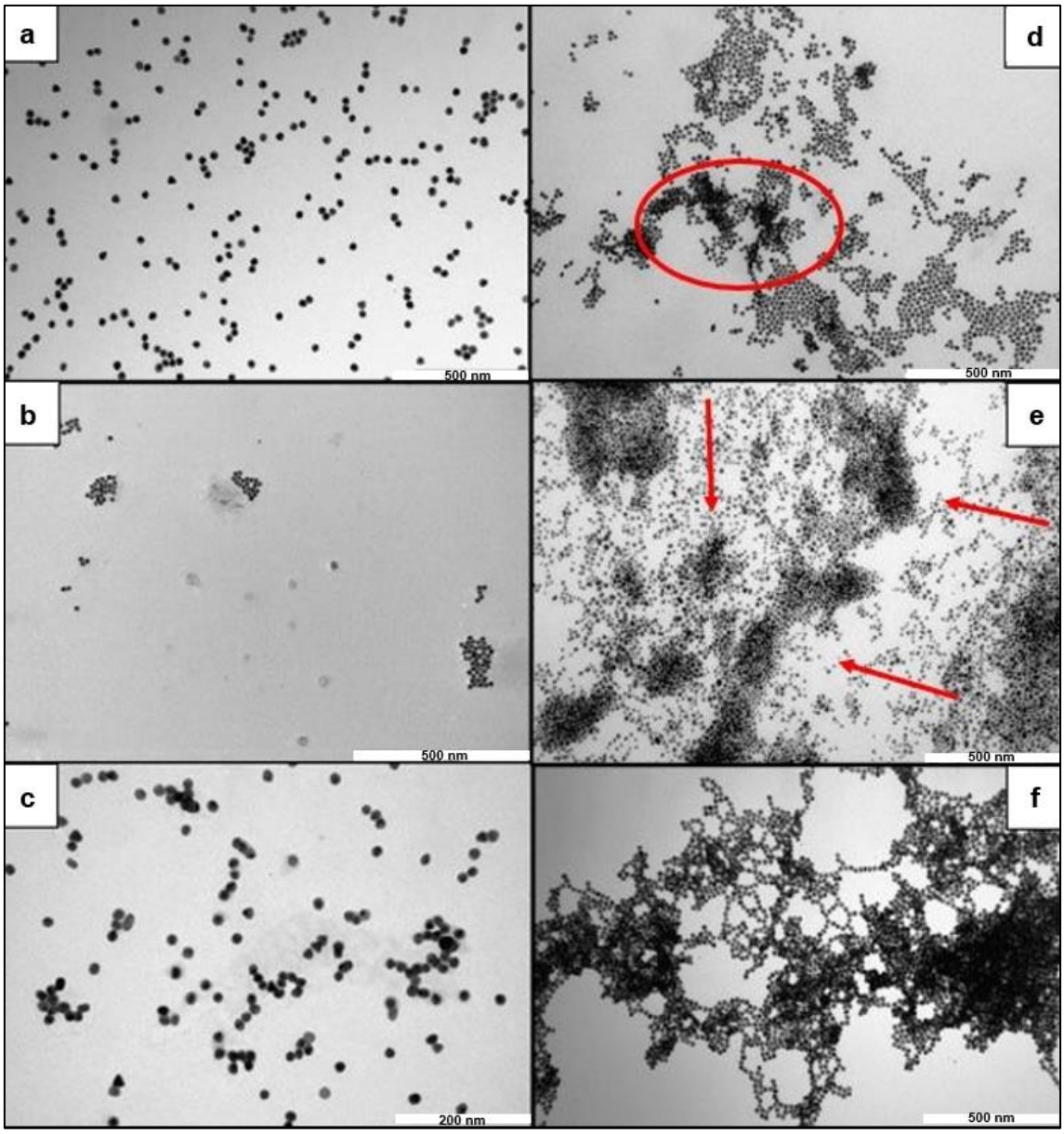

Figure 4. 3 TEM images for synthesised gold nanoparticles (left): (a) cit-Au NPs, (b) PEG-Au NPs, and (c) TA-Au NPs, in addition to the functionalised gold nanoparticles (right): (d) MUDA-cit-Au NPs, (e) MUDA-PEG-Au NPs, and (f) MUDA-TA-Au NPs. These images conducted at nanoscale bars 200 nm and 500 nm.

MUDA-cit-AuNPs, the carboxylate group in the citrate reagent is mainly characterised by two different C=O bands; the first can be seen in the region between 1510 cm^{-1} and 1650 cm^{-1} for the asymmetrical vibration and 1280-1400

cm^{-1} for the symmetrical vibration. The FTIR spectra for MUDA-cit-AuNPs in **Figure 4.4** shows that only one strong band appears at wavenumber 1696 cm^{-1}, which roughly belongs to the ester group (RCOOR′) (Smith, 2018). Whereas the two bands appearing at 2852 cm^{-1} and 2921 cm^{-1} are relatively representative of the (-CH) stretching in the MUDA. Thus, the absence of symmetrical and asymmetrical vibrations in the FTIR spectra and the presence of the carboxyl (-COOH) and ester (-COO) groups in addition to the (-CH) stretching confirm the successful binding of MUDA to the citrate-gold nanoparticles as demonstrated by Maréchal (1987). Furthermore, the absence of thiol groups in the functionalised form (MUDA-cit-AuNPs) is compared to their presence in the MUDA spectra at 2541 cm^{-1} as a result of their interaction with the gold atom to form a gold-sulfur bond. This would also confirm that the citrate on gold nanoparticles is displaced with MUDA molecules during the functionalisation process. However, in some cases, band positions of ligands attached to nanoparticles can be found at different wavenumbers due to interactions, or structural changes that occur during the functionalisation process (Araújo-Neto et al., 2014).

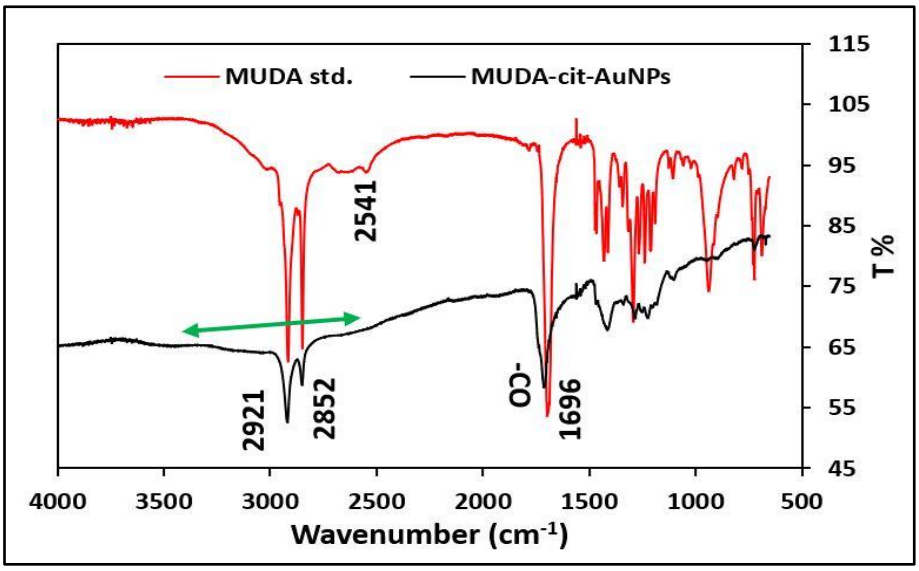

Figure 4. 4. FTIR spectra for the standard MUDA and MUDA-functionalised gold nanoparticles (MUDA-cit-Au NPs). The green line double arrow depicts the broad band for the carboxylic acid group in MUDA-functionalised Au NPs covering the region from 2500 cm^{-1} to 3500 cm^{-1}.

For MUDA modified polyethylene glycol (MUDA-PEG-Au NPs), it is known that the polyethylene glycol structure consists of a hydroxyl group (OH), which can be simply indicated by FTIR with a single broad band at wavenumbers between 3230 cm^{-1} and 3550 cm^{-1} (Maréchal, 1987). In addition, the hydroxyl group for both forms of the synthesised PEG-gold nanoparticles and the modified MUDA-PEG-AuNPs appeared at wavenumbers between 3040 cm^{-1} and 3622 cm^{-1} as shown in **Figure 4.5**. This confirms the functionalisation process of PEG gold nanoparticles with the MUDA molecule. Nonetheless, bands at 2883 cm^{-1} and 1557 cm^{-1} represent the (-CH) stretching in the PEG standard, whereas the bands at 2923 cm^{-1} and 2883 cm^{-1} indicate the presence of (-CH) stretching at the MUDA modified gold nanoparticles (**Figure 4.5**). However, the single strong band at 1114 cm^{-1} has been suggested by Shameli et al. (2012) to be for the detection

of the (C—O-H) and (-OH) stretching presence in the FTIR for polyethylene glycol. This was also investigated by Venkatasubbu et al. (2013), when they conjugate PEG to TiO_2 nanoparticles. Therefore, after MUDA functionalisation of PEG-coated gold nanoparticles, some changes in the FTIR spectra have been observed. It was noticed that various band positions shifted to the maximum wavenumber. For instance, two (-CH) stretching bands were detected at 2883 cm^{-1} and 2923cm^{-1}. Moreover, the single strong stretch at 1114 cm^{-1} for the standard PEG molecule has disappeared after MUDA functionalisation of the nanoparticles (**Figure 4.5**). Thus, this FTIR characterisation can show the binding mechanism between MUDA and PEG-gold nanoparticles.

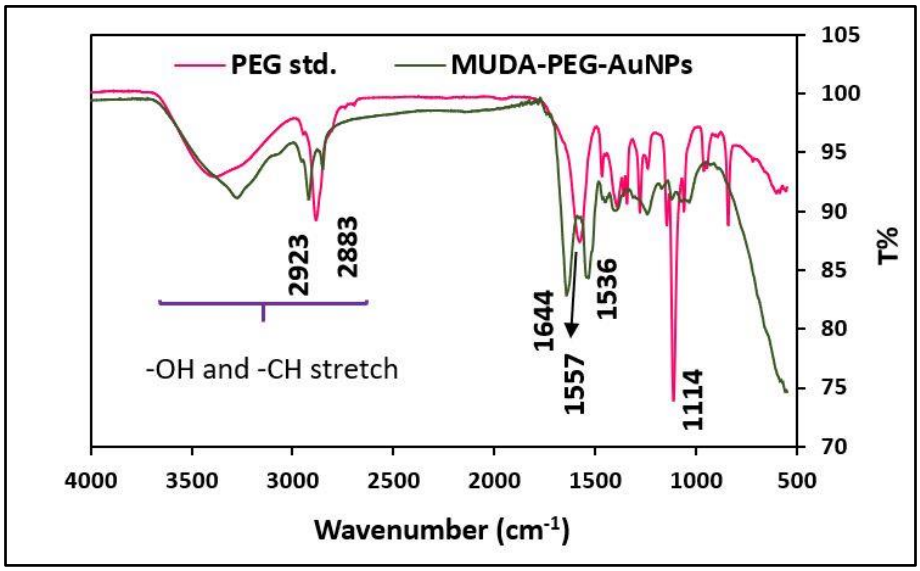

Figure 4. 5. FTIR spectra shows the main functional groups detected in the IR region for both synthesised PEG-AuNPs and MUDA modified gold nanoparticles.

4.2.2 Quantification of MUDA Content Bound to Gold Nanoparticles

The amount of the MUDA attached to the surface of gold nanoparticles can be quantified in different ways. For example, in a study conducted by Joshi et al.

(2011) for chloroquine drug bound to gold nanoparticles, the following equation was used:

$$\mathrm{OD} = \frac{[(\mathrm{A} - \mathrm{B})]}{\mathrm{A}} \times 100$$

Where, OD is the optical density, A is the absorbance of the ligand molecule before attaching to Au NPs, and B is the absorbance of the ligand in the supernatant.

This experiment was performed in triplicates by measuring the % MUDA loaded onto gold nanoparticle surface to each form of modified gold nanoparticles involving, MUDA-PEG-AuNPs, MUDA-cit-AuNPs and MUDA-TA-AuNPs and at concentration of MUDA (10 mM). As shown in **Table 4.1**, the surface of PEG-Au NPs was approximately covered by the largest amount of MUDA (64.31 ±1.6%), followed by TA-Au NPs (61.6 ±2%) and cit-Au NPs (53.9 ±0.7%). Hence, cit-Au NPs were observed to have the least amount of MUDA coverage on the nanoparticle surface.

Table 4. 1: % Loaded amount of MUDA molecule onto the surface of cit-Au NPs, PEG-Au NPs and TA-Au NPs

	MUDA (10 mM)	SD (%)
MUDA-PEG-Au NPs	64.3%	±1.6%
MUDA-cit-Au NPs	53.9%	±0.7%
MUDA-TA-Au NPs	61.6%	±2%

4.3 Drug Conjugation onto Gold Nanoparticles

4.3.1 Results and Discussion

4.3.1.1 Conjugation of Amantadine to Gold Nanoparticles

The conjugation process described here is based on a simple and cost-effective technique using 1-ethyl-3-(3-dimethylaminopropyl) carbodiimide hydrochloride (EDC) and N-hydroxysuccinimide (NHS) coupling reagents. Certain modifications to parameters such as pH, temperature and buffer solution were crucial for the success of the conjugation system. For instance, some medicines exhibit physiological activity in their deprotonated form at pH 8.5, which decreases as the pH becomes more acidic. This highlights the significance of pH in drug development and formulation, as the membrane permeability of deprotonated forms is higher compared to protonated ones (Chua et al., 2017; Pellegrini et al., 2014).

In this study, 4-(2-hydroxyethyl)-1-piperazineethanesulfonic acid, commonly known as HEPES buffer solution, was used in all experimental work involving the conjugation of amantadine (AMTD) drug to gold nanoparticles. HEPES is a widely utilised zwitterionic or dipolar ion buffering agent in laboratory research due to its ability to maintain physiological pH unlike changes that may occur in other bicarbonate buffers (Inam et al., 2022). After the conjugation process (Chapter 2 Section 2.3.4), the particle size and size distribution of amantadine conjugated to gold nanoparticles (AMTD/AuNPs) were measured using the ZetaSizer® DLS instrument. As shown in **Figure 4.6**, particle size has increased from 50 ±0.98 nm to approximately 160 nm after drug conjugation. The narrow distribution of both MUDA-modified gold nanoparticles (MUDA-cit-AuNPs) and amantadine

drug-conjugated gold nanoparticles (AMTD/AuNPs) would indicate that all nanoparticles are interestingly monodispersed in the colloidal solution, resulting in stable drug-formulated nanoparticles.

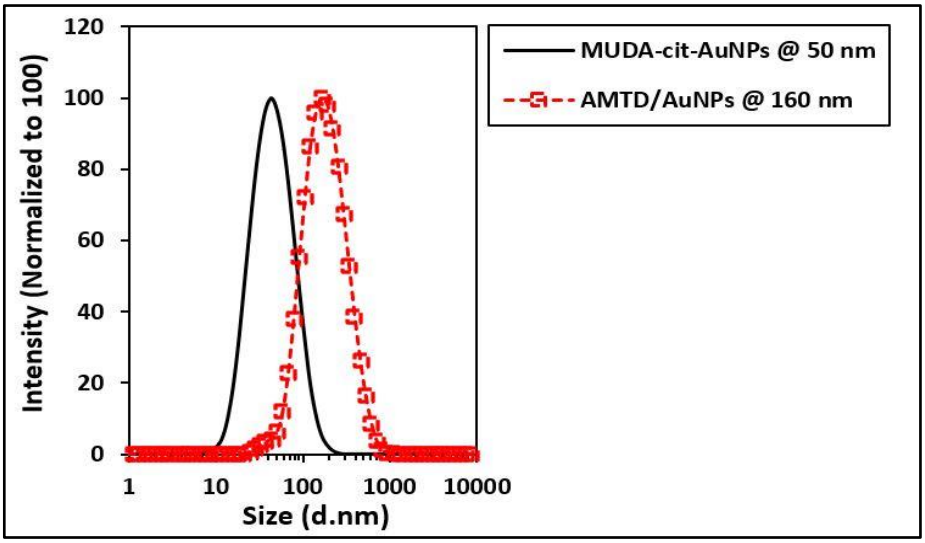

Figure 4. 6. Particle size and size distribution for MUDA functionalised Au NPs (MUDA-cit-AuNPs) and amantadine conjugated to gold nanoparticles (AMTD/AuNPs) measured by dynamic light scattering.

Moreover, the shift of the localised surface plasmon resonance (LSPR) absorption peaks for the synthesised gold nanoparticles, the MUDA-functionalised gold nanoparticles and the AMTD/AuNPs was determined based on the LSPR spectra (Joshi et al., 2011).

In **Figure 4.7**, the LSPR band of the synthesised citrate-gold nanoparticles (cit-Au NPs) was analysed within the wavelength range of 300-800 nm, with a maximum wavelength observed at 530 nm. Upon functionalisation, it was observed that the LSPR band exhibited broadening and shifted towards a new

maximum wavelength of approximately 572 nm, as depicted in **Figure 4.7**. This shift and broadening can be attributed to the increase in size and size distribution.

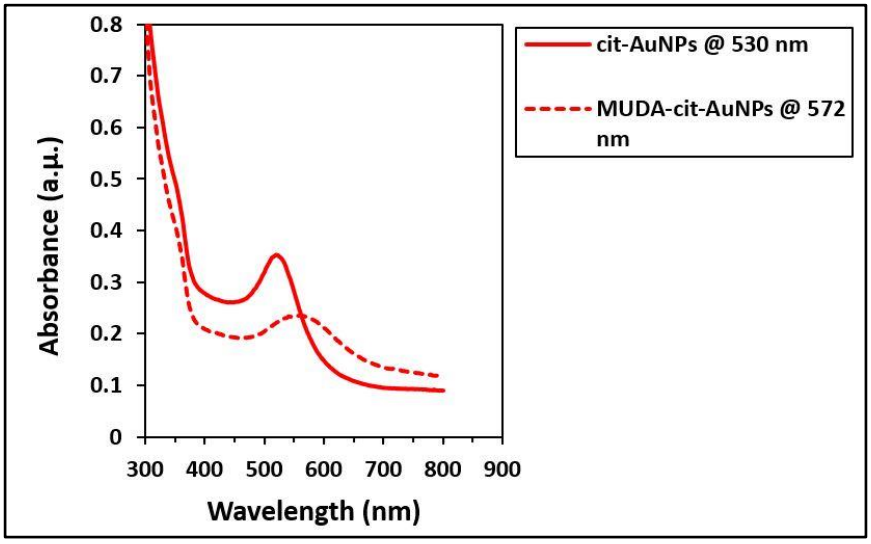

Figure 4. 7. UV-Vis spectroscopy utilised to measure the localised surface plasmon resonance (LSPR) peak shifts for synthesised and functionalised gold nanoparticles at 530 nm and 572 nm, respectively.

The LSPR peaks for the AMTD/AuNPs were further characterised in the region between 200 nm and 800 nm. In **Figure 4.8**, gold nanoparticles in the AMTD/AuNPs show a significant shift in the LSPR absorption peak towards a maximum wavelength of 575 nm. In addition, amantadine (AMTD) itself exhibited a distinct LSPR peak shift at a lower wavelength (265 nm). In contrast, in the absence of EDC carbodiimide crosslinker, the LSPR peak shift was investigated again, and it was found that the results demonstrated the existence of aggregation. This is related to the basic nature of the amine, which can deprotonate the carboxylic acid, resulting in the formation of a highly inert (unreactive) carboxylate group. Therefore, heating the reaction mixture above

100°C has been described as a method to facilitate the formation of an amide bond in the absence of the EDC cross-linker (Grieco et al., 1979). This comparison (**Figure 4.8**) serves to illustrate the critical role played by the EDC carbodiimide cross-linker in activating the carboxylic acid group, facilitating its reaction with the primary amine group in the amantadine drug molecule at room temperature. This activation process resulted in the formation of a sturdy amide bond, establishing a novel nanocarrier for potential application in combating Parkinson's disease (PD).

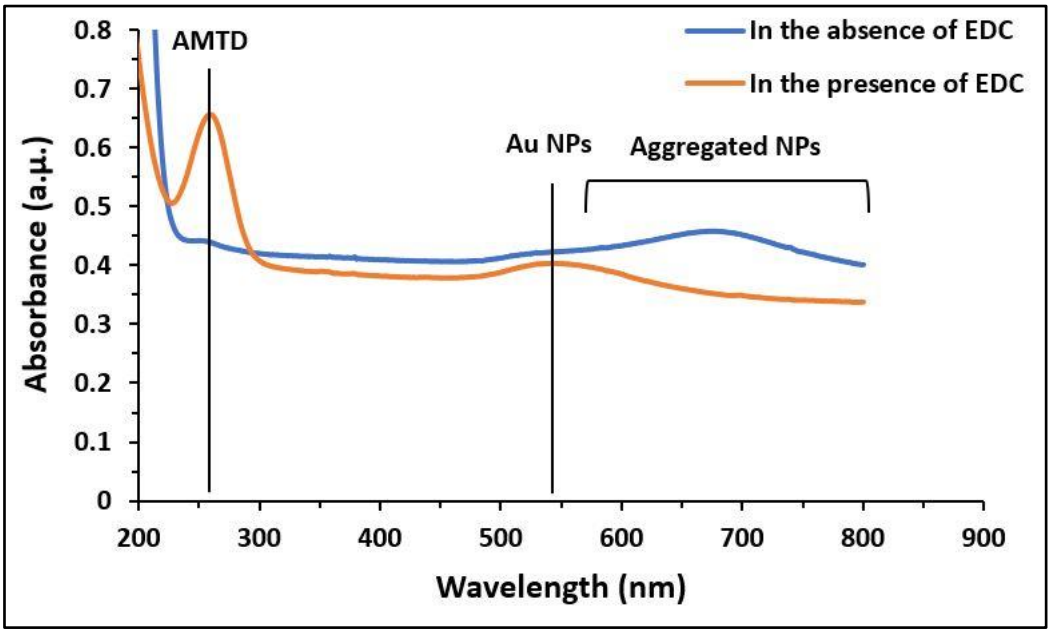

Figure 4. 8. LSPR peak shifts of amantadine conjugated to gold nanoparticles (AMTD/AuNPs) in the presence and absence of the EDC carbodiimide cross-linker. The shift in LSPR peaks provided information about the interaction between amantadine and gold nanoparticles, emphasising the role of the EDC cross-linker in influencing these spectral changes.

Further characterisation was conducted using nuclear magnetic resonance (NMR), which is a spectroscopic technique used to determine the absorbed energy by molecules in their nuclear spin state as stated by Abraham et al. (1998). NMR is a powerful tool employed for detecting the unique structures of drug molecules, proteins, antibodies and other compounds, providing detailed structural information at the atomic level (Abraham et al., 1998).

The NMR results for the amantadine-gold nanoparticles conjugated forms were obtained by observing hydrogen's chemical shift using the proton nuclear magnetic resonance or ^{1}H NMR. For example, **Figure 4.9** shows the ^{1}H NMR spectra for amantadine by indicating the hydrogen atom in the primary amine group (D), which can be observed with singlet (s) peak at low field (deshielded) at chemical shift 8.29 ppm. Whereas, both methyl groups (A and B) have emerged at high field (shielded) with chemical shifts at 1.68 ppm and 2.03 ppm as triplet (t) and double (d) peaks, respectively (**Figure 4.9**). The chemical shift of the hydrogen atom, termed as (C), has appeared as multiplet (m) peak at chemical shift 2.15 ppm. The difference in chemical shifts is usually related to the impact of electronegativity between atoms. When a proton is close to an electronegative atom or group, the proton will be de-shielded due to the removal of electron density (Abraham et al., 1998).

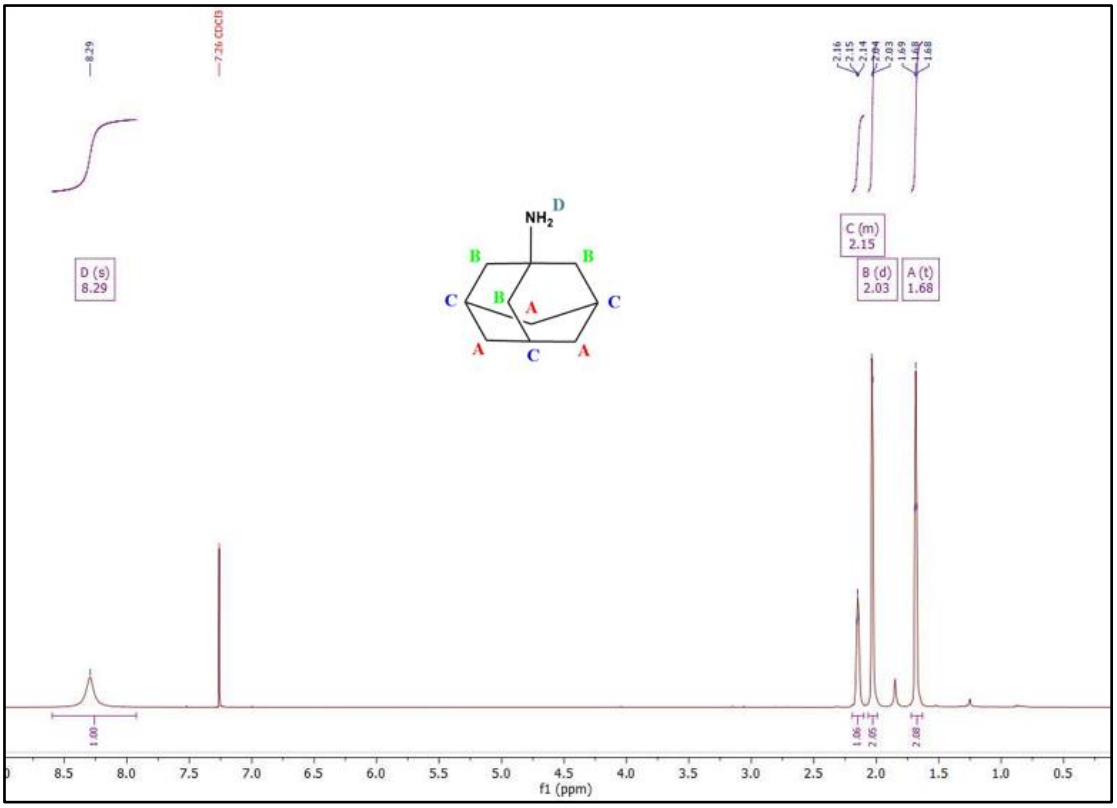

Figure 4. 9. ^{1}H NMR spectra of the amantadine (AMTD) drug, providing insights into the specific chemical shifts and proton environments within the molecular structure. The spectra were acquired in a suitable solvent deuterated chloroform ($CDCl_3$), providing information about the composition and arrangement of hydrogen atoms in the AMTD molecule.

The MUDA molecule was also investigated by ^{1}H NMR. The results showed that the hydrogen atom for the thiol group (-SH) in the MUDA molecule appeared at a high field or shielded as a triplet (t) signal peak at a frequency of 2.7 ppm (**Figure 4.10)**. This triplet peak is typically associated with the influence of neighbouring hydrogen atoms at carbon (b). In **Figure 4.10**, there are two hydrogen atoms connected to the neighbouring carbon (b) of the thiol group, indicating that the signal peak for the hydrogen in the thiol group will be observed

as a triplet peak in accordance with the spin-spin splitting rule (n+1) described by (Abraham et al., 1998). The "n" represents the number of hydrogen atoms attached to any neighbouring carbon. Additionally, the signal peak of the protons at carbon (b)appears as a quartet peak due to the presence of the three hydrogen atoms attached to neighbouring sulfur and carbon atom (d). Applying the simple equation (n+1), the number of hydrogens attached to sulfur at position (a) and carbon at position (d) can be considered as 3+1, which equals 4. Therefore, the signal peak of the protons at carbon (b) in the ^{1}H NMR spectra will be observed as a quartet (q) peak as shown in **Figure 4.10**, following the rule described by (Abraham et al., 1998). As mentioned earlier, the chemical shift of protons is influenced by the electronic environment around the proton being observed. Protons in a carboxylic acid group can show chemical shifts at relatively high ppm values (often around 10-12 ppm) due to the electron-withdrawing nature of the adjacent carbonyl group (C=O). The deshielding effect caused by the nearby electronegative oxygen atom in the carbonyl group pulls electron density away from the proton in the carboxylic acid, making it more shielded from the magnetic field. This leads to a high chemical shift value in the NMR spectrum.

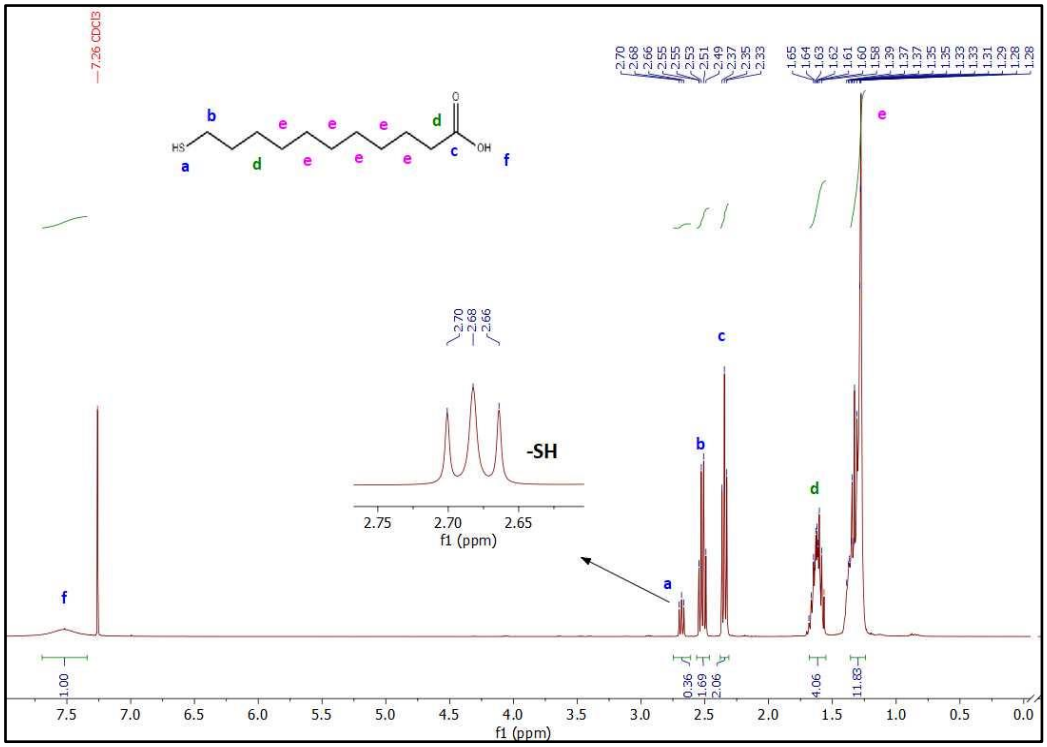

Figure 4. 10. ^{1}H NMR spectra highlighting the thiol group (-SH) in MUDA with a distinctive triplet peak at a chemical shift of 2.7 ppm. The presence of this thiol group is crucial for functionalisation with gold nanoparticles (Au NPs), as it serves as a reactive site for binding to the gold surface. The spectra were obtained by dissolving MUDA in an appropriate solvent, deuterated chloroform ($CDCl_3$). ^{1}H NMR spectra showed $CDCl_3$ peak at 7.26 ppm.

The ^{1}H NMR spectra after conjugation of AMTD to gold nanoparticles are shown in **Figure 4.11**. Several changes can be observed in the ^{1}H NMR spectra after the amantadine conjugation. AMTD/AuNPs showed an increase in the chemical shift (3.39 ppm) for the proton at carbon (A) due to the electronegativity effect of the nitrogen atom in the amide bond. On the other hand, the protons of carbon (B) in the spectrum were also de-shielded, appearing in the downfield region as a triplet (t) peak with a high chemical shift at 2.36 ppm. This can be attributed to the presence of the electronegative carbonyl (C=O) group in the amide bond. As

known from Little Jr and Jones, (1960), the nitrogen atom is more electronegative than the oxygen atom. Therefore, based on **Figure 4.11**, it is evident that nitrogen has a significant effect on the chemical shift of neighbouring protons attached to carbon atoms in the carbon-hydrogen system. Additionally, despite being far apart, both hydrogens D and E were de-shielded (downfield) with chemical shifts 1.64 ppm and 1.48 ppm, respectively. This can be assigned to the electronegativity effect of the oxygen atom in the carbonyl group, which is greater than that of the sulfur atom bound to the surface of the gold nanoparticles.

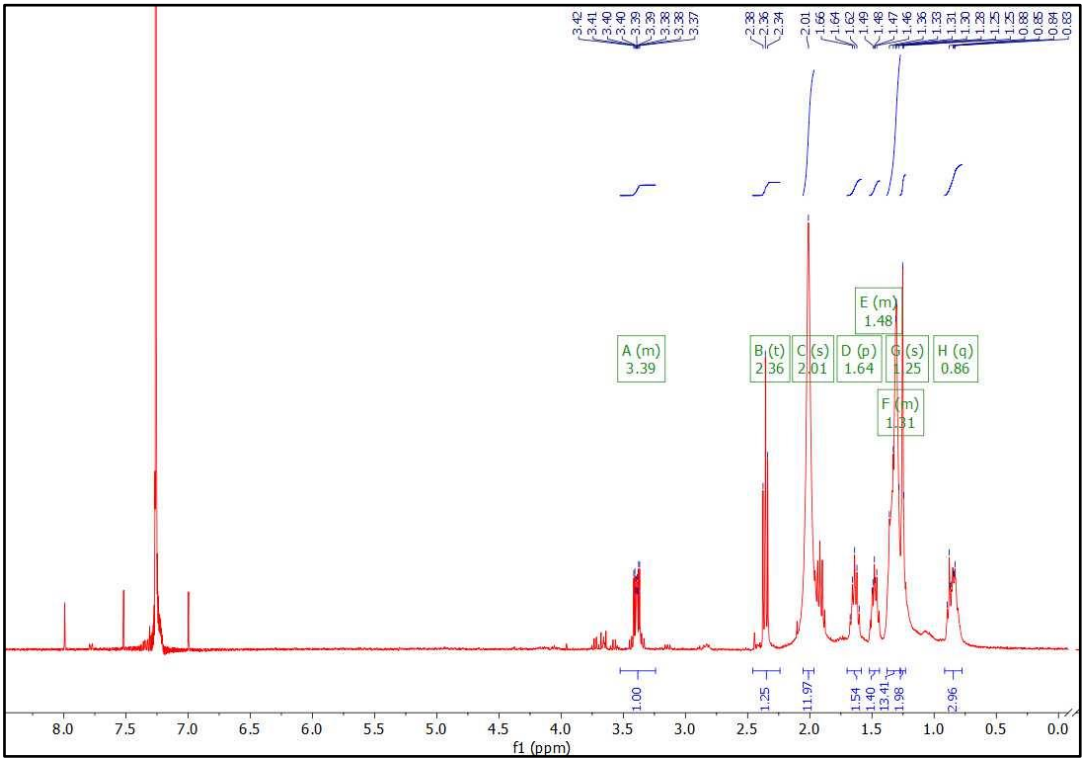

Figure 4. 11. ^{1}H NMR spectra for amantadine drug in its conjugated form with MUDA-functionalised gold nanoparticles (MUDA-cit-Au NPs). Notable changes observed in the NMR spectra following amantadine conjugation, with a majority of peaks exhibiting shielding towards the upfield region, particularly between 0.5 ppm and 3.5 ppm. These changes show the structural modifications and interactions induced by the conjugation process.

The conjugation of the amantadine drug to gold nanoparticles (AMTD/AuNPs) was also determined by investigating the carbon atoms in the chemical structure based on ^{13}C NMR characterisation. As shown in **Figure 4.12,** the carboxylic acid (-COOH) group of the MUDA compound appears as a single peak at a chemical shift of 180 ppm (indicated as 1 in the ^{13}C NMR spectra). Additionally, in **Figure 4.12**, both carbon atoms (C_2 and C_{10}) for the MUDA molecule were located downfield from other carbon atoms at the chemical shift 34 ppm. This was expected due to the high electronegativity of the oxygen atom at carbonyl (C=O) group which has the ability to withdraw electrons from its neighbouring carbons and other close carbons leading to an increase in the de-shielding effect downfield. In contrast, carbon (C_{11}) was observed with a chemical shift (δ) of approximately 25 ppm. This phenomenon is attributed to the thiol group's higher acidity compared to alcohols, resulting in more readily donated hydrogen atoms. Therefore, sulphur displaces hydrogen in hydroxyl groups. As a consequence, the diminished influence of negative charge results in weaker hydrogen bonds between thiols (Danehy & Parameswaran, 1968; Rayner, 1995). Furthermore, in the ^{13}C NMR spectra of MUDA, carbons C_3 and C_{11} exhibit shielding effects towards the high field, appearing with chemical shift around 25 ppm (**Figure 4.13**).

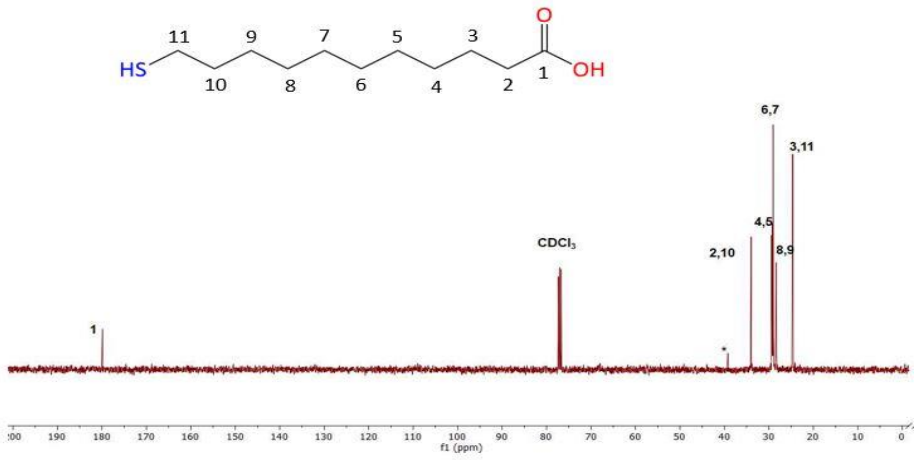

Figure 4. 12. ^{13}C NMR characterisation for MUDA thiol containing compound.

For amantadine, before conjugation, carbon C_1 exhibited a chemical shift around 53 ppm, indicating its de-shielding in a downfield direction (**Figure 4.13**). This is because of the electronegativity of the nitrogen atom in the primary amine group, which has the ability to withdraw electrons from the neighbouring carbon (C_1) more effectively than from any other carbons (Boeyens, 2008; Abraham et al., 1998). In **Figure 4.13**, carbons C_2 and C_3 which were observed at chemical shift 40 ppm and 35 ppm, respectively towards high field. Moreover, carbon (C_4) is observed at a relatively far position from the nitrogen atom with a single peak at chemical shift 30 ppm. This indicates the key role of the electronegative force of

nitrogen towards reducing electron density around chemical groups as described above.

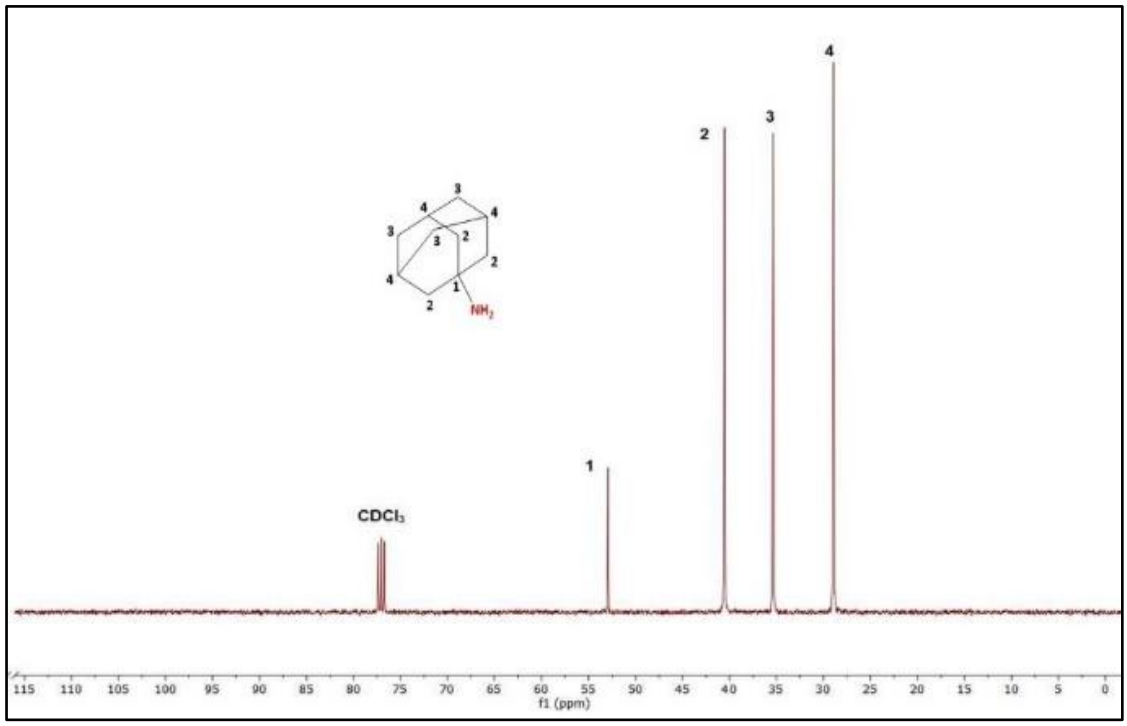

Figure 4. 13. ^{13}C NMR spectra illustrates the chemical shift of carbon atoms in amantadine drug before the conjugation process.

The conjugated form of amantadine-gold nanoparticles (AMTD/AuNPs) was also characterised under similar conditions. The chemical shift of carbonyl carbon atoms in molecules are typically shown in the range between 160 ppm and 220 ppm as described by (Rakhmatullin et al. 2022). Herein, the ^{13}C NMR spectra in **Figure 4.14** shows that carbon C_1, in amide bond (-NHCO-) in the drug-conjugated Au NPs, existed at chemical shift 180 ppm.

Furthermore, despite carbon's higher electronegativity compared to sulfur, carbons C_{10} and C_{11}, which are in neighbouring to sulfur, exhibit upfield shifts with very low chemical shift values of 34 ppm and 24 ppm, respectively. This can be attributed to their lower electronegative influence, as explained earlier (Boeyens, 2008).

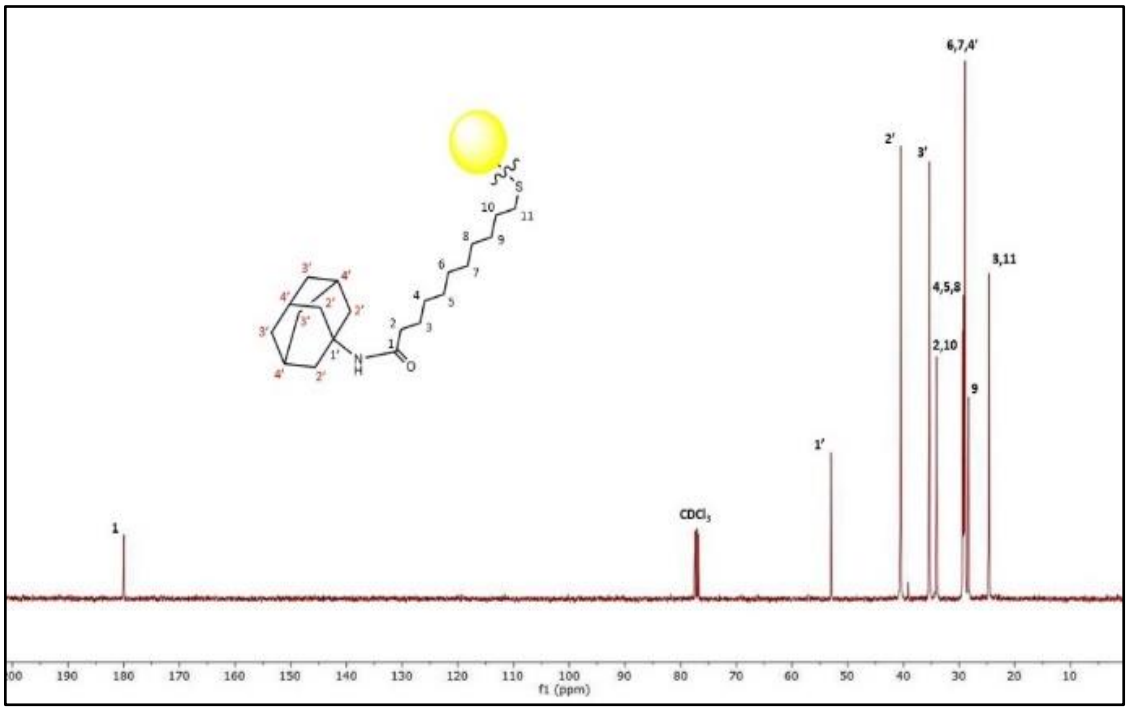

Figure 4. 14. ^{13}C NMR spectra depicting the chemical shift of carbon atoms in the AMTD/AuNPs conjugated form. The carbonyl carbon of the amide bond is noticeably observable at a far chemical shift of 180 ppm.

The examination of the quantity of amantadine bound to the surface of gold nanoparticles was performed using a thermogravimetric (TGA) analysis. A sample weighing 27.78 mg was placed in the chamber of the TGA. **Figure 4.15** illustrates the decomposition process of amantadine approximately 20 minutes after reaching 200°C. During this timeframe, the sample experienced a weight loss of around 25.78 mg, equivalent to roughly 92.8% of the initial mass (27.78

mg). Notably, the remaining 7.2% of the initial mass underwent complete decomposition after 25 minutes, as shown in Figure 4.15.

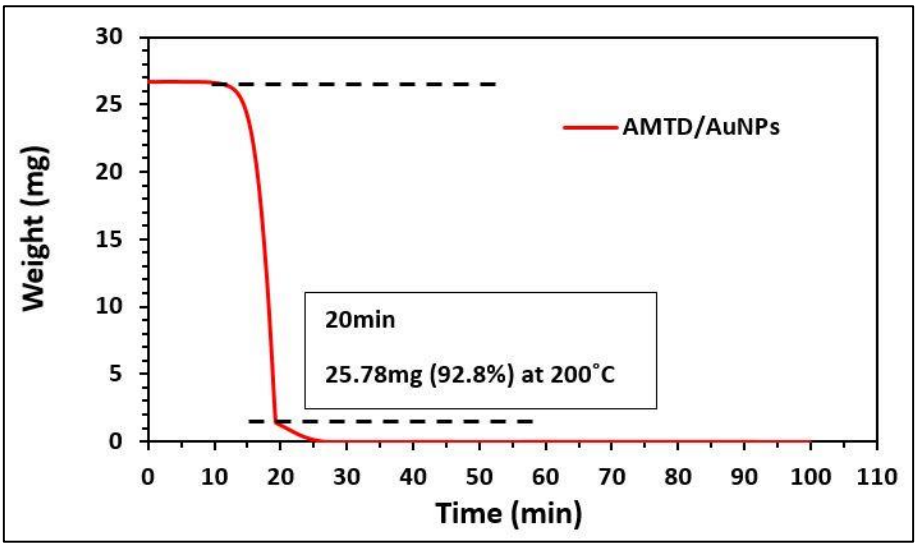

Figure 4. 15. Thermogravimetric Analysis (TGA) illustrates the decomposition process of amantadine bound to gold nanoparticles. Approximately 25.78 mg of the total amantadine drug decomposed within 20 minutes at 200°C.

4.3.1.2 Conjugation of Remdesivir (REM) to Gold Nanoparticles

Remdesivir (REM) is a nucleotide analogue with a broad-spectrum antiviral effect. When remdesivir penetrates the cell, its active metabolite (triphosphate analog) specifically attacks the ribonucleic acid (RNA) and interferes with the RNA-dependent RNA polymerase (RdRp) enzyme, thereby preventing RNA production or replication (Daka et al., 2021; Eastman et al., 2020). As a drug, Remdesivir possesses certain side effects involving, decreased pulse rate, variations in heart rate, instances of shortness of breath and the potential for liver cell damage (Daka et al. 2021). Hence, the present research study is focused on conjugation of REM to gold nanoparticles as an innovative nanocarrier. The

particle sizes of cit-AuNPs, functionalised gold nanoparticles (MUDA-AuNPs) and remdesivir-conjugated gold nanoparticles (REM/AuNPs) were determined by DLS analysis. Notably, a variation in size was identified, starting from the initial size of 20 nm to 40 nm and ultimately reaching a diameter of 165 nm following conjugation (**Figure 4.16**). The particle size analysis by DLS in **Figure 4.16** showed well-defined and narrow size distribution peak for the remdesivir-conjugated gold nanoparticles with diameter of 165 nm and a polydispersity index (PDI) of 0.323. The PDI is a useful parameter for assessing the uniformity or heterogeneity of nanoparticles in the colloidal suspension (Mudalige et al., 2019). Thus, according to obtained results in **Figure 4.16**, the REM/AuNPs show low polydispersity, which indicates a narrow distribution of particle sizes.

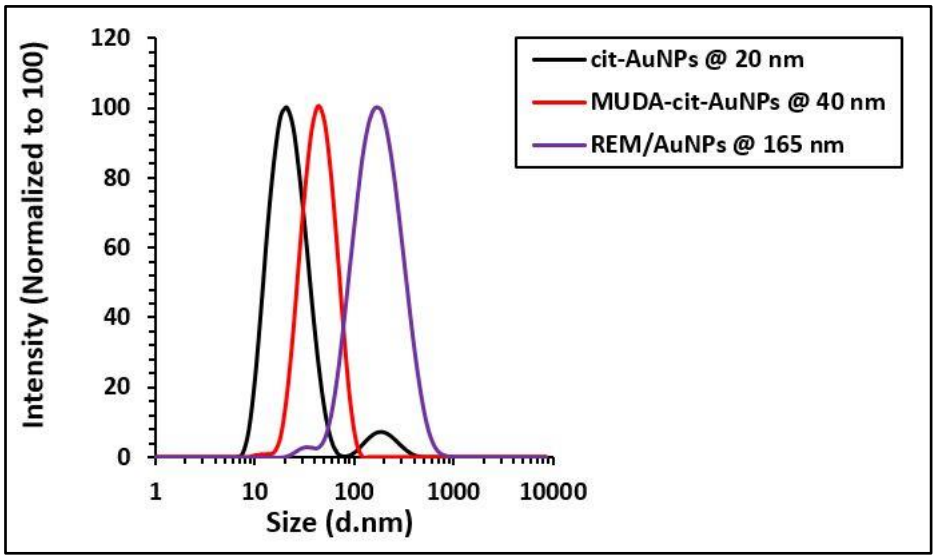

Figure 4. 16. DLS shows particles size measurements for the synthesised cit-AuNPs, MUDA functionalised cit-AuNPs and REM conjugated to Au NPs.

The relationship between particles size and localised surface plasmon resonance (LSPR) is a fundamental concept in the field of nanotechnology. Herein, the

particles size increase was also determined by measuring the LSPR peak shift for the conjugated nanoparticles REM/AuNPs. For example, **Figure 4.17** shows the surface plasmon resonance absorption peak of the synthesised citrate-gold nanoparticles where a significant shift can be observed following MUDA functionalisation (MUDA/AuNPs) from 522 nm to 570 nm. This observation strongly supports the phenomenon that the LSPR wavelength is highly sensitive to the size of the nanoparticles. As particles size increases, the LSPR wavelength typically shifts to longer wavelengths (red shift). In summary, the LSPR properties of metal nanoparticles play a critical role in determining the particles size.

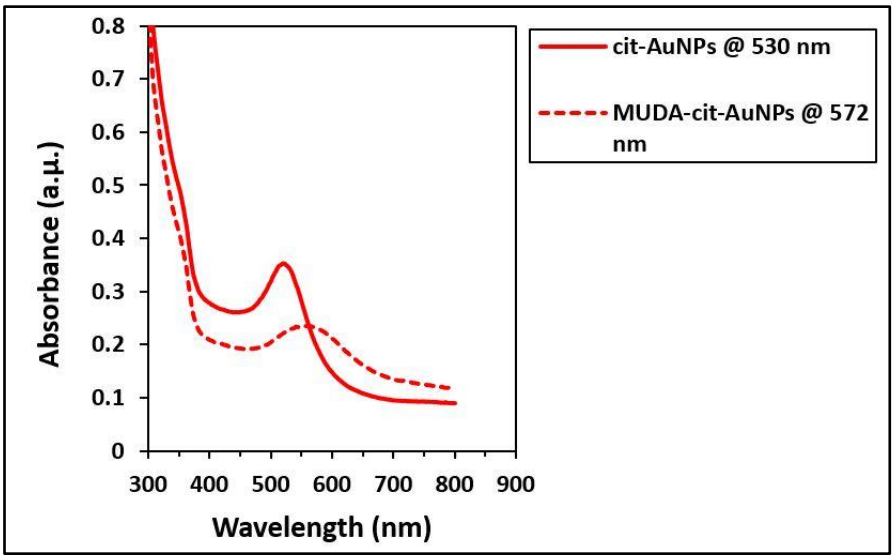

Figure 4. 17. Localised surface plasmon resonance peak shifts for the synthesised and functionalised gold nanoparticles determined by UV-Vis spectrophotometer at 522 nm and 570 nm for the citrate-gold nanoparticles and MUDA functionalised gold nanoparticles, respectively.

The LSPR of REM-conjugated gold nanoparticles (REM/AuNPs) exhibited remarkable broadening and a slight decrease in intensity when compared to the

spectra of the synthesised citrate-gold nanoparticles. Specifically, a considerable shift of the LSPR absorption peak to 590 nm was observed (**Figure 4.18**). Furthermore, an additional LSPR absorption peak was detected at 249 nm, corresponding to the presence of the remdesivir drug molecule (Joshi et al., 2011). This observation indicates that following the conjugation of gold nanoparticles with the remdesivir antiviral medicine, a significant shift in the nanoparticles' peak occurred, transitioning from 522 nm to approximately 590 nm. This shift is due to the increase in nanoparticles size. Consequently, both the absorption strength and the full width at half maximum (FWHM) of the absorption band are significantly influenced by the attachment of the remdesivir (ligand) to the surface of gold nanoparticles, as previously highlighted for the amantadine (Chapter 4 Section 4.3.1.1).

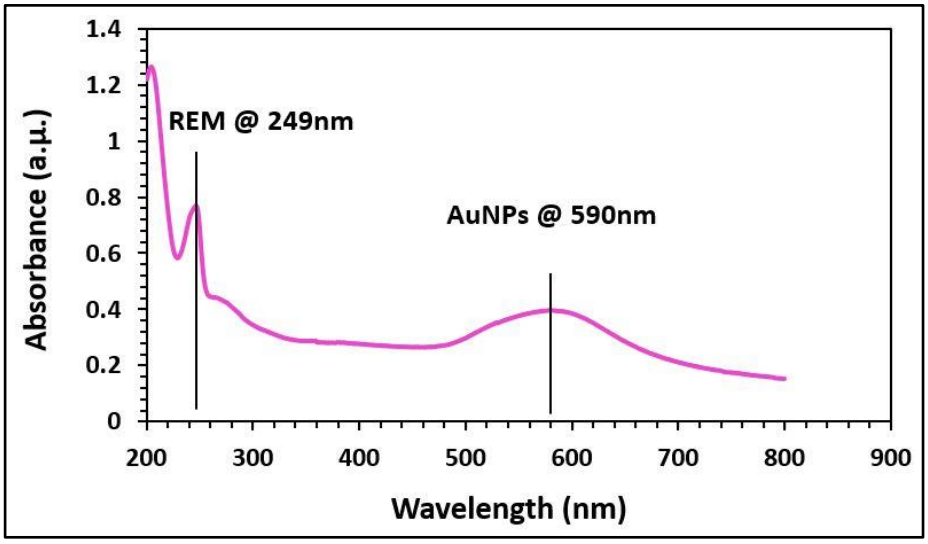

Figure 4. 18. LSPR absorption peak shift for the remdesivir conjugated gold nanoparticles (REM/AuNPs) measured by UV-Vis spectrophotometer at wavelengths of 249 nm and 590 nm.

FTIR was also employed to investigate the absorption bands attributed to amide groups in the REM/AuNPs. These bands include amide I, covering the wavenumber range of 1600-1800 cm^{-1}, amide II within 1470-1570 cm^{-1}, amide III at wavenumber 1250-1350 cm^{-1} and amide A, positioned between 3300 cm^{-1} and 3500 cm^{-1} as described by Ji et al. (2020). Herein, the FTIR results in **Figure 4.19** show that the -CH stretching observed at wavenumbers 2918 cm^{-1} and 2850 cm^{-1} for both functionalised (MUDA/AuNPs) and remdesivir conjugated to gold nanoparticles (REM/AuNPs). Additionally, a broad band corresponding to the carboxylic acid group (-COOH) which indicated by a black double-line arrow, covering a wavenumber range approximately from 2526 cm^{-1} to 3150 cm^{-1} (**Figure 4.19**). On the other hand, a single strong band at 1696 cm^{-1} is more likely to indicate the presence of both C=O and C=N groups. Moreover, bands that can be seen at 1412 cm^{-1} and 1226 cm^{-1} are, respectively, attributed to the presence of $-CH_3$ and C-N groups. Finally, a band with very low intensity at 723 cm^{-1} was expected to be present, representing the -NH group in the remdesivir conjugated form. It was noticed that the characteristic stretching band for the primary amine ($-NH_2$) group in remdesivir, was not detected in the region between 3250 and 3400 cm^{-1}. This can be due to the formation of an amide bond after the conjugation process.

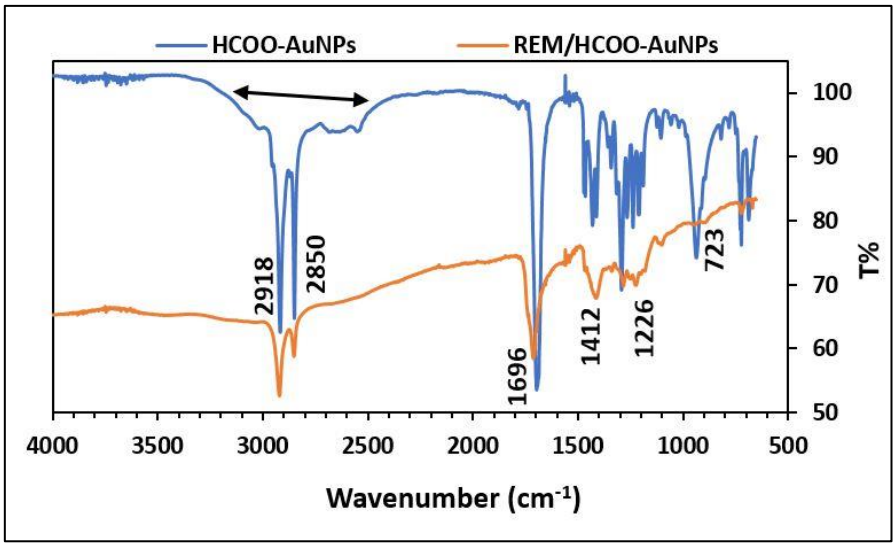

Figure 4. 19. Fourier Transform Infrared Spectroscopy (FTIR) spectra revealing the main functional groups following remdesivir conjugation to gold nanoparticles (REM/AuNPs). Significant changes are observed, including the disappearance of the primary amine group in remdesivir, in the region between 3250 and 3400 cm^{-1}, after conjugation with functionalised Au NPs.

For ^{1}H NMR characterisation, deuterated chloroform was used as the solvent for proton characterisation. The main reason for utilising the deuterated solvents is to avoid interference from the solvent peaks in the NMR spectrum. For instance, deuterium, a stable and heavier isotope of hydrogen, does not possess a nuclear magnetic moment, and therefore it does not contribute to the NMR signal. By using deuterated solvents, such as $CDCl_3$, the signals from the sample molecules can be observed without interference from the solvent peaks (Hanson, 2013).

Remdesivir is a drug molecule that bears a positive charge under acidic conditions at pH 2.0. The presence of a positive charge can influence the chemical shifts and splitting patterns observed in the ^{1}H NMR spectrum (Várnai

et al., 2022). Therefore, by characterisation of remdesivir using deuterated chloroform, any peaks corresponding to the drug molecule can only be observed without interference from the solvent peaks, providing valuable information about its chemical structure. **Figure 4.20** shows the chemical shift of the protons influenced by the electronegativity of neighbouring atoms. As mentioned earlier, when more electronegative groups or atoms are connected to the carbon-hydrogen (C-H) system, the electron density decreases, resulting in a higher chemical shift (ppm) downfield (Boeyens, 2008). The chemical shifts of the main proton signals can be attributed to H_4 and H_1. It is expected that H_4 has undergone deshielding, exhibiting a downfield shift at approximately 4.3 ppm, whereas H_1 has been shielded and showed an upfield shift at 0.8 ppm. This is due to the presence of an electronegative oxygen atom directly attached to the carbon atom of the proton H_4. Another example is the proton five (H_5), which is positioned between two functional groups, namely an ester and a secondary amine group, as depicted in the chemical structure of remdesivir shown in **Figure 4.20**.

Both the ester and secondary amine groups directly influence the chemical shift of H_5, causing a de-shielding effect that shifts the peak downfield to approximately 4.0 ppm. Similarly, the signals for H_7, H_8, H_9 and H_{10} are observed as overlapping signals and are de-shielded at approximately the same chemical shift of 4.0 ppm. This de-shielding effect is due to the presence of neighbouring hydroxyl groups as indicated in **Figure 4.20**. Additionally, the primary amine group in remdesivir shows a chemical shift around 8.3 ppm. This is similar to the chemical shift of the primary amine in the amantadine drug, which was previously determined to be at around 8.29 ppm (Chapter 4 Section 4.3.1.1). It is worth mentioning that the

resonances of N-H protons can vary significantly due to differences in the strength of hydrogen bonding (John D. Roberts and Marjorie C. Caserio, 2021).

From **Figure 4.20**, the (–NH) resonance is deshielded downfield at approximately 4.6 ppm compared to H7, attributed to the higher electronegativity of nitrogen. However, the aryl protons H_{12} and H_{13}, were observed in the region between 6.5 ppm and 7.5 ppm. This region is specific to those protons attached to the aromatic ring in the remdesivir drug molecule as described by (Campbell et al., 1975) (**Figure 4.20**).

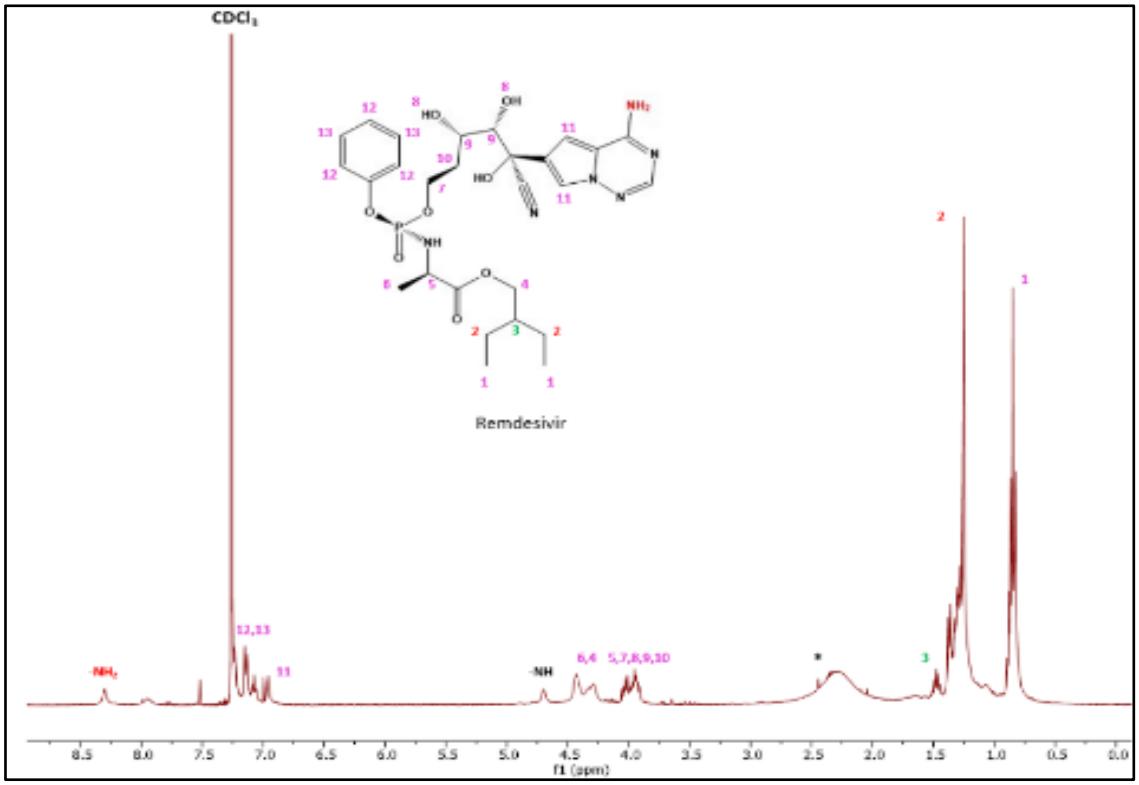

Figure 4. 20. ^{1}H NMR spectra shows the chemical shift of the standard remdesivir protons.

The appearance and characteristics of aryl protons in an NMR spectrum can vary significantly based on the unique molecular structure and its chemical environment. Therefore, the interpretation of ^{1}H NMR spectra for aryl protons in the context of the remdesivir drug involves analysing chemical shifts, multiplicity patterns, integration values, and coupling constants. These analyses contribute to illustrating the structural information about the molecule's aromatic rings and their neighbouring functional groups or substituents within the remdesivir compound.

The ^{1}H NMR spectra of remdesivir conjugated to gold nanoparticles were also investigated under similar conditions. It was observed that the majority of peaks of the remdesivir showed shielding effects after conjugation, resulting in up field shifts at low chemical shifts between 0.5 ppm and 2.0 ppm (**Figure 4.21**). For instance, a double peak at a chemical shift of 1.77 ppm was used as a reference signal with an integral ratio of 1.0, as depicted in **Figure 4.21**. The aryl proton peaks (H_{11}, H_{12} and H_{13}), attached to the aromatic ring in the drug molecule disappeared from the NMR spectrum after the conjugation process. This could be due to the electrophilic aromatic substitution reactions (EAS) during the conjugation with gold nanoparticles. Kulshrestha, (2000) demonstrated the effects of various electrophilic aromatic substitution reactions such as

halogenation, nitration, and sulfonation with sulfur trioxide. Therefore, this significant shift of protons could be related to the EAS.

The thermogravimetric analysis conducted under heating rate from 100°C to 900°C. From **Figure 4.22**, it was found that remdesivir decomposes in two stages. First, only 1.1 mg (39.3%) of the total sample (2.79 mg) has decomposed after around 15 minutes. Then, this continued over time until remdesivir decomposed again approximately 0.9 mg (32.3%) after 40 minutes. This means that the total amount of REM decomposed within 50 minutes is roughly 71.6% of the initial mass (2.79 mg). The decomposition effect stopped at 50 minutes at the residual mass 0.79 mg (**Figure 4.22**).

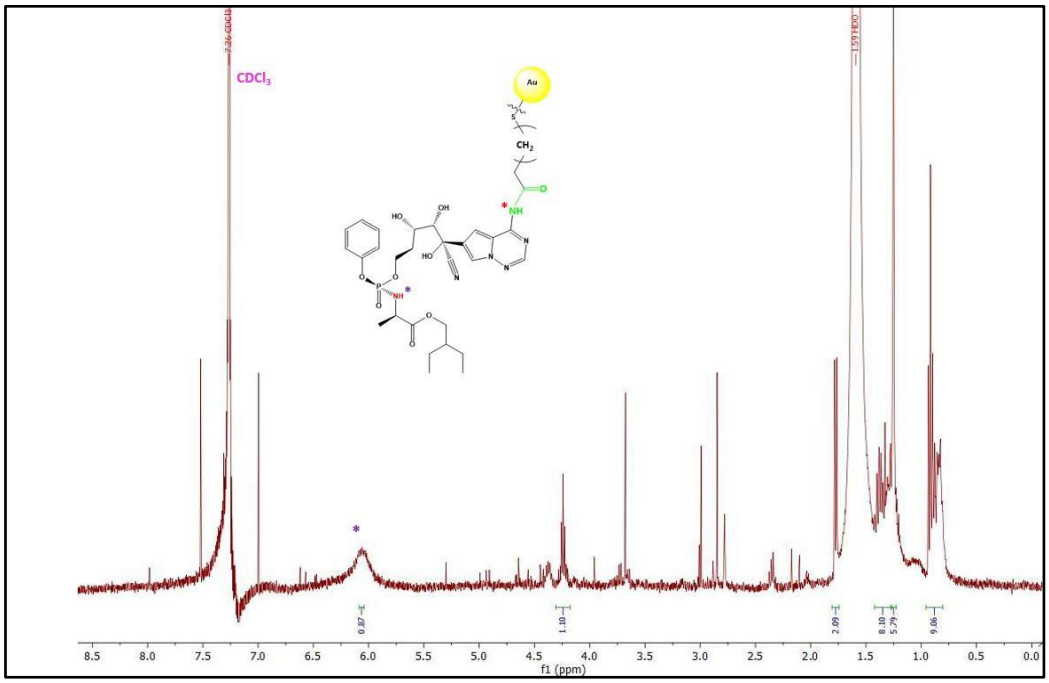

Figure 4. 21. 1H NMR spectra illustrating the conjugation of the remdesivir drug to gold nanoparticles. The majority of protons experience shielding, resulting in a shift towards the upfield region between 0.5 ppm and 2.0 ppm. Notably, aryl proton peaks (H12 and H13), attached to the aromatic ring in the drug molecule, disappeared from the NMR spectrum following the conjugation process.

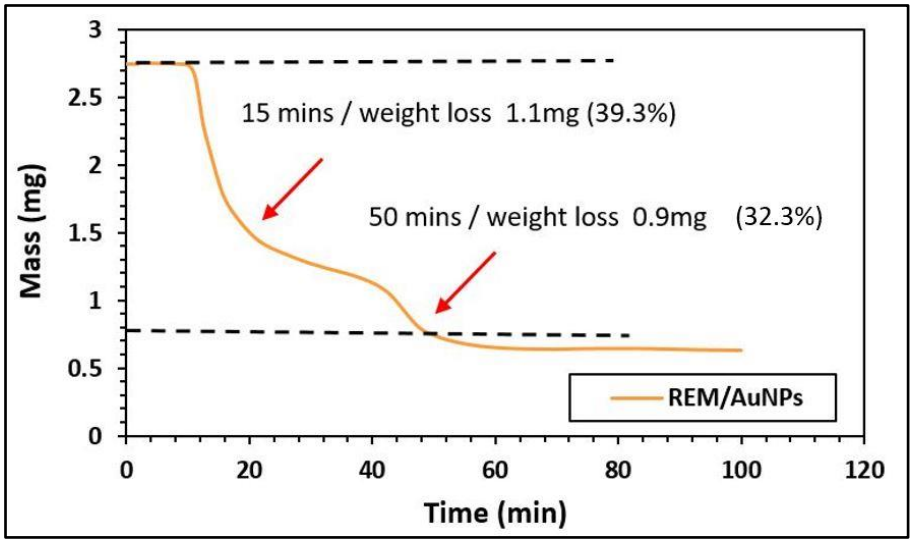

Figure 4. 22. Thermogravimetric Analysis (TGA) depicting the temperature-induced decomposition of the remdesivir drug from the surface of Au NPs. Approximately 71.6% of the initial amount undergoes decomposition during the analysis.

4.4 Drug Encapsulation

4.4.1 Encapsulation of Amantadine into Poly (lactic-co-glycolic acid) NPs

The Food and Drug Administration of the United States (US FDA) has approved the essential application of poly lactic-co-glycolic acid (PLGA) for drug delivery and various medical purposes due to its distinctive properties such as drug release (Lü et al., 2009). Poly lactic-co-glycolic acid nanoparticles (PLGA NPs) demonstrate the ability to regulate drug release over extended periods (Hines & Kaplan, 2013).

Thus, this study aimed to explore this property by encapsulating amantadine using PLGA NPs. Essentially, the encapsulation mechanism is explained in

chemistry as the interaction between the carboxyl group in the surfactant and the primary amine group in the amantadine drug. The amine group in amantadine possesses a high pKa, causing it to tend toward protonation at physiological pH 7.0, resulting in a positive charge. Conversely, the carboxylic acid group exhibits a low pKa and tends to donate a proton, resulting in a negative charge at pH 7.0. Consequently, this approach can be referred to as a proton transfer method (Nugrahani & Jessica, 2021). Amantadine was successfully encapsulated within PLGA polymeric nanoparticles using the precipitation solvent evaporation method (Chapter 2 Section 2.3.5). To improve encapsulation efficiency, the additive, oleic acid, was introduced in conjunction with Pluronic F68. The inclusion of oleic acid in the formulation is aimed at enhancing drug release kinetics from the nanoparticles due to its inherent hydrophobic properties. This characteristic can potentially slow down drug diffusion from the nanoparticle matrix, thereby facilitating controlled and sustained drug release over an extended duration (Atef et al., 2022; Lee & Yeo, 2015).

4.4.2 Results and Discussion

The particle size and ζ-potential measurements were examined by DLS. The scattering angles have been observed at 175° for particle size analysis, and at 45° for ζ-potential study.

The mean particle size and the polydispersity index of amantadine encapsulated into the poly lactic-co-glycolic acid nanoparticles (AMTD/PLGA-NPs) were determined at 190 nm and 0.451, respectively, indicating narrow particle size distribution in the sample (**Figure 4.23,** purple dash line). The red dash line in Figure 4.23 represents the amantadine conjugated to gold nanoparticles with size

of 165 nm. Polymeric nanoparticles are typically larger than metallic nanoparticles due to differences in their synthesis methods, molecular structure and material properties (Begines et al., 2020; Joudeh & Linke, 2022; Khan et al., 2019).

As can be seen in **Figure 4.23**, AMTD/PLGA- NPs are relatively larger than that amantadine conjugated to gold nanoparticles due to the molecular weight of the polymer. Additionally, it was observed that the microscopic images for AMTD/PLGA-NPs are well distributed without any sign of the aggregation (Chapter 4 Figure 4.26). This is related to the homogenous particle distribution in the sample during their preparation. A uniform distribution of nanoparticles can lead to enhanced material properties and performance. For example, in drug delivery applications, uniform dispersion of drug-loaded nanoparticles can result in more predictable and controlled drug release kinetics, leading to better therapeutic outcomes (Mitchell et al., 2021; Rizvi & Saleh, 2018). In this study, the primary amine group in amantadine drug contributes in polar interactions with the hydrophilic portion of oleic acid and Pluronic F68. This interaction led to increase the particle size while maintaining a homogeneous distribution of particle sizes (Prasanthan & Kishore, 2021). Furthermore, the Pluronic F68 surfactant possesses the capacity to form micelles (amphiphilic molecules) at its critical micelle concentration (CMC) (Ahmed, 2020).

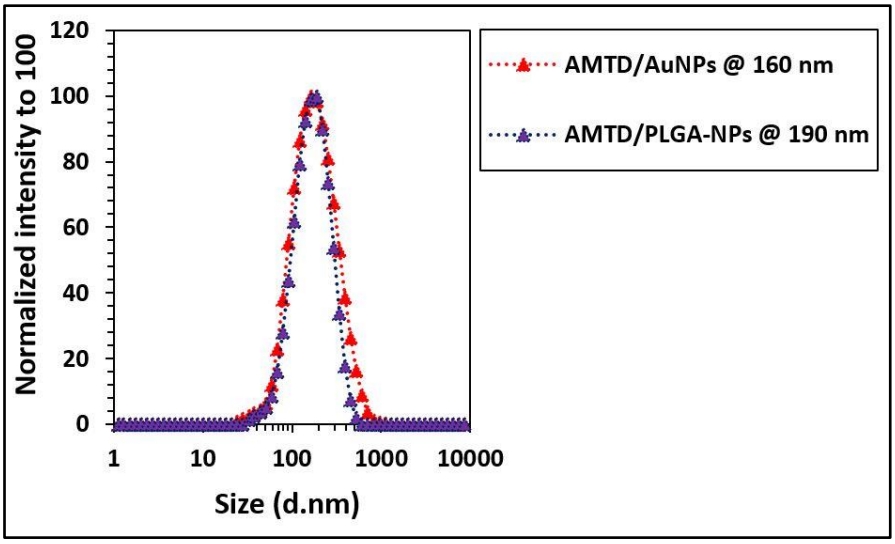

Figure 4. 23. DLS measurements shows the difference in particle size distribution between amantadine-encapsulated nanoparticles and those conjugated to gold nanoparticles.

The optical properties for the three different forms of amantadine encapsulated into PLGA NPs: AMTD/PLGA-NPs (1) (red), AMTD/PLGA-NPs (2) (pink), and AMTD/PLGA-NPs (3) (purple) were measured at maximum wavelength 550 nm using UV-Vis spectrophotometer. The LSPR for AMTD/PLGA-NPs (1), AMTD/PLGA-NPs (2) and AMTD/PLGA-NPs (3) was determined at 526 nm, 528 nm, and 536 nm, respectively (**Figure 4.24**). In contrast, amantadine conjugated to gold nanoparticles (green) was found at maximum wavelength 522 nm with low intensity peak. This significant difference in the absorbance peaks would explain the fact that amantadine encapsulated into PLGA polymeric nanoparticles has ability to absorb and scatter light more than that conjugated to gold nanoparticles. Thus, the shift of the LSPR absorption peaks will increase along with nanoparticle size increase (Yanjie Wang et al., 2016).

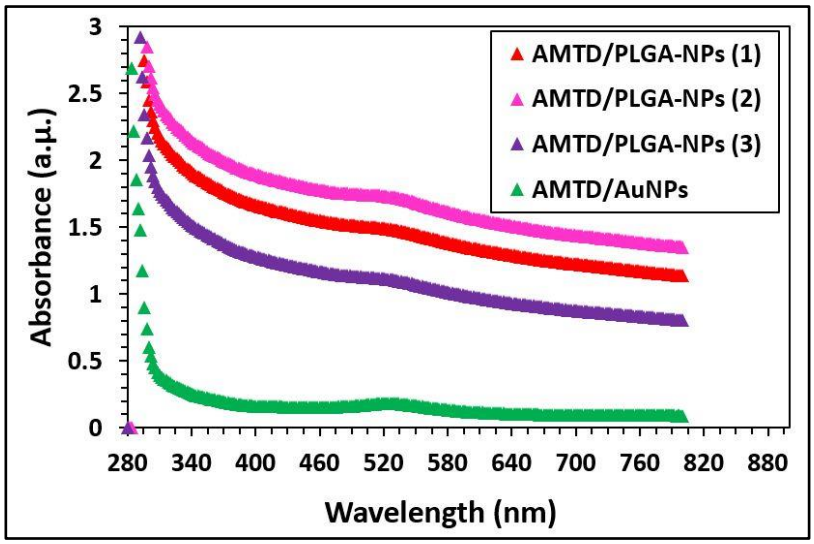

Figure 4. 24. LSPR absorption peak shifts for three different types of amantadine encapsulated into PLGA-NPs: AMTD/PLGA-NPs (1) (red), AMTD/PLGA-NPs (2) (pink), and AMTD/PLGA-NPs (3) (purple). The green absorption peak represents the amantadine conjugated gold nanoparticles prepared by the carbodiimide cross-linking chemistry.

FTIR characterisation was employed here to discover the functional groups in the chemical structure of the AMTD/PLGA-NPs. Herein, the standard poly lactic-co-glycolic acid (PLGA std.), amantadine drug (AMTD std.), and the amantadine encapsulated into PLGA nanoparticles (AMTD/PLGA NPs) were analysed using FTIR. **Figure 4.25** shows the changes in the FTIR spectra for the AMTD/PLGA NPs after the encapsulation process. For instance, the intensity (T%) of the carbonyl stretching peak at 1750 cm^{-1} has been notably reduced as a result of encapsulation, unlike the C-O-C stretching peak at 1020 cm^{-1}, which appears identical for both AMTD/PLGA NPs and standard PLGA. Furthermore, it can be seen that the (-CH) stretching peaks appeared at 2860 cm^{-1} and 2920 cm^{-1} for the standard poly lactic-co-glycolic acid (PLGA std.), amantadine (AMTD) drug

and amantadine encapsulated into PLGA nanoparticles (AMTD/PLGA NPs) respectively. Moreover, bands that observed at 1412 cm^{-1} and 1226 cm^{-1} are, respectively, for the -CH_3 and C-N groups.

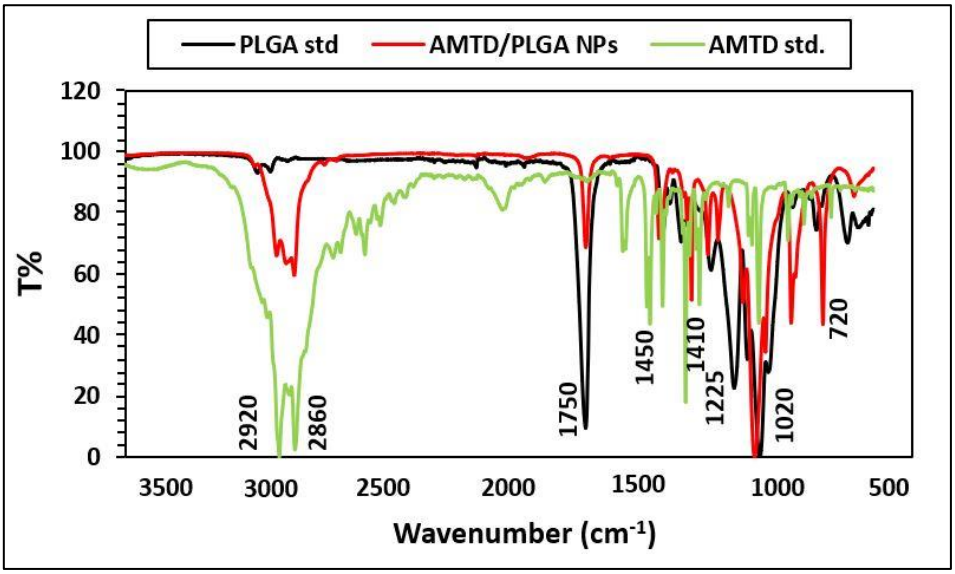

Figure 4. 25. FTIR spectra illustrating variations in the positions of functional groups after the encapsulation of amantadine into PLGA-NPs.

The morphology of drug encapsulated nanoparticles (AMTD/PLGA NPs) was investigated using TEM imaging. The amantadine was encapsulated in the presence of the Pluronic F68 (non-ionic surfactant) and oleic acid (anionic surfactant) by formation of micelles through trapping cationic amantadine inside these micelles. This is mainly based on providing sufficient concentration ratios of both surfactants at the critical micelle concentration (CMC)(Esmaeili et al., 2021). As can be seen in **Figure 4.26**, almost all nanoparticles are spherical and distributed uniformly, with approximate size 190 nm as determined earlier by dynamic light scattering and at low polydispersity index (PDI). The TEM image

showed well-distributed nanoparticles. These nanoparticles displayed a smooth external layer, which was assumed to be due to the encapsulation (**Figure 4.26**).

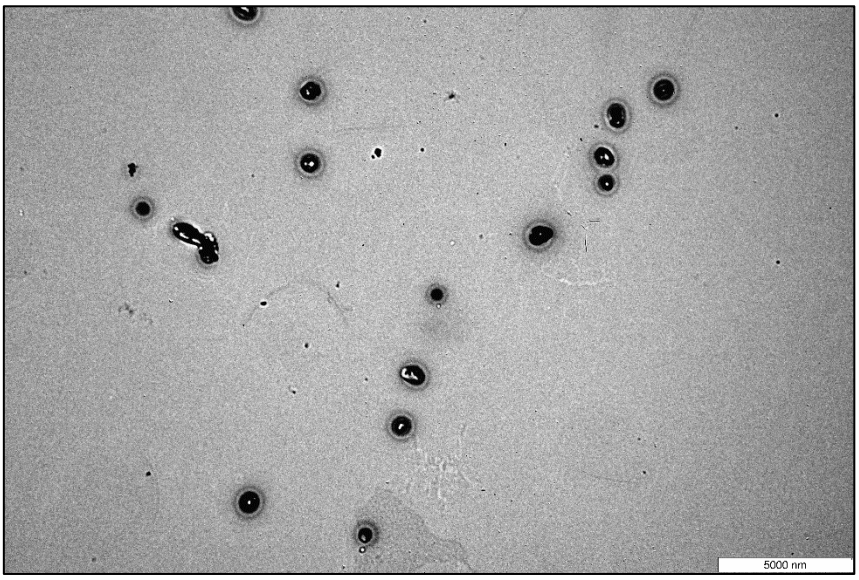

Figure 4. 26. TEM microscopic image for the amantadine encapsulated into PLGA NPs. This image was conducted at a nanoscale bar at 5000 nm.

The PLGA (standard) and amantadine encapsulated into PLGA nanoparticles were also characterised by the ^{1}H NMR. For the standard PLGA, **Figure 4.27** illustrates a peak at a chemical shift of 1.6 ppm, attributed to the methyl group in poly lactic acid (PLA). Additionally, peaks within the chemical shift range of 4.5 ppm to 5.5 ppm correspond to the -CH and -CH_2 groups, respectively, associated with lactic acid and glycolic acid (Pereira et al., 2016). Following encapsulation and in the presence of both oleic acid and Pluronic F68 surfactant, changes were observed in the ^{1}H NMR spectra of the formulated PLGA polymeric nanoparticles loaded with amantadine, as depicted in **Figure 4.27**. The signal from the primary amine group emerged at a chemical shift of 7.2 ppm. A study conducted by Yang

et al. (2014) discovered that the primary amine group after conjugation would emerge as an upfield chemical shift at 2.10 ppm.

The signal peak of the methylene group of lactic acid was shifted from 1.5 ppm to 1.0 ppm after the encapsulation process as shown in **Figure 4.27**. Furthermore, signal peaks of the -CH and -CH_2 for lactic acid and glycolic acid respectively were moved away from each other in the ^{1}H NMR spectrum.

Additional new peaks that emerged after encapsulation are suggested to be for Pluronic F68. For instance, the hydrophobic part polypropylene oxide (PPO) is expected to exhibit characteristic peaks within the chemical shift range of 1.0 ppm to 3.5 ppm. Specifically, the methyl group (-CH_3) was predicted to appear at a chemical shift of 1.3 ppm, as reported by Y. Liu et al. (2016). Similarly, the -CH_2 group was observed at a chemical shift of 3.8 ppm. Furthermore, the chemical shift of the -CH in polypropylene oxide (PPO) has been identified at 3.34 ppm. Additionally, minor intensity peaks correspond to the -CH_2 groups in the hydrophilic part named polyethylene oxide (PEO) were determined at approximately 3.6 ppm. Therefore, based on the ^{1}H NMR analysis, it can be stated that the encapsulation of amantadine into the poly lactic-co-glycolic acid nanoparticles was successful, with no indication of aggregation, as evidenced earlier by the microscopic imaging in Figure 4.26.

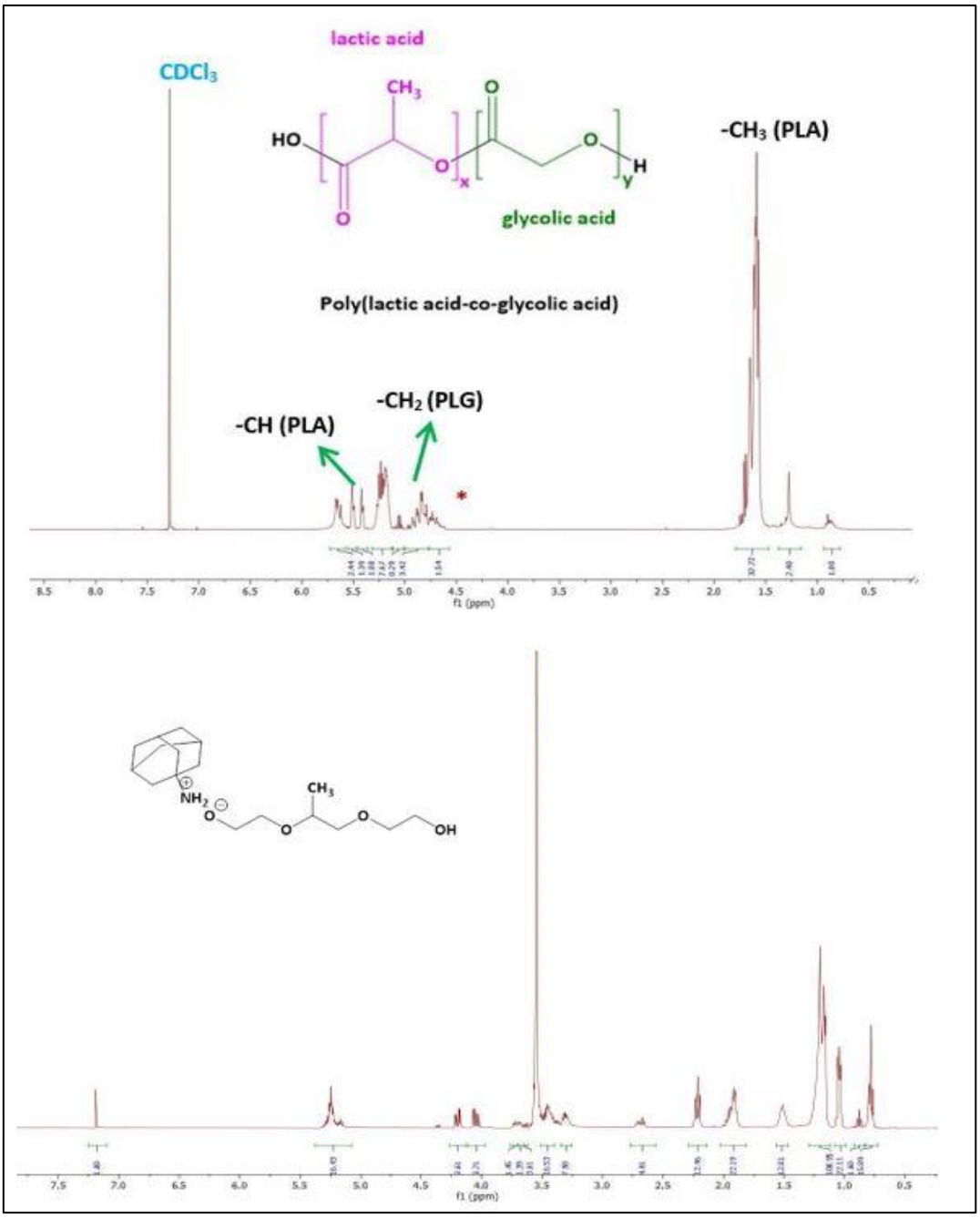

Figure 4. 27. Shows the ^{1}H NMR spectra for standard PLGA (top panel), while the bottom panel highlights the chemical shift peaks specific to AMTD/PLGA NPs after amantadine encapsulation.

The thermal degradation properties of the AMTD/PLGA-NPs were examined using thermogravimetric analysis. Herein, the sample experienced a heating from

100°C to 900°C at a rate of 20°C/ minute. As depicted in **Figure 4.28**, the thermal degradation of the polymeric nanoparticles loaded with amantadine begins gradually until the temperature reaches 450°C. At this point, the loaded nanoparticles undergo complete decomposition by losing 12 mg within 25 minutes at 450°C of TGA running (**Figure 4.28)**.

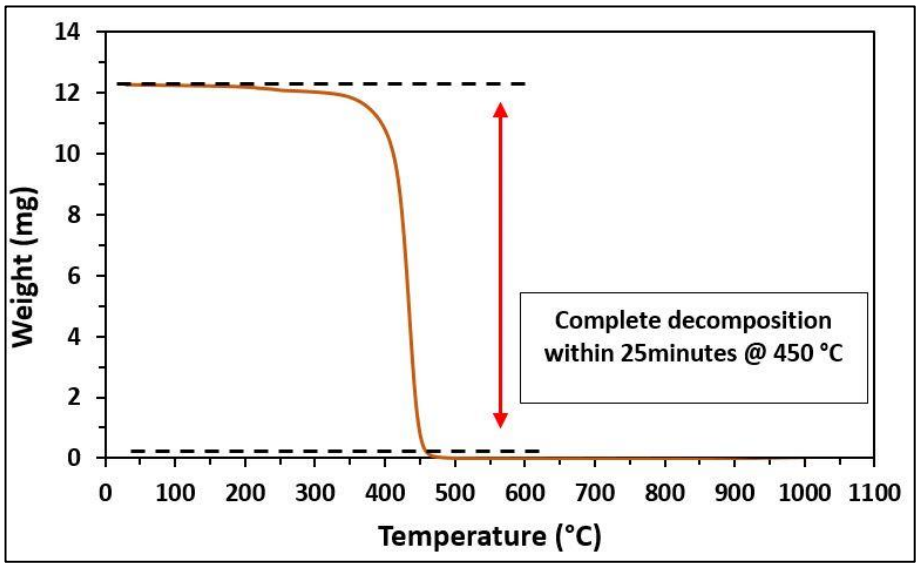

Figure 4. 28. Thermogravimetric analysis (TGA) of amantadine encapsulated within PLGA nanoparticles (AMTD/PLGA-NPs) demonstrates a reduction in mass with increasing temperature.

4.5 Conclusions

This chapter focused on the functionalisation of citrate-gold nanoparticles (cit-Au NPs with 11-mercaptoundecanoic acid (MUDA). This was carried out by attaching the thiol group of the MUDA molecule to gold atoms at the surface of the gold nanoparticles resulting in the formation of strong gold-sulfur (Au-S) bonds. Through characterisation, it was found that the functionalised gold nanoparticles (MUDA-cit-AuNPs) with 10 mM of the MUDA molecule, are reasonably stable at

low polydispersity index indicating narrow size distribution of the particles. Additionally, two types of medicines amantadine and remdesivir were conjugated to the functionalised gold nanoparticles using the carbodiimide cross-linking chemistry technique in the presence of the EDC and NHS coupling agents. Obtained results showed a significant increase in size for both AMTD/AuNPs (160 nm) and REM/AuNPs (165 nm) with low polydispersity index.

The ^{1}H NMR and ^{13}C NMR characterisation enabled identification of the conjugation system via determination of the amide bond formation.

The encapsulation of amantadine into the PLGA-NPs using both Pluronic F68 and oleic acid aimed to enhance the encapsulation efficiency by formation of amphiphilic molecules using the proton transfer method. Finally, TEM characterisation, showed that the polymeric nanoparticles (AMTD/PLGA-NPs) were uniformly monodispersed in the colloidal suspension without any sign of aggregation, the drug has been entrapped into the polymeric nanoparticles using the precipitation solvent evaporation technique.

Chapter (5): Stability assessment of Unconjugated and Drug-Conjugated Gold Nanoparticles

5.1 Introduction

Stability assessment is a crucial step following nanoparticles synthesis and drug conjugation to ensure the desired functionality has been achieved (Busch et al., 2019; Male et al., 2008; Shah et al., 2014; Shon et al., 2009; Vijayakumar, 2014). This assessment involves studying the physicochemical properties of the synthesised nanoparticles (Chapter 3 Table 3.1) *in vitro* under specific conditions. In this chapter, the stability of the synthesised gold nanoparticles and their conjugates was determined by investigating the impact of temperature, pH variation, various buffer solutions, and chemicals (e.g., reducing agents) used in the synthesis techniques.

The influence of the biological medium Dulbeccos Modification of Eagles Medium (DMEM), commonly used for cellular uptake was also examined. Citrate functionalised gold nanoparticles may undergo changes in the cell culture medium due to the presence of nutrients, proteins, and electrolytes (Sangwan & Seth, 2021). In addition, the binding of gold nanoparticles to the free cysteine residue in bovine serum albumin (BSA) was considered in this study. For example, the bonding between cit-AuNP (20.54 ±0.45 nm) and BSA may occur via electrostatic or hydrophobic interactions or by chemisorption of thiols onto the gold surface (Bolaños et al., 2019).

This chapter also demonstrates the concentration of gold ions released in various media, such as buffer solutions, ultrapure water (Milli-Q 18.8 MΩ-cm), and cell culture media. The ionic strength of sodium (Na^+) and potassium (K^+) ions was examined for its effect on size at different concentration ratios of sodium nitrate

and potassium nitrate salts, respectively. Furthermore, different coatings of gold nanoparticles (as described in Chapter 3 Table 3.1) were tested for their impact on Au ion release in different media.

5.2 Results and Discussion

5.2.1 Studying the Ions Release in Different Media

Dissolution expresses the transfer of ions from particles to the surrounding media to form a homogenous ionic solution; dissolution rate expresses the speed of this process (Aziz et al., 2017; Bhatt et al., 2011). The behaviour of gold nanoparticles in different media can be complex and vary based on factors such as nanoparticles size, shape, surface charge, concentration, and media content. Understanding the interactions between nanoparticles and different media is crucial for their successful application in various fields, particularly in biological and biomedical research (Mbanga et al., 2021; Y. Huang et al., 2022).

5.2.1.1 Citrate-Gold Nanoparticles

The dissolution test of this type of citrate gold nanoparticles (20.54 ±0.45 nm) was verified in four different types of media involving, phosphate buffer solution (PBS), 4-(2-hydroxyethyl)-1-piperazineethanesulfonic acid (HEPES) buffer, ultrapure water (Milli-Q 18.8 MΩ-cm), and Dulbecco's Modified Eagle Medium (DMEM) cell culture media. Herein, the dissolution test has been conducted in an incubator at 37°C under moderate stirring at five intervals 0, 6, 12, 24, and 240 hours.

Figure 5.1 shows that there was an increase in the release of gold ions with time, which reached a similar steady state into both PBS buffer solution and ultrapure

water at 0.121 mgL^{-1} and 0.102 mgL^{-1} respectively within 240 hours. The release of ions is due to the interaction between the nanoparticle surface and the buffer solution content. The purpose of performing the release over time studies is to investigate the stability of these nanoparticles in different biological media. For example, a very low release of ions will indicate longer shelf life and more stable nanoparticle formulation (Mbanga et al., 2021).

Figure 5.1 shows that there was a steady increase in the release of the gold ions of citrate-Au NPs 20.54 ±0.45 nm, starting after 6 hours in both ultrapure water (Milli-Q 18.8 MΩ-cm) and PBS buffer solution at concentration of 0.099 mgL^{-1} and 0.98 mgL^{-1}, respectively. The release of these ions continued to reach the concentration of approximately 0.101 and 0.99 mgL^{-1} respectively in the ultrapure water and PBS after 12 hours. Noticeably, within 24 hours, the concentration of the ions in both ultrapure water and PBS buffer solution remained steady at approximately 0.101 mgL^{-1} as end point of gold ions release.

The release of ions from citrate-gold nanoparticles in DMEM cell culture media and HEPES buffer solution was also studied. The final concentration of these ions in DMEM was higher compared to that in HEPES buffer. As shown in **Figure 5.1**, in DMEM, it reaches 0.468 mgL^{-1} after the first six hours followed by approximately 0.588 mgL^{-1} after twelve hours. Then, the released concentration is steadied at roughly 0.732 mgL^{-1} after 240 hours. In HEPES buffer, a significant difference in the release was observed, showing a significantly lower concentration of 0.122 mgL^{-1} after six hours. This increased to 0.232 mgL^{-1} at 12 hours. The final concentration reached was 0.279 mgL^{-1} at 240 hours (**Figure 5.1**). Consequently, the data analysis employing Cronbach's alpha (see Appendix

2, Figure S.1) showed a high level of consistency and reliability, reflected by a Cronbach's alpha value of α = 0.98.

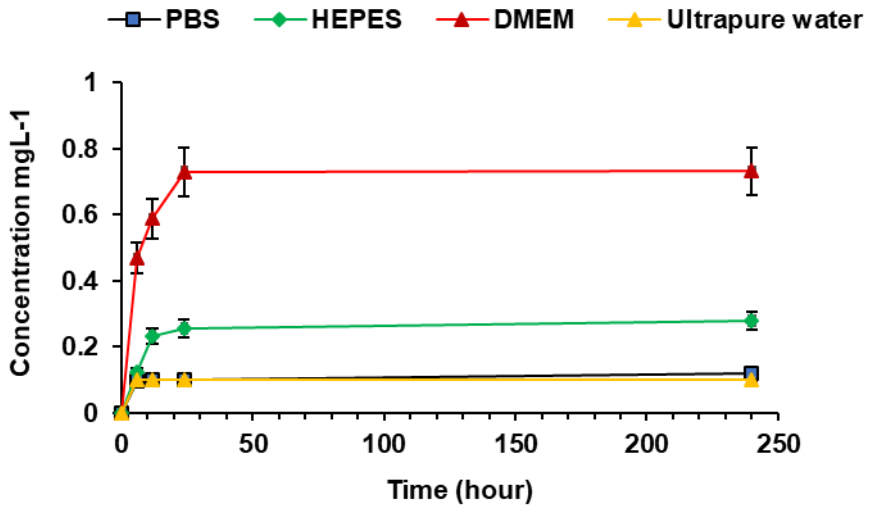

Figure 5.1. ICP-OES measurements of the gold ions release from citrate gold nanoparticles (20.54 ±0.45 nm) in four different media: DMEM cell culture medium, ultrapure water, PBS, and HEPES buffer at pH 7.4. Data was measured and analysed using Cronbach's alpha, showing high level of consistency and reliability at α = 0.98. In the meantime, one-way ANOVA used to measure the significant difference of gold ion release at $P < 0.001$.

5.2.1.2 Polyethylene Glycol-Gold Nanoparticles

Polyethylene glycol (PEG) is widely used in the pharmaceutical industry due to its unique properties, which include prolonged blood circulation time and enhanced drug efficacy (Harris, 1992; Hutanu et al., 2014). Moreover, it has received approval for medical use in drug delivery by the United States Food and Drug Administration (FDA)(U.S. Food & Drug Administration, 2023). PEG can be attached to gold nanoparticles either directly on the surface of the nanoparticles

or through various modification techniques tailored to specific biomedical applications (Mbanga et al., 2021).

The results shown in **Figure 5.2** indicated the release rate of gold ions in four different media PBS, ultrapure water, DMEM, and HEPES buffer. DMEM cell culture medium and ultrapure water, the gold ions started being released after 6 hours at similar concentration 0.090 mgL^{-1}. This increase was continued until reached to 0.093 mgL^{-1} and 0.092 mgL^{-1}, which can be considered as the maximum release that was observed within 240 hours of the release test. This difference in the released concentration may be due to the affinity forces between the gold ions in PEG-AuNPs and the contents of the cell culture media, such as proteins, which can interact and form complexes. In contrast, the interaction of these ions in the ultrapure water may be less noticeable, making it more challenging for PEG-AuNPs to dissolve due to the lower affinity forces in the aqueous environment (Abuchowski, 1977; Padín-González et al., 2022). Furthermore, Deol et al. (2015) have discussed how the behaviour of nanoparticles in cell culture media can be influenced by a range of forces and changes, stemming from their interactions with components within the media, including electrolytes, lipids, and proteins (Deol et al., 2015).

In HEPES and PBS buffers, under similar conditions at pH 7.4, it was observed that the gold ions in PEG-gold nanoparticles were released at concentrations exceeding 0.2 mgL^{-1} in both PBS and HEPES buffers after 240 hours (**Figure 5.2**). These changes may be attributed to the formation of complexes that occur when the nanoparticles interact with the components of the PBS and HEPES buffers, resulting in the detachment from the particle surfaces and their release

in the media (T. Wang et al., 2020; Mulder et al., 2019). However, the release of gold ions in the four different media was compared and shown statistically to have a high consistency at Cronbach's alpha value of α = 0.98 (see appendix 2, Figure S.2).

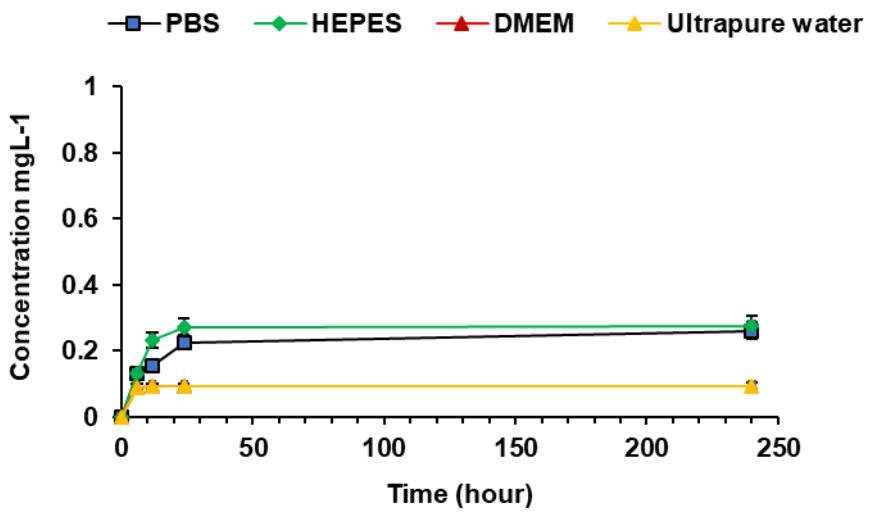

Figure 5. 2. Concentration release test of gold ions measured by ICP-OES for PEG-gold nanoparticles in PBS, ultrapure water, DMEM cell culture medium, and HEPES buffer at pH 7.4. the The data was evaluated using Cronbach's alpha, which demonstrated a high level of reliability and internal consistency with α = 0.98. Additionally, a one-way ANOVA was conducted to assess the significant differences in gold ion release PEG-Au NPs, with results indicating a significance level of $P < 0.05$.

5.2.1.3 Tannic Acid-Gold Nanoparticles

Tannic acid comprises multiple phenol groups that can potentially exhibit a strong affinity for the surface of gold nanoparticles (Ahmad, 2014). The release concentration of gold ions is mainly based on the properties of both gold

nanoparticles and employed media. For example, it has been reported that the more significant release in the presence of DMEM is due to the protein content in this media, whereby proteins attach on the particles potentially displacing tannic acid molecules and then causing the detachment of gold ions from the particles. In other words, the interaction between the tannic acid-gold nanoparticles and the components in the cell culture medium (such as proteins) might lead to the release of gold ions from the nanoparticle surface (P. Wang et al., 2015). Another study by Deol et al., (2015) suggested the dissociation possibility to tannic acid molecules on the surface of gold nanoparticles due to the effect of affinity force of the contents in PBS buffer solution leading to faster release of gold ions at an early stage.

Herein, **Figure 5.3** explains the release rates of gold ions in tannic acid gold nanoparticles in four different media: DMEM cell culture media, ultrapure water, PBS, and HEPES buffer at different time intervals 0, 6, 12, 24, and 240 hours. As shown in **Figure 5.3**, the gold ions in HEPES and PBS commenced releasing after 6 hours, reaching concentrations of approximately 0.098 mgL^{-1} and 0.189 mgL^{-1}, respectively. Importantly, there was a significant difference in the release of the gold ions within the first 6 hours, with the release concentration being approximately two times (2X) higher in the PBS buffer compared to the HEPES buffer. After twenty-four hours, the release concentration of these ions stabilised at about 0.257 mgL^{-1} in both buffers and then slightly increased to 0.274 mg L-1 in HEPES and 0.259 in PBS buffer after 240 hours.

In DMEM cell culture media, the TA-AuNPs began releasing gold ions at a concentration of 0.345 mgL^{-1} after 6 hours. Notably, over 240 hours, the TA-

AuNPs exhibited a significant release of gold ions, reaching a maximum concentration of 0.781 mgL^{-1}, which was the highest compared to other media. On the other hand, in ultrapure water, TA-AuNPs demonstrated the lowest gold ion release concentration, measuring at 0.231 mgL^{-1} after 240 hours. The comparison of gold ion release across the four different media was statistically analysed, showing a good consistency with a Cronbach's alpha value of $\alpha = 0.87$ (see appendix 2, Figure S.3).

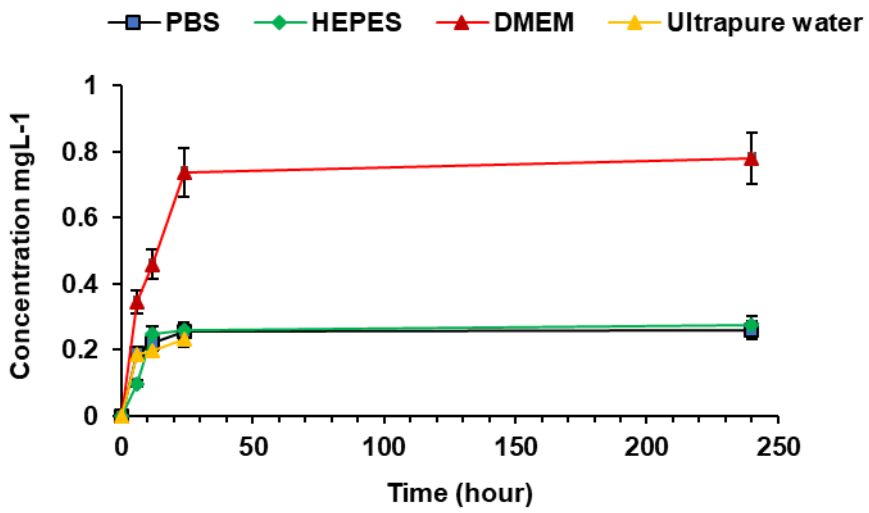

Figure 5. 3. ICP-OES measurements for gold ion release concentration in four different media: DMEM cell culture media, ultrapure water, PBS, and HEPES buffer at pH = 7.4. Cronbach's alpha was utilised to analyse the data, illustrating low consistency with a value of $\alpha = 0.87$. Furthermore, a one-way ANOVA was performed to determine significant differences in gold ion release of TA-Au NPs, yielding a significance level of $P < 0.001$.

5.2.2 Impact of K^+ and Na^+ Ionic Strength on the Surface of Au NPs

A series of concentrations (0.01, 0.05, 0.1, 0.2, 0.3, and 0.5 M) of potassium nitrate (KNO_3) and sodium nitrate ($NaNO_3$) were prepared in ultrapure water (Milli-Q 18.8 MΩ-cm) and mixed with different forms of synthesised gold nanoparticles: TA-Au NPs, cit-Au NPs and PEG-Au NPs at fixed concentration (3.75 mgL^{-1}). The aim of the study was to confirm the suitability of the formulated gold nanoparticles for further functionalisation and conjugation by examining the impact of K^+ and Na^+ ions on the size of gold nanoparticles (García-Garabal et al., 2021). Characterisation involved measuring the particle size using DLS. For example, a negligible increase in size was observed after mixing of gold nanoparticles with KNO_3 and $NaNO_3$ salts at low concentrations (0.01-0.05 M). This may be due to the weak and homogenous impact of ions on nanoparticle's surface. In contrast, at high concentrations (0.1-0.5 M) aggregation of gold nanoparticles was determined due to the strong affinity force of potassium and sodium ions to the surface of gold nanoparticles (Alba-Molina et al., 2017). The nanoparticles aggregated after adsorption of K^+ and Na^+ ions onto their surfaces (**Table 5.1**).

Table 5. 1: The effect of the ionic strength of sodium and potassium ions on gold nanoparticles' size

	Original size (d. nm)	**Mean size (nm) (0.01 M-0.05 M)**	**Mean size (nm) (0.1 M-0.5 M)**
TA- AU NPS ($NANO_3$)	15.11 ±0.64 nm	41.1 ±0.68 nm	90 ±0.76 nm
TA- AU NPS (KNO_3)	15.11 ±0.64 nm	39 ±0.87 nm	110 ±0.89 nm
CIT-AU NPS ($NANO_3$)	20.54 ±0.45 nm	30 ±0.67 nm	200 ±1.43 nm

CIT-AU NPS (KNO_3)	20.54 ±0.45 nm	32 ±1.23 nm	195 ±1.32 nm
PEG- AU NPS ($NANO_3$)	28.41 ±0.43 nm	25 ±0.32 nm	300 ±1.54 nm
PEG- AU NPS (KNO_3)	28.41 ±0.43 nm	21 ±0.92 nm	365 ±1.86 nm

5.2.3 The interaction between Bovine Serum Albumin and Au NPs

Understanding the interaction between citrate-gold nanoparticles (20.54 ±0.45 nm) and bovine serum albumin (BSA) can be regarded as one of the most significant *in vitro* investigations to discover the ability of gold nanoparticles to bind to proteins containing amino acids. This study aims to offer a comprehensive understanding of the binding mechanism between Au NPs and BSA.

The BSA protein molecule comprises 17 cysteine residues, which form eight disulfide (S-S) bonds and one unbound thiol (-SH) group. This unbound thiol can lead to side reactions that modify other functional groups in the protein (Maulik et al., 2009). In **Figure 5.5**, the yellow sphere indicates the location of this unbound thiol within a cysteine residue. However, certain metals can interact with BSA, causing a disruption in the protein's structure by breaking the disulfide bonds (Maulik et al., 2009).

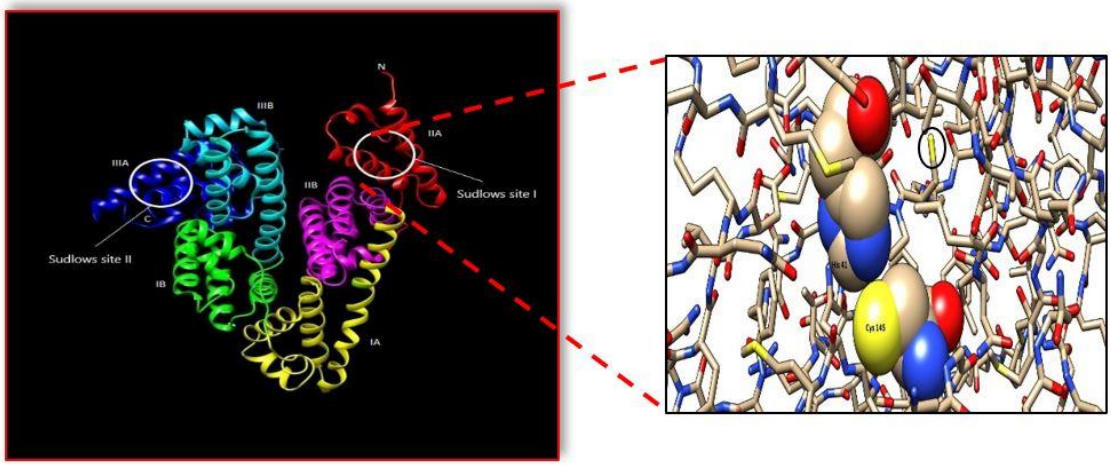

Figure 5. 2. Highlights the bovine serum albumin (BSA) structure (left) and the location of the unbound thiol group (the yellow sphere, right) within the cysteine residue in the structure of bovine serum albumin.

The mechanism of interaction between cit-Au NPs (20.54 ±0.45 nm) and BSA was studied by measuring the particle size (dynamic light scattering) and conducting fluorescence measurements (UV-Vis spectrophotometry to monitor the fluorescence changes upon binding of gold nanoparticles with BSA. For instance, **Figure 5.6** demonstrates that the particle size increased by approximately tenfold (191.1 ±1.6 nm) compared to the original size of the citrate-gold nanoparticles (20.54 ±0.45 nm) before the BSA conjugation. Moreover, a positive correlation coefficient at around 0.83 was observed, indicating that particles size tends to increase as time progresses (**Figure 5.6**).

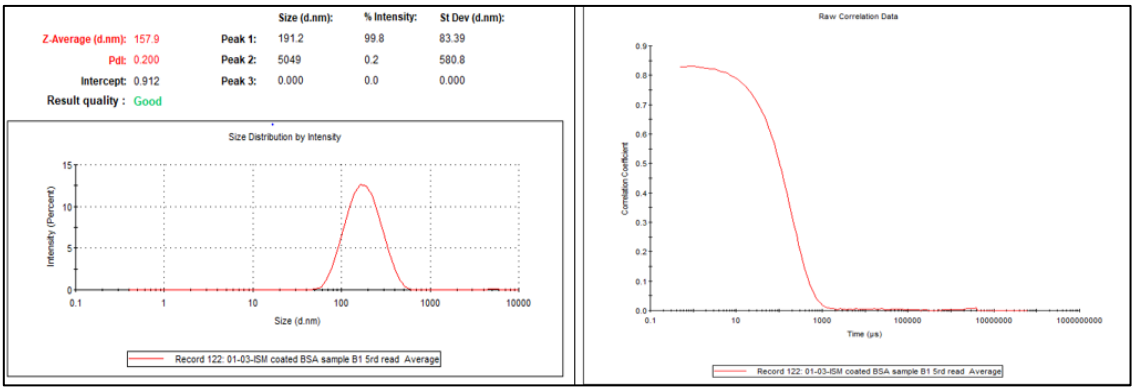

Figure 5. 3. DLS measurements depicts the particle size distribution and correlation data between particle size and time (µs) for BSA-gold nanoparticles.

The zeta potential for the BSA/Au NPs was also measured using DLS. Various concentrations (30, 50, 100, 150, 200 µM) of BSA were applied in this examination of their interaction with a fixed concentration (3.75 mgL^{-1}) of cit-AuNPs (20.54 ±0.45 nm).

The results presented in **Table 5.2** indicate that all measurements of surface charge were outside the critical range of aggregation (-10 mV to +10 mV).

Table 5. 2: Zeta potential measurements for various sizes of BSA/Au NPs:

BSA concentration (µM)	**Zeta potential (mV) BSA/Au NPs**	**STD (mV)**
200 µM	-33.9	±1.3
150 µM	-35.3	±0.9
100 µM	-22.8	±1.7
50 µM	-16.3	±2.1
30 µM	-31.0	±0.8
cit-Au NPs in the absence of BSA (mV)	-33.1	±1.1

The fluorescence measurements for the standard BSA (BSA std.), citrate-gold nanoparticles (20.54 ±0.45 nm) and BSA-gold nanoparticles (BSA/Au NPs) were measured using UV-Vis spectroscopy. The fluorescence intensity of BSA-gold nanoparticles increased by increasing BSA concentration, while the cit-Au NPs are non-fluorescent. This suggests that the interaction of cit-Au NPs with BSA is likely to induce fluorescence due to the presence of tryptophan residues in BSA (Shalaeva et al., 2019) (**Figure 5.7**).

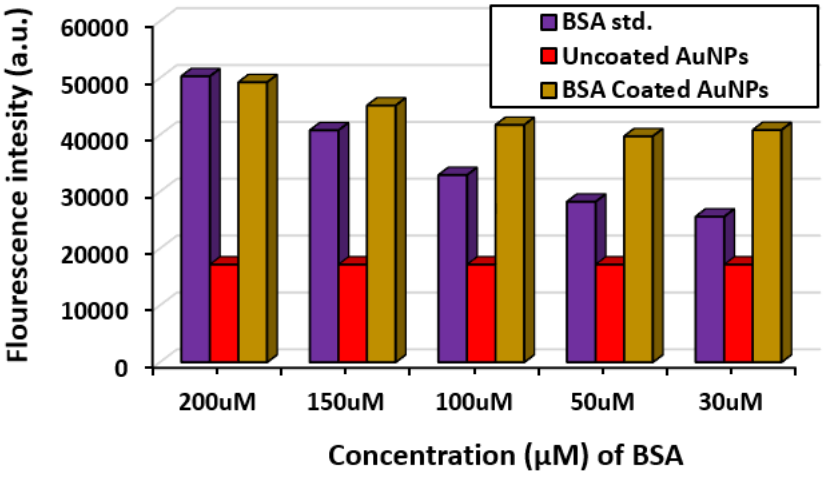

Figure 5. 4. Fluorescence intensity of citrate-gold nanoparticles after interaction with bovine serum albumin measured by the UV-Vis spectrophotometer.

5.2.5 Investigating the Influence of Temperature Control on BSA/Au NPs

Sodium dodecyl sulfate (SDS) can be classified as an anionic surfactant with both electrostatic and hydrophobic properties when interacting with proteins (J. Zhang et al., 2021). This research topic involves the investigation of temperature impact on three types of synthesised gold Au NPs: citrate-gold nanoparticles (cit-AuNPs), SDS-gold nanoparticles (SDS-Au NPs), and SDS-BSA-gold nanoparticles (SDS-BSA-Au NPs). The main reason of this examination is to

study how temperature can significantly impact the structure of BSA. Proteins like BSA have a specific three-dimensional structure that is crucial for their function. At moderate temperatures, the protein might undergo minor alterations, affecting its stability. However, as temperatures rise further, the hydrogen bonds, hydrophobic interactions, and other weak forces that maintain the protein's structure can become disrupted leading to the loss of its function, for example, its ability to bind to other molecules, such as drugs or metal ions. A study by Chodankar et al (2008) reported that the BSA protein can be influenced by temperatures exceeding 60°C, resulting in protein denaturation (unfolding of the protein by breaking the intramolecular bonds) and subsequent aggregation to the nanoparticles.

Herein, the structural changes in Bovine Serum Albumin (BSA) have been measured using a spectrophotometer based on absorbance (Figure 5. 8). These measurements were conducted by controlling the temperature over 360 minutes of the synthesis of nanoparticles. In the beginning, it was observed that all forms of the prepared Au NPs were stable up to 50 minutes. Noticeably, SDS-Au NPs and SDS-BSA-Au NPs exhibited a gradual increase in the absorbance over time and with increasing temperature (**Figure 5.8**). These changes in absorbance at specific wavelengths, typically in the UV range (200-280 nm) are assigned to the changes in BSA's structure, particularly alterations in its aromatic amino acid environments, which can affect its absorption spectra. The results observed in **Figure 5.8** were recorded at various temperatures (e.g., from 0 temperature to elevated temperatures up to 80°C) by measuring the absorbance. **Figure 5.8** illustrates the changes in peak intensities (absorbance) over 360 minutes.

Statically, results were compared with each other by measuring the Cronbach's alpha. The statistical results (appendix 2, figure S.4) showed that SDS-BSA-AuNPs and SDS-AuNPs are not highly correlated with each other with poor consistency at low (α) value = 0.01.

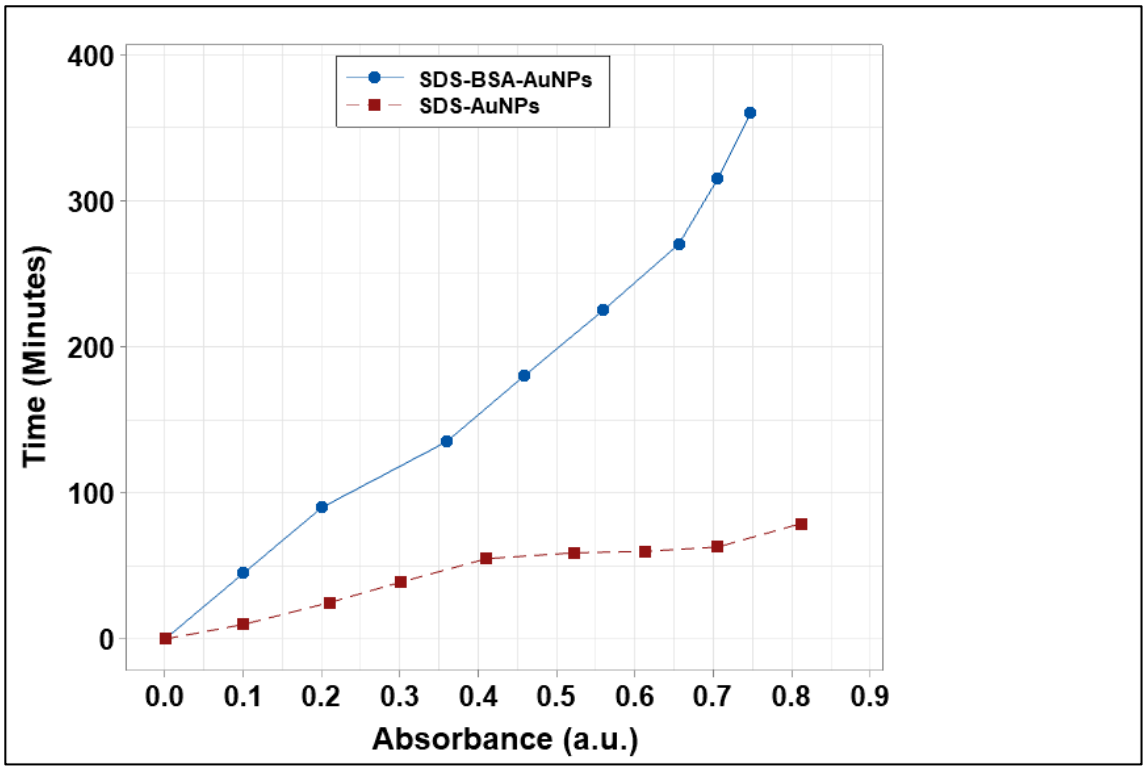

Figure 5. 5. An impact of temperature on the absorbance intensity of dodecyl sodium sulfate-gold nanoparticles (SDS-Au NPs), and SDS-BSA-Au NPs over time, as measured by a UV-Vis spectrophotometer. The data illustrates the dynamic changes in absorbance intensity over time under the effect temperature.

5.2.6 Enhancing the Physicochemical Properties of Au NPs

Gold nanoparticles have been widely used in the development of new diagnostic devices, engineering, and environmental safety. They can be easily functionalised, particularly with thiol-containing compounds, through the

formation of gold-sulfur bonds (Au-S). Herein, three types of thiol-containing compounds, specifically 11-mercaptoundecanoic acid (MUDA), 4-mercaptobenzoic acid (4-MBA), and meso-2,3-Dimercaptosuccinic acid (DMSA), were employed for the functionalisation of citrate-gold nanoparticles (20.54 ±0.45 nm) size. The localised surface plasmon resonance (LSPR) peak shifts of MUDA, 4-MBA, and DMSA-functionalised gold nanoparticles were determined at various wavelengths. **In Figure 5.9**, MUDA/AuNPs displayed well distributed and narrow LSPR peak shift at maximum wavelength 542 nm. Whereas, 4-MBA/AuNPs and DMSA/AuNPs presented as a broadening peak at two maximum wavelengths of 528-645 nm and 540-642nm, respectively.

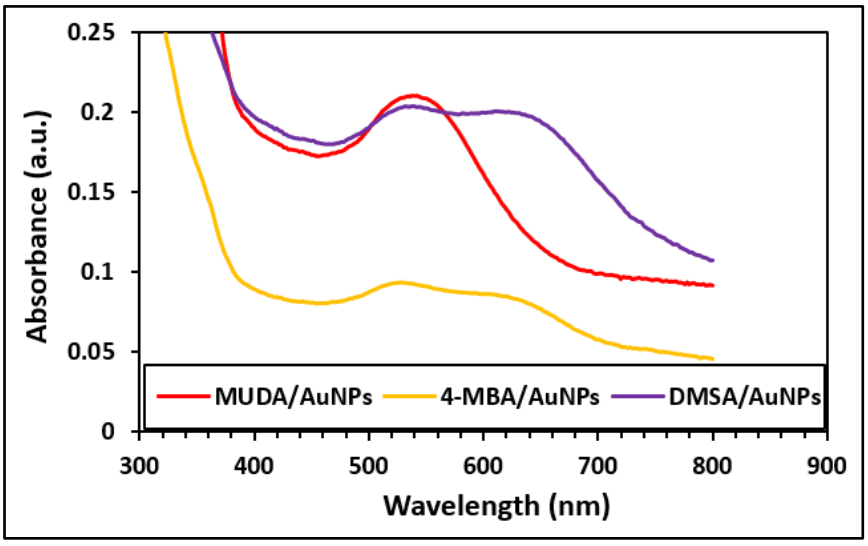

Figure 5. 6. Localised surface plasmon resonance peak shifts of functionalised gold nanoparticles: MUDA/Au NPs, 4-MBA/AuNPs and DMSA/AuNPs at different maximum wavelengths measured by UV-Vis spectrophotometry.

DLS characterisation in **Table 5.3** illustrates the increase in size of Au NPs after each form of functionalisation using MUDA, 4-MBA, and DMSA. A significant size increase for all three different forms of functionalisation: MUDA/AuNPs, 4-

MBA/AuNPs, and DMSA/AuNPs. Additionally, low polydispersity index (PDI) suggests a narrow size distribution of MUDA-functionalised gold nanoparticles, indicating that most of the particles in the sample are homogeneously distributed around a mean value.

Table 5. 3: Gold nanoparticles size distribution, poly dispersity index (PDI), zeta potential and the % loaded amount measurements before and after functionalisation with thiol containing compounds.

Thiol compo-unds	Size before functionalisation	Size after functionalisation	DLS (PDI)	DLS (ζ)	% loaded
11-MUDA	20.54 ±0.45 nm	50.39 ± 0.82 nm	0.260	-27.2	53.9%
4-MBA	20.54 ±0.45 nm	142.67 ± 1.45 nm	0.356	-40.9	37.5%
DMSA	20.54 ±0.45 nm	164.89 ± 1.92 nm	0.428	-50.4	31.5%

5.2.7 Microscopic Examination of Functionalised Gold Nanoparticles

The microscopic imaging was conducted by transmission electron microscopy (TEM) for the synthesised and functionalized gold nanoparticles: cit-Au NPs, MUDA-Au NPs, 4-MBA-Au NPs and DMSA-Au NPs. **Figure 5.10** illustrates an increase in particle size after functionalisation, accompanied by significant morphological changes in the nanoparticles. Notably, severe aggregation was observed when nanoparticles were functionalised with DMSA and 4-MBA thiol compounds. The aggregation observed in the case of 4-MBA/AuNPs is linked to a nucleophilic aromatic substitution (NAS) reaction, which involves the replacement of atoms or groups on an aromatic ring by a nucleophile, breaking

bonds within the molecule (Caron et al., 2003). In contrast, the MUDA/AuNPs exhibited uniform distribution after functionalisation, forming linked chains of nanoparticles. This phenomenon can be attributed to the strong affinity between the thiol group in MUDA and the gold atoms in Au NPs, as depicted in **Figure 5.10**.

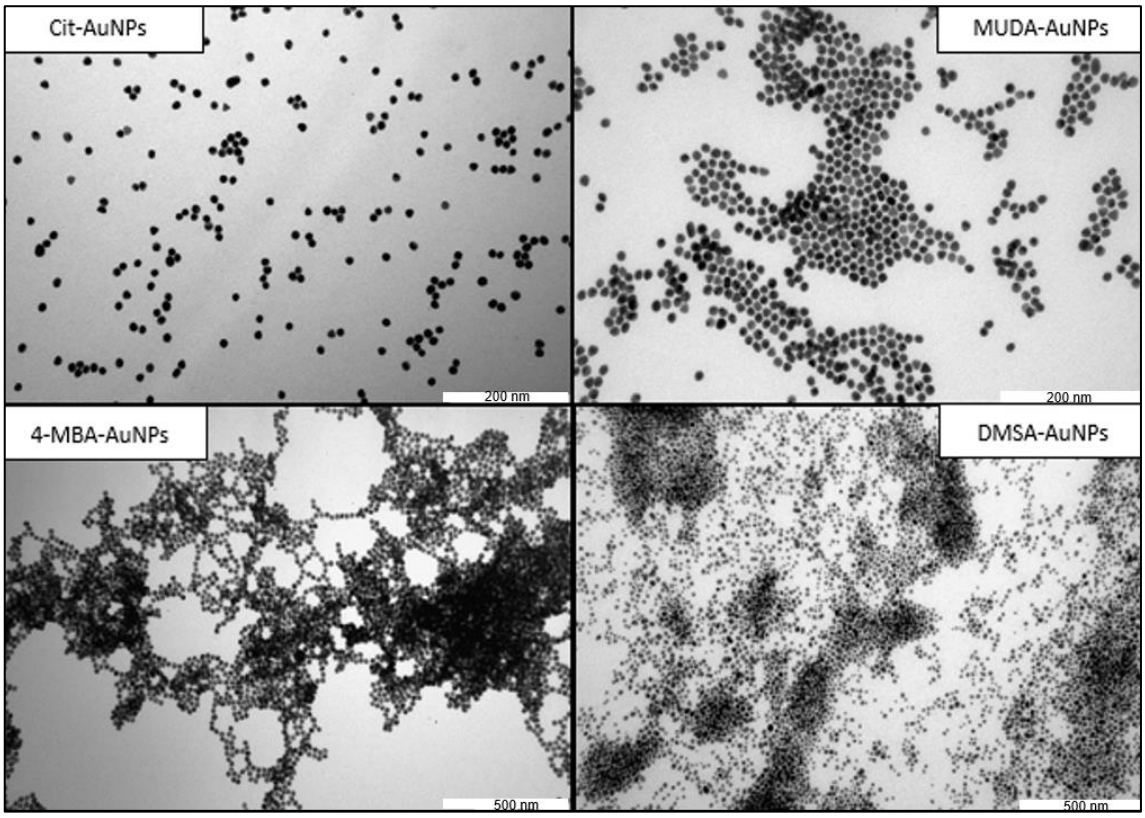

Figure 5. 7. TEM images displaying particle appearance and aggregation state for the synthesised and functionalised gold nanoparticles: cit-AuNPs, MUDA-AuNPs, 4-MBA-AuNPs, and DMSA-AuNPs. The images demonstrated at two different nanoscale bars 200 nm and 500 nm.

5.2.8 Effect of HEPES Buffer on Functionalised Au NPs

HEPES (4-(2-hydroxyethyl)-1-piperazineethanesulfonic acid) buffer is widely employed in numerous biomedical applications because of its unique ability to

maintain stable pH conditions and preserve the integrity of biological samples (Good et al., 1966; Stoll & Blanchard, 1990). In this study, three types of functionalised gold nanoparticles, namely MUDA/Au NPs, 4-MBA/Au NPs, and DMSA/Au NPs, were prepared in HEPES buffer at six different concentrations: 5 mM, 10 mM, 30 mM, 50 mM, 75 mM, and 100 mM. The HEPES buffer displayed minimal changes in particles size for MUDA/Au NPs across the six different concentrations (**Figure 5.11**). These observations can be attributed to the zwitterionic nature of HEPES in relation to MUDA/Au NPs (P. Liu et al., 2023; Taha et al., 2014). Consequently, the particles size distribution of MUDA/AuNPs remained consistently stable, with an average diameter (50.39 ± 0.82 nm). In contrast, 4-MBA/Au NPs displayed varying fluctuations in particle size distribution, especially at 30 mM of HEPES buffer solution.

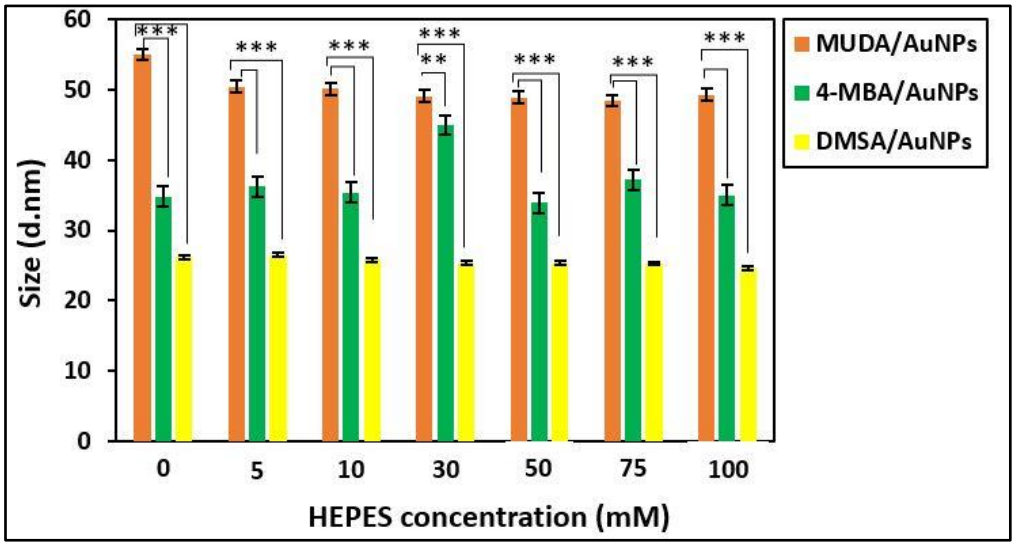

Figure 5. 11. Impact of the HEPES buffer solution (5 mM, 10 mM, 30 mM, 50 mM, 75 mM, and 100 Mm) on the functionalised gold nanoparticles: MUDA/AuNPs, 4-MBA/AuNPs, and DMSA/AuNPs. The variation was measured and compared with MUDA-cit-Au NPs by one-way ANOVA and it was found significant at ***P < 0.001.

5.3 Conclusions

This chapter involved the investigation of the physicochemical properties of synthesised and functionalised gold nanoparticles by measuring the concentration release of gold ions in various media, including DMEM cell culture media, PBS, HEPES, and ultrapure water (Milli-Q 18.8 MΩ-cm). All results were statistically compared by measuring the Cronbach's alpha or coefficient alpha (α) to indicate their consistency. For example, both cit-AuNPs (20.54 ±0.45 nm) and PEG-AuNPs (28.41 ±0.43 nm) showed a high consistency of data analysis at α values 0.98. Whereas the data analysis for TA-AuNPs (15.11 ±0.64 nm) show a good consistency with a Cronbach's alpha value of α = 0.87. Additionally, the coefficient alpha (α) has been used to analyse the correlation between the functionalisation of AuNPs with the anionic surfactant sodium dodecyl sulfate (SDS) and bovine serum albumin (BSA). It was found that SDS provides more stability for Au NPs than BSA particularly at higher temperatures up to 80°C. This relates to how temperature can significantly impact the structure of bovine serum albumin (BSA) leading to disruption of the hydrogen bonds in its structure. The Cronbach's alpha data analysis indicated that SDS-BSA-AuNPs and SDS-AuNPs are not highly correlated with each other at lower consistency with Cronbach's alpha (α) value 0.01.

Often, gold nanoparticles are functionalised with ligands or molecules carrying different surface charges. These ligands or molecules provide stability for gold nanoparticles. In some cases, adsorbed ions can influence the surface charge and reactivity of the nanoparticles leading to their aggregation. For example, ions can promote nanoparticle aggregation by reducing the electrostatic repulsion

between particles. Therefore, in this chapter, the impact of the ionic strength of Na^+ and K^+ ions was also studied. It was found that at high concentrations (0.1-0.5 M) of these ions, the electric double layer around particles was suppressed, leading to the formation of aggregated nanoparticles.

Other compatibility studies were also conducted on the functionalised gold nanoparticles: MUDA-cit-AuNPs,4-MBA-cit-AuNPs, and DMSA-cit-Au NPs. This study includes the interaction of the thiol group in the thiol containing compounds MUDA, 4-MBA, and DMSA with gold atoms in cit-Au NPs (20.54 ±0.45 nm), resulting in the formation of a strong gold-sulfur (Au-S) bonds. Furthermore, the TEM microscopic images showed that both 4-MBA/AuNPs and DMSA/Au NPs were significantly influenced by HEPES buffer (100 mM), in contrast to MUDA-cit-AuNPs, which maintained well-defined particle size distribution and is thus highly compatible for drug conjugation. Furthermore, the UV-Vis spectroscopy examination displayed well distributed and narrow LSPR peak shift at maximum wavelength 542 nm for MUDA-cit-AuNPs, whereas, 4-MBA-cit-AuNPs and DMSA-cit-AuNPs presented as a broadening peak at two maximum wavelengths of 528-645 nm and 540-642nm, respectively.

In summary, the selection of citrate-gold nanoparticles (20.54 ± 0.45 nm) for functionalisation and further conjugation with amantadine (AMTD) and remdesivir drugs was determined based on their unique properties. These nanoparticles serve as an optimal platform for effective drug conjugation.

Chapter (6): Cellular Uptake and Cytotoxicity

6.1 Introduction

Nanotechnology has experienced rapid development, particularly in the delivery of medicines for treating various diseases and for diagnostic purposes. This progress is attributed to a large extend on the development of nanomaterials, and their exceptional and effective properties resulting from operating at the nanoscale (Patra et al., 2018). For instance, current applications of gold nanoparticles involve imaging, diagnostics, drug delivery systems, food safety, and cosmetics (Kaul et al., 2018; Rastogi et al., 2021).

Nanomaterials, however, may also exhibit distinct toxic effects, whether on human organ systems or other living cells. Therefore, this study centres on the biological impact of formulated and drug-conjugated gold nanoparticles, specifically on J774 cell line macrophages, representing immune cells.

The toxicity mechanism of nanoparticles can be understood through the production of excess reactive oxygen species (ROS). For instance, Sharifi et al., (2012) proposed that one of the toxicity mechanisms of nanoparticles involves the formation of $COOH^{\bullet}$ and $OH^{\bullet}$ radicals through the reduction of hydrogen peroxide (H_2O_2) via the Fenton reaction. It was reported that during this reaction, damage to cell biological membranes occurs due to high levels of ROS. This may result in alterations to protein structure, DNA disruption, interference with biological functions, or undesirable gene mutations, ultimately culminating in cell death (Sharifi et al., 2012). However, this type of reaction varies from one nanoparticle (NPs) to another depending on their ability to reach mitochondria (Jin et al., 2021). Thus, ROS levels play a crucial role in inducing toxicity in cells. N. Li et al (2008) described that low levels of ROS stimulate the defence genes,

whereas higher levels of oxidative stress can lead to the activation of inflammation genes, resulting in mitochondrial DNA damage. Conversely, the toxicity of targeted cell tissues can be influenced by various factors, including nanoparticle size, shape, surface charge, composition and coating. This chapter will present an in-depth investigation of cellular uptake and the comprehensive evaluation of toxic effects induced by the formulated and conjugated gold nanoparticles. The toxicity assessment encompassed the utilisation of two toxicology assays, including 1-(4,5-Dimethylthiazol-2-yl)-3,5-diphenylformazan (MTT) and Sulforhodamine-B (SRB).

6.2 Cellular Uptake

6.2.1 Results and Discussion

6.2.1.1 Cellular Uptake Utilising J774 Cell Line Macrophages

J774 cell line macrophages have been considered as an ideal model for establishing macrophage functions *in vitro* (Lam et al., 2009). Cellular uptake can be influenced by factors such as particle size, concentration, incubation time, or cell type (Augustine et al., 2020).

6.2.1.2 Evaluating Cellular Uptake: Au NPs with Citrate, PEG, and TA Coatings

The impact of the synthesised citrate, PEG, and TA-gold nanoparticles on cellular uptake using J774 cell line macrophages was investigated, considering various factors such as surface charge, shape, and size (Kettler et al., 2014; Petithory et al., 2021). Firstly, two different sizes, 15 and 30 nm of citrate-gold nanoparticles were introduced into J774 cells seeded in a 6-well plate and incubated at 37°C with 5% CO_2 for 48 hours. Subsequently, the cells were washed with phosphate-buffered saline and fixed with 2 ml of 2.5% glutaraldehyde prepared in 0.1 M phosphate-buffered saline (PBS) at room temperature. Following cell sectioning, TEM imaging was employed to investigate the intracellular uptake of these synthesised NPs.

The size of citrate-gold nanoparticles can significantly influence the cellular uptake into macrophages. Generally, smaller nanoparticles tend to be internalised more readily compared to larger ones due to several factors such as surface area to volume ratio. For example, smaller nanoparticles have a higher

surface area to volume ratio, which facilitates better diffusion and penetration through cell membranes. This enhanced surface area allows for more interactions with the cell membrane, aiding in cellular uptake. As can be seen in **Figure 6.1**, TEM images shown that nanoparticles with a small size of 15 nm interacted with the cell membrane of the macrophages leading to their internalisation within cell vesicles. In addition, nanoparticles with 30 nm size were also internalised, potentially at slower rates. Notably, the cellular uptake mechanisms can be size-dependent, as well as dependent on the surface properties of nanoparticles, or the biological environment.

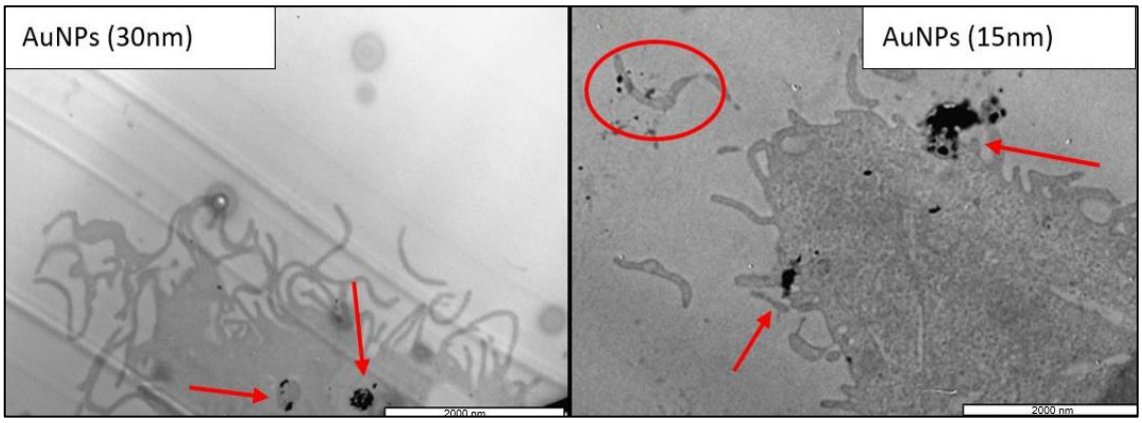

Figure 6. 1. TEM images illustrate the interaction and internalisation of 15 nm and 30 nm cit-Au NPs into J774 cell line macrophages. The red arrows indicate the location of nanoparticles at the cell membrane and inside the cell vesicles. The cellular uptake of these nanoparticles imaged at nanoscale bar 2000 nm.

Herein, J774 cell macrophages were also exposed to two different concentrations (1 mgL^{-1} and 6 mgL^{-1}) of three types of prepared gold nanoparticles: citrate-gold nanoparticles (20.54 ±0.45 nm), PEG-gold nanoparticles (28.41 ±0.43 nm), and TA-AuNPs (15.11 ±0.64 nm). The surface coating of nanoparticles plays a crucial

role in their cellular uptake, influencing how they interact with biological systems. Surface coatings can affect the physicochemical properties of nanoparticles, determining their stability, biocompatibility, and ability to interact with cell membranes. Polyethylene glycol, trisodium citrate, and tannic acid reagents were applied to gold nanoparticles, which were subsequently introduced (1 and 6 mgL^{-1}) into the cells and incubated for 24 hours at 37˚C with 5% CO_2 under similar conditions. As depicted in **Figure 6.2**, PEG-gold nanoparticles, and citrate-gold nanoparticles were observed to be entirely internalised into J774 cell vesicles at both concentrations of 1 mgL^{-1} and 6 mgL^{-1}. Whereas, the tannic acid-nanoparticles showed a low cellular uptake, particularly at 6 mgL^{-1}. The cellular uptake of gold nanoparticles at different concentrations can have distinct effects on the internalisation process by cells. At a lower concentration, such as 1 mgL^{-1}, the number of gold nanoparticles available for uptake by cells is comparatively limited. Therefore, cells will encounter fewer nanoparticles in their vicinity, resulting in a slower rate of internalisation. With a higher concentration of 6 mgL^{-1}, there's a greater abundance of gold nanoparticles in the surrounding environment of the cells. This will provide more nanoparticles for potential interaction with the cells, leading to higher rates of internalisation (**Figure 6.2**).

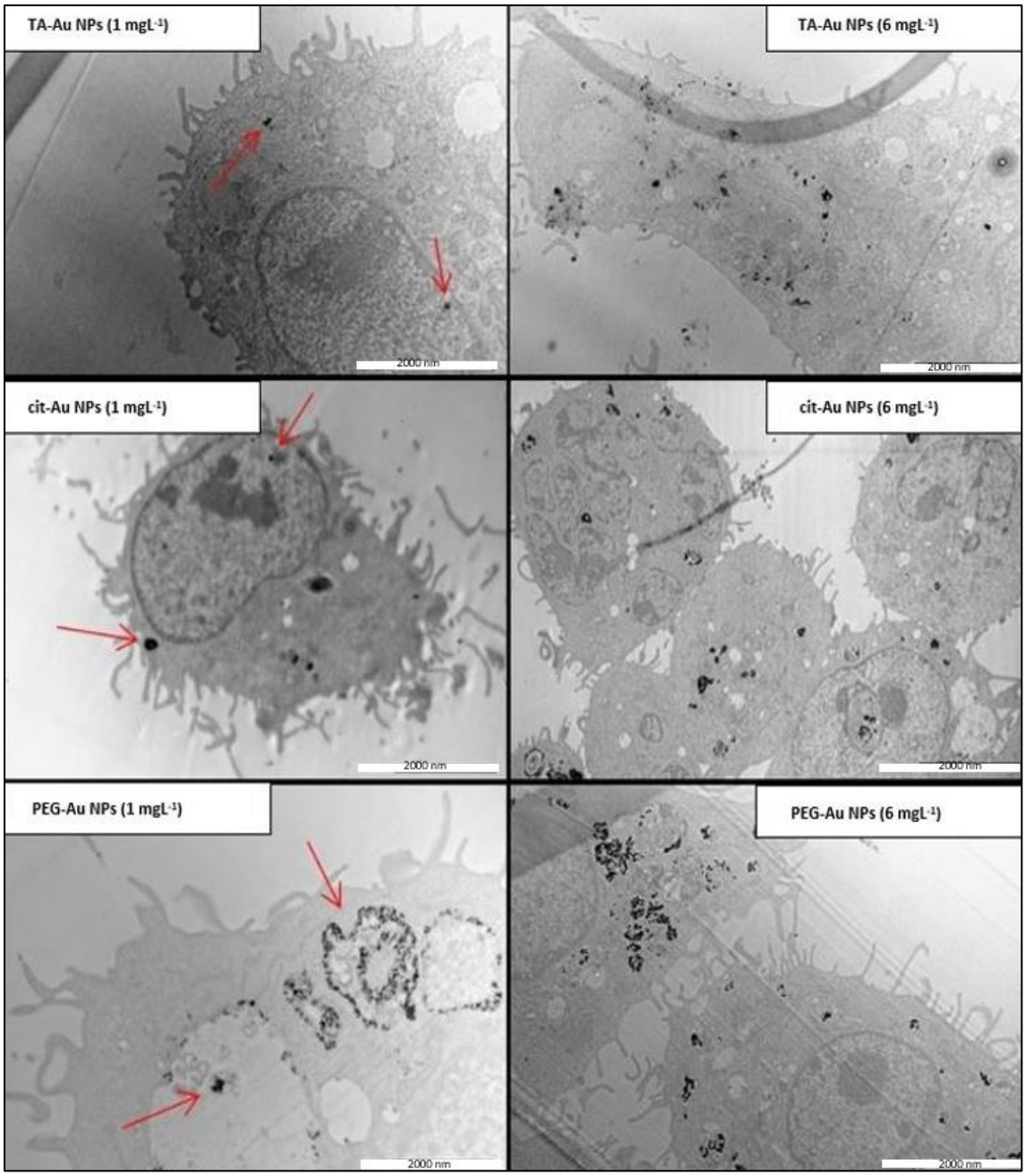

Figure 6. 2. TEM images at nanoscale bar 2000 nm, depict the cellular uptake of three forms of coated gold nanoparticles: tannic acid gold nanoparticles (TA-Au NPs), citrate gold nanoparticles (cit-Au NPs), and polyethylene glycol gold nanoparticles (PEG-Au NPs) introduced into J774 cell line macrophages at two different concentrations (1 mgL^{-1} and 6 mgL^{-1}). Red arrows presenting the accumulation of Au NPs inside the macrophage cells.

6.2.1.3 Cellular Uptake of Amantadine (AMTD)-Conjugated Gold Nanoparticles

Most therapeutic pharmaceuticals must be effective, particularly in targeting infected cells (Zhao et al., 2020). One major challenge in cell-targeted therapeutics is the lack of cell selectivity (Y. Wu et al., 2022). Consequently, efforts have been made in the development of drug delivery systems to overcome these limitations by precisely controlling the delivery of medicines to specific sites without adversely affecting normal cells (Mitragotri et al., 2014).

The transportation of foreign nanoparticles into the body can be considered challenging due to the reticuloendothelial system (RES) (Gunatillake et al., 2003). The RES is a network of cells or tissues that play a crucial role in the immune system in the clearance of foreign substances (Baas et al., 1994). In this study, the transmission electron microscopy (TEM) investigation of amantadine conjugated to Au NPs in **Figure 6.3** showed that gold nanoparticles were completely internalised into vesicles within cell macrophages. The larger particles surrounding the cell macrophages appeared to correspond to the drug molecules, which were released due to the action of specific enzymes present in the intracellular environment. For instance, cell macrophages produce enzymes within the intracellular environment that trigger the release of the drug by cleaving certain bonds in the nanoparticle structure, leading to drug release (Cao et al., 2019; M. Zhang et al., 2021).

The mechanism of delivery is not yet fully understood; however, Bahrami et al (2017) described the ligand-receptor interaction. Ligands attached to nanoparticles have an affinity to bind to targeted cells through ligand-receptor

interactions. Subsequently, the drug is released at these targeted cells, allowing nanoparticles to become free and bind with proteins, making them recognisable by phagocytic cells. This recognition facilitates the clearance of nanoparticles out of the body (Song et al., 2014).

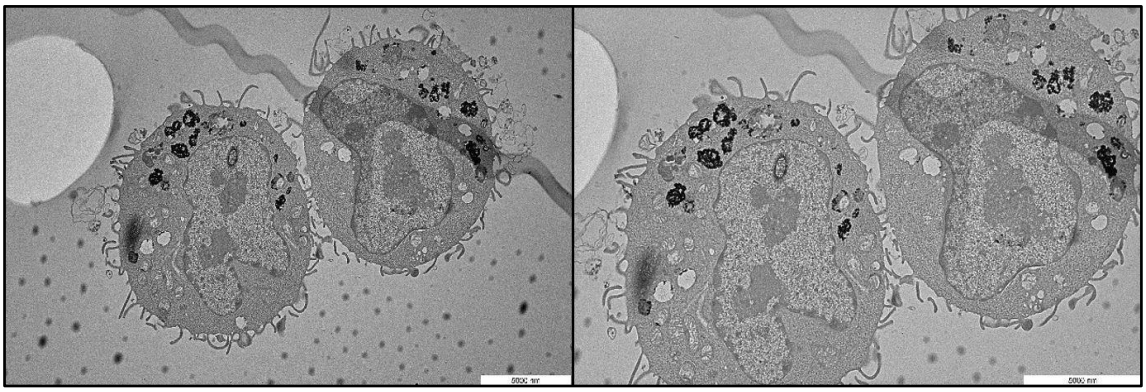

Figure 6. 3. TEM microscopic images demonstrating cellular uptake of the amantadine conjugated Au NPs at two different magnifications (scale bar 5000 nm.)

6.2.1.4 Cellular Uptake of Remdesivir (REM)-Conjugated Gold Nanoparticles

Remdesivir has been classified as an inhibitor of RNA-dependent viruses, particularly capable of inhibiting the viral activity of SARS-CoV (Gordon et al., 2020). Understanding the clinical effectiveness of remdesivir necessitates an assessment of its uptake and intracellular conversion into the active antiviral agent known as GS-441524 triphosphate. As depicted in **Figure 6.4**, the cellular absorption of remdesivir is evident and diminished. Various factors can influence the cellular uptake of remdesivir, whether extracellular or intracellular. Research indicates that under hypoxic and inflammatory conditions, the cellular uptake of

remdesivir may decrease due to a reduction in the expression of adenosine transporters (Rasmussen et al., 2021). Extracellular and intracellular adenosine levels during critical illnesses, has the potential to competitively delay the cellular uptake rate and phosphorylation of the remdesivir drug molecule.

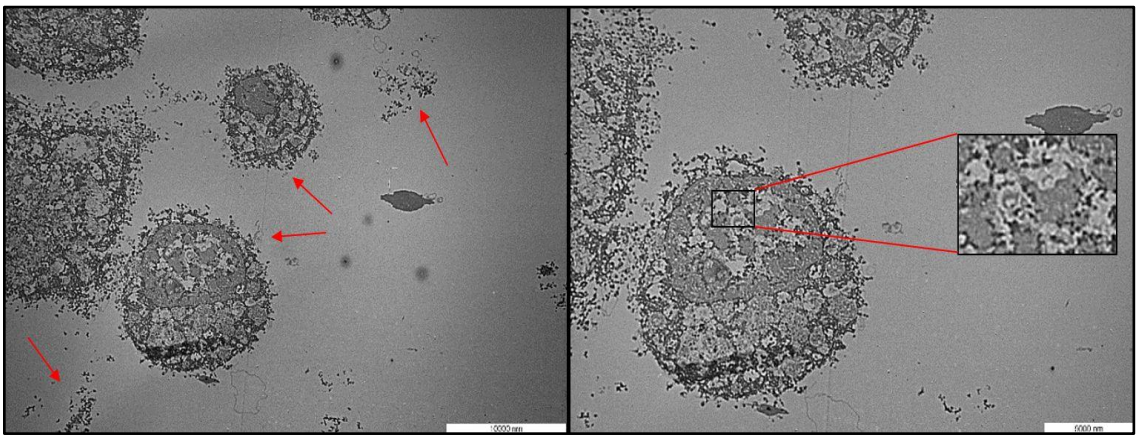

Figure 6. 4. TEM microscopic images illustrating the cellular uptake of remdesivir (REM)-conjugated to gold nanoparticles. The red arrows highlight the accumulation of nanoparticles at the cell membrane of JJ7 cell line macrophages.

6.3 In Vitro Approaches to Cytotoxicity Testing

Toxicity evaluation of nanoparticles is crucial, whether conducted *in vitro* or *in vivo* (Kus-Liśkiewicz et al., 2021). In this study, J774 cell line macrophages were employed to assess the toxicity effects of formulated and drug-conjugated gold nanoparticles. Two different toxicity assays, including 1-(4,5-Dimethylthiazol-2-yl)-3,5-diphenylformazan (MTT) and sulforhodamine B (SRB), were utilised to ensure accuracy and generate reliable results.

6.3.1 MTT Assay

The MTT assay, also known as the 1-(4,5-Dimethylthiazol-2-yl)-3,5-diphenylformazan assay, is used to assess the cytotoxicity of gold nanoparticles (Chapter 2, Section 2.5.3.1). The test measures the insoluble formazan generated by the mitochondria in viable cells (Vijayakumar & Ganesan, 2012). Herein, various formulations of synthesised and drug conjugated Au NPs: citrate-gold nanoparticles (20.54 ±0.45 nm, 40.59 ±0.83 nm, and 60.67 ±0.71 nm), PEG-gold nanoparticles (28.41 ±0.43 nm), TA-AuNPs (15.11 ±0.64 nm), AMTD/AuNPs (160 nm), and REM/AuNPs (165 nm) were employed for toxicity assessment.

Figure 6.5 depicted the effects of two distinct sizes, 40.59 ±0.83 nm and 60.67 ±0.71 nm, of citrate-gold nanoparticles on J774 cell macrophages. It was observed that at approximately 15 μgL^{-1}, roughly half of the total macrophage cell population experienced cell death, especially when exposed to nanoparticles of larger size (60.67 ±0.71 nm). Conversely, fewer than 40% of cells were killed due to the toxicity induced by nanoparticles of 40.59 ±0.83 nm size. Upon analysing the statistical variation between these sizes, a significant difference in toxicity effects was observed at the concentration of 15 $\mu g\ L^{-1}$, with a reported p-value of 0.162. However, Carnovale et al. proposed that existing literature does not provide clear evidence to solely attribute toxicity dependency to nanoparticle size (Carnovale et al., 2019).

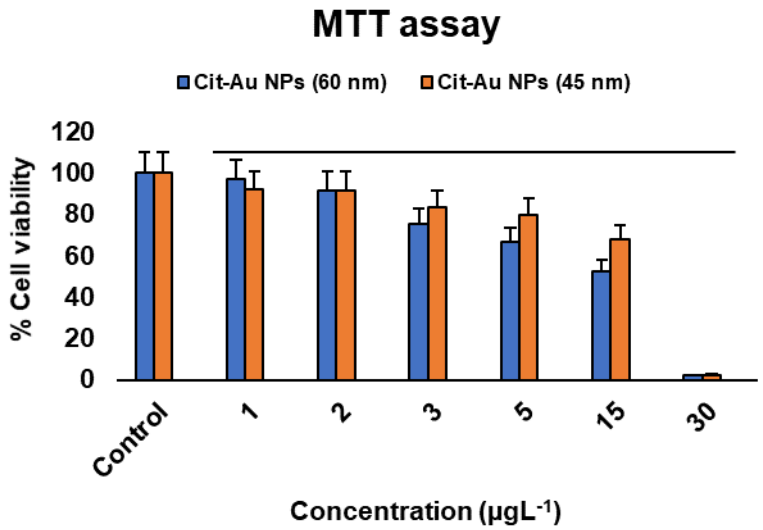

Figure 6. 5. MTT assay measurements for citrate-gold nanoparticles of two different sizes, 60 nm and 45 nm. A one-way ANOVA was used to assess the differences in variation relative to control cells. The toxic effects observed showed a significant difference, with a ***P value < 0.001.

In **Figure 6.6**, the toxicity effect of three coatings, citrate, PEG, and TA, was investigated using the MTT assay. The impact of various coatings on gold nanoparticles (Au NPs) can significantly influence their interaction with cell macrophages and subsequent toxicity. They can alter the physicochemical properties of nanoparticles, inducing their cytotoxic effects. Whereas biocompatible coatings can reduce the interactions between nanoparticles and cellular components, potentially lowering cytotoxic effects.

Citrate-gold nanoparticles (20.54 ±0.45 nm) exhibited the lowest level of toxicity among the various coatings, notably at a concentration of 5 μgL^{-1}. The maximum toxicity effect was observed at 30 μgL^{-1} where about 70% of the cells were killed. In contrast, PEG-gold nanoparticles (28.41 ±0.43 nm) and TA-gold nanoparticles

(15.11 ±0.64 nm) displayed high levels of toxicity effects. Macrophage cells exhibited an over 80% impact in terms of toxicity at a concentration of 15 μgL^{-1}(**Figure 6.6**). The observed toxic effects displayed significant variation, as indicated by a P value < 0.001. These results are supported by various studies in the literature, highlighting that citrate-gold nanoparticles larger than 10 nm are typically safe, non-toxic, and suitable for medical applications at low concentrations, as outlined by Boldeiu et al. (2019), Freese et al. (2012), and Vishwakarma et al. (2010).

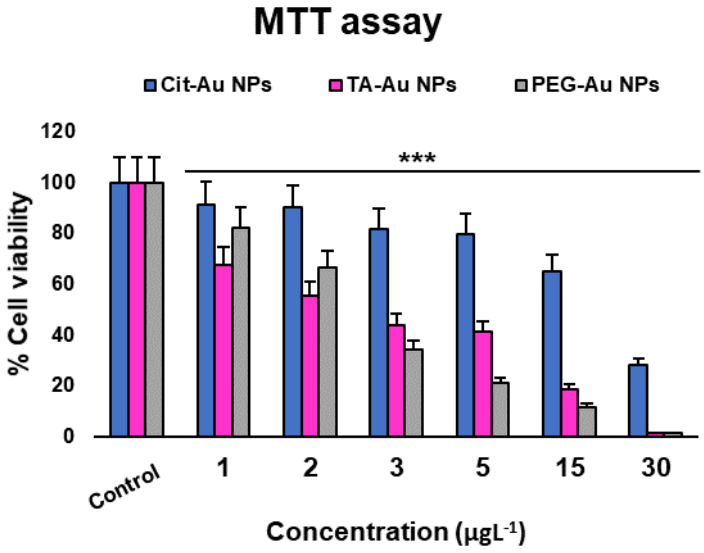

Figure 6. 6. MTT assay measurements for gold nanoparticles with various coatings including, citrate (cit) (20.54 ±0.45 nm), polyethylene glycol (PEG) (28.41 ±0.43 nm), and tannic acid (TA) (15.11 ±0.64 nm). One-way ANOVA utilised to measure the variation compared to control or untreated cells. The observed toxic effects displayed significant variation, as indicated by a ***P value < 0.001.

Moreover, the toxicity impact of the drug conjugated to gold nanoparticles on J774 cell line macrophages was measured using the MTT assay. In **Figure 6.7**, when amantadine was administered alone, it exhibited high toxicity to cell macrophages, particularly at a concentration of 5 μgL^{-1}, where over 50% of cells were adversely affected and killed. However, this toxicity was notably reduced to less than 20% when amantadine was conjugated with Au NPs. Therefore, it is evident that modifying nanoparticles with the amantadine drug significantly reduced its toxicity. This observation aligns with the research conducted by De Jong & Borm (2008), which demonstrated that the conjugation of drug molecules to nanoparticles resulted in a notable reduction in the toxicity and associated side effects of these therapeutic agents.

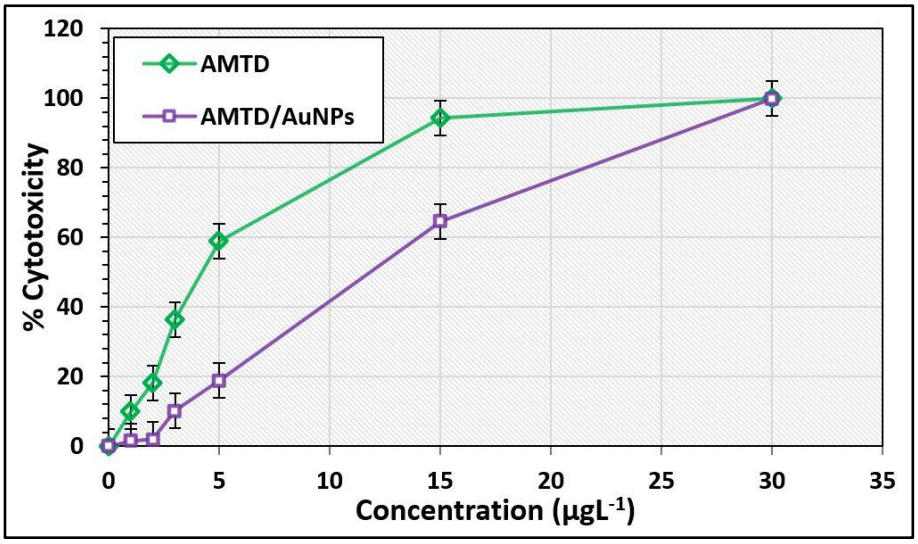

Figure 6. 7. Comparative toxicity impact of amantadine when used alone and when conjugated to gold nanoparticles on cell macrophages. The measurement was conducted using the MTT assay.

The conjugation of remdesivir to gold nanoparticles (REM/AuNPs) demonstrated a notable reduction in toxicity effects. At a concentration of 5 μgL^{-1}, both REM (used alone) and REM/AuNPs exhibited significant toxicity, affecting more than 50% of cells, resulting in reported cell death (**Figure 6.8**). Consequently, based on the obtained results, it can be assumed that AMTD/AuNPs were comparatively less toxic than REM/AuNPs at a similar dose (5 μgL^{-1}) under equivalent conditions. However, toxicity represents a complex field that demands comprehensive assessment, and it cannot be assessed by only one type of cell because some cells show high sensitivity to a certain type of nanoparticles while others do not (Freese et al., 2012).

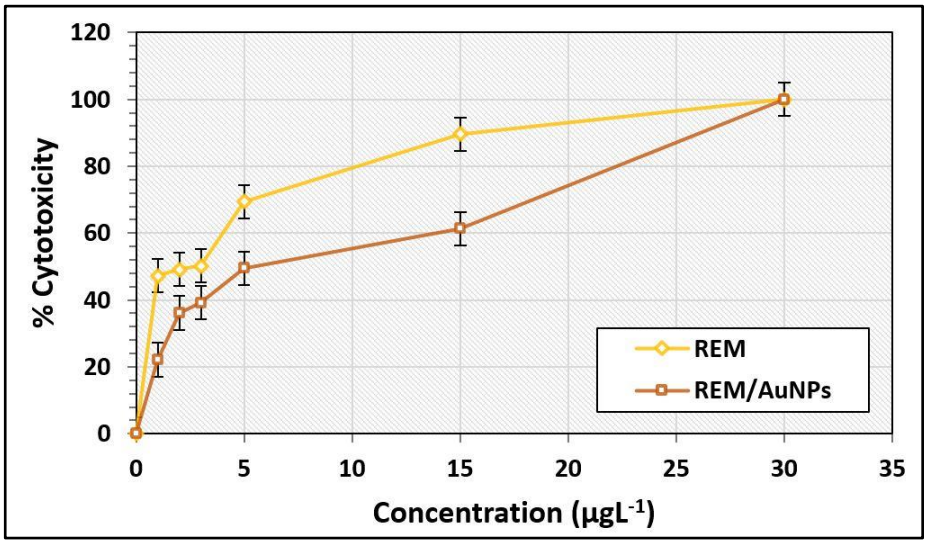

Figure 6. 8. Toxicity effects of the remdesivir (REM) drug and its conjugation form REM/AuNPs, evaluated using the MTT assay.

6.3.3 Sulforhodamine-B (SRB) Assay

This assay is primarily used to measure cell density to assess cell proliferation or cytotoxicity. The assay is based on the binding of SRB, a bright-pink

aminoxanthene dye, to cellular proteins under mild acidic conditions (Chapter 2, Section 2.5.3.2). Herein, SRB assay was applied to determine the inhibition of cell proliferation rate (% cell viability) of both remdesivir, and amantadine drugs conjugated to citrate-gold nanoparticles (20.54 ±0.45 nm). Data was analysed based on measuring the absorbance at specific wavelength 540 nm for the SRB dye.

$$\text{The \% cell viability} = \frac{\text{OD of the treated cells}}{\text{OD of the controlled cells}} \times 100$$

This equation was employed to quantify the impact of REM/AuNPs and AMTD/AuNPs on cell viability or proliferation. However, the cytotoxicity concentration (CC_{50}) represents the concentration of a substance required to reduce cell viability by 50% compared to untreated control cells. In **Figure 6.9**, it can be observed that the cell proliferation rate for REM/AuNPs was significantly reduced particularly at concentration (2.8 μgL^{-1}), which can be indicated as the cytotoxicity concentration required to reduce cell viability by 50%.

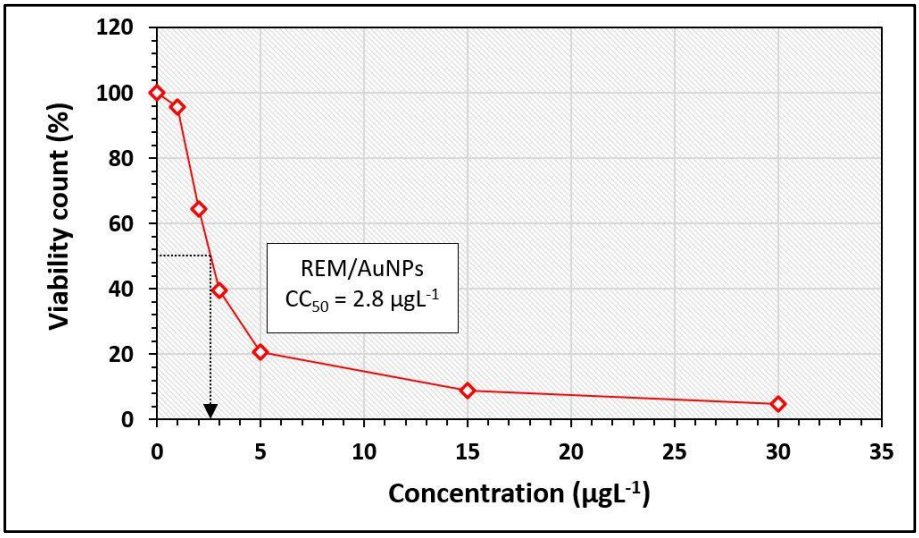

Figure 6. 9. Measuring the cytotoxicity concentration (CC_{50}) required to reduce the cell viability by 50% for REM/AuNPs, as determined by Sulforhodamine-B (SRB) assay.

On the other hand, AMTD/AuNPs have been indicated with concentration toxicity (CC_{50}) at 4.5 μgL^{-1} (**Figure 6.10**). This means that AMTD/AuNPs has lower levels of toxicity effect on the J744 cell macrophages compared to REM/AuNPs. In other words, the results in SRB assays indicated that J774 cell macrophages exhibited lower sensitivity to amantadine drug-conjugated gold nanoparticles compared to remdesivir-conjugated gold nanoparticles. This observation could be linked to differences in drug potency.

In summary, as mentioned above the main purpose of this toxicity assay is to determine the cytotoxicity concentration (CC_{50}), which indicated the potency of each drug-NPs conjugates at 2.8 μgL^{-1} and 4.5 μgL^{-1} for REM/AuNPs and AMTD/AuNPs, respectively.

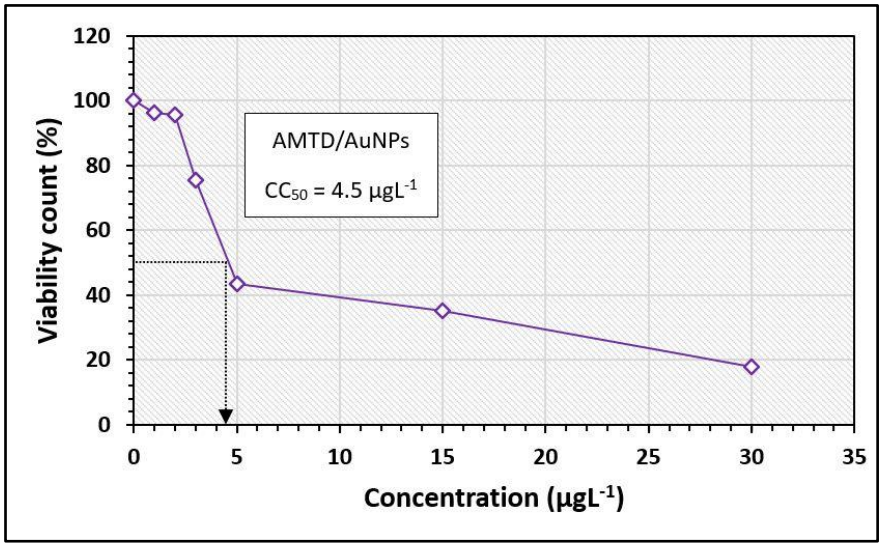

Figure 6. 10. Cytotoxic concentration (CC50) measurement for amantadine-conjugated gold nanoparticles (AMTD/AuNPs) determined by the SRB assay.

6.4 Conclusions

In this chapter, the cellular uptake and toxicity effects of various forms of synthesised and drug conjugated gold nanoparticles including citrate-gold nanoparticles, TA-gold nanoparticles, PEG-gold nanoparticles, REM/AuNPs, and AMTD/AuNPs were investigated based on several factors such as size, shape, ligands attached on the surface of gold nanoparticles.

The cellular uptake of these nanoparticles was investigated by TEM imaging. Citrate-gold nanoparticles with smaller size (15 nm) tend to be internalised to cell macrophages more readily compared to larger ones (30 nm) due to their high surface area. The cellular uptake for other coated-gold nanoparticles such as PEG-AuNPs and TA-AuNPs was microscopically investigated using TEM. The results showed that PEG-gold nanoparticles (28.41 ±0.43 nm) were observed to be entirely internalised into J774 cell vesicles at both concentrations of 1 mgL^{-1} and 6 mgL^{-1}. Whereas, TA-gold nanoparticles (15.11 ±0.64 nm) showed a low cellular uptake, particularly at 6 mgL^{-1}. It was observed that the cellular uptake of gold nanoparticles varies depending on their concentration. Notably, at a lower concentration (1 mgL^{-1}), there was fewer gold nanoparticles around the cell macrophages. Consequently, cells encounter a limited number of nanoparticles nearby, leading to a slower internalisation process. In contrast, higher

concentration (6 mgL^{-1}) results in a greater number of nanoparticles surrounding the cells, leading to a faster rate of internalisation.

The cellular uptake for drug-conjugated nanoparticles, it is hypothesised that the release of amantadine drug molecules occurs due to the action of specific enzymes present in the intracellular environment. This enzymatic action is believed to cause the cleavage of certain bonds within the nanoparticle structure, facilitating drug release (Cao et al., 2019; M. Zhang et al., 2021).

The cytotoxicity studies using the MTT assay discovered that the synthesised citrate-gold nanoparticles (20.54 ±0.45 nm, 40.59 ±0.83 nm, and 60.67 ±0.71 nm), PEG-gold nanoparticles (28.41 ±0.43 nm), and TA-AuNPs (15.11 ±0.64 nm) show various toxicity effects. For example, observations showed that at around 15 μgL^{-1}, about half of the macrophage cell population underwent cell death, notably when exposed to larger-sized nanoparticles (60.67 ±0.71 nm). In contrast, fewer than 40% of cells killed due to toxicity from smaller-sized nanoparticles (40.59 ±0.83 nm). This significant variation was statistically measured at p-value of 0.162. On the other hand, PEG-gold nanoparticles (28.41 ±0.43 nm), and TA-AuNPs (15.11 ±0.64 nm) showed high levels of toxicity effects over 80% at concentration of 15 μgL^{-1}. The REM/AuNPs and AMTD/AuNPs conjugates notably reduced the toxicity effects to less than 20% and 50%, respectively, compared to the use of these medicines alone.

Finally, according to the SRB assay, the cytotoxicity concentration (CC_{50}) for REM/AuNPs and AMTD/AuNPs was determined at 2.8 μgL^{-1} and 4.5 μgL^{-1}, respectively. This indicates that a higher dose of AMTD/AuNPs is required to

achieve a 50% reduction in cell viability compared to REM/AuNPs. In other words, The drug conjugation process to gold nanoparticles reduces the potency of each drug at 2.8 μgL^{-1} and 4.5 μgL^{-1} for REM/AuNPs and AMTD/AuNPs, respectively.

Chapter (7): General Discussion, Conclusions and Future Work

7.1 General Discussion and Conclusions

This thesis involves a number of research topics described separately in chapters 3-6. The first topic was about the synthesis of gold nanoparticles in the size range 8-60 nm (Chapter 3, Table 3.1). This synthesis involved application and modification of several techniques, such as the citrate reduction method and size tuning based on controlling pH or concentration ratios of the reduction agents (Chapter 2, Section 2.3). In addition, three different types of thiol-containing compounds specifically 11-mercaptoundecanoic acid (MUDA), 4-mercaptobenzoic acid (4-MBA), and meso-2,3-Dimercaptosuccinic acid (DMSA), were employed for the functionalisation of citrate-gold nanoparticles (20.54 ±0.45 nm) size (Chapter 4, Section 4.2). Furthermore, these MUDA functionalised gold nanoparticles (50 ±0.98 nm) were utilised for both amantadine (AMTD) and remdesivir (REM) drug conjugation showing an increase in the particles size at 160 nm and 165 nm, respectively (Chapter 4, Section 4.3).

As explained in Chapter 1, Section 1.7 gold nanoparticles exhibit several unique properties, including low toxicity, uniform morphology, and a large surface-to-volume ratio. One of the significant physical properties of Au NPs is the localised surface plasmon resonance (LSPR), which is closely related to their optical properties. Herein, in this research, an extensive examination for the prepared gold nanoparticles was employed using various characterisation techniques (Chapter 2, Section 2.4). The obtained results measured by DLS showed that most of the prepared nanoparticles are stable in the colloidal solution at various zeta potential values outside the critical range for aggregation of -10 mV to +10 mV (Chapter 3, Table 3.1). The LSPR characterisation of the prepared gold

nanoparticles (60.67 ±0.71 nm) showed a significant absorption peak shift to maximum wavelengths at 538 nm. In contrast to the smaller nanoparticles, K-TA-Au NPs (8.77 ±0.928 nm), showing absorption peak shift at maximum wavelength 516 nm.

The stability of the prepared citrate-gold nanoparticles (20.54 ±0.45 nm) was also studied and compared with other gold nanoparticles, PEG-AuNPs (28.41 ±0.43 nm) and TA-AuNPs (15.11 ±0.64 nm), based on their ion concentration release in four different media: DMEM cell culture media, ultrapure water (Milli-Q 18.8 MΩ-cm), PBS, and HEPES buffer (Chapter 5, Section 5.2.1). Cronbach's alpha or coefficient alpha (α) has been used for data analysis to indicate the consistency or data reliability between all forms of gold nanoparticles. For example, both citrate-gold nanoparticles and PEG-gold nanoparticles show that they have high level of consistency at α = 0.98 (Chapter 5, Sections 5.2.1.1 and 5.2.1.2). Whereas, TA-gold nanoparticles showed good consistency at Cronbach's alpha value of α = 0.87 (Chapter 5, Section 5.2.1.3). Statistically all measurements were also fully described and icompared in Appendix 2, Figures S1, S2, and S3.

The impact of the Na^+ and K^+ ionic strength on the citrate-gold nanoparticles (20.54 ±0.45 nm) was investigated and it was observed that at high concentrations (0.1-0.5 M), aggregation of gold nanoparticles was determined due to the strong affinity force of potassium and sodium ions to the surface of gold nanoparticles. The nanoparticles aggregated after adsorption of K^+ and Na^+ ions onto their surfaces. In contrast, a negligible increase in size was observed after mixing of gold nanoparticles with KNO_3 and $NaNO_3$ salts at low concentrations (0.01-0.05 M) as demonstrated in Chapter 5, Table 5.1. The effect

of bovine serum albumin (BSA) to citrate-gold nanoparticles (20.54 ±0.45 nm) and the impact of temperature on BSA/AuNPs were investigated and demonstrated in this thesis (chapter 5, Section 5.2.5). Observations show a significant increase for the size of citrate-gold nanoparticles by ten folds (from 20.54 ±0.45 nm to approximately 191.1 ±1.6 nm). This would explain the mechanism of interaction between cit-Au NPs (20.54 ±0.45 nm) and BSA, through the unbound thiol (-SH) group. This unbound thiol can lead to side reactions that modify other functional groups in the protein.

This study paved the way for the next step in this research, which involved functionalising citrate-gold nanoparticles (20.54 ± 0.45) with the MUDA thiol-containing compound. The main insight from this functionalisation is the formation of gold-sulfur (Au-S) bonds through the interaction between the thiol group and gold atoms (Chapter 4, Section 4.2). The prepared MUDA-cit-AuNPs have been characterised using several techniques. For example, TEM imaging of these functionalised gold nanoparticles in Chapter 4, Figure 4.3d, showed a significant change in particles size and size distribution with moderate aggregation after functionalisation with MUDA. Further characterisation was conducted by FTIR to observe whether any changes occurred in the chemical structure of MUDA-cit-AuNPs after the functionalisation process (Chapter 4, Figure 4.4). The FTIR spectra showed that MUDA-cit-AuNPs display an additional strong band at wavenumber 1696 cm^{-1}, which belongs to the ester group (RCOOR′). In addition, the two bands appearing at 2852 cm^{-1} and 2921 cm^{-1} are representative of the (-CH) stretching in the MUDA. Hence, the absence of symmetrical and asymmetrical vibrations in the FTIR spectra and the presence of the carboxyl (-

COOH) and ester (-COO) groups' stretching indicate successful binding of MUDA to the citrate-gold nanoparticles as shown in Chapter 4, Figure 4.4. Finally, the drug conjugation system in this research involved the application of two different types of medicines amantadine (AMTD) and remdesivir (REM). This conjugation was employed in the presence of EDC/NHS coupling reagents (Chapter 2, Section 2.3.4). Both EDC carbodiimide cross-linker and NHS play a crucial role in the reactivity of the carboxyl groups and preventing the hydrolysis of the active intermediate, respectively. **Figure 7.1** illustrates the process of functionalisation for citrate-gold nanoparticles (20.54 ± 0.45) with MUDA, a thiol-containing compound, followed by its conjugation with the amantadine drug. Similar

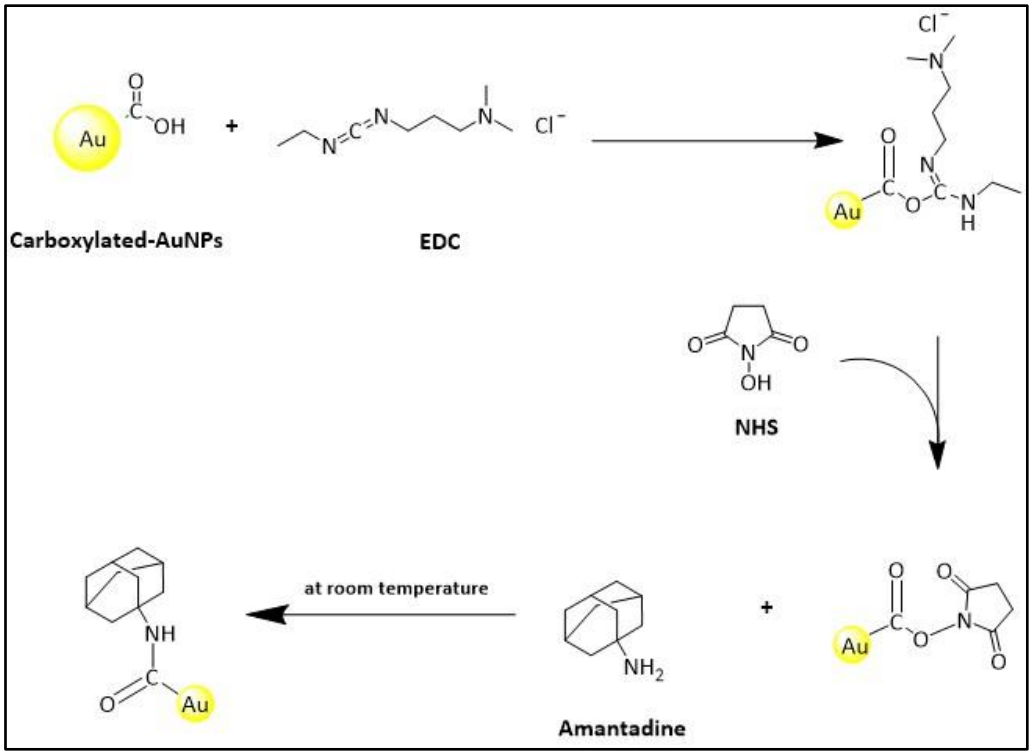

Figure 7. 1. Schematic representation of the conjugation system depicting the attachment of amantadine (AMTD) drug to the functionalised MUDA-cit-Au NPs facilitated by EDC (carbodiimide cros-linker) and NHS coupling reagent.

procedure was conducted for the remdesivir drug under similar conditions (Chapter 2, Section 2.3.4).

Both forms of drug conjugated-gold nanoparticles, AMTD/AuNPs and REM/AuNPs, were characterised using various techniques such as DLS, FTIR, NMR, TGA and UV-Vis (Chapter 2, section 2.4). The results showed that AMTD/AuNPs and REM/AuNPs have well size distribution measured by DLS at different sizes 160 nm and 165 nm, respectively (Chapter 4, Figures 4.6 and 4.16).

The LSPR spectra for the AMTD/AuNPs and REM/AuNPs were further characterised in the region between 200 nm and 800 nm. AMTD/AuNPs showed a significant shift in the LSPR absorption peak towards a maximum wavelength of 575 nm. In addition, amantadine (AMTD) itself exhibited a distinct LSPR peak shift at a lower wavelength (265 nm). Whereas, REM/AuNPs displayed LSPR peak shifts at maximum wavelengths 249 nm for remdesivir drug and 590 nm for the cit-AuNPs (20.54 ± 0.45) as shown in Figures 4.8 and 4.18, Chapter 4. Notably, the LSPR for the conjugated form (AMTD/AuNPs) was investigated in the absence of EDC carbodiimide cross-linker (Chapter 4, Figure 4.8). It was observed that under these conditions Au NPs underwent significant aggregation. However, the basic nature of the amine group in amantadine's chemical structure, which can deprotonate the carboxylic acid in the MUDA-cit-AuNPs, resulting in the formation of unreactive carboxylate group. In addition, NMR characterisation was conducted to track the structural changes of AMTD and REM after their conjugation with MUDA functionalised-gold nanoparticles (Chapter 4, Sections 4.3.1.1 and 4.3.1.2). The NMR results for the amantadine-gold nanoparticles

(AMTD/AuNPs) conjugated forms were obtained by observing hydrogen's chemical shift using proton nuclear magnetic resonance or ^{1}H NMR (Chapter 4, Figure 4.11). Notably, a significant change in the ^{1}H NMR spectra was observed for the AMTD drug after its conjugation with MUDA-cit-AuNPs, indicating the formation of amide bond via interaction between the primary amine in AMTD and carboxylic acid group in MUDA-cit-AuNPs. The result was similar for the remdesivir drug-conjugated to MUDA-cit-AuNPs. In short, the ^{1}H NMR and ^{13}C NMR characterisation were very useful to identify the conjugation system via determination of the amide bond formation.

Finally, the amount of loading for both drugs remdesivir and amantadine was determined by TGA analysis. The results showed the decomposition process of amantadine approximately 20 minutes after reaching 200°C. The sample experienced a weight loss of around 25.78 mg, equivalent to roughly 92.8% of the initial mass (27.78 mg) (Chapter 4, Figure 4.15). The thermogravimetric analysis for REM/AuNPs exhibited two stages of remdesivir decomposition, the first after 15 minutes, involving the loss of only 1.1 mg (39.3) of the total sample, followed by approximately 0.9 mg (32.3%) after 40 minutes (Chapter 4, Figure 4.22).

This thesis also involved the investigation of the cellular uptake and cytotoxicity assessment of unconjugated and drug-conjugated gold nanoparticles using J774 cell line macrophages (Chapter 6, Sections 6.2 and 6.3). The findings in Chapter 6, Section 6.2.1, demonstrated that several factors (e.g. size, shape, or concentration) can impact the internalisation of particles into cellular vesicles. For example, J774 macrophage cells were exposed to two different concentrations

(1 mgL^{-1} and 6 mgL^{-1}) of citrate, PEG, and TA-gold nanoparticles. It was found that there was a limited number of the prepared gold nanoparticles surrounding the cell macrophages, leading to a slower rate of internalisation. Conversely, at higher concentration of NPs, the internalisation rate into cell vesicles increased by approximately two folds (Chapter 6, Figure 6.2).

For amantadine (AMTD)-conjugated gold nanoparticles, gold nanoparticles were completely internalised into vesicles within cell macrophages, releasing the larger particles (AMTD drug molecules) surrounding the cell macrophages. This drug release was attributed to the action of specific enzymes present in the intracellular environment. For instance, cell macrophages produce enzymes within the intracellular environment that trigger the release of the drug by cleaving certain bonds in the nanoparticle structure as illustrated in Chapter 6, Section 6.2.1.3, and Figure 6.3. However, the remdesivir (REM)-conjugated gold nanoparticles displayed a distinct cellular uptake mechanism indicating a slower internalisation rate due to a reduction in the expression of adenosine transporters (Chapter 6, Section 6.2.1.4, Figure 6.4). To conclude, gold nanoparticles play a pivotal role in targeting cells and safeguarding conjugated drugs from enzymatic degradation.

In this research, J774 cell line macrophages were also used to evaluate the toxicity impacts of formulated and drug-conjugated gold nanoparticles (Chapter 6, Section 6.3). In comparison between citrate-gold nanoparticles (20.54 ±0.45 nm), PEG-gold nanoparticles (28.41 ±0.43 nm), and TA-gold nanoparticles (15.11 ±0.64 nm), the MTT assay showed that citrate-gold nanoparticles (20.54 ±0.45 nm) exhibited the lowest level of toxicity among the various coatings,

notably at a concentration of 5 μgL^{-1} (Chapter 6, Figure 6.6). This variation was statistically indicated at p-value < 0.01. In addition, the sulforhodamine-B (SRB) Assay was applied to determine the inhibition of cell proliferation rate (% cell viability) of both remdesivir (REM), and amantadine (AMTD) drugs-conjugated to citrate-gold nanoparticles (20.54 ±0.45 nm). Data was analysed based on measuring the absorbance at specific wavelength 540 nm for the SRB dye. SRB indicated the cytotoxic concentration for AMTD/AuNPs and REM/AuNPs at 4.5 μgL^{-1} and 2.8 μgL^{-1}, respectively. Specifically, in this scenario, 2.8 μgL^{-1} indicates that REM/AuNPs is more cytotoxic to the 50% of macrophage cells than AMTD/AuNPs at 4.5 μgL^{-1}.

7.2 Future work

This study shows a promising conjugation for amantadine (AMTD) to citrate-gold nanoparticles (20.54 ±0.45 nm). The impressive results and unique properties of this form of conjugation (AMTD/AuNPs), could pave the way to develop this research to advanced stages by investigating the interaction between amantadine (AMTD) conjugated-gold nanoparticles and Organic Cation Transporter 3 (OCT3 or SLC22A3) in the brain. Within the brain, OCT3 is involved in the regulation of neurotransmitter levels. It contributes to the uptake of neurotransmitters from the synaptic cleft back into neurons and astrocytes, influencing neurotransmission and maintaining appropriate neurotransmitter concentrations. OCT3 plays a role in the disposition of drugs by facilitating their movement across biological barriers, such as the blood-brain barrier (BBB). This transporter can influence drug absorption, distribution, metabolism, and excretion.

Amantadine is a weak base and a cationic compound, and organic cation transporters like OCT3 typically transport positively charged molecules. It is important to note that the transport of amantadine across the BBB and its interaction with OCT3 may involve a combination of passive diffusion and active transport processes. In addition, amantadine could potentially compete with endogenous substrates for binding to OCT3.

Amantadine recently classified as anti-Parkinson's drug that affects the brain by several mechanisms. One of its primary actions is to block the NMDA (N-methyl-D-aspartate) glutamate receptors, which modulates the release of neurotransmitters such as dopamine, serotonin and norepinephrine, leading to

alleviate symptoms of Parkinson's disease. The interaction between medications and transporter proteinsssuch as OCT3 can sometimes be complex and might not be extensively studied or understood, especially in terms of direct interactions with specific drugs such as amantadine. However, any future research could further centre on the investigation of interaction between the amantadine (AMTD)-conjugated gold nanoparticles and OCT3 protein transporter using innovative microfluidic devices.

This study not only supports drug delivery systems but also presents a substantial advantage, particularly for elderly Parkinson's patients. Furthermore, this pioneering therapeutic research stands to significantly diminish healthcare expenses for this age group.

References

Abraham, R. J., Fisher, J., & Loftus, P. (1998). *Introduction to NMR spectroscopy* (Vol. 2). Wiley New York.

Abuchowski, A. (1977). Van Es T, Palczuk NC, and Davis FF. *Alteration of Immunological Properties of Bovine Serum Albumin by Covalent Attachment of Polyethylene Glycol. J Biol Chem*, *252*, 3578–3581.

Afzal, O., Altamimi, A. S. A., Nadeem, M. S., Alzarea, S. I., Almalki, W. H., Tariq, A., Mubeen, B., Murtaza, B. N., Iftikhar, S., & Riaz, N. (2022). Nanoparticles in Drug Delivery: From History to Therapeutic Applications. *Nanomaterials*, *12*(24), 4494.

Ahluwalia, V. K. (2023). Thermogravimetric Analysis. In *Instrumental Methods of Chemical Analysis* (pp. 81–89). Springer.

Ahmad, T. (2014). Reviewing the tannic acid mediated synthesis of metal nanoparticles. *Journal of Nanotechnology*, *2014*.

Ahmed, E. (2020). *“Breaking Down” Surfactants*.

Ai, J., Biazar, E., Jafarpour, M., Montazeri, M., Majdi, A., Aminifard, S., Zafari, M., Akbari, H. R., & Rad, H. G. (2011). Nanotoxicology and nanoparticle safety in biomedical designs. *International Journal of Nanomedicine*, 1117–1127.

Alba-Molina, D., Martín-Romero, M. T., Camacho, L., & Giner-Casares, J. J. (2017). Ion-mediated aggregation of gold nanoparticles for light-induced heating. *Applied Sciences*, *7*(9), 916.

Allahyari, M., & Mohit, E. (2016). Peptide/protein vaccine delivery system based

on PLGA particles. *Human Vaccines & Immunotherapeutics*, *12*(3), 806–828.

Amendola, V., Pilot, R., Frasconi, M., Maragò, O. M., & Iatì, M. A. (2017). Surface plasmon resonance in gold nanoparticles: a review. *Journal of Physics: Condensed Matter*, *29*(20), 203002.

Amina, S. J., & Guo, B. (2020). A review on the synthesis and functionalization of gold nanoparticles as a drug delivery vehicle. *International Journal of Nanomedicine*, 9823–9857.

An, K., & Somorjai, G. A. (2012). Size and shape control of metal nanoparticles for reaction selectivity in catalysis. *ChemCatChem*, *4*(10), 1512–1524.

Anik, M. I., Mahmud, N., Al Masud, A., & Hasan, M. (2022). Gold nanoparticles (GNPs) in biomedical and clinical applications: A review. *Nano Select*, *3*(4), 792–828.

Ansar, S. M., Chakraborty, S., & Kitchens, C. L. (2018). pH-responsive mercaptoundecanoic acid functionalized gold nanoparticles and applications in catalysis. *Nanomaterials*, *8*(5), 339.

Araújo-Neto, R. P., Silva-Freitas, E. L., Carvalho, J. F., Pontes, T. R. F., Silva, K. L., Damasceno, I. H. M., Egito, E. S. T., Dantas, A. L., Morales, M. A., & Carriço, A. S. (2014). Monodisperse sodium oleate coated magnetite high susceptibility nanoparticles for hyperthermia applications. *Journal of Magnetism and Magnetic Materials*, *364*, 72–79.

Arvizo, R., Bhattacharya, R., & Mukherjee, P. (2010). Gold nanoparticles:

opportunities and challenges in nanomedicine. *Expert Opinion on Drug Delivery*, *7*(6), 753–763.

Asadishad, B., Vossoughi, M., & Alemzadeh, I. (2010). Folate-receptor-targeted delivery of doxorubicin using polyethylene glycol-functionalized gold nanoparticles. *Industrial & Engineering Chemistry Research*, *49*(4), 1958–1963.

Ashcroft, J. M., Gu, W., Zhang, T., Hughes, S. M., Hartman, K. B., Hofmann, C., Kanaras, A. G., Kilcoyne, D. A., Le Gros, M., & Yin, Y. (2008). TiO 2 nanoparticles as a soft X-ray molecular probe. *Chemical Communications*, *21*, 2471–2473.

Asiaei, S., Smith, B., & Nieva, P. (2015). Enhancing conjugation rate of antibodies to carboxylates: Numerical modeling of conjugation kinetics in microfluidic channels and characterization of chemical over-exposure in conventional protocols by quartz crystal microbalance. *Biomicrofluidics*, *9*(6), 64115.

Assael, M. J., Metaxa, I. N., Kakosimos, K., & Constantinou, D. (2006). Thermal conductivity of nanofluids-experimental and theoretical. *International Journal of Thermophysics*, *27*(4), 999–1017.

Atef, B., Ishak, R. A. H., Badawy, S. S., & Osman, R. (2022). Exploring the potential of oleic acid in nanotechnology-mediated dermal drug delivery: An up-to-date review. *Journal of Drug Delivery Science and Technology*, *67*, 103032.

Augustine, R., Hasan, A., Primavera, R., Wilson, R. J., Thakor, A. S., & Kevadiya, B. D. (2020). Cellular uptake and retention of nanoparticles: Insights on

particle properties and interaction with cellular components. *Materials Today Communications*, *25*, 101692.

Austin, L. A., Kang, B., & El-Sayed, M. A. (2015). Probing molecular cell event dynamics at the single-cell level with targeted plasmonic gold nanoparticles: A review. *Nano Today*, *10*(5), 542–558.

Averitt, R. D., Sarkar, D., & Halas, N. J. (1997). Plasmon resonance shifts of Au-coated Au 2 S nanoshells: insight into multicomponent nanoparticle growth. *Physical Review Letters*, *78*(22), 4217.

Awotunde, O., Okyem, S., Chikoti, R., & Driskell, J. D. (2020). Role of free thiol on protein adsorption to gold nanoparticles. *Langmuir*, *36*(31), 9241–9249.

Aziz, S. B., Abdullah, R. M., Rasheed, M. A., & Ahmed, H. M. (2017). Role of ion dissociation on DC conductivity and silver nanoparticle formation in PVA: AgNt based polymer electrolytes: Deep insights to ion transport mechanism. *Polymers*, *9*(8), 338.

Baas, J., Senninger, N., & Elser, H. (1994). The reticuloendothelial system. An overview of function, pathology and recent methods of measurement. *Zeitschrift Fur Gastroenterologie*, *32*(2), 117–123.

Babick, F. (2020). Dynamic light scattering (DLS). In *Characterization of Nanoparticles* (pp. 137–172). Elsevier.

Bahrami, B., Hojjat-Farsangi, M., Mohammadi, H., Anvari, E., Ghalamfarsa, G., Yousefi, M., & Jadidi-Niaragh, F. (2017). Nanoparticles and targeted drug delivery in cancer therapy. *Immunology Letters*, *190*, 64–83.

Bajaj, M., Wangoo, N., Jain, D. V. S., & Sharma, R. K. (2020). Quantification of adsorbed and dangling citrate ions on gold nanoparticle surface using thermogravimetric analysis. *Scientific Reports*, *10*(1), 8213.

Bancsi, A., Houle, S. K. D., & Grindrod, K. A. (2019). Shoulder injury related to vaccine administration and other injection site events. *Canadian Family Physician*, *65*(1), 40–42.

Bartczak, D., & Kanaras, A. G. (2011). Preparation of peptide-functionalized gold nanoparticles using one pot EDC/Sulfo-NHS coupling. *Langmuir*. https://doi.org/10.1021/la2022177

Begines, B., Ortiz, T., Pérez-Aranda, M., Martínez, G., Merinero, M., Argüelles-Arias, F., & Alcudia, A. (2020). Polymeric nanoparticles for drug delivery: Recent developments and future prospects. *Nanomaterials*, *10*(7), 1403.

Berne, B. J., & Pecora, R. (2000). *Dynamic light scattering: with applications to chemistry, biology, and physics*. Courier Corporation.

Betancourt-Galindo, R., Reyes-Rodriguez, P. Y., Puente-Urbina, B. A., Avila-Orta, C. A., Rodríguez-Fernández, O. S., Cadenas-Pliego, G., Lira-Saldivar, R. H., & García-Cerda, L. A. (2014). Synthesis of copper nanoparticles by thermal decomposition and their antimicrobial properties. *Journal of Nanomaterials*, *2014*, 10.

Bhatt, N., Huang, P.-J. J., Dave, N., & Liu, J. (2011). Dissociation and degradation of thiol-modified DNA on gold nanoparticles in aqueous and organic solvents. *Langmuir*, *27*(10), 6132–6137.

Boeyens, J. C. A. (2008). The periodic electronegativity table. *Zeitschrift Für Naturforschung B*, *63*(2), 199–209.

Bolaños, K., Kogan, M. J., & Araya, E. (2019). Capping gold nanoparticles with albumin to improve their biomedical properties. *International Journal of Nanomedicine*, *14*, 6387.

Boldeiu, A., Simion, M., Mihalache, I., Radoi, A., Banu, M., Varasteanu, P., Nadejde, P., Vasile, E., Acasandrei, A., & Popescu, R. C. (2019). Comparative analysis of honey and citrate stabilized gold nanoparticles: In vitro interaction with proteins and toxicity studies. *Journal of Photochemistry and Photobiology B: Biology*, *197*, 111519.

Brust, M., Walker, M., Bethell, D., Schiffrin, D. J., & Whyman, R. (1994). Synthesis of Thiol-derivatised Gold Nanoparticles in a Two-phase Liquid-Liquid System. In *J. CHEM. SOC., CHEM. COMMUN*.

Bürgi, T. (2015). Properties of the gold–sulphur interface: from self-assembled monolayers to clusters. *Nanoscale*, *7*(38), 15553–15567.

Busch, R. T., Karim, F., Weis, J., Sun, Y., Zhao, C., & Vasquez, E. S. (2019). Optimization and Structural Stability of Gold Nanoparticle-Antibody Bioconjugates. *ACS Omega*. https://doi.org/10.1021/acsomega.9b02276

Campbell, I. D., Dobson, C. M., & Williams, R. J. P. (1975). Assignment of the 1H NMR spectra of proteins. *Proceedings of the Royal Society of London. A. Mathematical and Physical Sciences*, *345*(1640), 23–40.

Cao, Z., Li, W., Liu, R., Li, X., Li, H., Liu, L., Chen, Y., Lv, C., & Liu, Y. (2019).

pH-and enzyme-triggered drug release as an important process in the design of anti-tumor drug delivery systems. *Biomedicine & Pharmacotherapy*, *118*, 109340.

Carnovale, C., Bryant, G., Shukla, R., & Bansal, V. (2019). Identifying trends in gold nanoparticle toxicity and uptake: size, shape, capping ligand, and biological corona. *ACS Omega*, *4*(1), 242–256.

Caron, S., Wojcik, J. M., & Vazquez, E. (2003). Nucleophilic Aromatic Substitution of Aryl Fluorides by Secondary Nitriles: Preparation of 2-(2-Methoxyphenyl)-2-Methylpropionitrile: Benzeneacetonitrile, 2-methoxy-α, α-dimethyl-. *Organic Syntheses*, *79*, 209.

Castro, J. V, Ward, R. M., Gilbert, R. G., & Fitzgerald, M. A. (2005). Measurement of the molecular weight distribution of debranched starch. *Biomacromolecules*, *6*(4), 2260–2270.

Chabal, Y. J. (1988). Surface infrared spectroscopy. *Surface Science Reports*, *8*(5–7), 211–357.

Chaffey, N. (2003). *Alberts, B., Johnson, A., Lewis, J., Raff, M., Roberts, K. and Walter, P. Molecular biology of the cell. 4th edn.* Oxford University Press.

Chairam, S., Konkamdee, W., & Parakhun, R. (2017). Starch-supported gold nanoparticles and their use in 4-nitrophenol reduction. *Journal of Saudi Chemical Society*, *21*(6), 656–663.

Chan, K.-Y., Yang, D., Demir, B., Mouritz, A. P., Lin, H., Jia, B., & Lau, K.-T. (2019). Boosting the electrical and mechanical properties of structural

dielectric capacitor composites via gold nanoparticle doping. *Composites Part B: Engineering*, *178*, 107480.

Chang, S. H., Custer, P. L., Mohadjer, Y., & Scott, E. (2009). Use of lorenz titanium implants in orbital fracture repair. *Ophthalmic Plastic and Reconstructive Surgery*, *25*(2), 119–122. https://doi.org/10.1097/IOP.0b013e31819ac7c5

Charpentier, T., Kroll, P., & Mauri, F. (2009). First-principles nuclear magnetic resonance structural analysis of vitreous silica. *The Journal of Physical Chemistry C*, *113*(18), 7917–7929.

Chatterjee, A., & Deopura, B. L. (2002). Carbon nanotubes and nanofibre: an overview. *Fibers and Polymers*, *3*, 134–139.

Chaudhari, S. P., & Patil, P. S. (2012). Pharmaceutical excipients: a review. *Int J Adv Pharm Biol Chem*, *1*(1), 21–34.

Chenthamara, D., Subramaniam, S., Ramakrishnan, S. G., Krishnaswamy, S., Essa, M. M., Lin, F.-H., & Qoronfleh, M. W. (2019). Therapeutic efficacy of nanoparticles and routes of administration. *Biomaterials Research*, *23*(1), 1–29.

Chodankar, S., Aswal, V. K., Kohlbrecher, J., Vavrin, R., & Wagh, A. G. (2008). Structural evolution during protein denaturation as induced by different methods. *Physical Review E*, *77*(3), 31901.

Choi, J., Yang, J., Jang, E., Suh, J.-S., Huh, Y.-M., Lee, K., & Haam, S. (2011). Gold nanostructures as photothermal therapy agent for cancer. *Anti-Cancer*

Agents in Medicinal Chemistry (Formerly Current Medicinal Chemistry-Anti-Cancer Agents), *11*(10), 953–964.

Chua, J., Senft, J. L., Lockett, S. J., Brett, P. J., Burtnick, M. N., DeShazer, D., & Friedlander, A. M. (2017). pH alkalinization by chloroquine suppresses pathogenic Burkholderia type 6 secretion system 1 and multinucleated giant cells. *Infection and Immunity*, *85*(1), e00586-16.

Colomban, P. (2009). The use of metal nanoparticles to produce yellow, red and iridescent colour, from bronze age to present times in lustre pottery and glass: solid state chemistry, spectroscopy and nanostructure. *Journal of Nano Research*, *8*, 109–132.

Crous, A., & Abrahamse, H. (2020). Effective gold nanoparticle-antibody-mediated drug delivery for photodynamic therapy of lung cancer stem cells. *International Journal of Molecular Sciences*, *21*(11), 3742.

Dahiya, R., & Dahiya, S. (2021). Advanced drug delivery applications of self-assembled nanostructures and polymeric nanoparticles. In *Handbook on Nanobiomaterials for Therapeutics and Diagnostic Applications* (pp. 297–339). Elsevier.

Daka, V. N., Bandi, L. S., Alla, S., Cheedella, V. S., & Galaba, S. R. (2021). Brief review on remdesivir. *International Journal of Health Care and Biological Sciences*, 57.

Danehy, J. P., & Parameswaran, K. N. (1968). Acidic dissociation constants of thiols. *Journal of Chemical & Engineering Data*, *13*(3), 386–389.

Dasari, A., Xue, J., & Deb, S. (2022). Magnetic nanoparticles in bone tissue engineering. *Nanomaterials*, *12*(5), 757.

Davis, M. E., & Brewster, M. E. (2004). Cyclodextrin-based pharmaceutics: past, present and future. *Nature Reviews Drug Discovery*, *3*(12), 1023–1035.

De Jong, W. H., & Borm, P. J. A. (2008). Drug delivery and nanoparticles: applications and hazards. *International Journal of Nanomedicine*, *3*(2), 133–149.

De Marchi, L., Oliva, M., Freitas, R., Neto, V., Figueira, E., Chiellini, F., Morelli, A., Soares, A. M. V. M., & Pretti, C. (2019). Toxicity evaluation of carboxylated carbon nanotubes to the reef-forming tubeworm Ficopomatus enigmaticus (Fauvel, 1923). *Marine Environmental Research*. https://doi.org/10.1016/j.marenvres.2018.10.015

De, R., Mahata, M. K., & Kim, K. (2022). Structure-Based Varieties of Polymeric Nanocarriers and Influences of Their Physicochemical Properties on Drug Delivery Profiles. *Advanced Science*, *9*(10), 2105373.

Del Castillo-Castro, T., Larios-Rodriguez, E., Molina-Arenas, Z., Castillo-Ortega, M. M., & Tanori, J. (2007). Synthesis and characterization of metallic nanoparticles and their incorporation into electroconductive polymer composites. *Composites Part A: Applied Science and Manufacturing*, *38*(1), 107–113.

del Castillo-Santaella, T., Ortega-Oller, I., Padial-Molina, M., O'Valle, F., Galindo-Moreno, P., Jódar-Reyes, A. B., & Peula-García, J. M. (2019). Formulation, colloidal characterization, and in vitro biological effect of BMP-2 loaded

PLGA nanoparticles for bone regeneration. *Pharmaceutics*, *11*(8), 388.

Demir, B., Chan, K.-Y., Yang, D., Mouritz, A., Lin, H., Jia, B., Lau, K.-T., & Walsh, T. R. (2019). Epoxy-gold nanoparticle nanocomposites with enhanced thermo-mechanical properties: An integrated modelling and experimental study. *Composites Science and Technology*, *174*, 106–116.

Deol, S., Weerasuriya, N., & Shon, Y.-S. (2015). Stability, cytotoxicity and cell uptake of water-soluble dendron–conjugated gold nanoparticles with 3, 12 and 17 nm cores. *Journal of Materials Chemistry B*, *3*(29), 6071–6080.

Derman, S., Mustafaeva, Z. A., Abamor, E. S., Bagirova, M., & Allahverdiyev, A. (2015). Preparation, characterization and immunological evaluation: canine parvovirus synthetic peptide loaded PLGA nanoparticles. *Journal of Biomedical Science*, *22*, 1–12.

DeVetter, B. M., Mukherjee, P., Murphy, C. J., & Bhargava, R. (2015). Measuring binding kinetics of aromatic thiolated molecules with nanoparticles via surface-enhanced Raman spectroscopy. *Nanoscale*, *7*(19), 8766–8775.

Dey, A. K., Gonon, A., Pécheur, E.-I., Pezet, M., Villiers, C., & Marche, P. N. (2021). Impact of gold nanoparticles on the functions of macrophages and dendritic cells. *Cells*, *10*(1), 96.

Dhas, N. L., Kudarha, R. R., Acharya, N. S., & Acharya, S. R. (2018). Polymeric immunonanoparticles mediated cancer therapy: Versatile nanocarriers for cell-specific cargo delivery. *Critical Reviews™ in Therapeutic Drug Carrier Systems*, *35*(1).

Din, F. U., Aman, W., Ullah, I., Qureshi, O. S., Mustapha, O., Shafique, S., & Zeb, A. (2017). Effective use of nanocarriers as drug delivery systems for the treatment of selected tumors. *International Journal of Nanomedicine*, 7291–7309.

Dodda, J. M., Remiš, T., Rotimi, S., & Yeh, Y.-C. (2022). Progress in the drug encapsulation of poly (lactic-co-glycolic acid) and folate-decorated poly (ethylene glycol)–poly (lactic-co-glycolic acid) conjugates for selective cancer treatment. *Journal of Materials Chemistry B*.

Dong, F., Koodali, R. T., Wang, H., & Ho, W. (2014). Nanomaterials for environmental applications. *Journal of Nanomaterials*, *2014*, 7.

Düzgüneş, N., Simões, S., Slepushkin, V., Pretzer, E., Flasher, D., Salem, I. I., Steffan, G., Konopka, K., & Pedroso de Lima, M. C. B. T.-M. in E. (2005). Delivery of Antiviral Agents in Liposomes. In *Liposomes* (Vol. 391, pp. 351–373). Academic Press. https://doi.org/https://doi.org/10.1016/S0076-6879(05)91020-3

Dykman, L. A., & Bogatyrev, V. A. (2007). Gold nanoparticles: preparation, functionalisation and applications in biochemistry and immunochemistry. *Russian Chemical Reviews*, *76*(2), 181.

Dykman, L., & Khlebtsov, N. (2012). Gold nanoparticles in biomedical applications: recent advances and perspectives. *Chemical Society Reviews*, *41*(6), 2256–2282.

Eastman, R. T., Roth, J. S., Brimacombe, K. R., Simeonov, A., Shen, M., Patnaik, S., & Hall, M. D. (2020). Remdesivir: a review of its discovery and

development leading to emergency use authorization for treatment of COVID-19. *ACS Central Science*, *6*(5), 672–683.

El-Sayed, A., & Kamel, M. (2020). Advances in nanomedical applications: diagnostic, therapeutic, immunization, and vaccine production. *Environmental Science and Pollution Research*, *27*(16), 19200–19213.

El-Zayat, S. R., Sibaii, H., & Mannaa, F. A. (2019). Toll-like receptors activation, signaling, and targeting: an overview. *Bulletin of the National Research Centre*, *43*(1), 1–12.

Elia, P., Zach, R., Hazan, S., Kolusheva, S., Porat, Z., & Zeiri, Y. (2014). Green synthesis of gold nanoparticles using plant extracts as reducing agents. *International Journal of Nanomedicine*, *9*, 4007.

Escalona-Rayo, O., Fuentes-Vázquez, P., Jardon-Xicotencatl, S., García-Tovar, C. G., Mendoza-Elvira, S., & Quintanar-Guerrero, D. (2019). Rapamycin-loaded polysorbate 80-coated PLGA nanoparticles: optimization of formulation variables and in vitro anti-glioma assessment. *Journal of Drug Delivery Science and Technology*, *52*, 488–499.

Esmaeili, H., Mousavi, S. M., Hashemi, S. A., Lai, C. W., Chiang, W.-H., & Bahrani, S. (2021). Application of biosurfactants in the removal of oil from emulsion. In *Green Sustainable Process for Chemical and Environmental Engineering and Science* (pp. 107–127). Elsevier.

Evano, G., Blanchard, N., & Toumi, M. (2008). Copper-mediated coupling reactions and their applications in natural products and designed biomolecules synthesis. *Chemical Reviews*, *108*(8), 3054–3131.

Farhana, A., & Lappin, S. L. (2022). Biochemistry, lactate dehydrogenase. In *StatPearls [Internet]*. StatPearls Publishing.

Farkas, N., & Kramar, J. A. (2021). Dynamic light scattering distributions by any means. *Journal of Nanoparticle Research*, *23*(5), 120.

Farooq, M. U., Novosad, V., Rozhkova, E. A., Wali, H., Ali, A., Fateh, A. A., Neogi, P. B., Neogi, A., & Wang, Z. (2018). RETRACTED ARTICLE: Gold Nanoparticles-enabled Efficient Dual Delivery of Anticancer Therapeutics to HeLa Cells. *Scientific Reports*, *8*(1), 2907.

Filopoulou, A., Vlachou, S., & Boyatzis, S. C. (2021). Fatty acids and their metal salts: A review of their infrared spectra in light of their presence in cultural heritage. *Molecules*, *26*(19), 6005.

Forse, A. C., Merlet, C., Allan, P. K., Humphreys, E. K., Griffin, J. M., Aslan, M., Zeiger, M., Presser, V., Gogotsi, Y., & Grey, C. P. (2015). New insights into the structure of nanoporous carbons from NMR, Raman, and pair distribution function analysis. *Chemistry of Materials*, *27*(19), 6848–6857.

Franken, L. E., Grünewald, K., Boekema, E. J., & Stuart, M. C. A. (2020). A technical introduction to transmission electron microscopy for soft-matter: Imaging, possibilities, choices, and technical developments. *Small*, *16*(14), 1906198.

Freese, C., Uboldi, C., Gibson, M. I., Unger, R. E., Weksler, B. B., Romero, I. A., Couraud, P.-O., & Kirkpatrick, C. J. (2012). Uptake and cytotoxicity of citrate-coated gold nanospheres: comparative studies on human endothelial and epithelial cells. *Particle and Fibre Toxicology*, *9*, 1–11.

Gao, J., Huang, X., Liu, H., Zan, F., & Ren, J. (2012). Colloidal stability of gold nanoparticles modified with thiol compounds: bioconjugation and application in cancer cell imaging. *Langmuir*, *28*(9), 4464–4471.

García-Barrasa, J., López-de-Luzuriaga, J. M., & Monge, M. (2011). Silver nanoparticles: synthesis through chemical methods in solution and biomedical applications. *Central European Journal of Chemistry*, *9*, 7–19.

García-Garabal, S., Domínguez-Pérez, M., Cabeza, O., Arosa, Y., Varela, L. M., Fernández-López, C., Pérez-Juste, J., & Pastoriza-Santos, I. (2021). Effect of gold nanoparticles on transport properties of the protic ionic liquid propylammonium nitrate. *Journal of Chemical & Engineering Data*, *66*(8), 3028–3037.

García-Pinel, B., Porras-Alcalá, C., Ortega-Rodríguez, A., Sarabia, F., Prados, J., Melguizo, C., & López-Romero, J. M. (2019). Lipid-based nanoparticles: application and recent advances in cancer treatment. *Nanomaterials*, *9*(4), 638.

Gawande, M. B., Goswami, A., Felpin, F.-X., Asefa, T., Huang, X., Silva, R., Zou, X., Zboril, R., & Varma, R. S. (2016). Cu and Cu-based nanoparticles: synthesis and applications in catalysis. *Chemical Reviews*, *116*(6), 3722–3811.

Gebreel, R. M., Edris, N. A., Elmofty, H. M., Tadros, M. I., El-Nabarawi, M. A., & Hassan, D. H. (2021). Development and characterization of PLGA nanoparticle-laden hydrogels for sustained ocular delivery of norfloxacin in the treatment of pseudomonas keratitis: An experimental study. *Drug*

Design, Development and Therapy, 399–418.

Ghasemiyeh, P., & Mohammadi-Samani, S. (2018). Solid lipid nanoparticles and nanostructured lipid carriers as novel drug delivery systems: Applications, advantages and disadvantages. *Research in Pharmaceutical Sciences*, *13*(4), 288.

Ghosh, P., Han, G., De, M., Kim, C. K., & Rotello, V. M. (2008). Gold nanoparticles in delivery applications. *Advanced Drug Delivery Reviews*, *60*(11), 1307–1315.

Giljohann, D. A., Seferos, D. S., Daniel, W. L., Massich, M. D., Patel, P. C., & Mirkin, C. A. (2010). Gold nanoparticles for biology and medicine. *Angewandte Chemie International Edition*, *49*(19), 3280–3294.

Gomes, A., Carnerero, J. M., Jimenez-Ruiz, A., Grueso, E., Giráldez-Pérez, R. M., & Prado-Gotor, R. (2021). Lysozyme–AuNPs Interactions: Determination of Binding Free Energy. *Nanomaterials*, *11*(8), 2139.

Gomes, H. I. O., Martins, C. S. M., & Prior, J. A. V. (2021). Silver nanoparticles as carriers of anticancer drugs for efficient target treatment of cancer cells. *Nanomaterials*, *11*(4), 964.

Good, N. E., Winget, G. D., Winter, W., Connolly, T. N., Izawa, S., & Singh, R. M. M. (1966). Hydrogen ion buffers for biological research. *Biochemistry*, *5*(2), 467–477.

Gordon, C. J., Tchesnokov, E. P., Woolner, E., Perry, J. K., Feng, J. Y., Porter, D. P., & Götte, M. (2020). Remdesivir is a direct-acting antiviral that inhibits

RNA-dependent RNA polymerase from severe acute respiratory syndrome coronavirus 2 with high potency. *Journal of Biological Chemistry*, *295*(20), 6785–6797.

Götze, M., Pettelkau, J., Fritzsche, R., Ihling, C. H., Schäfer, M., & Sinz, A. (2014). Automated assignment of MS/MS cleavable cross-links in protein 3D-structure analysis. *Journal of the American Society for Mass Spectrometry*, *26*(1), 83–97.

Grela, E., Ząbek, A., & Grabowiecka, A. (2015). Interferences in the optimization of the MTT assay for viability estimation of Proteus mirabilis. *Avicenna Journal of Medical Biotechnology*, *7*(4), 159.

Grieco, P. A., Clark, D. S., & Withers, G. P. (1979). Direct conversion of carboxylic acids into amides. *The Journal of Organic Chemistry*, *44*(16), 2945–2947.

Gunatillake, P. A., Adhikari, R., & Gadegaard, N. (2003). Biodegradable synthetic polymers for tissue engineering. *Eur Cell Mater*, *5*(1), 1–16.

Gutiérrez-Wing, C., Esparza, R., Vargas-Hernández, C., García, M. E. F., & José-Yacamán, M. (2012). Microwave-assisted synthesis of gold nanoparticles self-assembled into self-supported superstructures. *Nanoscale*, *4*(7), 2281–2287.

Hage, C., Iacobucci, C., Rehkamp, A., Arlt, C., & Sinz, A. (2017). The first zero-length mass spectrometry-cleavable cross-linker for protein structure analysis. *Angewandte Chemie*, *129*(46), 14743–14747.

Halnor, V. V, Pande, V. V, Borawake, D. D., & Nagare, H. S. (2018).

Nanoemulsion: A novel platform for drug delivery system. *J Mat Sci Nanotechol*, *6*(1), 104.

Hammami, I., & Alabdallah, N. M. (2021). Gold nanoparticles: Synthesis properties and applications. *Journal of King Saud University-Science*, *33*(7), 101560.

Hanby, A. R., Walsh, S. J., Counsell, A. J., Ashman, N., Mortensen, K. T., Carroll, J. S., & Spring, D. R. (2022). Antibody dual-functionalisation enabled through a modular divinylpyrimidine disulfide rebridging strategy. *Chemical Communications*, *58*(67), 9401–9404.

Hanson, J. E. (2013). NMR Spectroscopy in Nondeuterated Solvents (No-D NMR): Applications in the Undergraduate Organic Laboratory. In *NMR Spectroscopy in the Undergraduate Curriculum* (pp. 69–81). ACS Publications.

Harris, J. M. (1992). *Poly (ethylene glycol) chemistry: biotechnical and biomedical applications*. Springer Science & Business Media.

Haruta, M., & Daté, M. (2001). Advances in the catalysis of Au nanoparticles. *Applied Catalysis A: General*, *222*(1–2), 427–437.

Hassanisaadi, M., Bonjar, G. H. S., Rahdar, A., Pandey, S., Hosseinipour, A., & Abdolshahi, R. (2021). Environmentally safe biosynthesis of gold nanoparticles using plant water extracts. *Nanomaterials*, *11*(8), 2033.

He, C., & Lin, W. (2015). Hybrid nanoparticles for cancer imaging and therapy. *Nanotechnology-Based Precision Tools for the Detection and Treatment of*

Cancer, 173–192.

Henrich-Noack, P., Nikitovic, D., Neagu, M., Docea, A. O., Engin, A. B., Gelperina, S., Shtilman, M., Mitsias, P., Tzanakakis, G., & Gozes, I. (2019). The blood–brain barrier and beyond: Nano-based neuropharmacology and the role of extracellular matrix. *Nanomedicine: Nanotechnology, Biology and Medicine*, *17*, 359–379.

Herizchi, R., Abbasi, E., Milani, M., & Akbarzadeh, A. (2016). Current methods for synthesis of gold nanoparticles. *Artificial Cells, Nanomedicine, and Biotechnology*, *44*(2), 596–602.

Heuer-Jungemann, A., Feliu, N., Bakaimi, I., Hamaly, M., Alkilany, A., Chakraborty, I., Masood, A., Casula, M. F., Kostopoulou, A., & Oh, E. (2019). The role of ligands in the chemical synthesis and applications of inorganic nanoparticles. *Chemical Reviews*, *119*(8), 4819–4880.

Hines, D. J., & Kaplan, D. L. (2013). Poly (lactic-co-glycolic) acid− controlled-release systems: experimental and modeling insights. *Critical Reviews™ in Therapeutic Drug Carrier Systems*, *30*(3).

Homayun, B., Lin, X., & Choi, H.-J. (2019). Challenges and recent progress in oral drug delivery systems for biopharmaceuticals. *Pharmaceutics*, *11*(3), 129.

Hong, S., Choi, D. W., Kim, H. N., Park, C. G., Lee, W., & Park, H. H. (2020). Protein-based nanoparticles as drug delivery systems. *Pharmaceutics*, *12*(7), 604.

Hong, T.-K., Yang, H.-S., & Choi, C. J. (2005). Study of the enhanced thermal conductivity of Fe nanofluids. *Journal of Applied Physics*, *97*(6), 64311.

Hou, P.-X., Liu, C., & Cheng, H.-M. (2008). Purification of carbon nanotubes. *Carbon*, *46*(15), 2003–2025.

Hou, X., & Jones, B. T. (2000). Inductively coupled plasma/optical emission spectrometry. In *Encyclopedia of analytical chemistry* (Vol. 2000, pp. 9468–9485). John Wiley & Sons Chichester, UK.

Hu, X., Zhang, Y., Ding, T., Liu, J., & Zhao, H. (2020). Multifunctional gold nanoparticles: a novel nanomaterial for various medical applications and biological activities. *Frontiers in Bioengineering and Biotechnology*, *8*, 990.

Huang, M., Xiong, E., Wang, Y., Hu, M., Yue, H., Tian, T., Zhu, D., Liu, H., & Zhou, X. (2022). Fast microwave heating-based one-step synthesis of DNA and RNA modified gold nanoparticles. *Nature Communications*, *13*(1), 1–14.

Huang, X., & El-Sayed, M. A. (2010). Gold nanoparticles: Optical properties and implementations in cancer diagnosis and photothermal therapy. *Journal of Advanced Research*, *1*(1), 13–28.

Huang, Y., Li, X., Cao, J., Wei, X., Li, Y., Wang, Z., Cai, X., Li, R., & Chen, J. (2022). Use of dissociation degree in lysosomes to predict metal oxide nanoparticle toxicity in immune cells: Machine learning boosts nano-safety assessment. *Environment International*, *164*, 107258.

Hussain, S., Vanoirbeek, J. A. J., & Hoet, P. H. M. (2012). Interactions of nanomaterials with the immune system. *Wiley Interdisciplinary Reviews:*

Nanomedicine and Nanobiotechnology, *4*(2), 169–183.

Hutanu, D., Frishberg, M. D., Guo, L., & Darie, C. C. (2014). Recent applications of polyethylene glycols (PEGs) and PEG derivatives. *Mod. Chem. Appl*, *2*(2), 1–6.

Ide, M. S., & Davis, R. J. (2014). The important role of hydroxyl on oxidation catalysis by gold nanoparticles. *Accounts of Chemical Research*, *47*(3), 825–833.

Inam, W., Bhadane, R., Akpolat, R. N., Taiseer, R. A., Filippov, S. K., Salo-Ahen, O. M. H., Rosenholm, J. M., & Zhang, H. (2022). Interactions between polymeric nanoparticles and different buffers as investigated by zeta potential measurements and molecular dynamics simulations. *View*, *3*(4), 20210009.

Jafari, H., Ghaffari, P., Niknezhad, V., Abedi, A., Izadifar, Z., Mohammadinejad, R., Varma, R. S., & Shavandi, A. (2022). Tannic acid: a versatile polyphenol for design of biomedical hydrogels. *Journal of Materials Chemistry B*.

Jain, P. K., Huang, X., El-Sayed, I. H., & El-Sayed, M. A. (2008). Noble metals on the nanoscale: optical and photothermal properties and some applications in imaging, sensing, biology, and medicine. *Accounts of Chemical Research*, *41*(12), 1578–1586.

Jayalakshmi, K., Ibrahim, M., & Rao, K. V. (2014). Effect of pH on the size of gold nanoparticles. *International Journal of Electronic and Electrical Engineering*, *7*(2), 159–164.

Jha, B., Prasad, K., & Jha, A. K. (2018). *Cytotoxicity of Biogenic Gold Nanoparticles against Lung Cancer Cell Line (A549): An Application*. *December*, 1–7. https://doi.org/10.20944/preprints201812.0308.v1

Jha, N., & Ramaprabhu, S. (2008). Synthesis and thermal conductivity of copper nanoparticle decorated multiwalled carbon nanotubes based nanofluids. *The Journal of Physical Chemistry C*, *112*(25), 9315–9319.

Ji, Y., Yang, X., Ji, Z., Zhu, L., Ma, N., Chen, D., Jia, X., Tang, J., & Cao, Y. (2020). DFT-calculated IR spectrum amide I, II, and III band contributions of N-methylacetamide fine components. *ACS Omega*, *5*(15), 8572–8578.

Jiang, Y., Wang, Z., Duan, W., Liu, L., Si, M., Chen, X., & Fang, C.-J. (2020). The critical size of gold nanoparticles for overcoming P-gp mediated multidrug resistance. *Nanoscale*, *12*(31), 16451–16461.

Jin, X., Yu, H., Zhang, Z., Cui, T., Wu, Q., Liu, X., Gao, J., Zhao, X., Shi, J., & Qu, G. (2021). Surface charge-dependent mitochondrial response to similar intracellular nanoparticle contents at sublethal dosages. *Particle and Fibre Toxicology*, *18*, 1–15.

John D. Roberts and Marjorie C. Caserio. (2021). *Spectroscopic Properties of Amines*. https://chem.libretexts.org/Bookshelves/Organic_Chemistry/Basic_Principles_of_Organic_Chemistry_(Roberts_and_Caserio)/23%3A_Organonitrogen_Compounds_I_-_Amines/23.05%3A_Spectroscopic_Properties_of_Amines

Joshi, P., Chakraborty, S., Dey, S., Shanker, V., Ansari, Z. A., Singh, S. P., &

Chakrabarti, P. (2011). Binding of chloroquine-conjugated gold nanoparticles with bovine serum albumin. *Journal of Colloid and Interface Science*, *355*(2), 402–409. https://doi.org/10.1016/j.jcis.2010.12.032

Joudeh, N., & Linke, D. (2022). Nanoparticle classification, physicochemical properties, characterization, and applications: a comprehensive review for biologists. *Journal of Nanobiotechnology*, *20*(1), 262.

Kamnev, A. A. (2013). Infrared spectroscopy in studying biofunctionalised gold nanoparticles. *Nanomaterials Imaging Techniques, Surface Studies, and Applications: Selected Proceedings of the FP7 International Summer School Nanotechnology: From Fundamental Research to Innovations, August 26-September 2, 2012, Bukovel, Ukraine*, 35–50.

Kant, A. M., De, P., Peng, X., Yi, T., Rawlings, D. J., Kim, J. S., & Durden, D. L. (2002). SHP-1 regulates Fcγ receptor–mediated phagocytosis and the activation of RAC. *Blood, The Journal of the American Society of Hematology*, *100*(5), 1852–1859.

Kataoka, K., Harada, A., & Nagasaki, Y. (2012). Block copolymer micelles for drug delivery: Design, characterization and biological significance. *Advanced Drug Delivery Reviews*, *64*(SUPPL.), 37–48. https://doi.org/10.1016/j.addr.2012.09.013

Kaufman, E. D., Belyea, J., Johnson, M. C., Nicholson, Z. M., Ricks, J. L., Shah, P. K., Bayless, M., Pettersson, T., Feldotö, Z., & Blomberg, E. (2007). Probing protein adsorption onto mercaptoundecanoic acid stabilized gold nanoparticles and surfaces by quartz crystal microbalance and ζ-potential

measurements. *Langmuir*, *23*(11), 6053–6062.

Kaul, S., Gulati, N., Verma, D., Mukherjee, S., & Nagaich, U. (2018). Role of nanotechnology in cosmeceuticals: a review of recent advances. *Journal of Pharmaceutics*, *2018*.

Kettler, K., Veltman, K., van De Meent, D., van Wezel, A., & Hendriks, A. J. (2014). Cellular uptake of nanoparticles as determined by particle properties, experimental conditions, and cell type. *Environmental Toxicology and Chemistry*, *33*(3), 481–492.

Khalid, A. H., & Kontis, K. (2008). Thermographic phosphors for high temperature measurements: principles, current state of the art and recent applications. *Sensors*, *8*(9), 5673–5744.

Khan, I., Saeed, K., & Khan, I. (2019). Nanoparticles: Properties, applications and toxicities. *Arabian Journal of Chemistry*, *12*(7), 908–931.

Kim, H., Seo, Y. S., Kim, K., Han, J. W., Park, Y., & Cho, S. (2016). Concentration effect of reducing agents on green synthesis of gold nanoparticles: size, morphology, and growth mechanism. *Nanoscale Research Letters*, *11*, 1–9.

Kim, J., & De Jesus, O. (2022). Medication routes of administration. In *StatPearls [Internet]*. StatPearls Publishing.

Kim, Y., Beck-Broichsitter, M., & Banga, A. K. (2019). Design and evaluation of a poly (lactide-co-glycolide)-based in situ film-forming system for topical delivery of trolamine salicylate. *Pharmaceutics*, *11*(8), 409.

Kimling, J., Maier, M., Okenve, B., Kotaidis, V., Ballot, H., & Plech, A. (2006).

Turkevich method for gold nanoparticle synthesis revisited. *The Journal of Physical Chemistry B*, *110*(32), 15700–15707.

Klębowski, B., Depciuch, J., Parlińska-Wojtan, M., & Baran, J. (2018). Applications of noble metal-based nanoparticles in medicine. *International Journal of Molecular Sciences*, *19*(12), 4031.

Kokkin, D. L., Zhang, R., Steimle, T. C., Wyse, I. A., Pearlman, B. W., & Varberg, T. D. (2015). Au–S bonding revealed from the characterization of diatomic gold sulfide, AuS. *The Journal of Physical Chemistry A*, *119*(48), 11659–11667.

Kong, F.-Y., Zhang, J.-W., Li, R.-F., Wang, Z.-X., Wang, W.-J., & Wang, W. (2017). Unique roles of gold nanoparticles in drug delivery, targeting and imaging applications. *Molecules*, *22*(9), 1445.

Konhäuser, M., Kannaujiya, V. K., Steiert, E., Schwickert, K., Schirmeister, T., & Wich, P. R. (2022). Co-encapsulation of l-asparaginase and etoposide in dextran nanoparticles for synergistic effect in chronic myeloid leukemia cells. *International Journal of Pharmaceutics*, *622*, 121796.

Kovács, D., Igaz, N., Gopisetty, M. K., & Kiricsi, M. (2022). Cancer therapy by silver nanoparticles: fiction or reality? *International Journal of Molecular Sciences*, *23*(2), 839.

Kulshrestha, P. (2000). *Halo acids and DMSO: Electrophilic aromatic substitution at room temperature conditions*.

Kus-Liśkiewicz, M., Fickers, P., & Ben Tahar, I. (2021). Biocompatibility and

cytotoxicity of gold nanoparticles: recent advances in methodologies and regulations. *International Journal of Molecular Sciences*, *22*(20), 10952.

Laaksonen, T., Ahonen, P., Johans, C., & Kontturi, K. (2006). Stability and Electrostatics of Mercaptoundecanoic Acid-Capped Gold Nanoparticles with Varying Counterion Size. *ChemPhysChem*, *7*(10), 2143–2149.

Lafuente, E. M., Niedergang, F., & Rosales, C. (2020). Phagocytosis: Molecular Mechanisms and Physiological Implications. In *Frontiers in Immunology* (Vol. 11, p. 586918). Frontiers Media SA.

Lam, J., Herant, M., Dembo, M., & Heinrich, V. (2009). Baseline mechanical characterization of J774 macrophages. *Biophysical Journal*, *96*(1), 248–254.

Lambros, M., Tran, T., Fei, Q., & Nicolaou, M. (2022). Citric acid: A multifunctional pharmaceutical excipient. *Pharmaceutics*, *14*(5), 972.

Langer, R., & Peppas, N. A. (2003). Advances in Biomaterials, Drug Delivery, and Bionanotechnology. *AIChE Journal*, *49*(12), 2990–3006. https://doi.org/10.1002/aic.690491202

Lee, J. H., & Yeo, Y. (2015). Controlled drug release from pharmaceutical nanocarriers. *Chemical Engineering Science*, *125*, 75–84.

Li, C. H., & Peterson, G. P. (2007). The effect of particle size on the effective thermal conductivity of Al 2 O 3-water nanofluids. *Journal of Applied Physics*, *101*(4), 44312.

Li, N., Xia, T., & Nel, A. E. (2008). The role of oxidative stress in ambient particulate matter-induced lung diseases and its implications in the toxicity

of engineered nanoparticles. *Free Radical Biology and Medicine*, *44*(9), 1689–1699.

Liang, J.-J., Zhou, Y.-Y., Wu, J., & Ding, Y. (2014). Gold nanoparticle-based drug delivery platform for antineoplastic chemotherapy. *Current Drug Metabolism*, *15*(6), 620–631.

Lim, J.-M., Cai, T., Mandaric, S., Chopra, S., Han, H., Jang, S., Choi, W. Il, Langer, R., Farokhzad, O. C., & Karnik, R. (2019). Drug loading augmentation in polymeric nanoparticles using a coaxial turbulent jet mixer: Yong investigator perspective. *Journal of Colloid and Interface Science*, *538*, 45–50.

Lim, S.-W., Loh, H.-S., Ting, K.-N., Bradshaw, T. D., & Allaudin, Z. N. (2015). Reduction of MTT to purple formazan by vitamin E isomers in the absence of cells. *Tropical Life Sciences Research*, *26*(1), 111.

Lin, S.-Y., Tsai, Y.-T., Chen, C.-C., Lin, C.-M., & Chen, C. (2004). Two-step functionalization of neutral and positively charged thiols onto citrate-stabilized Au nanoparticles. *The Journal of Physical Chemistry B*, *108*(7), 2134–2139.

Little Jr, E. J., & Jones, M. M. (1960). A complete table of electronegativities. *Journal of Chemical Education*, *37*(5), 231.

Liu, P., Sun, J., Peng, W., Gu, Y., Ji, X., Su, Z., Liu, P., & Shen, J. (2023). Zwitterionic betaines over HEPES as the new generation biocompatible pH buffers for cell culture. *Bioactive Materials*, *24*, 376–386.

Liu, S., & Lämmerhofer, M. (2019). Functionalized gold nanoparticles for sample preparation: A review. *Electrophoresis*, *40*(18–19), 2438–2461. https://doi.org/10.1002/elps.201900111

Liu, Y., Xu, Y., Wu, M., Fan, L., He, C., Wan, J.-B., Li, P., Chen, M., & Li, H. (2016). Vitamin E succinate-conjugated F68 micelles for mitoxantrone delivery in enhancing anticancer activity. *International Journal of Nanomedicine*, *11*, 3167.

Loganathan, S., Valapa, R. B., Mishra, R. K., Pugazhenthi, G., & Thomas, S. (2017). Thermogravimetric analysis for characterization of nanomaterials. In *Thermal and Rheological Measurement Techniques for Nanomaterials Characterization* (pp. 67–108). Elsevier.

López-Lorente, Á. I., Soriano, M. L., & Valcárcel, M. (2014). Analysis of citrate-capped gold and silver nanoparticles by thiol ligand exchange capillary electrophoresis. *Microchimica Acta*, *181*, 1789–1796.

Lu, B., Lv, X., & Le, Y. (2019). Chitosan-modified PLGA nanoparticles for control-released drug delivery. *Polymers*, *11*(2), 304.

Lü, J.-M., Wang, X., Marin-Muller, C., Wang, H., Lin, P. H., Yao, Q., & Chen, C. (2009). Current advances in research and clinical applications of PLGA-based nanotechnology. *Expert Review of Molecular Diagnostics*, *9*(4), 325–341.

Lu, L., Duong, V. T., Shalash, A. O., Skwarczynski, M., & Toth, I. (2021). Chemical conjugation strategies for the development of protein-based subunit nanovaccines. *Vaccines*, *9*(6), 563.

Lu, W., Sun, Q., Wan, J., She, Z., & Jiang, X.-G. (2006). Cationic albumin–conjugated pegylated nanoparticles allow gene delivery into brain tumors via intravenous administration. *Cancer Research*, *66*(24), 11878–11887.

Lu, W., Tan, Y.-Z., Hu, K.-L., & Jiang, X.-G. (2005). Cationic albumin conjugated pegylated nanoparticle with its transcytosis ability and little toxicity against blood–brain barrier. *International Journal of Pharmaceutics*, *295*(1–2), 247–260.

Mabrouk, M., Das, D. B., Salem, Z. A., & Beherei, H. H. (2021). Nanomaterials for biomedical applications: Production, characterisations, recent trends and difficulties. *Molecules*, *26*(4), 1077.

Mahler, S., & Roy, I. (2015). Advances in Drug Delivery. *Journal of Chemical Technology and Biotechnology*, *90*(7), 1167–1168. https://doi.org/10.1002/jctb.4689

Majumder, J., Taratula, O., & Minko, T. (2019). Nanocarrier-based systems for targeted and site specific therapeutic delivery. *Advanced Drug Delivery Reviews*, *144*, 57–77.

Makadia, H. K., & Siegel, S. J. (2011). Poly lactic-co-glycolic acid (PLGA) as biodegradable controlled drug delivery carrier. *Polymers*, *3*(3), 1377–1397.

Male, K. B., Li, J., Buh, C. C., Ng, S. C., & Luong, J. H. T. (2008). Synthesis and stability of fluorescent gold nanoparticles by sodium borohydride in the presence of mono-6-deoxy-6-pyridinium-β-cyclodextrin chloride. *Journal of Physical Chemistry C*, *112*(2), 443–451. https://doi.org/10.1021/jp7099515

Mali, A. D. (2015). An updated review on transdermal drug delivery systems. *Skin*, *8*(9).

Manson, J., Kumar, D., Meenan, B. J., & Dixon, D. (2011). Polyethylene glycol functionalized gold nanoparticles: the influence of capping density on stability in various media. *Gold Bulletin*, *44*(2), 99–105.

Marciniak, L., Nowak, M., Trojanowska, A., Tylkowski, B., & Jastrzab, R. (2020). The effect of pH on the size of silver nanoparticles obtained in the reduction reaction with citric and malic acids. *Materials*, *13*(23), 5444.

Maréchal, Y. (1987). IR spectra of carboxylic acids in the gas phase: A quantitative reinvestigation. *The Journal of Chemical Physics*, *87*(11), 6344–6353.

Mathaes, R., Koulov, A., Joerg, S., & Mahler, H.-C. (2016). Subcutaneous injection volume of biopharmaceuticals—pushing the boundaries. *Journal of Pharmaceutical Sciences*, *105*(8), 2255–2259.

Mather, J. P., & Roberts, P. E. (1998). *Introduction to cell and tissue culture: theory and technique*. Springer Science & Business Media.

Maulik, V. T., Jennifer, S. L., & Teruna, J. S. (2009). The role of thiols and disulfides in protein chemical and physical stability. *Curr Protein Pept Sci*, *10*, 614–625.

Mazloomi-Rezvani, M., Salami-Kalajahi, M., Roghani-Mamaqani, H., & Pirayesh, A. (2018). Effect of surface modification with various thiol compounds on colloidal stability of gold nanoparticles. *Applied Organometallic Chemistry*,

32(2), e4079.

Mazumdar, S., Chitkara, D., & Mittal, A. (2021). Exploration and insights into the cellular internalization and intracellular fate of amphiphilic polymeric nanocarriers. *Acta Pharmaceutica Sinica B*, *11*(4), 903–924.

Mbanga, O., Cukrowska, E., & Gulumian, M. (2021). Dissolution of citrate-stabilized, polyethylene glycol–coated carboxyl and amine-functionalized gold nanoparticles in simulated biological fluids and environmental media. *Journal of Nanoparticle Research*, *23*, 1–16.

Milan-Rois, P., Rodriguez-Diaz, C., Castellanos, M., & Somoza, A. (2022). Conjugation of Nucleic Acids and Drugs to Gold Nanoparticles. In *Antisense RNA Design, Delivery, and Analysis* (pp. 103–116). Springer US New York, NY.

Mitchell, M. J., Billingsley, M. M., Haley, R. M., Wechsler, M. E., Peppas, N. A., & Langer, R. (2021). Engineering precision nanoparticles for drug delivery. *Nature Reviews Drug Discovery*, *20*(2), 101–124.

Mitragotri, S., Burke, P. A., & Langer, R. (2014). Overcoming the challenges in administering biopharmaceuticals: formulation and delivery strategies. *Nature Reviews Drug Discovery*, *13*(9), 655–672.

Mohamed, N. A., Marei, I., Crovella, S., & Abou-Saleh, H. (2022). Recent developments in nanomaterials-based drug delivery and upgrading treatment of cardiovascular diseases. *International Journal of Molecular Sciences*, *23*(3), 1404.

Moncalvo, F., Martinez Espinoza, M. I., & Cellesi, F. (2020). Nanosized delivery systems for therapeutic proteins: clinically validated technologies and advanced development strategies. *Frontiers in Bioengineering and Biotechnology*, *8*, 89.

Morsy, S. M. I. (2014). Role of surfactants in nanotechnology and their applications. *Int. J. Curr. Microbiol. App. Sci*, *3*(5), 237–260.

Mudalige, T., Qu, H., Van Haute, D., Ansar, S. M., Paredes, A., & Ingle, T. (2019). Characterization of nanomaterials: Tools and challenges. *Nanomaterials for Food Applications*, 313–353.

Muhamad12, I. I., Selvakumaran, S., & Lazim, N. A. M. (2014). Designing polymeric nanoparticles for targeted drug delivery system. *Nanomed*, *287*, 287.

Mulder, D. W., Phiri, M. M., Jordaan, A., & Vorster, B. C. (2019). Modified HEPES one-pot synthetic strategy for gold nanostars. *Royal Society Open Science*, *6*(6), 190160.

Murthy, S. K. (2007). Nanoparticles in modern medicine: state of the art and future challenges. *International Journal of Nanomedicine*, *2*(2), 129–141.

Naiim, M., Boualem, A., Ferre, C., Jabloun, M., Jalocha, A., & Ravier, P. (2015). Multiangle dynamic light scattering for the improvement of multimodal particle size distribution measurements. *Soft Matter*, *11*(1), 28–32.

Nazary Abrbekoh, F., Salimi, L., Saghati, S., Amini, H., Fathi Karkan, S., Moharamzadeh, K., Sokullu, E., & Rahbarghazi, R. (2022). Application of

microneedle patches for drug delivery; doorstep to novel therapies. *Journal of Tissue Engineering*, *13*, 20417314221085390.

Neethirajan, S., & Jayas, D. S. (2011). Nanotechnology for the food and bioprocessing industries. *Food and Bioprocess Technology*, *4*(1), 39–47.

Negishi, Y., Kurashige, W., Niihori, Y., & Nobusada, K. (2013). Toward the creation of stable, functionalized metal clusters. *Physical Chemistry Chemical Physics*, *15*(43), 18736–18751.

Ng, C. T., Tang, F. M. A., Li, J. J., Ong, C., Yung, L. L. Y., & Bay, B. H. (2015). Clathrin-mediated endocytosis of gold nanoparticles in vitro. *The Anatomical Record*, *298*(2), 418–427.

Ngo, V. K. T., Nguyen, D. G., Huynh, T. P., & Lam, Q. V. (2016). A low cost technique for synthesis of gold nanoparticles using microwave heating and its application in signal amplification for detecting Escherichia Coli O157: H7 bacteria. *Advances in Natural Sciences: Nanoscience and Nanotechnology*, *7*(3), 35016.

Nikoobakht, B., & El-Sayed, M. A. (2003). Preparation and growth mechanism of gold nanorods (NRs) using seed-mediated growth method. *Chemistry of Materials*. https://doi.org/10.1021/cm020732l

Nugrahani, I., & Jessica, M. A. (2021). Amino acids as the potential co-former for co-crystal development: a review. *Molecules*, *26*(11), 3279.

Oh, E., Delehanty, J. B., Sapsford, K. E., Susumu, K., Goswami, R., Blanco-Canosa, J. B., Dawson, P. E., Granek, J., Shoff, M., & Zhang, Q. (2011).

Cellular uptake and fate of PEGylated gold nanoparticles is dependent on both cell-penetration peptides and particle size. *ACS Nano*, *5*(8), 6434–6448.

Padín-González, E., Lancaster, P., Bottini, M., Gasco, P., Tran, L., Fadeel, B., Wilkins, T., & Monopoli, M. P. (2022). Understanding the role and impact of poly (ethylene glycol)(PEG) on nanoparticle formulation: implications for COVID-19 vaccines. *Frontiers in Bioengineering and Biotechnology*, *10*.

Patel, H. E., Das, S. K., Sundararajan, T., Sreekumaran Nair, A., George, B., & Pradeep, T. (2003). Thermal conductivities of naked and monolayer protected metal nanoparticle based nanofluids: Manifestation of anomalous enhancement and chemical effects. *Applied Physics Letters*, *83*(14), 2931–2933.

Pathak, C., Vaidya, F. U., Waghela, B. N., Jaiswara, P. K., Gupta, V. K., Kumar, A., Rajendran, B. K., & Ranjan, K. (2023). Insights of endocytosis signaling in health and disease. *International Journal of Molecular Sciences*, *24*(3), 2971.

Patra, J. K., Das, G., Fraceto, L. F., Campos, E. V. R., Rodriguez-Torres, M. del P., Acosta-Torres, L. S., Diaz-Torres, L. A., Grillo, R., Swamy, M. K., & Sharma, S. (2018). Nano based drug delivery systems: recent developments and future prospects. *Journal of Nanobiotechnology*, *16*(1), 1–33.

Pedersen, D. B., & Duncan, E. J. (2005). *Surface plasmon resonance spectroscopy of gold nanoparticle-coated substrates: Use as an indicator of exposure to chemical warfare simulants*. DEFENCE RESEARCH AND

DEVELOPMENT SUFFIELD (ALBERTA).

PEG, B. (2021). *FDA Approved PEGylated Drugs*. https://www.biochempeg.com/article/58.html

Pellegrini, P., Strambi, A., Zipoli, C., Hägg-Olofsson, M., Buoncervello, M., Linder, S., & De Milito, A. (2014). Acidic extracellular pH neutralizes the autophagy-inhibiting activity of chloroquine: implications for cancer therapies. *Autophagy*, *10*(4), 562–571.

Peng, J. W., Lepre, C. A., Fejzo, J., Abdul-Manan, N., & Moore, J. M. (2001). Nuclear magnetic resonance-based approaches for lead generation in drug discovery. *Methods in Enzymology*, *338*, 202–230.

Peng, S., McMahon, J. M., Schatz, G. C., Gray, S. K., & Sun, Y. (2010). Reversing the size-dependence of surface plasmon resonances. *Proceedings of the National Academy of Sciences*, *107*(33), 14530–14534.

Pereira, E. D., Cerruti, R., Fernandes, E., Peña, L., Saez, V., Pinto, J. C., Ramón, J. A., Oliveira, G. E., & Souza Júnior, F. G. de. (2016). Influence of PLGA and PLGA-PEG on the dissolution profile of oxaliplatin. *Polímeros*, *26*, 137–143.

Perera, G. S., Athukorale, S. A., Perez, F., Pittman Jr, C. U., & Zhang, D. (2018). Facile displacement of citrate residues from gold nanoparticle surfaces. *Journal of Colloid and Interface Science*, *511*, 335–343.

Perez, C., Sanchez, A., Putnam, D., Ting, D., Langer, R., & Alonso, M. J. (2001). Poly (lactic acid)-poly (ethylene glycol) nanoparticles as new carriers for the

delivery of plasmid DNA. *Journal of Controlled Release*, *75*(1–2), 211–224.

Petithory, T., Pieuchot, L., Josien, L., Ponche, A., Anselme, K., & Vonna, L. (2021). Size-dependent internalization efficiency of macrophages from adsorbed nanoparticle-based monolayers. *Nanomaterials*, *11*(8), 1963.

Piella, J., Bastús, N. G., & Puntes, V. (2016). Size-Controlled Synthesis of Sub-10-nanometer Citrate-Stabilized Gold Nanoparticles and Related Optical Properties. *Chemistry of Materials*. https://doi.org/10.1021/acs.chemmater.5b04406

Piludu, M., Medda, L., Monduzzi, M., & Salis, A. (2018). Gold nanoparticles: a powerful tool to visualize proteins on ordered mesoporous silica and for the realization of theranostic nanobioconjugates. *International Journal of Molecular Sciences*, *19*(7), 1991.

Podsiadlo, P., Sinani, V. A., Bahng, J. H., Kam, N. W. S., Lee, J., & Kotov, N. A. (2008). Gold nanoparticles enhance the anti-leukemia action of a 6-mercaptopurine chemotherapeutic agent. *Langmuir*, *24*(2), 568–574.

Polte, J., Ahner, T. T., Delissen, F., Sokolov, S., Emmerling, F., Thünemann, A. F., & Kraehnert, R. (2010). Mechanism of gold nanoparticle formation in the classical citrate synthesis method derived from coupled in situ XANES and SAXS evaluation. *Journal of the American Chemical Society*, *132*(4), 1296–1301.

Porwal, M., Rastogi, V., & Kumar, A. (2017). An overview on carbon nanotubes. *MOJ Bioequiv Availab*, *3*(5), 114–116.

Prasanthan, P., & Kishore, N. (2021). Self-assemblies of pluronic micelles in partitioning of anticancer drugs and effectiveness of this system towards target protein. *RSC Advances*, *11*(36), 22057–22069.

Prijic, S., & Sersa, G. (2011). Magnetic nanoparticles as targeted delivery systems in oncology. *Radiology and Oncology*, *45*(1), 1–16.

Proniewicz, E., Tąta, A., łowska, E., & Prahl, A. (2021). Is the Use of Surface-Enhanced Infrared Spectroscopy Justified in the Selection of Peptide Fragments That Play a Role in Substrate–Receptor Interactions? Adsorption of Amino Acids and Neurotransmitters on Colloidal Ag and Au Nanoparticles. *The Journal of Physical Chemistry B*, *125*(9), 2328–2338.

Pudlarz, A., & Szemraj, J. (2018). Nanoparticles as carriers of proteins, peptides and other therapeutic molecules. *Open Life Sciences*, *13*(1), 285–298.

Purdue University. (2023). *The Chemistry of Nitrogen and Phosphorous*. https://chemed.chem.purdue.edu/genchem/topicreview/bp/ch10/group5.php

Putnam, S. A., Cahill, D. G., Braun, P. V, Ge, Z., & Shimmin, R. G. (2006). Thermal conductivity of nanoparticle suspensions. *Journal of Applied Physics*, *99*(8), 84308.

Rakhmatullin, I. Z., Efimov, S. V, Klochkov, A. V, Gnezdilov, O. I., Varfolomeev, M. A., & Klochkov, V. V. (2022). NMR chemical shifts of carbon atoms and characteristic shift ranges in the oil sample. *Petroleum Research*, *7*(2), 269–274.

Ralph, P., & Nakoinz, I. (1975). Phagocytosis and cytolysis by a macrophage tumour and its cloned cell line. *Nature*, *257*(5525), 393–394.

Ralph, P., & Nakoinz, I. (1977). Antibody-dependent killing of erythrocyte and tumor targets by macrophage-related cell lines: enhancement by PPD and LPS. *The Journal of Immunology*, *119*(3), 950–954.

Rao, K. N. (1971). *Infrared Spectroscopy.* OHIO STATE UNIV COLUMBUS DEPT OF PHYSICS.

Rasmussen, H. B., Jürgens, G., Thomsen, R., Taboureau, O., Zeth, K., Hansen, P. E., & Hansen, P. R. (2021). Cellular uptake and intracellular phosphorylation of GS-441524: implications for its effectiveness against COVID-19. *Viruses*, *13*(7), 1369.

Rastogi, S., Kumari, V., Sharma, V., & Ahmad, F. J. (2021). Gold Nanoparticle-based Sensors in Food Safety Applications. *Food Analytical Methods*, 1–17.

Rayner, C. M. (1995). Synthesis of thiols, sulfides, sulfoxides and sulfones. *Contemporary Organic Synthesis*, *2*(6), 409–440.

Reusch, W. (1999). *Virtual textbook of organic chemistry*.

Rizvi, S. A. A., & Saleh, A. M. (2018). Applications of nanoparticle systems in drug delivery technology. *Saudi Pharmaceutical Journal*, *26*(1), 64–70.

Rocha, C. V., Gonçalves, V., da Silva, M. C., Bañobre-López, M., & Gallo, J. (2022). PLGA-based composites for various biomedical applications. *International Journal of Molecular Sciences*, *23*(4), 2034.

Rosenblum, D., Joshi, N., Tao, W., Karp, J. M., & Peer, D. (2018). Progress and

challenges towards targeted delivery of cancer therapeutics. *Nature Communications*, *9*(1), 1410.

Rzasa Lynn, R., & Galinkin, J. L. (2018). Naloxone dosage for opioid reversal: current evidence and clinical implications. *Therapeutic Advances in Drug Safety*, *9*(1), 63–88.

Saeedi, M., Eslamifar, M., Khezri, K., & Dizaj, S. M. (2019). Applications of nanotechnology in drug delivery to the central nervous system. *Biomedicine & Pharmacotherapy*, *111*, 666–675.

Saha, K., Agasti, S. S., Kim, C., Li, X., & Rotello, V. M. (2012). Gold nanoparticles in chemical and biological sensing. *Chemical Reviews*, *112*(5), 2739–2779.

Sangwan, S., & Seth, R. (2021). Synthesis, characterization and stability of gold nanoparticles (AuNPs) in different buffer systems. *Journal of Cluster Science*, 1–16.

Sapsford, K. E., Algar, W. R., Berti, L., Gemmill, K. B., Casey, B. J., Oh, E., Stewart, M. H., & Medintz, I. L. (2013). Functionalizing nanoparticles with biological molecules: developing chemistries that facilitate nanotechnology. *Chemical Reviews*, *113*(3), 1904–2074.

Šatkauskas, S., Jakštys, B., Ruzgys, P., & Jakutavičiūtė, M. (2016). Different cell viability assays following electroporation in vitro. *Handbook of Electroporation [Electronic Resource]/Editor Damijan Miklavcic. Cham, Switzerland: Springer International Publishing, 2016*.

Schneider-Futschik, E. K., & Reyes-Ortega, F. (2021). Advantages and

disadvantages of using magnetic nanoparticles for the treatment of complicated ocular disorders. *Pharmaceutics*, *13*(8), 1157.

Schulz, F., Dahl, G. T., Besztejan, S., Schroer, M. A., Lehmkühler, F., Grübel, G., Vossmeyer, T., & Lange, H. (2016). Ligand Layer Engineering to Control Stability and Interfacial Properties of Nanoparticles. *Langmuir*. https://doi.org/10.1021/acs.langmuir.6b01704

Senapati, S., Mahanta, A. K., Kumar, S., & Maiti, P. (2018). Controlled drug delivery vehicles for cancer treatment and their performance. *Signal Transduction and Targeted Therapy*, *3*(1), 7.

Shah, R., Eldridge, D., Palombo, E., & Harding, I. (2014). Optimisation and stability assessment of solid lipid nanoparticles using particle size and zeta potential. *Journal of Physical Science*, *25*(1).

Shalaeva, Y. V, Morozova, J. E., Shumatbaeva, A. M., Nizameev, I. R., Kadirov, M. K., & Antipin, I. S. (2019). Binding of L-tryptophan and bovine serum albumin by novel gold nanoparticles capped with amphiphilic sulfonatomethylated calixresorcinarenes. *Journal of Molecular Liquids*, *286*, 110879.

Shalkevich, N., Escher, W., Bürgi, T., Michel, B., Si-Ahmed, L., & Poulikakos, D. (2010). On the thermal conductivity of gold nanoparticle colloids. *Langmuir*, *26*(2), 663–670.

Shameli, K., Ahmad, M. Bin, Jazayeri, S. D., Sedaghat, S., Shabanzadeh, P., Jahangirian, H., Mahdavi, M., & Abdollahi, Y. (2012). Synthesis and characterization of polyethylene glycol mediated silver nanoparticles by the

green method. *International Journal of Molecular Sciences*, *13*(6), 6639–6650.

Shareef, M. A., Khar, R. K., Ahuja, A., Ahmad, F. J., & Raghava, S. (2003). Colonic drug delivery: an updated review. *AAPS Pharmsci*, *5*(2), E17–E17.

Sharifi, S., Behzadi, S., Laurent, S., Forrest, M. L., Stroeve, P., & Mahmoudi, M. (2012). Toxicity of nanomaterials. *Chemical Society Reviews*, *41*(6), 2323–2343.

Sharma, V., Verma, D., & Okram, G. S. (2020). Influence of surfactant, particle size and dispersion medium on surface plasmon resonance of silver nanoparticles. *Journal of Physics: Condensed Matter*, *32*(14), 145302.

Shilo, M., Berenstein, P., Dreifuss, T., Nash, Y., Goldsmith, G., Kazimirsky, G., Motiei, M., Frenkel, D., Brodie, C., & Popovtzer, R. (2015). Insulin-coated gold nanoparticles as a new concept for personalized and adjustable glucose regulation. *Nanoscale*, *7*(48), 20489–20496. https://doi.org/10.1039/c5nr04881h

Shon, Y.-S., Chuc, S., & Voundi, P. (2009). Stability of tetraoctylammonium bromide-protected gold nanoparticles: Effects of anion treatments. *Colloids and Surfaces A: Physicochemical and Engineering Aspects*, *352*(1–3), 12–17. https://doi.org/10.1016/J.COLSURFA.2009.09.037

Shukla, R., Bansal, V., Chaudhary, M., Basu, A., Bhonde, R. R., & Sastry, M. (2005). Biocompatibility of gold nanoparticles and their endocytotic fate inside the cellular compartment: a microscopic overview. *Langmuir*, *21*(23), 10644–10654.

Siegel, S. J., Kahn, J. B., Metzger, K., Winey, K. I., Werner, K., & Dan, N. (2006). Effect of drug type on the degradation rate of PLGA matrices. *European Journal of Pharmaceutics and Biopharmaceutics*, *64*(3), 287–293.

Simon-Deckers, A., Gouget, B., Mayne-L'Hermite, M., Herlin-Boime, N., Reynaud, C., & Carriere, M. (2008). In vitro investigation of oxide nanoparticle and carbon nanotube toxicity and intracellular accumulation in A549 human pneumocytes. *Toxicology*, *253*(1–3), 137–146.

Simon, J., Flahaut, E., & Golzio, M. (2019). Overview of carbon nanotubes for biomedical applications. *Materials*, *12*(4), 624.

Singh, A. P., Biswas, A., Shukla, A., & Maiti, P. (2019). Targeted therapy in chronic diseases using nanomaterial-based drug delivery vehicles. *Signal Transduction and Targeted Therapy*, *4*(1), 33.

Singh, R., & Lillard Jr, J. W. (2009). Nanoparticle-based targeted drug delivery. *Experimental and Molecular Pathology*, *86*(3), 215–223.

Sivaraman, S. K., Kumar, S., & Santhanam, V. (2010). Room-temperature synthesis of gold nanoparticles - Size-control by slow addition. *Gold Bulletin*. https://doi.org/10.1007/BF03214997

Smith, B. (2018). The C= O bond, part VI: Esters and the rule of three. *Spectroscopy*, *33*(7), 20–23.

Song, G., S Petschauer, J., J Madden, A., & C Zamboni, W. (2014). Nanoparticles and the mononuclear phagocyte system: pharmacokinetics and applications for inflammatory diseases. *Current Rheumatology Reviews*, *10*(1), 22–34.

Spicer, C. D., Pashuck, E. T., & Stevens, M. M. (2018). Achieving controlled biomolecule–biomaterial conjugation. *Chemical Reviews*, *118*(16), 7702–7743.

Stadtman, E. R. (1990). Metal ion-catalyzed oxidation of proteins: biochemical mechanism and biological consequences. *Free Radical Biology and Medicine*, *9*(4), 315–325.

Steckiewicz, K. P., Barcinska, E., Malankowska, A., Zauszkiewicz–Pawlak, A., Nowaczyk, G., Zaleska-Medynska, A., & Inkielewicz-Stepniak, I. (2019). Impact of gold nanoparticles shape on their cytotoxicity against human osteoblast and osteosarcoma in in vitro model. Evaluation of the safety of use and anti-cancer potential. *Journal of Materials Science: Materials in Medicine*, *30*, 1–15.

Stoll, V. S., & Blanchard, J. S. (1990). [4] Buffers: Principles and practice. In *Methods in enzymology* (Vol. 182, pp. 24–38). Elsevier.

Stuart, B. (2000). Infrared spectroscopy. *Kirk-Othmer Encyclopedia of Chemical Technology*.

Su, S., & M. Kang, P. (2020). Recent advances in nanocarrier-assisted therapeutics delivery systems. *Pharmaceutics*, *12*(9), 837.

Suchomel, P., Kvitek, L., Prucek, R., Panacek, A., Halder, A., Vajda, S., & Zboril, R. (2018). Simple size-controlled synthesis of Au nanoparticles and their size-dependent catalytic activity. *Scientific Reports*, *8*(1), 1–11. https://doi.org/10.1038/s41598-018-22976-5

Suk, J. S., Xu, Q., Kim, N., Hanes, J., & Ensign, L. M. (2016). PEGylation as a strategy for improving nanoparticle-based drug and gene delivery. *Advanced Drug Delivery Reviews*, *99*, 28–51.

Sur, S., Rathore, A., Dave, V., Reddy, K. R., Chouhan, R. S., & Sadhu, V. (2019). Recent developments in functionalized polymer nanoparticles for efficient drug delivery system. *Nano-Structures & Nano-Objects*, *20*, 100397.

Susumu, K., Medintz, I. L., Delehanty, J. B., Boeneman, K., & Mattoussi, H. (2010). Modification of poly (ethylene glycol)-capped quantum dots with nickel nitrilotriacetic acid and self-assembly with histidine-tagged proteins. *The Journal of Physical Chemistry C*, *114*(32), 13526–13531.

Susumu, K., Uyeda, H. T., Medintz, I. L., & Mattoussi, H. (2007). Design of biotin-functionalized luminescent quantum dots. *Journal of Biomedicine and Biotechnology*, *2007*.

Susumu, K., Uyeda, H. T., Medintz, I. L., Pons, T., Delehanty, J. B., & Mattoussi, H. (2007). Enhancing the stability and biological functionalities of quantum dots via compact multifunctional ligands. *Journal of the American Chemical Society*, *129*(45), 13987–13996.

Sztandera, K., Gorzkiewicz, M., & Klajnert-Maculewicz, B. (2018). Gold nanoparticles in cancer treatment. *Molecular Pharmaceutics*, *16*(1), 1–23.

Taha, M., e Silva, F. A., Quental, M. V, Ventura, S. P. M., Freire, M. G., & Coutinho, J. A. P. (2014). Good's buffers as a basis for developing self-buffering and biocompatible ionic liquids for biological research. *Green Chemistry*, *16*(6), 3149–3159.

Tang, L., He, M., Na, X., Guan, X., Zhang, R., Zhang, J., & Gu, J. (2019). Functionalized glass fibers cloth/spherical BN fillers/epoxy laminated composites with excellent thermal conductivities and electrical insulation properties. *Composites Communications*, *16*, 5–10.

Tester, R. F., Karkalas, J., & Qi, X. (2004). Starch—composition, fine structure and architecture. *Journal of Cereal Science*, *39*(2), 151–165.

Thambiraj, S., Hema, S., & Ravi Shankaran, D. (2018). Functionalized gold nanoparticles for drug delivery applications. *Materials Today: Proceedings*, *5*(8), 16763–16773. https://doi.org/10.1016/J.MATPR.2018.06.030

Thompson, J. M. (2018). *Infrared spectroscopy*. CRC Press.

Tiernan, H., Byrne, B., & Kazarian, S. G. (2020). ATR-FTIR spectroscopy and spectroscopic imaging for the analysis of biopharmaceuticals. *Spectrochimica Acta Part A: Molecular and Biomolecular Spectroscopy*, *241*, 118636.

Tiwari, G., Tiwari, R., Sriwastawa, B., Bhati, L., Pandey, S., Pandey, P., & Bannerjee, S. K. (2012). Drug delivery systems: An updated review. *International Journal of Pharmaceutical Investigation*, *2*(1), 2.

Tiwari, P. M., Vig, K., Dennis, V. A., & Singh, S. R. (2011). Functionalized gold nanoparticles and their biomedical applications. *Nanomaterials*, *1*(1), 31–63.

Tommalieh, M. J., Ibrahium, H. A., Awwad, N. S., & Menazea, A. A. (2020). Gold nanoparticles doped polyvinyl alcohol/chitosan blend via laser ablation for electrical conductivity enhancement. *Journal of Molecular Structure*, *1221*,

128814.

Tsolekile, N., Parani, S., Matoetoe, M. C., Songca, S. P., & Oluwafemi, O. S. (2017). Evolution of ternary I–III–VI QDs: Synthesis, characterization and application. *Nano-Structures & Nano-Objects*, *12*, 46–56.

Turkevitch, J., Stevenson, P. C., & Hillier, J. (1951). *Discuss. Faraday Soc*.

U.S. Food & Drug Adminstration. (2023). *FDA Approved PEGylated Drugs Up To 2023*. https://www.fda.gov/

Uhrich, K. E., Cannizzaro, S. M., Langer, R. S., & Shakesheff, K. M. (1999). Polymeric systems for controlled drug release. *Chemical Reviews*, *99*(11), 3181–3198.

Unkeless, J. C., Kaplan, G., Plutner, H., & Cohn, Z. A. (1979). Fc-receptor variants of a mouse macrophage cell line. *Proceedings of the National Academy of Sciences*, *76*(3), 1400–1404.

Van de Voort, F. R. (1992). Fourier transform infrared spectroscopy applied to food analysis. *Food Research International*, *25*(5), 397–403.

Várnai, B., Malanga, M., Sohajda, T., & Béni, S. (2022). Molecular interactions in remdesivir-cyclodextrin systems. *Journal of Pharmaceutical and Biomedical Analysis*, *209*, 114482.

Vedhanayagam, M., Andra, S., Muthalagu, M., & Sreeram, K. J. (2022). Influence of Functionalized Gold Nanorods on the Structure of Cytochrome–C: An Effective Bio-nanoconjugate for Biomedical Applications. *Inorganic Chemistry Communications*, *146*, 110182.

Venditti, I. (2019). Engineered gold-based nanomaterials: Morphologies and functionalities in biomedical applications. a mini review. *Bioengineering*, *6*(2), 53.

Venkatasubbu, G. D., Ramasamy, S., Ramakrishnan, V., & Kumar, J. (2013). Folate targeted PEGylated titanium dioxide nanoparticles as a nanocarrier for targeted paclitaxel drug delivery. *Advanced Powder Technology*, *24*(6), 947–954.

Veronese, F. M., Schiavon, O., Pasut, G., Mendichi, R., Andersson, L., Tsirk, A., Ford, J., Wu, G., Kneller, S., & Davies, J. (2005). PEG− doxorubicin conjugates: influence of polymer structure on drug release, in vitro cytotoxicity, biodistribution, and antitumor activity. *Bioconjugate Chemistry*, *16*(4), 775–784.

Vichai, V., & Kirtikara, K. (2006). Sulforhodamine B colorimetric assay for cytotoxicity screening. *Nature Protocols*, *1*(3), 1112–1116.

Vijayakumar, S. (2014). In vitro stability studies on gold nanoparticles with different stabilizing agents. *Int J Curr Sci*, *11*, 84–93.

Vijayakumar, S., & Ganesan, S. (2012). In vitro cytotoxicity assay on gold nanoparticles with different stabilizing agents. *Journal of Nanomaterials*, *2012*, 14.

Vishwakarma, V., Samal, S. S., & Manoharan, N. (2010). Safety and risk associated with nanoparticles-a review. *J. Miner. Mater. Charact. Eng*, *9*(5), 455–459.

Voigt, W. (2005). *Sulforhodamine B assay and chemosensitivity*. Springer.

Waheed, S., Li, Z., Zhang, F., Chiarini, A., Armato, U., & Wu, J. (2022). Engineering nano-drug biointerface to overcome biological barriers toward precision drug delivery. *Journal of Nanobiotechnology*, *20*(1), 395.

Walker, C., Mojares, E., & del Río Hernández, A. (2018). Role of extracellular matrix in development and cancer progression. *International Journal of Molecular Sciences*, *19*(10), 3028.

Walsh, S. J., Omarjee, S., Dannheim, F. M., Couturier, D. L., Bexheti, D., Mendil, L., Cronshaw, G., Fewster, T., Gregg, C., Brodie, C., Miller, J. L., Houghton, R., Carroll, J. S., & Spring, D. R. (2022). Divinylpyrimidine reagents generate antibody-drug conjugates with excellent: In vivo efficacy and tolerability. *Chemical Communications*, *58*(12), 1962–1965. https://doi.org/10.1039/d1cc06766d

Wang, P., Wang, X., Wang, L., Hou, X., Liu, W., & Chen, C. (2015). Interaction of gold nanoparticles with proteins and cells. *Science and Technology of Advanced Materials*, *16*(3), 34610.

Wang, S., Yu, H., & Wickliffe, J. K. (2011). Limitation of the MTT and XTT assays for measuring cell viability due to superoxide formation induced by nano-scale TiO2. *Toxicology in Vitro*, *25*(8), 2147–2151.

Wang, T., Guo, Y., He, Y., Ren, T., Yin, L., Fawcett, J. P., Gu, J., & Sun, H. (2020). Impact of molecular weight on the mechanism of cellular uptake of polyethylene glycols (PEGs) with particular reference to P-glycoprotein. *Acta Pharmaceutica Sinica B*, *10*(10), 2002–2009.

Wang, W., Wei, Q.-Q., Wang, J., Wang, B.-C., Zhang, S., & Yuan, Z. (2013). Role of thiol-containing polyethylene glycol (thiol-PEG) in the modification process of gold nanoparticles (AuNPs): stabilizer or coagulant? *Journal of Colloid and Interface Science*, *404*, 223–229.

Wang, X., & Chen, X. (2018). *Novel nanomaterials for biomedical, environmental and energy applications*. Elsevier.

Wang, Y., Murcia Valderrama, M. A., van Putten, R.-J., Davey, C. J. E., Tietema, A., Parsons, J. R., Wang, B., & Gruter, G.-J. M. (2022). Biodegradation and non-enzymatic hydrolysis of poly (lactic-co-glycolic acid)(PLGA12/88 and PLGA6/94). *Polymers*, *14*(1), 15.

Wang, Y., Strohm, E. M., Sun, Y., Wang, Z., Zheng, Y., Wang, Z., & Kolios, M. C. (2016). Biodegradable polymeric nanoparticles containing gold nanoparticles and Paclitaxel for cancer imaging and drug delivery using photoacoustic methods. *Biomedical Optics Express*, *7*(10), 4125–4138.

Wang, Z., Sun, X., Huang, T., Song, J., & Wang, Y. (2020). A sandwich nanostructure of gold nanoparticle coated reduced graphene oxide for photoacoustic imaging-guided photothermal therapy in the second NIR window. *Frontiers in Bioengineering and Biotechnology*, *8*, 655.

Wei, M.-Z., Deng, T.-S., Zhang, Q., Cheng, Z., & Li, S. (2021). Seed-mediated synthesis of gold nanorods at low concentrations of CTAB. *ACS Omega*, *6*(13), 9188–9195.

Weisbecker, C. S., Merritt, M. V, & Whitesides, G. M. (1996). Molecular self-assembly of aliphatic thiols on gold colloids. *Langmuir*, *12*(16), 3763–3772.

Whetten, R. L., Khoury, J. T., Alvarez, M. M., Murthy, S., Vezmar, I., Wang, Z. L., Stephens, P. W., Cleveland, C. L., Luedtke, W. D., & Landman, U. (1996). Nanocrystal gold molecules. *Advanced Materials*, *8*(5), 428–433.

Whitehead, C. B., Özkar, S., & Finke, R. G. (2021). LaMer's 1950 model of particle formation: a review and critical analysis of its classical nucleation and fluctuation theory basis, of competing models and mechanisms for phase-changes and particle formation, and then of its application to silver halide, semiconductor, metal, and metal-oxide nanoparticles. *Materials Advances*, *2*(1), 186–235.

Wilschefski, S. C., & Baxter, M. R. (2019). Inductively coupled plasma mass spectrometry: introduction to analytical aspects. *The Clinical Biochemist Reviews*, *40*(3), 115.

Woehrle, G. H., Brown, L. O., & Hutchison, J. E. (2005). Thiol-functionalized, 1.5-nm gold nanoparticles through ligand exchange reactions: Scope and mechanism of ligand exchange. *Journal of the American Chemical Society*, *127*(7), 2172–2183.

Wrigglesworth, E. G., & Johnston, J. H. (2017). The use of dual reductants in gold nanoparticle syntheses. *RSC Advances*, *7*(72), 45757–45762.

Wu, X. S., & Wang, N. (2001). Synthesis, characterization, biodegradation, and drug delivery application of biodegradable lactic/glycolic acid polymers. Part II: biodegradation. *Journal of Biomaterials Science, Polymer Edition*, *12*(1), 21–34.

Wu, Y., Wan, S., Yang, S., Hu, H., Zhang, C., Lai, J., Zhou, J., Chen, W., Tang,

X., & Luo, J. (2022). Macrophage cell membrane-based nanoparticles: a new promising biomimetic platform for targeted delivery and treatment. *Journal of Nanobiotechnology*, *20*(1), 542.

Xu, R. (2008). Progress in nanoparticles characterization: Sizing and zeta potential measurement. *Particuology*, *6*(2), 112–115.

Yadav, K. S., & Sawant, K. K. (2010). Modified nanoprecipitation method for preparation of cytarabine-loaded PLGA nanoparticles. *Aaps Pharmscitech*, *11*, 1456–1465.

Yafout, M., Ousaid, A., Khayati, Y., & El Otmani, I. S. (2021). Gold nanoparticles as a drug delivery system for standard chemotherapeutics: A new lead for targeted pharmacological cancer treatments. *Scientific African*, *11*, e00685.

Yahia, Lh. (2017). History and Applications of Hydrogels. *Journal of Biomedical Sciencies*, *04*(02), 1–23. https://doi.org/10.4172/2254-609x.100013

Yang, X., Ji, X., Shi, C., Liu, J., Wang, H., & Luan, Y. (2014). Investigation on the ion pair amphiphiles and their in vitro release of amantadine drug based on PLGA–PEG–PLGA gel. *Journal of Nanoparticle Research*, *16*, 1–14.

Yao, Y., Zhou, Y., Liu, L., Xu, Y., Chen, Q., Wang, Y., Wu, S., Deng, Y., Zhang, J., & Shao, A. (2020). Nanoparticle-based drug delivery in cancer therapy and its role in overcoming drug resistance. *Frontiers in Molecular Biosciences*, *7*, 193.

Yeh, Y.-C., Creran, B., & Rotello, V. M. (2012). Gold nanoparticles: preparation, properties, and applications in bionanotechnology. *Nanoscale*, *4*(6), 1871–

1880.

Yeung, V., Miller, D. D., & Rutzke, M. A. (2017). Atomic absorption spectroscopy, atomic emission spectroscopy, and inductively coupled plasma-mass spectrometry. *Food Analysis*, 129–150.

Yin, I. X., Zhang, J., Zhao, I. S., Mei, M. L., Li, Q., & Chu, C. H. (2020). The antibacterial mechanism of silver nanoparticles and its application in dentistry. *International Journal of Nanomedicine*, 2555–2562.

Zare, H., Ahmadi, S., Ghasemi, A., Ghanbari, M., Rabiee, N., Bagherzadeh, M., Karimi, M., Webster, T. J., Hamblin, M. R., & Mostafavi, E. (2021). Carbon nanotubes: Smart drug/gene delivery carriers. *International Journal of Nanomedicine*, *16*, 1681.

Zhang, J., Wang, C., Zhang, F., & Lin, W. (2021). Anionic surfactant sulfate dodecyl sodium (SDS)-induced thermodynamics and conformational changes of collagen by ultrasensitive microcalorimetry. *Journal of Leather Science and Engineering*, *3*, 1–6.

Zhang, M., Gao, S., Yang, D., Fang, Y., Lin, X., Jin, X., Liu, Y., Liu, X., Su, K., & Shi, K. (2021). Influencing factors and strategies of enhancing nanoparticles into tumors in vivo. *Acta Pharmaceutica Sinica B*, *11*(8), 2265–2285.

Zhang, Q., Chen, G., Yoon, S. F., Ahn, J., Wang, S. G., Zhou, Q., Wang, Q., & Li, J. Q. (2002). Thermal conductivity of multiwalled carbon nanotubes. *Physical Review B*, *66*(16), 165440.

Zhang, X.-F., Liu, Z.-G., Shen, W., & Gurunathan, S. (2016). Silver nanoparticles:

synthesis, characterization, properties, applications, and therapeutic approaches. *International Journal of Molecular Sciences*, *17*(9), 1534.

Zhao, Z., Ukidve, A., Kim, J., & Mitragotri, S. (2020). Targeting strategies for tissue-specific drug delivery. *Cell*, *181*(1), 151–167.

Zhou, J., Ralston, J., Sedev, R., & Beattie, D. A. (2009). Functionalized gold nanoparticles: Synthesis, structure and colloid stability. *Journal of Colloid and Interface Science*. https://doi.org/10.1016/j.jcis.2008.12.002

Zhu, H. T., Zhang, C. Y., Tang, Y. M., & Wang, J. X. (2007). Novel synthesis and thermal conductivity of CuO nanofluid. *The Journal of Physical Chemistry C*, *111*(4), 1646–1650.

Zielińska, A., Carreiró, F., Oliveira, A. M., Neves, A., Pires, B., Venkatesh, D. N., Durazzo, A., Lucarini, M., Eder, P., & Silva, A. M. (2020). Polymeric nanoparticles: production, characterization, toxicology and ecotoxicology. *Molecules*, *25*(16), 3731.

Appendix 1: <u>Zeta potential in stability studies of gold nanoparticles:</u>

Six measurements were conducted by DLS to measure the zeta potential for the synthesised Au NPs: K-TA-AuNPs (8.77 ±0.92 nm), SDS-AuNPs (16.31 ±0.38 nm), PEG-AuNPs (28.41 ±0.43 nm), cit-AuNPs (20.54 ±0.45 nm), Na-TA-AuNPs (10.68 ±0.68 nm), and TA-AuNPs (15.11 ±0.64 nm) (described in Chapter 3, Section 3.2.2). Then, the mean (¯μ) and standard deviation (σ) were indicated statistically using Orange Data Mining as following:

K-TA-AuNPs	SDS-AuNPs	PEG-AuNPs	cit-AuNPs	Na-TA-AuNPs	TA-AuNPs (0.5mM	
-38.10 mV	-37.10 mV	-33.80 mV	-33.61 mV	-21.50 mV	-11.80 mV	
-38.12 mV	-37.12 mV	-33.70 mV	-34.60 mV	-21.52 mV	-10.90 mV	
-38.45 mV	-37.13 mV	-33.80 mV	-33.60 mV	-21.55 mV	-11.20 mV	
-38.23 mV	-37.16 mV	-33.90 mV	-33.67 mV	-21.86 mV	-11.54 mV	
-38.91 mV	-37.98 mV	-33.33 mV	-33.68 mV	-21.57 mV	-11.90 mV	
-38.14 mV	-37.31 mV	-33.33 mV	-33.68 mV	-21.45 mV	-11.33 mV	
-38.33 mV	-37.30 mV	-33.81 mV	-33.64 mV	-21.58 mV	-11.45 mV	**Mean (¯μ)**
0.28	0.31	0.35	0.22	0.13	0.34	**STD (σ)**
0.099	0.117	0.063	0.152	0.021	0.142	**Variance**

Appendix 2: Data analysis using Cronbach's alpha:

Cronbach's alpha, α (or coefficient alpha), developed by Lee Cronbach in 1951. It is a powerful method for assessing the reliability or internal consistency of a set of measurement scales or survey items. Cronbach's Alpha is a statistical tool used in social sciences and research. The formula for Cronbach's alpha is:

$$\text{Cronbach's alpha } (\alpha) = \frac{N.\bar{c}}{\bar{v} + (N-1)\cdot\bar{c}}$$

Where:

N = the number of items, $\bar{c}$ = average covariance between item-pairs, and $\bar{v}$ = average variance.

Cronbach's Alpha value is typically ranging from 0 to 1, and a higher (α) value indicates greater consistency among the items, suggesting a stronger reliability of the measurements:

Cronbach's alpha	**Internal consistency '' or Reliability''**
$\alpha \geq 0.9$	Excellent
$0.9 > \alpha \geq 0.8$	Good
$0.8 > \alpha \geq 0.7$	Acceptable
$0.7 > \alpha \geq 0.6$	Questionable
$0.6 > \alpha \geq 0.5$	Poor
$0.5 > \alpha$	Unacceptable

In this study, the consistency of results of Au ions releases of the synthesised gold nanoparticles cit-AuNPs (20.54 ±0.45 nm), PEG-AuNPs (28.41 ±0.43 nm), and TA-AuNPs (15.11 ±0.64 nm) in four different media ultrapure water, DMEM cell culture medium, PBS and HEPES buffer solution was indicated and statistically compared by measuring the Cronbach's alpha, α (or coefficient alpha). Results showed that cit-AuNPs and PEG-AuNPs (Figure S. 1 and S. 2) have a high coefficient alpha at α = 0.98, followed by TA-AuNPs (Figure S. 3) with lower consistency at Cronbach's alpha (α) value = 0.87.

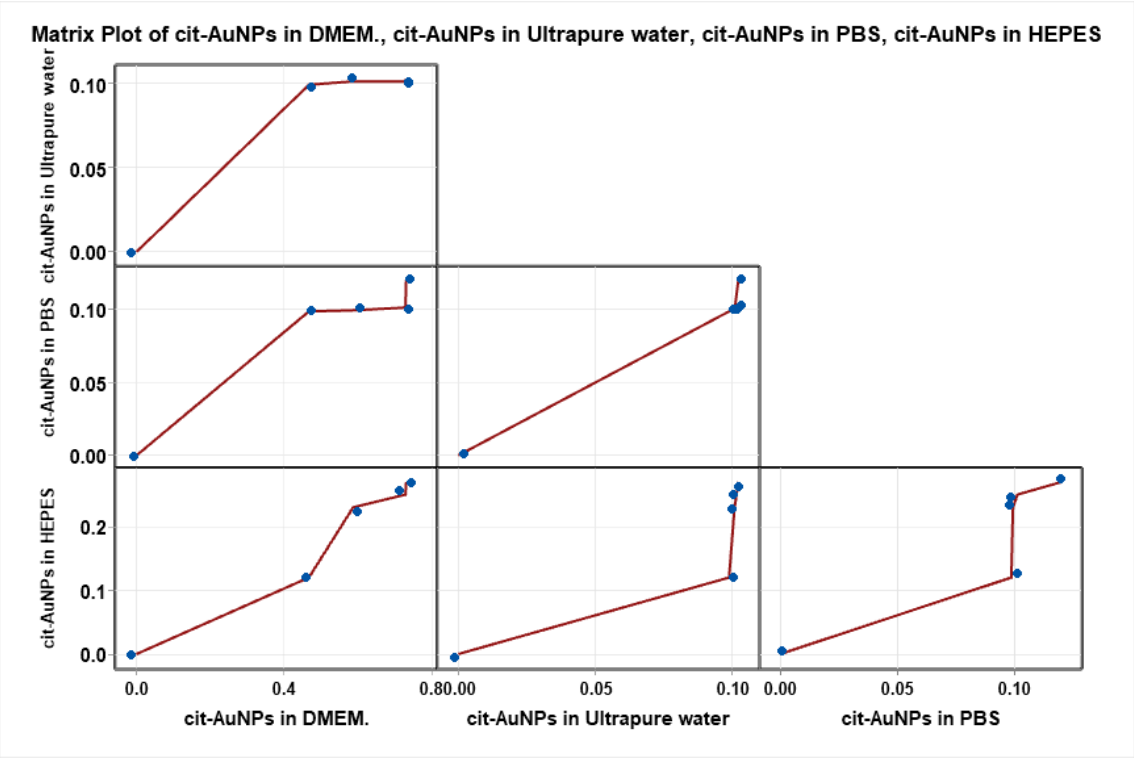

Figure S. 1. Comparison for Au ion concentration release of cit-AuNPs in four different media: DMEM cell culture media, ultrapure water, PBS, and HEPES. This comparison statistically employed by measuring the Cronbach's alpha, α (or coefficient alpha) at 0.98. The first column compares the concentration release of Au ions in MDEM, HEPES, PBS, and ultrapure water. The second column involves the comparison between ultrapure water, HEPES, and PBS, and the third column compares the concentration Au ion release in PBS and HEPES.

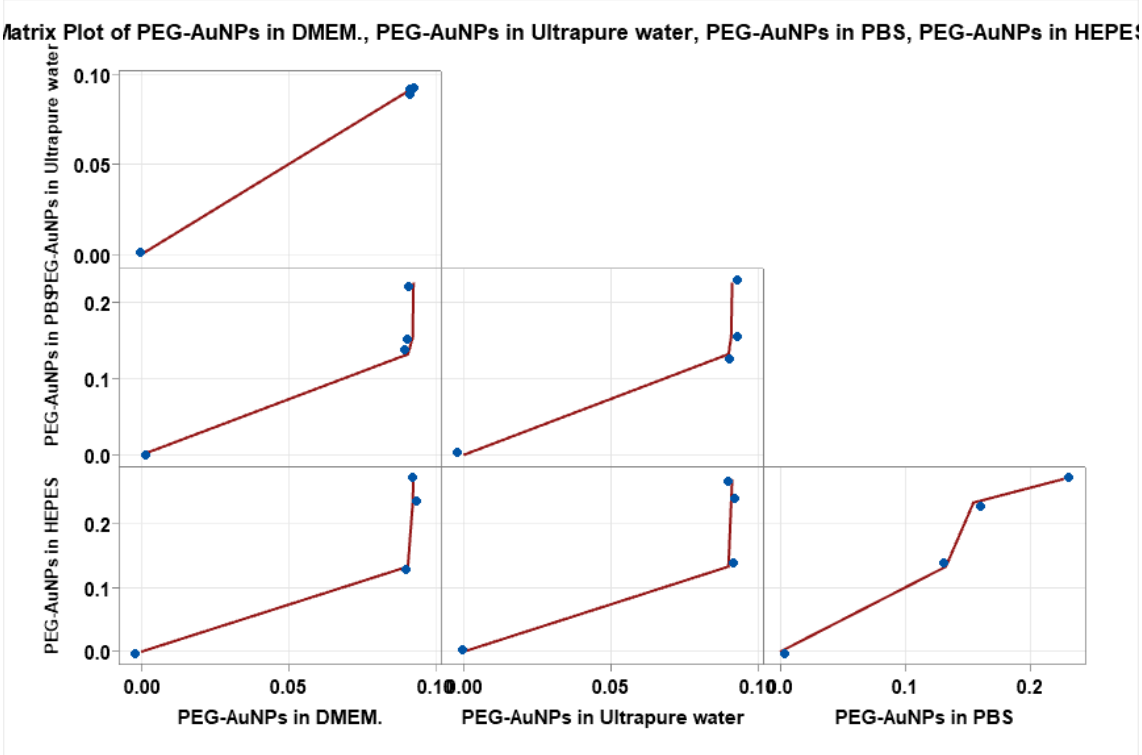

Figure S. 2. Comparison for Au ion concentration release of PEG-AuNPs in four different media: DMEM cell culture media, ultrapure water, PBS, and HEPES. This comparison statistically employed by measuring the Cronbach's alpha, α (or coefficient alpha) at 0.98. The first column compares the concentration release between MDEM, HEPES, PBS, and ultrapure water. The second column involves the comparison between ultrapure water, HEPES, and PBS, the third column compares the concentration Au ion release in PBS and HEPES.

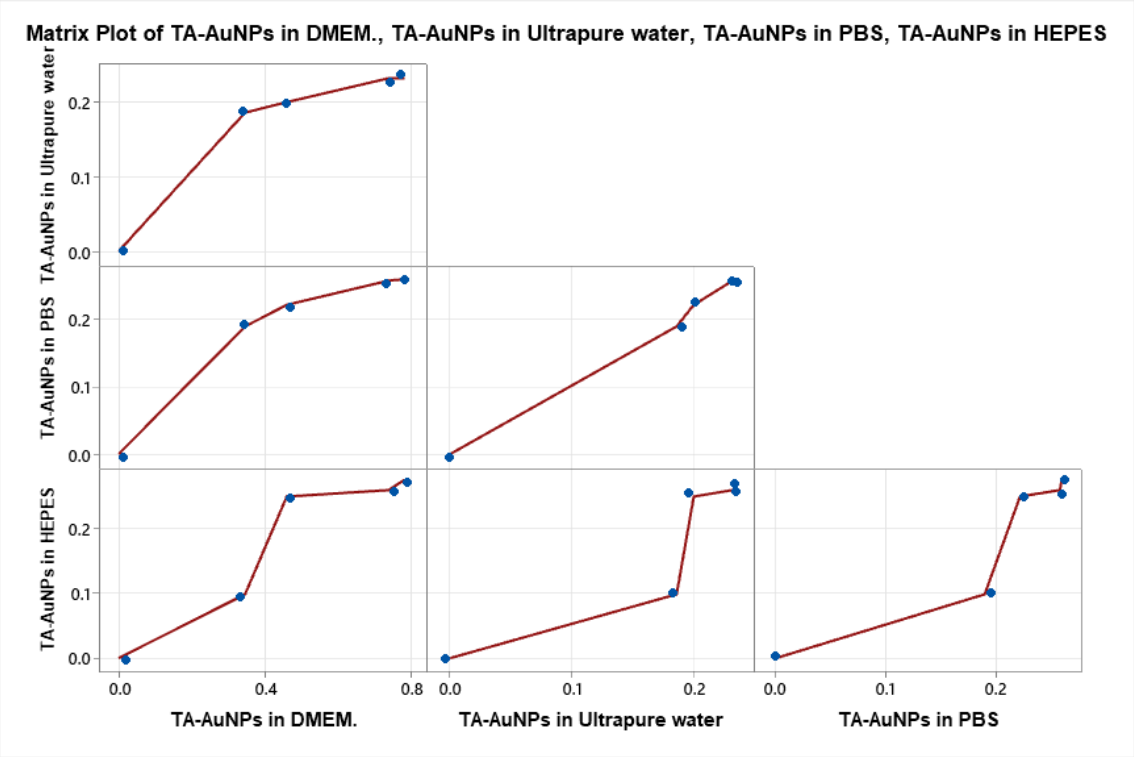

Figure S. 3. Comparison for Au ion concentration release of TA-AuNPs in four different media: DMEM cell culture media, ultrapure water, PBS, and HEPES. This comparison statistically employed by measuring the Cronbach's alpha, α (or coefficient alpha) at 0.87. The first column compares the concentration release between MDEM, HEPES, PBS, and ultrapure water. The second column involves the comparison between ultrapure water, HEPES, and PBS, the third column compares the concentration Au ion release in PBS and HEPES.

Appendix 3: The impact of temperature control on unconjugated and BSA-conjugated gold nanoparticles:

The impact of temperature on the unconjugated and BSA protein conjugated-gold nanoparticles was measured as described in Chapter 5, Section 5.2.5. Figure S.4, compares between the influences of temperature on SDS-AuNPs versus BSA-SDS-AuNPs over 360 minutes at temperature range from 25˚C up to 80˚C.

Data were analysed by measuring the Cronbach's alpha, α (or coefficient alpha) to indicate their consistency. The statistical results in Figure S.4 showed that SDS-BSA-AuNPs and SDS-AuNPs are not highly correlated with each other with poor consistency at low (α) value = 0.01.

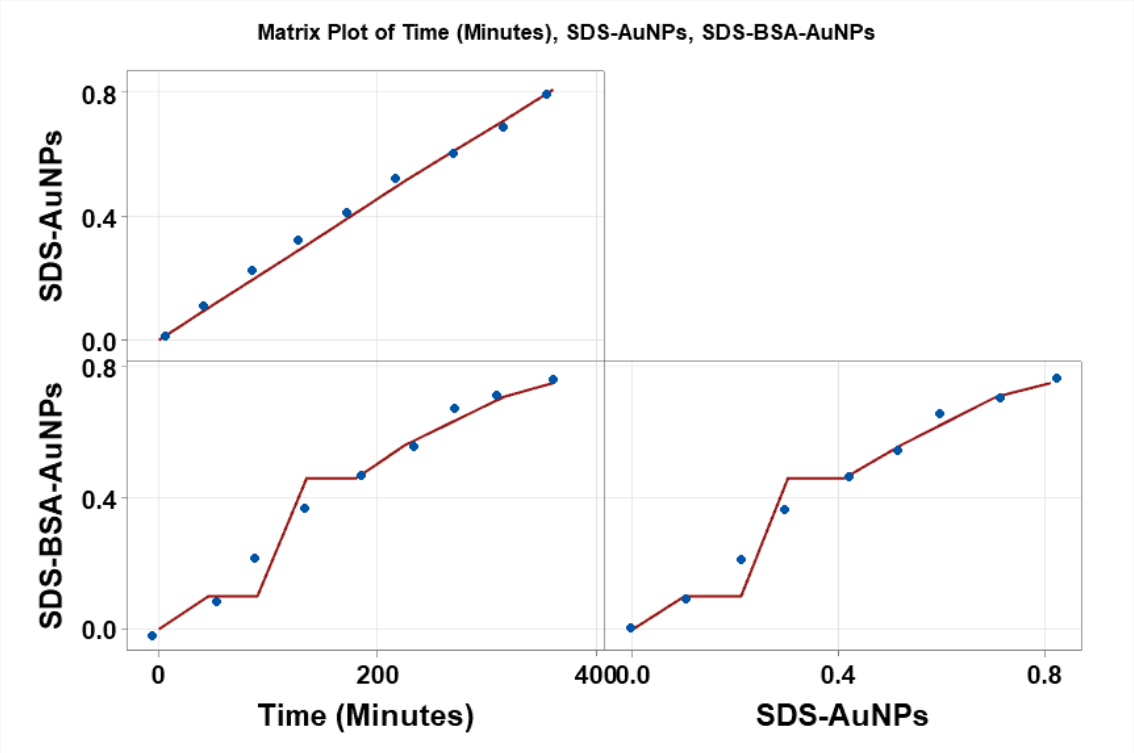

Figure S. 4. Data analysis illustrating the comparison between the synthesised SDS-gold nanoparticles and BSA conjugated-gold nanoparticles by measuring their consistency via Cronbach's alpha or coefficient alpha.

Appendix 4: Quantification of Au ions in the unconjugated and drug-conjugated gold nanoparticles:

In the cellular uptake assessment, the J774 exposed to 1 mL of two distinct concentrations 1 mgL^{-1} and 6 mgL^{-1} of the unconjugated and drug-conjugated gold nanoparticles: K-TA-AuNPs (8.77 ±0.928 nm), cit-Au NPs (20.54 ±0.45 nm),

MUDA-cit-Au NPs (50 ±0.98 nm), AMTD/AuNPs (160 nm), and REM/AuNPs (165 nm). The gold content has been determined by ICP-OES as shown in the following table:

cit-AuNPs	MUDA-cit-AuNPs	AMTD/AuNPs	REM/AuNPs	
1.1290 mgL^{-1}	1.0850 mgL^{-1}	0.3534 mgL^{-1}	0.4110 mgL^{-1}	
1.1310 mgL^{-1}	1.0950 mgL^{-1}	0.3544 mgL^{-1}	0.4210 mgL^{-1}	
1.1128 mgL^{-1}	1.0020 mgL^{-1}	0.3634 mgL^{-1}	0.4190 mgL^{-1}	
1.1208 mgL^{-1}	1.0993 mgL^{-1}	0.3594 mgL^{-1}	0.4130 mgL^{-1}	
1.1320 mgL^{-1}	1.0010 mgL^{-1}	0.3694 mgL^{-1}	0.4110 mgL^{-1}	
0.9890 mgL^{-1}	0.8842 mgL^{-1}	0.3514 mgL^{-1}	0.4010 mgL^{-1}	
1.1024 mgL^{-1}	**1.0277 mgL^{-1}**	**0.3586 mgL^{-1}**	**0.4127 mgL^{-1}**	**Mean**
0.0561	**0.0836**	**0.0069**	**0.0071**	**STD (σ)**

Appendix 5: High magnification TEM images for the unconjugated and drug-conjugated gold nanoparticles:

TEM investigation with high magnification images for the prepared gold nanoparticles: Na-TA-AuNPs (10.68 ±0.68 nm), K-TA-AuNPs (8.77 ±0.928 nm), TA-AuNPs 0.5 mM (15.11 ±0.64 nm), cit-AuNPs (20.54 ±0.45 nm), 4-MBA-cit-AuNPs, and MUDA-cit-AuNPs, were measured at various nanoscale bars (50 nm, 100 nm, 200 nm, 500 nm, 1000 nm, and 2000 nm), and introduced here in Figures S. 5, S. 6, S. 7, S. 8, S. 9, and S. 10), respectively.

These images can clarify one of the main reasons of choosing the citrate-gold nanoparticles (20.54 ±0.45 nm) to be functionalised with MUDA and further conjugated with amantadine and remdesivir. These type of nanoparticles showed a unique properties and they have been observed at high level of stability compared to the other prepared NPs, particularly over the assessment of their

physicochemical properties. In addition to their lower level of toxicity on J774 macrophage cells, the optimal size (20.54 ±0.45 nm) of these nanoparticles (cit-AuNPs) exhibited the lowest level of toxicity among the various NPs, notably at a concentration of 5 μgL^{-1}.

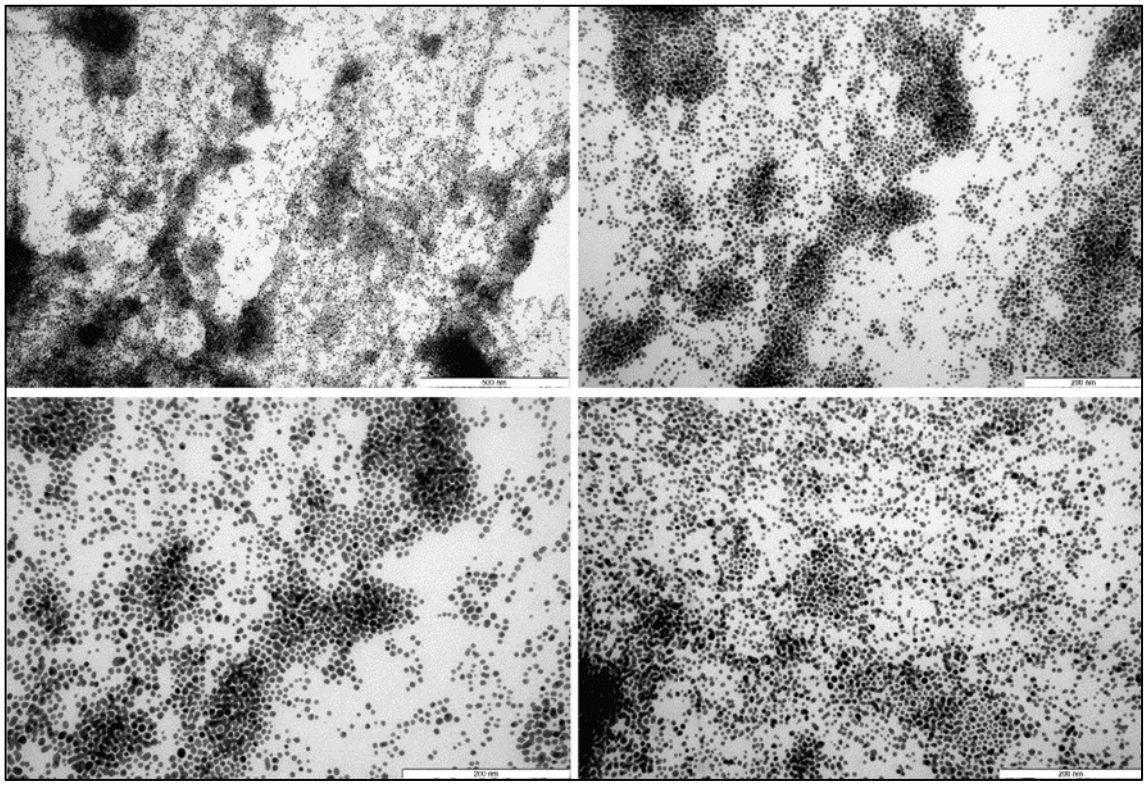

Figure S. 5. TEM images at various nanoscale bars (200 and 500 nm) for the prepared Na-TA-AuNPs.

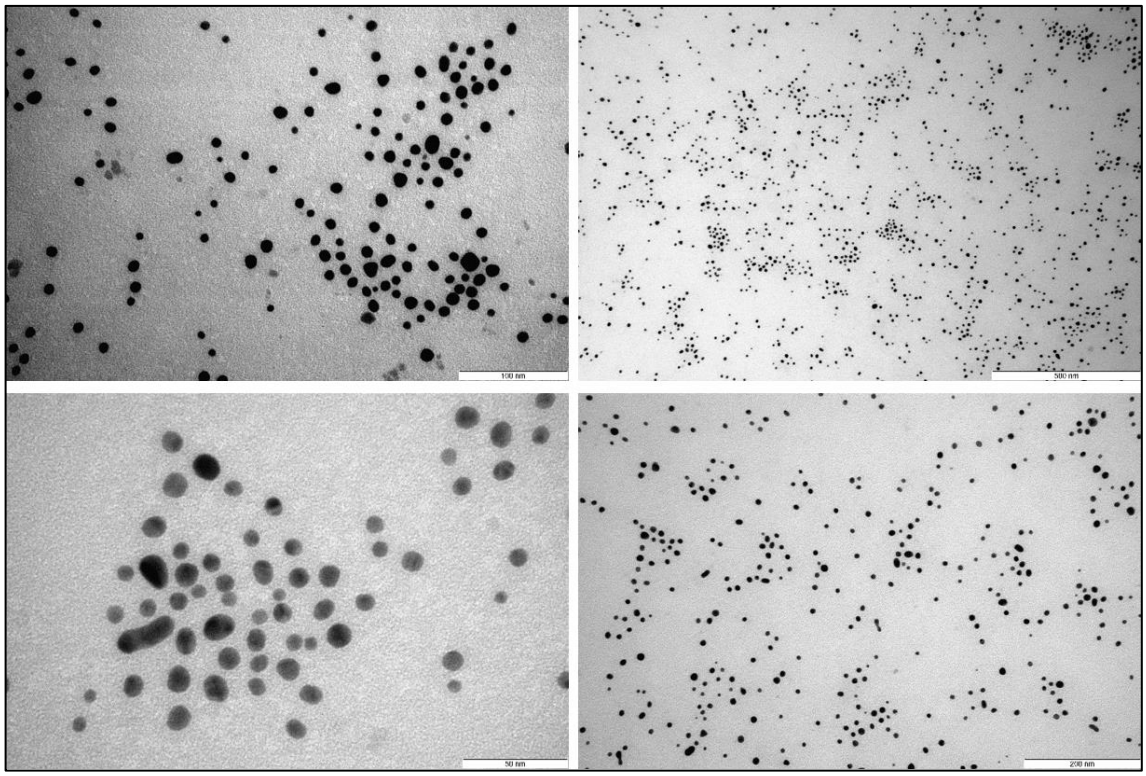

Figure S. 6. TEM high magnification images at various nanoscale bars at 50, 100, 200, and 500 nm for the K-TA-AuNPs.

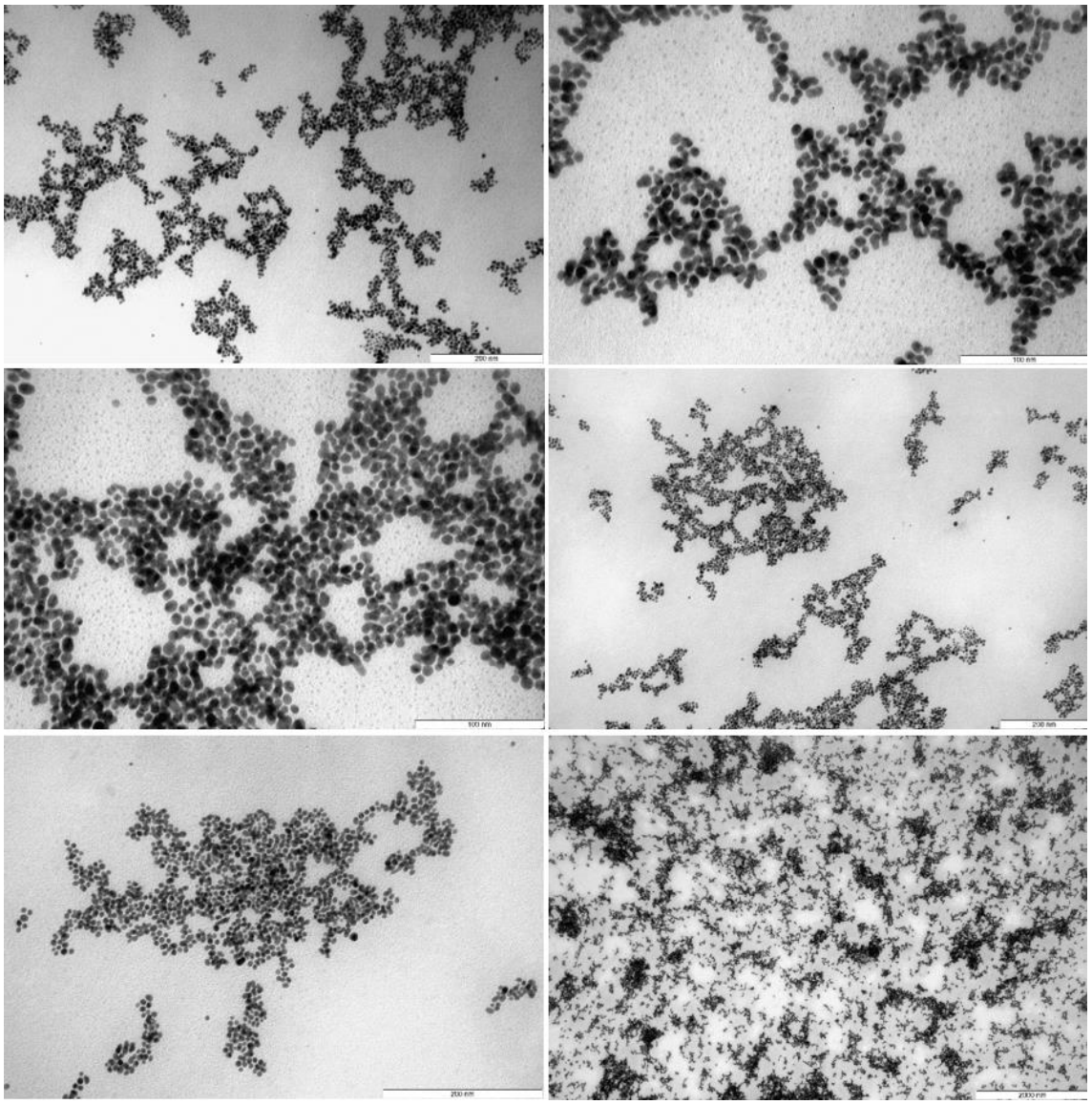

Figure S. 7. High magnification TEM images at nanoscale bars 100, 200, and 2000 nm, illustrate the aggregation effect of TA-AuNPs (0.5 mM, 15 nm).

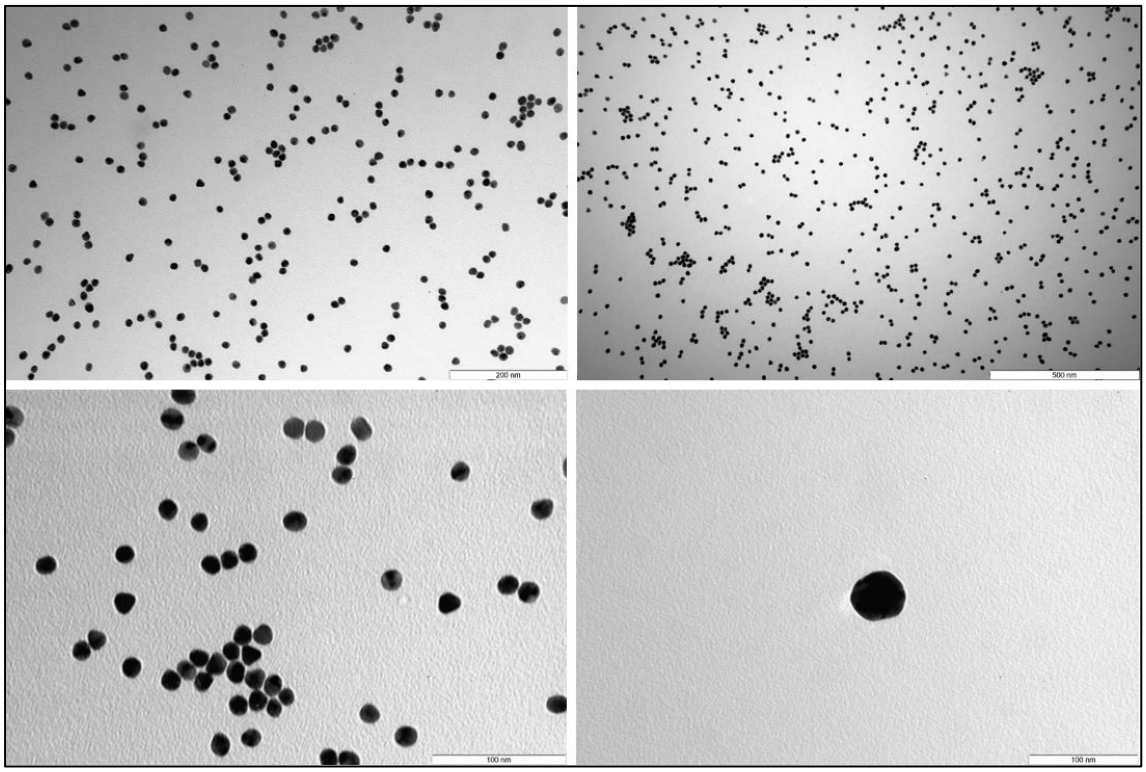

Figure S. 8. TEM high magnification images for the synthesised citrate-gold nanoparticles (20.54 ±0.45 nm) at various nanoscale bars (100 nm, 200 nm, and 500 nm).

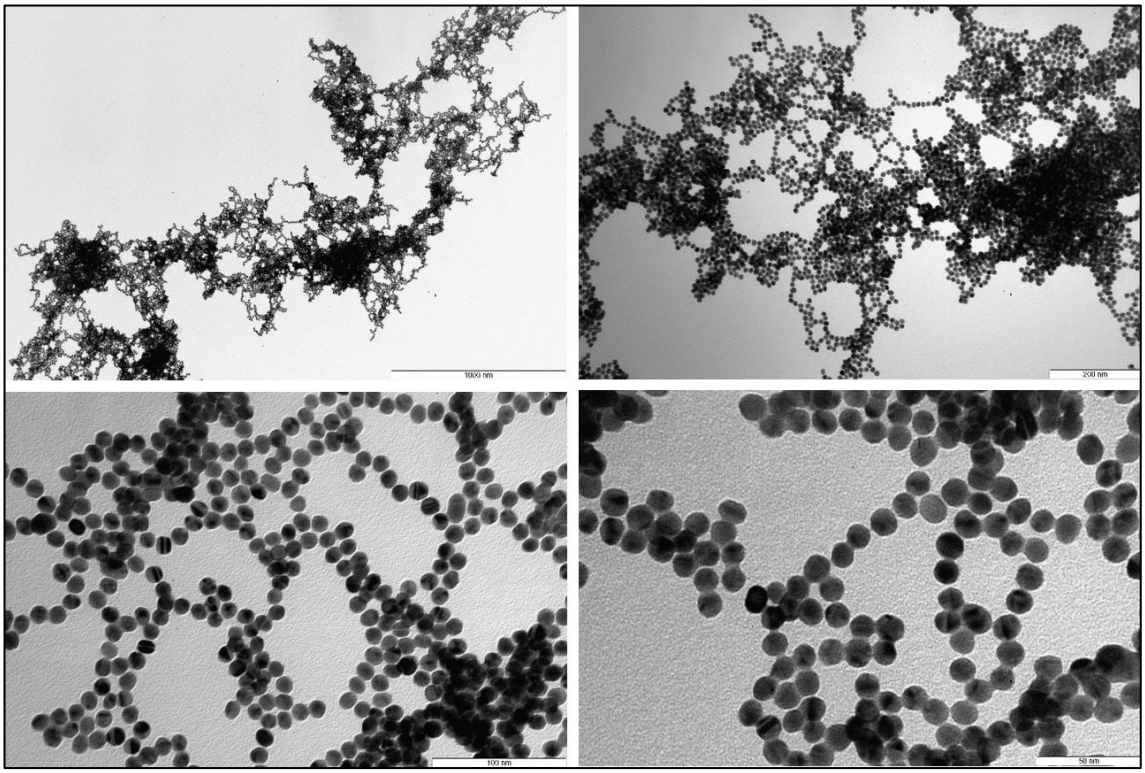

Figure S. 9. High magnification TEM images for the functionalised-gold nanoparticles 4-MBA-cit-AuNPs at various nanoscale bars (50, 100, 200, and 1000 nm).

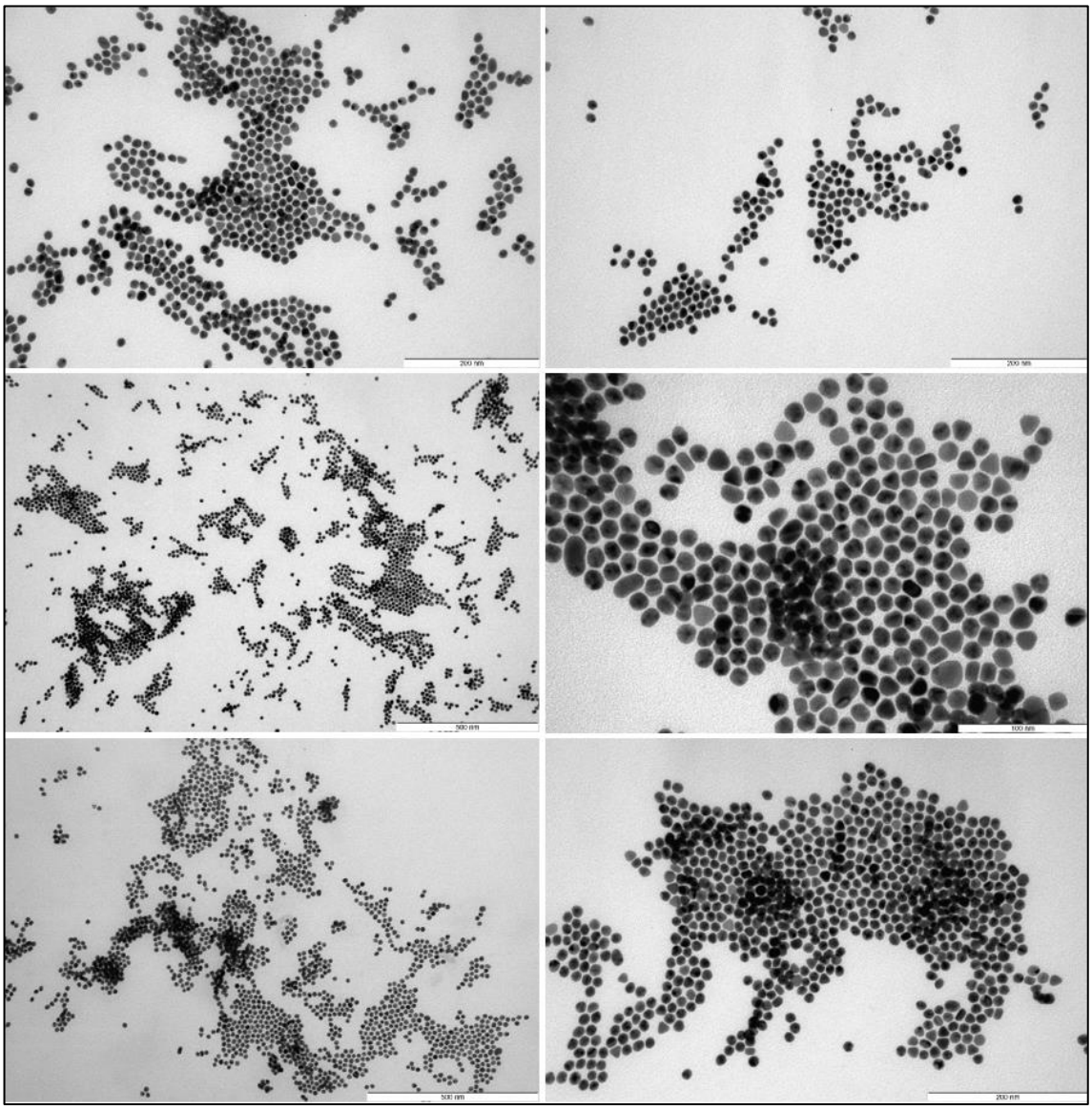

Figure S. 10. High magnification TEM images illustrate the size distribution of the MUDA-cit-AuNPs. These images conducted at different nanoscale bars 100, 200, and 500 nm.